Continental Deformation: New Tools and New Constraints on Convergent and Collisional Tectonic Systems from the Greater Caucasus

by

Alexander Tye

A dissertation submitted in partial fulfillment
of the requirements for the degree of
Doctor of Philosophy
(Earth and Environmental Sciences)
in the University of Michigan
2019

Doctoral Committee:

Professor Nathan Niemi, Chair
Professor Catherine Badgley
Associate Professor Eric Hetland
Assistant Research Scientist Aaron Wolf

Tufandag, Azerbaijan

Alexander R. Tye
alextye@umich.edu
ORCID ID: 0000-0002-5573-9115

In his hand are the depths of the earth; the heights of the mountains are his also. – Psalm 95:4

For my parents

ACKNOWLEDGMENTS

This dissertation reflects years of vital intellectual exchange and support provided by my friends and mentors. My parents have provided unwavering support of my interests as they have evolved over the years. Jan Tullis, Peter Gromet, Jim Head, and John Geissman helped me to identify and develop my interest in geology as an undergraduate student.

As a graduate student, my knowledge and interests have been shaped by my committee members and other members of the department. Aaron Wolf has been a constant source of creative ideas and enthusiastic support that I deeply appreciated. Eric Hetland has been a joy to learn from and his statistics knowledge has been very helpful. Catherine Badgley has been a generous and thoughtful committee member who has offered a distinct perspective and useful advice. Tim Stahl, though not on my committee, has been a great mentor and a prolific coauthor. Ben van der Pluijm, Kacey Lohmann, Becky Lange, Adam Simon, and Marin Clark have helped me to broaden my knowledge and develop my teaching strategies.

Several people were particularly helpful in the execution of my research. Megan Hendrick, Heather Kirkpatrick, and Lindsey Abdale helped with sample preparation and analyses. Rafiq Safarov was a dedicated and thoughtful field partner during my work in Azerbaijan. Amanda Maslyn has my deepest gratitude for all of the sample preparation, training, and other help she has provided me in the lab over the years. Kendra Murray and Eric Portenga provided useful and interesting discussions on research.

Friends within and outside the department have enriched my time in graduate school, including Adrianna, Alex, Alyssa, Becca, Billy, Charlie, Emma, Eric, Erin, Jenny, Katy, Kirk, Mark, Nik, Noveen, Pete, Petr, Rachel, Ryan, Sally, Xiaofei, and many others.

Finally, I am grateful to my advisor, Nathan Niemi. Nathan's generosity, advocacy, support, and the freedom he has offered me over the years have been exceptional. As his student, I have experienced some of the most intellectually rewarding work of my life.

TABLE OF CONTENTS

Dedication . . . . . **ii**

Acknowledgments . . . . . **iii**

List of Figures . . . . . **x**

List of Tables . . . . . **xii**

List of Appendices . . . . . **xiii**

Abstract . . . . . **xiv**

Chapter

1 Introduction **1**

1.1 Dissertation focus and contribution 1
1.2 Influence of surface processes 2
1.3 Relative and absolute dating 2
1.3.1 Geo- and thermochronology 3
1.3.1.1 Radioactive decay 3
1.3.1.2 Application of radioactive decay to geo- and thermochronology 4
1.3.1.3 Detrital zircon U-Pb geochronology 4
1.3.2 Relative dating methods 7
1.4 Bayesian inference 8
1.4.1 Selection between multiple model forms 9
1.5 Dissertation outline 11

2 Bayesian Population Correlation: A Probabilistic Approach to Inferring and Comparing Population Distributions for Detrital Zircon Ages **13**

2.1 Introduction 14
2.2 A Bayesian method for inferring ensembles of detrital zircon age populations 17
2.2.1 Representation of detrital zircon age distributions using b-splines 19
2.2.2 Quantifying the likelihood 21
2.2.3 Prior assumptions 23
2.2.4 Aggregation of probability model ensembles (PMEs) 25

2.3 Estimating correspondence between PMEs: Bayesian Population Correlation (BPC) . . . 26
2.4 Testing the behavior of BPC . . . 29
2.4.1 BPC behavior in a simple case . . . 29
2.4.2 Independence from sample size bias . . . 31
2.4.3 Interpreting the meaning of BPC values . . . 33
2.4.4 Limitations of our implementation of BPC . . . 36
2.5 Estimation of BPC uncertainties . . . 37
2.6 Implications of PMEs and BPC for analysis of detrital geochronology data 38
2.7 Conclusions . . . 39

3 Quantifying the Effects of Sediment Sorting, Transport, and Sequestration on Detrital Zircon U-Pb Age Populations Using Bayesian Population Correlation 41

3.1 Introduction . . . 42
3.2 Methods . . . 43
3.2.1 Relation of BPC to $\mathrm{zr_d}$ . . . 44
3.2.2 Using BPC-derived $\mathrm{zr_d}$ values to constrain catchment size, transport distance, and sediment transport processes . . . 46
3.3 BPC results and interpretation . . . 48
3.3.1 Hydraulic sorting of detrital zircon populations in river microenvironments . . . 48
3.3.2 Inferring sediment transport distance from zircon age group dilution . . . 50
3.3.3 Detrital zircon evidence for sediment sequestration in a fluvial system . . . 54
3.4 Conclusions . . . 57

4 Field Estimate of Paleoseismic Slip on a Normal Fault Using the Schmidt Hammer and Terrestrial LiDAR: Methods and Application to the Hebgen Fault (Montana, USA) . . . 59

4.1 Introduction . . . 60
4.2 Background . . . 61
4.2.1 Significance of single-event displacements in paleoseismology . . . 61
4.2.2 Geomorphic framework for relative dating of SEDs . . . 61
4.2.3 The Schmidt hammer in rock weathering and relative-age dating studies . . . 64
4.2.4 Identification of bedrock fault scarp slip patches using microtopography . . . 65
4.2.5 Study site . . . 66
4.3 Methods . . . 68
4.3.1 Schmidt hammer framework and field protocol . . . 68
4.3.2 Terrestrial LiDAR scanning (TLS) and roughness analysis . . . 70
4.3.3 Curve-fitting and SED determination . . . 70
4.3.4 Model selection . . . 71
4.4 Results . . . 72

4.4.1 Adjusted Geologic Strength Index (AGSI) . . . 72
4.4.2 Schmidt hammer R-values . . . 73
4.4.3 Model comparison of ΔR . . . 76
4.4.4 TLS-derived surface roughness . . . 76
4.5 Discussion . . . 78
4.5.1 Use of ΔR as preferred Schmidt hammer metric . . . 78
4.5.2 Apparent steps and SEDs of the Hebgen fault . . . 78
4.5.3 Reconciling SEDs with other records . . . 80
4.5.4 Practical considerations of Schmidt hammer methodology . . . 82
4.5.5 Applicability of step function fitting to SED identification . . . 84
4.6 Conclusions . . . 84

5 Schmidt Hammer and Terrestrial Laser Scanning (TLS) Used to Detect Single Event Displacements on the Pleasant Valley Fault (Nevada, USA) . . . 86

5.1 Introduction . . . 87
5.2 Background . . . 88
5.2.1 Relative age dating techniques . . . 88
5.3 Methods . . . 90
5.3.1 Study site . . . 90
5.3.2 Schmidt hammer methods . . . 93
5.3.3 Terrestrial Laser Scanning (TLS) methods . . . 93
5.3.4 Curve-fitting . . . 94
5.4 Results . . . 94
5.4.1 Schmidt hammer . . . 94
5.4.2 TLS . . . 98
5.5 Discussion . . . 101
5.5.1 Preferred model and demarcation of single event displacements (SEDs) . . . 101
5.5.2 Sources of uncertainty in determining SEDs . . . 102
5.5.3 Application to other limestone fault scarps—where can this be used and how can it be improved? . . . 103
5.6 Conclusions . . . 104

6 Sedimentary Response to Collisional Orogeny Recorded in Detrital Zircon Provenance of Greater Caucasus Foreland Basin Sediments . . . 106

6.1 Introduction . . . 107
6.2 Geological background . . . 111
6.2.1 Tectonic setting and history . . . 113
6.2.2 Potential sources of Cenozoic foreland-basin sediment . . . 114
6.3 Methods . . . 116
6.3.1 Sampling . . . 116
6.3.2 Data visualization . . . 121
6.4 Source-area detrital zircon signatures . . . 124
6.4.1 Detrital zircon age signatures of potential sources for Caucasus Cenozoic sediment . . . 124

6.4.2 Defining and representing detrital zircon source endmembers . . . 127
6.5 Foreland basin zircon U-Pb characteristics and provenance interpretation . 130
6.5.1 Distributed foreland basin samples of the western Greater Caucasus 130
6.5.2 Western foreland basin section . . . 132
6.5.3 Central foreland basin section . . . 134
6.5.4 Eastern foreland basin section . . . 135
6.5.5 Far eastern foreland basin section . . . 136
6.6 Tectonic context of observed zircon crystallization ages . . . 137
6.6.1 Cenozoic zircon crystallization . . . 137
6.6.2 Permian to Mesozoic zircon crystallization . . . 137
6.6.3 Precambrian to Carboniferous zircon crystallization . . . 138
6.7 Implications of Caucasus detrital zircon U-Pb age data for terrane boundaries and Tethyan tectonics . . . 139
6.7.1 Detrital zircon U-Pb age constraints on the original locations of Scythia, Greater Caucasus basement, and Transcaucasus basement domains . . . 141
6.7.2 Detrital zircon age constraints on the relationship between Greater Caucasus basement and Scythia . . . 141
6.7.3 Detrital zircon age constraints on the similarities and differences between Greater Caucasus basement and Transcaucasus basement 142
6.7.4 Constraints on the timing of accretion of Scythia, Greater Caucasus basement, and Transcaucasus basement to Eurasia . . . 143
6.7.5 Suture locations . . . 145
6.8 Implications for stratigraphic records of collision . . . 145
6.8.1 Late Cenozoic provenance and facies changes of Caucasus foreland basin sediment . . . 147
6.8.2 Drivers of observed facies and provenance changes . . . 148
6.8.3 Correlating basin width with facies and provenance changes . . . 151
6.8.4 Temporal links between collisional and sedimentary processes in the Caucasus . . . 151
6.8.5 Implications for other collisional orogens . . . 152
6.9 Conclusions . . . 154

7 Structural and Thermochronometric Data Provide Insight into Strain Accommodation within an Active Accretionary Prism, the Eastern Greater Caucasus . . . 156

7.1 Introduction . . . 157
7.2 Geological Background . . . 160
7.3 Methods . . . 161
7.3.1 Geologic mapping and cross-section construction . . . 161
7.3.2 Thermochronometry . . . 163
7.4 Structural and thermochronometric results and interpretation . . . 169
7.4.1 Agsu transect . . . 170
7.4.1.1 Geological description . . . 170
7.4.1.2 Structural interpretation . . . 171

7.4.1.2.1 Agsu thrust . . . 173
7.4.1.2.2 Northern thrust . . . 173
7.4.1.2.3 Internal deformation within the Eocene to Miocene turbidite sequence (EMtb) . . . 173
7.4.1.3 Shortening estimate . . . 174
7.4.2 Lahij transect . . . 175
7.4.2.1 Geological description . . . 175
7.4.2.2 Thermochronometric data . . . 179
7.4.2.3 Structural interpretation . . . 180
7.4.2.3.1 Basgal nappe thrust sheet . . . 180
7.4.2.3.2 Lithologic contrast and structural relationship between Vandam Zone and northern tectonostratigraphic packages . . . 182
7.4.2.3.3 Subsurface structure of the Lahij transect . . . 183
7.4.2.4 Shortening estimate . . . 185
7.4.3 Salavat Transect . . . 186
7.4.3.1 Geological description . . . 186
7.4.3.1.1 Southern segment . . . 186
7.4.3.1.2 Central segment . . . 188
7.4.3.1.3 Northern segment . . . 188
7.4.3.2 Thermochronometric data . . . 190
7.4.3.2.1 Central segment . . . 190
7.4.3.2.2 Northern segment . . . 191
7.4.3.3 Structural interpretation . . . 192
7.4.3.3.1 Southern segment . . . 192
7.4.3.3.2 Central segment . . . 194
7.4.3.3.3 Northern segment . . . 196
7.4.3.4 Shortening estimates . . . 199
7.4.3.4.1 Southern segment . . . 199
7.4.3.4.2 Central segment . . . 200
7.4.3.4.3 Northern segment . . . 200
7.4.4 Tahirjal transect . . . 201
7.4.4.1 Geological description . . . 201
7.4.4.2 Thermochronometric data . . . 202
7.4.4.3 Structural interpretation . . . 202
7.5 Discussion . . . 202
7.5.1 Range-wide structure and total shortening . . . 202
7.5.1.1 Geometry of major faults . . . 203
7.5.1.1.1 Modern basal detachment . . . 203
7.5.1.1.2 Zangi thrust . . . 203
7.5.1.2 Stratigraphic relationship between the Vandam Zone and northern, turbiditic stratigraphic packages . . . 206
7.5.1.3 Total shortening and internal deformation within the pervasively folded sequences of the range . . . 207
7.5.1.4 Finite strain partitioning in the range . . . 208

7.5.2 Temporal constraints on deformation . . . 208
7.5.2.1 Initiation of deformation within the Eastern Greater Caucasus . . . 209
7.5.2.1.1 Constraints from geodesy and paleomagnetic data . . . 209
7.5.2.1.2 Constraints from thermochronometry . . . 209
7.5.2.2 Initiation of slip on the present basal detachment . . . 210
7.5.2.2.1 Constraints from foreland basin deformation and stratigraphy . . . 210
7.5.2.2.2 Constraints from thermochronometry . . . 211
7.5.2.3 Strain partitioning between the basal detachment and the prism interior through time . . . 212
7.5.2.3.1 Constraints from thermochronometry . . . 212
7.5.2.3.2 Constraints from stratigraphy . . . 217
7.5.3 Implications for tectonics of the Greater Caucasus and the Arabia-Eurasia collision zone . . . 218
7.5.3.1 Along-strike variation in the magnitude of shortening accommodated within the Greater Caucasus . . . 218
7.5.3.2 Evolution of the Arabia-Eurasia collision zone . . . 219
7.5.4 Implications for accretionary prism deformation . . . 220
7.5.4.1 Modes of internal thickening of prisms . . . 220
7.5.4.2 Strain partitioning in accretionary prisms . . . 221
7.5.4.3 Temporal relationship between in-sequence and out-of-sequence prism deformation . . . 221
7.5.4.4 Prism growth . . . 222
7.6 Conclusions . . . 223

8 Conclusions . . . 225

8.1 Introduction . . . 225
8.2 Contributions . . . 225
8.2.1 Interpretation of detrital geochronology data . . . 225
8.2.2 Interpreting the paleoseismic slip history of bedrock fault scarps . 226
8.2.3 Sedimentary record of continental collision . . . 226
8.2.4 Internal deformation within an active accretionary prism . . . 227
8.3 Synthesis and future directions . . . 227

Appendices . . . 229

Bibliography . . . 246

LIST OF FIGURES

1.1 Impact of geologic processes versus sampling effects on detrital zircon age datasets . . . 5
1.2 Inferring depositional system characteristics from detrital zircon population dilution . . . 6

2.1 Impact of geologic processes versus sampling effects on detrital zircon age datasets . . . 15
2.2 Probability model ensembles (PMEs) for detrital zircon age datasets . . . 18
2.3 Modeling probability density functions using third order b-splines . . . 20
2.4 Calculating likelihood for candidate detrital zircon age probability density functions . . . 22
2.5 Endmember scenarios for Bayesian Population Correlation (BPC) normalization 27
2.6 BPC results for synthetic detrital zircon age populations . . . 30
2.7 BPC results for random subsamples of large detrital zircon age datasets . . . 32
2.8 Predictability of BPC as a function of the proportion of ages shared between two detrital zircon populations . . . 34
2.9 Evaluating BPC uncertainties . . . 37

3.1 Inferring depositional system characteristics from detrital zircon population dilution . . . 45
3.2 BPC results for distinct sedimentary microenvironments in a fluvial system . . 49
3.3 BPC constraints on paleo-stream length from detrital zircon population dilution 51
3.4 BPC constraints on sediment storage in fluvial systems . . . 55

4.1 Hebgen fault location, Montana, USA . . . 66
4.2 Expected Schmidt hammer R-values and cosmogenic nuclide ages for bedrock normal fault scarps . . . 68
4.3 Field photos and Adjusted Geological Strength Index for the Hebgen fault surface . . . 72
4.4 Hebgen fault scarp Schmidt hammer R-values . . . 73
4.5 Hebgen fault R-value range, *I5, and *Imax variation with scarp height . . . 74
4.6 Modeling ΔR as a function of scarp height . . . 75
4.7 Microtopographic roughness analysis of the Hebgen fault scarp . . . 77
4.8 Correspondence of Schmidt hammer R-value and cosmogenic nuclide data for the Hebgen fault scarp . . . 81

5.1 Pleasant Valley fault scarp location, Nevada, USA . . . 91

5.2 Pleasant Valley fault scarp Schmidt hammer R-value results 95
5.3 Modeling ΔR as a function of scarp height, Pleasant Valley north transect . . . 96
5.4 Modeling ΔR as a function of scarp height, Pleasant Valley south transect . . . 97
5.5 Microtopographic roughness analysis of Pleasant Valley fault scarp 99

6.1 Conceptual model of the transition from subduction to collision 109
6.2 Location and tectonic setting of the Caucasus 112
6.3 Detrital zircon sampling strategy 117
6.4 Existing and new detrital zircon sampling coverage for the Caucasus and Eurasia 118
6.5 Simplified geology and detrital zircon sample locations in the Greater and Lesser Caucasus 119
6.6 Photographs of sampled Cenozoic foreland-basin strata 120
6.7 Color scheme for detrital zircon sample symbology 122
6.8 Detrital zircon U-Pb age source signatures 123
6.9 Detrital zircon U-Pb age distributions from Caucasus foreland-basin strata . . . 128
6.10 Caucasus foreland-basin detrital zircon U-Pb age samples in stratigraphic context 129
6.11 Tectonic model of southern Eurasia Paleozoic terrane accretion constrained by detrital zircon U-Pb age data 144
6.12 Timeline of the sedimentary and kinematic effects of continental collision in the Caucasus 146

7.1 Eastern Greater Caucasus geology and tectonic setting 158
7.2 New geologic swath maps across the Eastern Greater Caucasus 159
7.3 Agsu transect geologic cross section 172
7.4 Photographs of important Eastern Greater Caucasus field relations 178
7.5 Modeled time-temperature histories for selected thermochronometry samples . 180
7.6 Lahij transect geologic cross section 181
7.7 Age-elevation plots for vertical thermochronometry sampling transects 190
7.8 Salavat transect, southern segment geologic cross section 193
7.9 Salavat transect, central segment geologic cross section 195
7.10 Salavat transect, northern segment geologic cross section 197
7.11 Eastern Greater Caucasus orogen-wide interpretive geologic cross section . . . 204
7.12 Inference of post-cooling rotation of thermochronometry sampling transects . . 214

A.1 Linear and logarithmic age scales for detrital zircon probability model ensembles (PMEs) 231
A.2 Likelihood, posterior, and prior calculation for detrital zircon probability density function modeling 232
A.3 Markov chain for typical PME inference 233
A.4 Performance of cumulative distribution function based detrital zircon correspondence metrics 237
A.5 Comparison of BPC with existing detrital zircon correspondence metrics for random subsamples of large published datasets 238

B.1 Hebgen scarp photo showing distribution of Schmidt hammer sample locations 245

LIST OF TABLES

4.1 Overview of methods for distinguishing weathering zones on fault scarps . . . 63
4.2 Bayesian Information Criterion (BIC) values for models of log ΔR versus scarp height, Hebgen fault . . . 76
4.3 BIC values for models of log topographic variance versus scarp height, Hebgen fault . . . 79

5.1 BIC values for models of log ΔR versus scarp height, Pleasant Valley fault . . 98
5.2 BIC values for models of scarp microtopographic roughness, Pleasant Valley fault . . . 100

6.1 Detrital zircon U-Pb age characteristics of sediment sources in the Caucasus region . . . 127

7.1 Names and locations of thermochronometry samples . . . 164
7.2 Apatite (U-Th)/He data . . . 167
7.3 Zircon (U-Th)/He data . . . 168
7.4 Apatite fission track sample data . . . 169

A.1 Calculation of expected Bayesian Population Correlation (BPC) values . . . 240

LIST OF APPENDICES

A Supporting information for Chapter 2. Bayesian Population Correlation: A Probabilistic Approach to Inferring and Comparing Population Distributions for Detrital Zircon Ages 229

B Supporting Information for Chapter 4. Field Estimate of Paleoseismic Slip on a Normal Fault Using the Schmidt Hammer and Terrestrial LiDAR: Methods and Application to the Hebgen Fault (Montana, USA) 243

ABSTRACT

The distribution of strain in continents is of primary importance in determining Earth's topography, the distribution of Earth resources, and hazards. This dissertation explores several records of continental deformation on timescales from thousands to millions of years and spatial scales from single faults to whole orogens. Many of these records are influenced by a complex set of factors and have limited sampling, so I develop and use new Bayesian statistical approaches in order to rigorously quantify uncertainties in data and interpretations. The dissertation work is broadly centered on three themes.

First, a novel Bayesian statistical method for modeling and comparing detrital zircon U-Pb age distributions is developed (Chapters 2, 3). It is shown that this method can be used to accurately infer uncertainties on population age distributions inferred from samples, leading to more robust interpretations of geologic processes from detrital geochronology datasets. In addition, the new method is shown to permit robust quantitative inferences of mixing and dilution between detrital zircon populations.

Second, the potential to infer paleoseismic slip histories from bedrock fault scarp rock properties including strength and roughness is explored using bedrock scarps of the Hebgen Fault, Montana, and the Pleasant Valley Fault, Nevada (Chapters 4, 5). It is demonstrated that on bedrock normal fault scarps, Schmidt hammer strength measurements and micro-topographic roughness are distributed in a stepwise pattern up-scarp, suggesting that these physical properties reflect exposure of patches of the scarp during successive earthquakes. The number and timing of paleoseismic events inferred from bedrock scarp strength and microtopography are consistent with available independent constraints on paleoseismic slip history for the analyzed scarps.

Third, the structural and stratigraphic effects of the transition from subduction to continental collision are investigated using the Greater Caucasus as a natural laboratory (Chapters 6, 7). A structural and thermochronometric investigation of the Eastern Greater Caucasus, where subduction is active, reveals that pervasive out-of-sequence folding in the core of the range plays a significant role in thickening the accretionary wedge as it grows in order to maintain a critical taper. Detrital zircon provenance of three foreland basin stratigraphic sections distributed along strike of the orogen reveals a detailed picture of the changes in source exposure and sediment routing that accompany the transition from subduction to collision. Initial entrance of tapered lower plate continental lithosphere into the subduction zone occurred between 15 and 8 Ma in the Caucasus, 3 - 10 Myrs before plate kinematic and exhumational effects of collision began at 5 Ma. Inferred collision-related slowing of plate convergence and acceleration of exhumation in the Caucasus coincided with the development of erosive conditions in the foreland basin between the two colliding continents and the concomitant formation of an axial drainage network that transported sediment laterally within the foreland basin.

The chapters of the dissertation are unified in their exploration of how continental deformation at different temporal and spatial scales is preserved in the geologic record. Because of the complexity of many of these records and the uncertainties inherent in their interpretation, Bayesian statistical methods offer a promising way to increase the reliability of quantitative geological interpretations, as documented in several of the chapters. In addition, the dissertation makes a significant contribution to our understanding of the transition from subduction to collision.

CHAPTER 1

Introduction

1.1 Dissertation focus and contribution

Tectonic deformation of Earth's continents drives the formation of topography (e.g., *England and Houseman*, 1986), regional and global changes in climate (e.g., *Edmond*, 1992; *Molnar et al.*, 2010; *Jagoutz et al.*, 2016), and the distribution of Earth resources. Unlike oceanic lithosphere, deformation of continental lithosphere is not restricted to plate boundaries, but can be distributed over small or large regions (e.g., *Oldow et al.*, 1990; *Wernicke et al.*, 2008). Understanding how strain is distributed in continental tectonic systems is key to assessing hazards, interpreting the geologic record of continental deformation (*van Hinsbergen et al.*, 2012; *Cowgill et al.*, 2016), and understanding the structure and rheology of continental lithosphere.

This dissertation makes new contributions to our understanding of strain accommodation within continents on temporal scales from thousands to millions of years and spatial scales from single faults to orogens. The contributions include new characterizations of the structural and sedimentary effects of geologic processes such as subduction and collision, as well as new tools and techniques for determining fault slip histories and changes in sediment routing. Many of the available datasets that constrain continental deformation on timescales of thousands to millions of years are affected by a complex set of tectonic and surface processes and sampling is often limited. Thus, rigorous quantification of the uncertainties associated with measurements and the resulting interpretation is essential. This dissertation makes several contributions to quantifying uncertainty and confidence in geologic datasets using a Bayesian statistical framework. Bayesian methods are well-suited to inference problems in Earth science where sampling is limited, solutions are often non-unique, and assumptions may significantly affect the outcome. The common threads of the chapters of the dissertation are a focus on exploiting connections between tectonic and surface processes to understand tectonic systems, use of multiple relative and absolute dat-

ing techniques to characterize the timing and pace of deformation processes, and the use of Bayesian statistics to interpret complex datasets. In this introduction, I discuss the influence of surface processes on the records investigated in the dissertation, review the relative and absolute dating methods employed in the dissertation, and discuss the Bayesian statistical framework and why it is useful in an Earth science context. I then provide a brief outline of the individual chapters.

1.2 Influence of surface processes

The processes of weathering, erosion, and sediment transport act to reduce the overall gravitational potential energy of Earth's landscapes, and therefore they have a dynamic relationship with tectonic processes that alter topography in the course of translating and deforming lithosphere (e.g., *Montgomery et al.*, 2001; *Wobus et al.*, 2006; *Molnar et al.*, 2007). The tectonic conclusions made in this dissertation rely in large part on records of weathering, erosion, and sediment transport from which changes in topography and exposure are inferred and related to tectonism. Several chapters deal with sediment provenance as a means to constrain tectonically-driven changes to topography, sedimentary basin geometry, and the exposure of sediment source areas. Two chapters use the intensity of weathering across bedrock fault scarps as a means to constrain their exposure history. Finally, one chapter uses thermochronometric measurements, which are influenced primarily by erosion on million-year timescales, in order to understand the history of deformation within an orogen. In these chapters, surface processes influence the relative and absolute age data that serve as a basis for the tectonic investigations presented here. Thus, attention is paid to the potential for climate (e.g., *Soreghan et al.*, 2002; *Litty et al.*, 2017), stochastic erosion events (e.g., *Ivanov et al.*, 2016), and autogenic processes (*Jerolmack and Paola*, 2010) to influence the investigated records, in addition to tectonic processes.

1.3 Relative and absolute dating

Relative and absolute dating methods permit the determination of the timing and pace of Earth processes. Several chapters of this dissertation use geo- and thermochronological methods that exploit the decay of radiogenic isotopes in order to constrain the history of mineral crystallization and cooling (*Faure*, 1977; *Reiners and Brandon*, 2006; *Dickin*, 2018). In addition, two chapters use rock strength and microtopography in order to determine relative ages of exposure at the outcrop scale (e.g., *Matthews and Shakesby*, 1984; *Goudie*, 2006; *Wei et al.*, 2013; *Wiatr et al.*, 2015; *He et al.*, 2016). Here, we briefly discuss

these methods, leaving more substantive discussions to the chapters where these techniques are used.

1.3.1 Geo- and thermochronology

Geochronology is the geologic age interpretation of measured radiogenic isotopes in rock and mineral systems, as well as paleomagnetic data and fossil assemblages. Techniques used in this dissertation are related to radiogenic isotope decay. Unstable radiogenic isotopes spontaneously decay at known rates in geologic materials, yielding daughter products. Measured concentrations of radioactive parents and daughters can be used to calculate the duration of time over which the daughter products have accumulated (*Faure*, 1977; *Dickin*, 2018). In this section, I discuss the basic mathematics of radioactive decay and the mineral and isotope systems that are radiometrically dated in this dissertation.

1.3.1.1 Radioactive decay

Radioactive decay is a chemical reaction in which an unstable, radioactive isotope decays to a different isotope by emission of radiation from its nucleus. The emitted radiation could take the form of an alpha particle, which is composed of two protons and two neutrons, or a beta particle, which is an electron or a positron (*Faure*, 1977; *Dickin*, 2018). The rate of decay of an unstable isotope, which equals the rate of production of daughter products, is proportional to the concentration of the unstable isotope in a geologic material:

$$-\frac{dN}{dt} = \lambda N, \tag{1.1}$$

where N is the concentration (number) of a particular unstable isotope and λ is a constant of proportionality known as the decay constant (*Faure*, 1977; *Dickin*, 2018). Thus, the concentration of the unstable isotope decreases exponentially over time:

$$N(t) = N_0 e^{-\lambda t}, \tag{1.2}$$

where N_0 is the initial concentration of the unstable isotope and $N(t)$ is the concentration after time t. The amount of daughter product equals the amount of the radioactive parent that has decayed:

$$D(t) = N_0 \left(1 - e^{-\lambda t}\right), \tag{1.3}$$

where $D(t)$ is the amount of daughter product after time t. Experiments have determined λ for many decay reactions. N_0 can often be assumed to be equal to the sum of $N(t)$ and

$D(t)$, so Eqns. (1.2, 1.3) can be solved to find t, the time since the accumulation of the daughter began (*Faure*, 1977; *Dickin*, 2018).

1.3.1.2 Application of radioactive decay to geo- and thermochronology

Geo- and thermochronology differ in the retentivity of the daughter product of interest in a geologic material. For instance, if a given daughter product is retained in a mineral at all temperatures beneath the melting temperature of the mineral, then the time t inferred from Eqns. (1.2, 1.3) reflects the duration of time since the mineral crystallized. This is the case with the U-Pb system in zircon under typical conditions (*Cherniak and Watson*, 2001), a system used for geochronology. On the other hand, many daughter products of radioactive decay can more readily diffuse out of a mineral than Pb can diffuse out of zircon. Diffusion is temperature and time dependent, and in such systems a measured radiometric age depends on the particularities of the time-temperature history of a given sample (*Wolf et al.*, 1998). Thermochronology is the use of radiometric ages measured from these systems to constrain the time-temperature history of a given sample. The behavior of a thermochronometric system can be characterized by a nominal 'closure temperature,' the temperature or range of temperatures that correspond to a measured radiometric age for a set of prescribed time-temperature histories (*Dodson*, 1973). The closure temperatures of common thermochronometers range from 60° C to >500° C (*Reiners and Brandon*, 2006). In this dissertation, I use a variety of geo- and thermochronometric systems. In this introduction, I provide a brief summary of the use of U-Pb ages of detrital zircons as a sediment provenance indicator because of the use of this technique in several chapters, and I leave discussions of other geo- and thermochronometric systems to their respective chapters.

1.3.1.3 Detrital zircon U-Pb geochronology

Because zircon U-Pb ages are robust to Earth surface conditions (*Cherniak and Watson*, 2001; *Gehrels*, 2012), the ages of detrital zircons are commonly used as a tracer of sediment transport in modern and ancient depositional systems (summarized in *Gehrels*, 2012). Populations of detrital zircon ages are determined by a combination of factors including the ages of zircons present in source areas, the zircon concentration within source areas, spatial and temporal variations in erosion, and sediment transport and storage processes (e.g., *Amidon et al.*, 2005; *Dickinson*, 2008; *Tranel et al.*, 2011; *Gehrels*, 2012; *Satkoski et al.*, 2013; *Garçon and Chauvel*, 2014). Detrital zircon age populations are often multi-peaked probability distributions that cannot easily be fit to well-described distribution types (Fig.

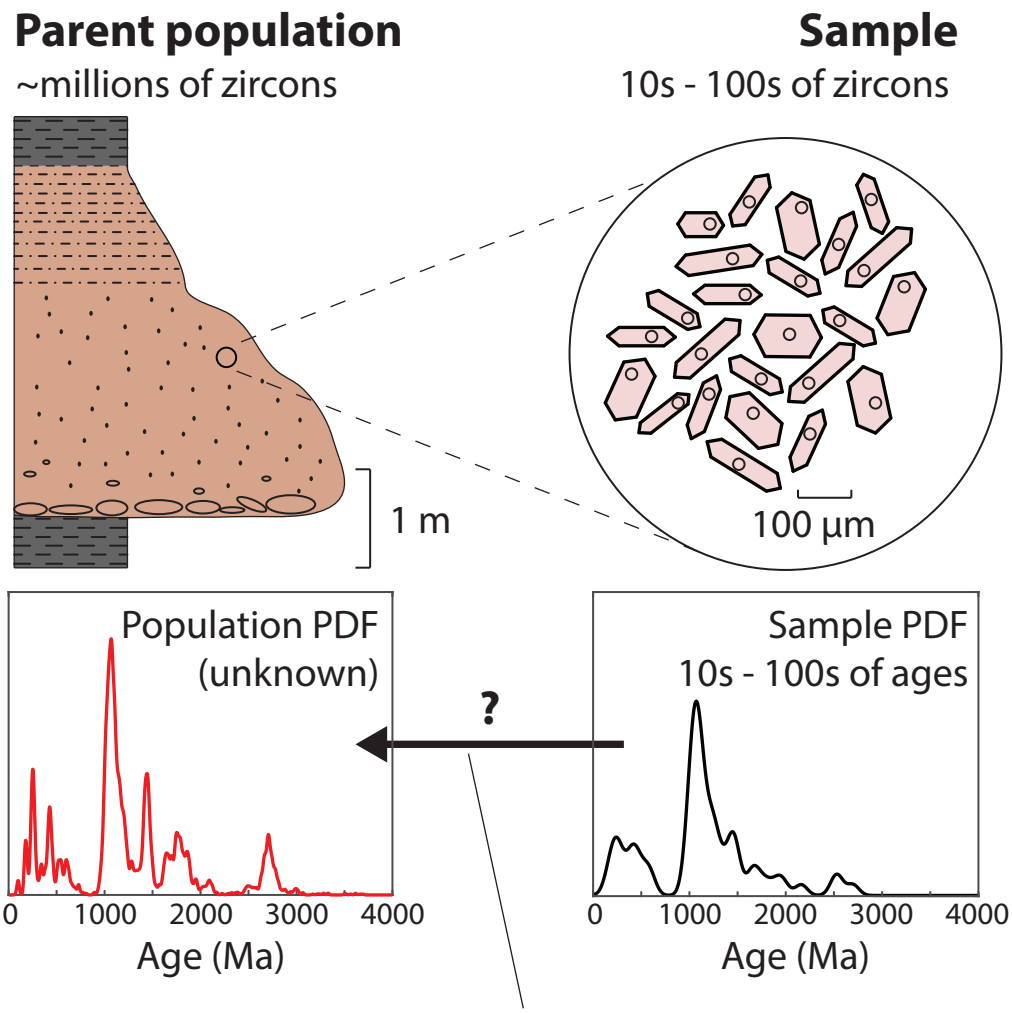

Figure 1.1: Detrital zircon populations are shaped by geologic processes and detrital zircon samples are influenced both by these geologic processes and by sampling effects. A sample age distribution can deviate significantly from its parent population distribution, though it is the unknown parent population that is relevant for geological interpretation. Thus, the choice of how to infer parent population characteristics from samples is critical. The population shown is a large detrital zircon dataset (*Pullen et al.*, 2014) and the sample is a random subsample (n = 60) of the dataset. Plots use the kernel density estimation method of *Botev et al.* (2010). Reproduced from Chapter 2.

2.1). Because of the complexity of these population age distributions, detrital zircon U-Pb age samples are subject to significant sampling effects such that sample age distributions differ significantly from population age distributions (Fig. 2.1; e.g., *Dodson et al.*, 1988; *Vermeesch*, 2004; *Andersen*, 2005).

If characteristics such as the relative proportions of different U-Pb age peaks can be inferred in detrital zircon populations, then samples can be used to make quantitative in-

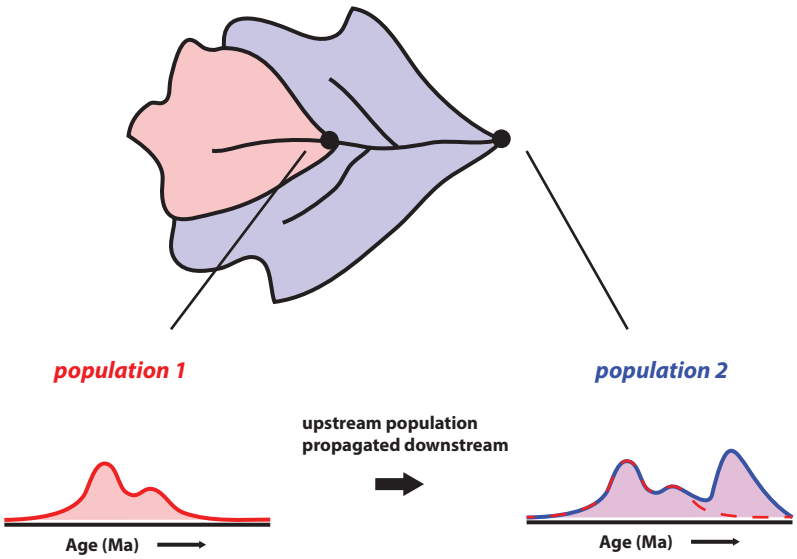

Figure 1.2: If two detrital zircon U-Pb age samples come from two different positions within the same depositional system, then the dilution of ages between the two samples carries information about zircon fertility, sediment storage, and/or spatial differences in erosion. The figure shows a schematic diagram of a catchment in which two samples were collected, and the zircon age distributions of the two sampled populations are shown below. The red portion of the catchment corresponds to the area upstream of sample 1 whereas the blue portion of the catchment corresponds to the area upstream of sample 2, but not sample 1. Reproduced from Chapter 3.

ferences about erosion, zircon fertility, and other factors that influence the zircon U-Pb age populations in a sedimentary environment (Fig. 3.1; e.g., *Niemi*, 2013). However, given typical sample sizes of detrital zircon U-Pb age studies ($n \sim 100$; *Sharman et al.*, 2018), the effects of limited sampling typically inhibit reliable inference of U-Pb age population characteristics from detrital zircon samples (*Andersen*, 2005). The inability to accurately infer U-Pb age population characteristics from samples is evidenced by sample size biasing exhibited by most quantitative comparative metrics for detrital zircon datasets, where at typical sample sizes, two samples randomly drawn from the same population are not recognized as having potentially identical parent populations (*Satkoski et al.*, 2013; *Saylor and Sundell*, 2016; *Tye et al.*, 2019). In this dissertation, I develop a statistical method that is capable of accurately inferring candidate parent populations and their uncertainties from detrital zircon U-Pb age samples. This method has the potential to significantly enhance the interpretation of tectonic and surface processes from detrital zircon U-Pb ages and other quantitative sediment provenance tracers. I employ a Bayesian statistical framework for the new method because of the ease with which uncertainties in inferred detrital zircon U-Pb age populations can be assessed.

1.3.2 Relative dating methods

The use of relative dating techniques is common in geomorphology, and where relative ages are correlated with absolute ages they can yield important information about the timing and pace of landscape evolution (*Birkeland*, 1982; *Matthews and Shakesby*, 1984; *Shiraiwa and Watanabe*, 1991; *Nishiizumi et al.*, 1993; *Gosse and Phillips*, 2001; *Goudie*, 2006; *Shakesby et al.*, 2006). In this dissertation, I use Schmidt hammer rock strength measurements and microtopographic roughness as means of relative dating. The use of both of these techniques is briefly discussed here.

The Schmidt hammer is a handheld strength testing device originally designed for use on concrete that has been applied to studies of rock weathering in many contexts (*Matthews and Shakesby*, 1984; *Goudie*, 2006). Though several types of Schmidt hammers exist, the most commonly used by geomorphologists is the N type (*Goudie*, 2006). The Schmidt hammer measures rock strength on a unitless scale from 0 to 100, the value of which is referred to as the R value. R values are correlated with uniaxial compressive strength and Young's modulus (see review in *Goudie*, 2006). Schmidt hammer R values have been shown to vary with the intensity of weathering on a rock surface, permitting their use as an indicator of relative exposure ages of these surfaces (*Matthews and Shakesby*, 1984; *Aydin and Basu*, 2005; *Stahl et al.*, 2013; *Matthews et al.*, 2016). Different authors have

explored different methods of quantifying weathering intensity using individual R values or differences between R values measured from successive impacts at a single location (*Aydin and Basu*, 2005; *Shakesby et al.*, 2006; *Matthews et al.*, 2016). R values are also sensitive to lithology (e.g., *Matthews et al.*, 2016), making relative exposure dating difficult when multiple lithologic types are involved. In this dissertation, I present Schmidt hammer results from two bedrock fault scarps in the western U.S. from which relative exposure ages are inferred.

I also make use of topographic roughness as a measure of weathering intensity, a proxy for relative exposure age. Relationships between topography and landform age have been explored across a variety of spatial scales including whole-orogen scales (e.g., *Baldwin et al.*, 2003), landform scale (*Andrews and Hanks*, 1985; *Andrews and Bucknam*, 1987), and the scale of microtopography of bedrock outcrops (*Wei et al.*, 2013; *Wiatr et al.*, 2015; *He et al.*, 2016). This dissertation makes use of millimeter-scale microtopography of bedrock fault scarp outcrops, measured using terrestrial lidar, as a means of relative exposure age dating. Previous studies indicate that surface roughness increases over time due to weathering, particularly on spatial scales of several centimeters and smaller (*Wei et al.*, 2013; *Wiatr et al.*, 2015; *He et al.*, 2016). In the dissertation, I use this expected roughening as a proxy for relative exposure age of large patches of bedrock fault scarps inferred to have been exposed during successive earthquakes. Existing studies of microtopography as a proxy for relative exposure age (*Wei et al.*, 2013; *Wiatr et al.*, 2015; *He et al.*, 2016), including those within this dissertation, are confined to carbonate lithologies, and the utility of this method on non-carbonate lithologies is unknown.

1.4 Bayesian inference

Many problems in Earth science are undersampled, have non-unique solutions, and are strongly influenced by assumptions. Bayesian methods are useful for such problems because they require an explicit statement of the assumptions used for parameter estimation and permit the rigorous quantification of uncertainty (*Raftery*, 1995; *Kruschke*, 2013). Because of their utility, Bayesian methods have found use in many branches of Earth science, including geochronology, geodesy, and paleoseismology (*Bronk Ramsey*, 2009; *Gallagher*, 2012; *Cowie et al.*, 2017; *Hines and Hetland*, 2017; *Tye and Stahl*, 2018; *Tye et al.*, 2019).

Bayesian inference is based on Bayes' Therem, which arises from the definition of conditional probability:

$$\mathrm{P}(B|A) = \frac{\mathrm{P}(A|B)\ \mathrm{P}(B)}{\mathrm{P}(A)}, \tag{1.4}$$

where A and B are two events. Bayes' theorem can be used in model selection to quantify the acceptable distribution of model parameters $\boldsymbol{\theta}$ given the distribution of data $\boldsymbol{d}$ (*Raftery*, 1995):

$$\mathrm{P}(\boldsymbol{\theta}|\boldsymbol{d}) = \frac{\mathrm{P}(\boldsymbol{d}|\boldsymbol{\theta})\ \mathrm{P}(\boldsymbol{\theta})}{\mathrm{P}(\boldsymbol{d})} \tag{1.5}$$

Because a given dataset $\boldsymbol{d}$ does not change as a function of model parameters $\boldsymbol{\theta}$, $\mathrm{P}(\boldsymbol{d})$ can be ignored for model parameter estimation for a given dataset. $\mathrm{P}(\boldsymbol{\theta}|\boldsymbol{d})$ is referred to as the posterior and represents the statistical support the data provide for a given set of model parameters. $\mathrm{P}(\boldsymbol{d}|\boldsymbol{\theta})$ is referred to as the likelihood and is the probability of observing the dataset for a given set of model parameters. $\mathrm{P}(\boldsymbol{\theta})$ is referred to as the prior and reflects foreknowledge or assumptions about the model parameters that are independent of the observed data (*Raftery*, 1995; *Kruschke*, 2013). Eqn. 1.5 can be used with random draws of candidate model parameters $\boldsymbol{\theta}$, referred to as Monte Carlo sampling, in order to characterize the distribution of $\mathrm{P}(\boldsymbol{\theta}|\boldsymbol{d})$, which describes the permissible model parameters $\boldsymbol{\theta}$ given the data $\boldsymbol{d}$ and prior assumptions about the model parameters $\mathrm{P}(\boldsymbol{\theta})$. The shape and width of the distribution of $\mathrm{P}(\boldsymbol{\theta}|\boldsymbol{d})$ indicate the uncertainties on inferred model parameters and the covariance structure.

An important aspect of Bayesian inference is the expression of foreknowledge or assumptions about the model using the prior term $\mathrm{P}(\boldsymbol{\theta})$. What type of prior distribution to use is determined by an investigator and depends on the availability of independent constraints on the model parameters $\boldsymbol{\theta}$ that the investigator seeks to infer. Prior distributions can range from uniform distributions, which signify minimal foreknowledge of the model parameters, to narrow probability distributions where parameters are well constrained, for instance by previous study (e.g., *Kruschke*, 2013). Thus, prior distributions provide a transparent and explicit statement of assumptions about a given system.

This dissertation includes a new Bayesian approach to modeling the probability distributions of detrital zircon U-Pb age samples. The Bayesian approach uses a set of parameters $\boldsymbol{\theta}$ to represent a U-Pb age distribution and uses Eqn. 1.5, together with random generation of candidate model parameters, to infer the set of U-Pb age distributions that are consistent with an observed set of zircon ages $\boldsymbol{d}$. This new approach permits analysis of the uncertainty inherent in inferring a population distribution from a sample.

1.4.1 Selection between multiple model forms

In instances where the functional form of a model is not known, it can be desirable to compare the probabilistic support for two different hypothesized model forms. A Bayesian framework can be used to accomplish such a comparison by using the Bayes factor (*Jef-*

freys, 1998):

$$K = \frac{\int \mathrm{P}(\boldsymbol{\theta_1}|\boldsymbol{d})\ d\boldsymbol{\theta_1}}{\int \mathrm{P}(\boldsymbol{\theta_2}|\boldsymbol{d})\ d\boldsymbol{\theta_2}}, \tag{1.6}$$

where $\boldsymbol{\theta_1}$ and $\boldsymbol{\theta_2}$ represent sets of model parameters that correspond to two different functional forms that are being compared to one another. Thus, the Bayes factor integrates the posteriors of two different model forms over their respective parameter spaces and then uses the ratio of one integrated posterior to the other as a measure of which model form has greater statistical support.

In cases where it is impossible or impractical to calculate the integral of the posterior for two different model forms, different metrics can be used to compare the statistical support for two different model forms. These metrics include the Bayesian Information Criterion (BIC; *Schwarz et al.*, 1978), and the Akaike Information Criterion (AIC; *Akaike*, 1981, 1998). BIC and AIC are functions of the maximum likelihood of a given model form, the number of model parameters, and the sample size (*Schwarz et al.*, 1978; *Akaike*, 1981, 1998). Both metrics seek to determine which of two model forms yields the most appropriate fit by maximizing likelihood but also penalizing models that overfit the data (*Burnham and Anderson*, 2004). BIC was derived as an approximation to the Bayes factor (*Schwarz et al.*, 1978; *Burnham and Anderson*, 2004), and AIC can be formulated as an approximation to the Bayes factor given certain priors (*Burnham and Anderson*, 2004). *Burnham and Anderson* (2004) argue that if the data can be modeled by a set of many effects of variable influence and the model is intended to capture all of these effects, then AIC is the most appropriate selection criterion, and BIC may favor models that are too simple and do not account for some of the subtler effects. However, if the data can be modeled by a small number of major effects, then BIC is the most appropriate selection criterion (*Burnham and Anderson*, 2004).

As part of this dissertation, I use these techniques to determine the most appropriate model of the distribution of rock strength and microtopographic roughness on bedrock fault scarps. The purpose of the analysis is to recover the broad trends of rock strength and topographic roughness that may yield insight into the exposure history of an entire outcrop. Modeling smaller magnitude effects such as minor lithologic heterogeneities is not desired. Therefore, I use BIC rather than AIC to select between a variety of functional forms to fit the data.

1.5 Dissertation outline

This dissertation consists of this introduction, six content chapters, and a conclusion. Here, I briefly introduce the remaining chapters, mentioning the major topics and aims of each chapter.

Chapter 2 introduces a Bayesian statistical framework to address a longstanding issue with detrital zircon U-Pb geochronology sediment provenance studies. U-Pb ages of detrital zircons are commonly used as a tracer of sediment provenance. The distributions of these ages in a given sample can be highly complex, and previous methods for modeling and comparing these datasets are biased with respect to sample size, potentially affecting the validity and reliability of tectonic and sedimentological interpretations that could be made from the data. The Bayesian method introduced in the chapter, called Bayesian Population Correlation (BPC), quantifies sampling-related uncertainties and permits more robust quantitative tectonic and sedimentological interpretations of detrital zircon U-Pb datasets.

Chapter 3 presents a series of applications of BPC to published detrital zircon U-Pb age datasets. The applications demonstrate the utility of BPC for quantifying the effects of sedimentary processes such as sorting, dilution, and storage on detrital zircon populations. The chapter develops a series of equations that can easily be applied in combination with BPC analysis to test for the effects of these sedimentary processes in other detrital zircon U-Pb age datasets.

Chapter 4 presents a new method for inferring paleoseismic slip histories on faults with exposed bedrock fault scarps. The chapter explores the use of the distribution of rock strength on a bedrock fault scarp as an indicator of the boundaries of paleoseismic slip patches that were exposed in successive earthquake events. We use a Bayesian model selection technique, the Bayesian Information Criterion (*Schwarz et al.*, 1978), to assess the structure of the distribution of rock strength on the Hebgen Lake fault surface in Montana, as measured by a Schmidt hammer, a standard strength testing device. We find that the distribution of rock strength on the Hebgen Lake fault is best fit by a step function, consistent with the effects of instantaneous exposure of slip patches during successive earthquakes.

Chapter 5 builds on the rock strength paleoseismic method presented in chapter 4, applying the method to the Pleasant Valley fault scarp in Nevada, where the paleoseismic history is well-constrained and there is space to conduct multiple Schmidt hammer rock strength surveys. We compare the results of the strength testing to other techniques such as measurement of fault scarp surface roughness, finding that available observational and quantitative methods agree on a single paleoseismic slip history for the scarp. This study

provides additional support for rock strength testing as a method for assessing paleoseismic slip histories. Together, Chapters 4 and 5 provide new data that constrain the spatial and temporal distribution of strain in the Basin and Range province, a region of extensional deformation distributed throughout a broad section of western North American lithosphere.

Chapter 6 explores the sedimentary record of the initiation of continental collision in the Greater Caucasus orogen, in which continental collision is inferred to have begun $\sim$5 Ma. The chapter combines a comprehensive detrital zircon U-Pb age dataset from the region with a compilation of published stratigraphic interpretations to characterize the evolution of foreland basin sedimentation, sediment sources, and drainage networks during the initiation of collision. The study yields a set of specific observable criteria for the beginning of continental collision that may clarify the timing of initial collision in more mature collisional orogens. In this way, the study provides a basis for testing hypotheses about the climatic and tectonic effects of the initiation of continental collision in Earth's largest orogens.

Chapter 7 uses a new structural and thermochronometric dataset to characterize the crustal structure and deformation history of an active accretionary prism, the Eastern Greater Caucasus. Structural geologic mapping from across the range is used to constrain the crustal architecture of the accretionary prism. Thermochronometry data are used in order to characterize how strain is accommodated within the prism over time. The study increases our understanding of how convergent tectonic deformation is accommodated along plate boundaries.

Chapter 8 briefly summarizes the findings of the chapters and discusses the overall contributions of the dissertation.

CHAPTER 2

Bayesian Population Correlation: A Probabilistic Approach to Inferring and Comparing Population Distributions for Detrital Zircon Ages *

Abstract

Populations of detrital zircons are shaped by geologic factors such as sediment transport, erosion mechanisms, and the zircon fertility of source areas. Zircon U-Pb age datasets are influenced both by these geologic factors and by the statistical effects of sampling. Such statistical effects introduce significant uncertainty into the inference of parent population age distributions from detrital zircon samples. This uncertainty must be accounted for in order to understand which features of sample age distributions are attributable to earth processes and which are sampling effects. Sampling effects are likely to be significant at a range of common detrital zircon sample sizes (particularly when $n \lesssim 300$).

In order to more accurately account for the uncertainty in estimating parent population age distributions, we introduce a new method to infer probability model ensembles (PMEs) from detrital zircon samples. Each PME represents a set of the potential parent populations that are likely to have produced a given zircon age sample. PMEs form the basis of a new metric of correspondence between two detrital zircon samples, Bayesian Population Correlation (BPC), which is shown in a suite of numerical experiments to be unbiased with respect to sample size. BPC uncertainties can be directly estimated for a specific sample comparison, and BPC results conform to analytical predictions when comparing popula-

*Chapter 2 is published in *Chemical Geology*: Tye, A. R., Wolf, A. S., & Niemi, N. A. (2019). Bayesian population correlation: A probabilistic approach to inferring and comparing population distributions for detrital zircon ages. Chemical Geology, 518, 67-78. Supplemental material is available in Appendix A. Software that facilitates our analysis can be found at https://github.com/alextye/BPC

tions with known proportions of shared ages. We implement all of these features in a set of MATLAB® scripts made freely available as open-source code and as a standalone application. The robust uncertainties, lack of sample size bias, and predictability of BPC are desirable features that differentiate it from existing detrital zircon correspondence metrics. Additionally, analysis of other sample limited datasets with complex probability distributions may also benefit from our approach.

2.1 Introduction

Detrital zircon U-Pb ages can provide a robust indicator of the provenance of sedimentary rocks or modern sediment through comparison with the ages of potential source rocks. The population of zircon ages in a sedimentary rock or modern sedimentary environment depends on source ages, zircon fertility of source areas, spatial and temporal variations in erosion, and sediment transport processes in the catchment (e.g., *Amidon et al.*, 2005; *Dickinson*, 2008; *Tranel et al.*, 2011; *Gehrels*, 2012; *Satkoski et al.*, 2013; *Garçon and Chauvel*, 2014). Often, these zircon age populations are multi-modal, with the number and distribution of peaks unknown. A set of detrital zircon U-Pb age measurements thus reflects the influence of earth processes, operator choices about which part of a grain to analyze (e.g., *Hanchar and Miller*, 1993), and the statistical effects of random sampling. Given the complexity of many detrital zircon age distributions, sampling effects can be significant and it is important to consider the method by which parent population characteristics are inferred from samples (Fig. 2.1).

Historically, detrital zircon sample sizes have been chosen based on the probability of detecting the presence or absence of particular zircon age groups (*Dodson et al.*, 1988; *Vermeesch*, 2004, suggest sample sizes of 60 and 117, respectively). Unfortunately, these sample sizes have been found to be inadequate for representing the relative proportions of age groups in the parent population (*Andersen*, 2005). Recent analytical advances facilitate the acquisition of larger samples (n = 300 - 4000) that more fully represent the underlying parent population (*Fedo et al.*, 2003; *Gehrels et al.*, 2008; *Pullen et al.*, 2014), but a significant portion of published samples, even in recent studies, are characterized by smaller sample sizes ($n \sim$ 80 - 120; *Sharman et al.*, 2018).

The dominant tool for detrital zircon interpretation has traditionally been visual comparison of probability density plots (*Hurford et al.*, 1984) or age histograms. With the widespread recognition that visual inspection is prone to analyst bias (e.g., *Sircombe*, 2000; *Satkoski et al.*, 2013), several workers have proposed quantitative metrics for assessing the correspondence between detrital zircon samples (e.g., *Gehrels*, 2000; *DeGraaff-Surpless*

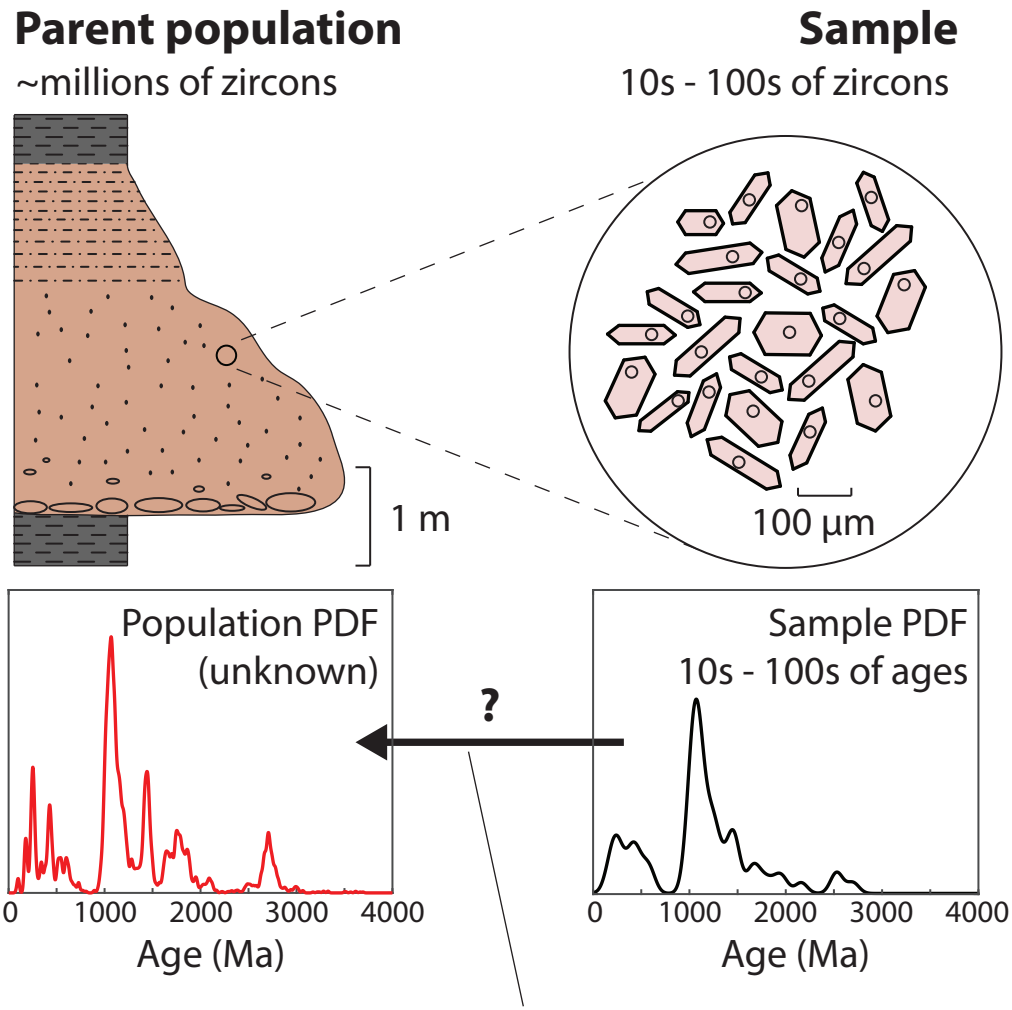

Figure 2.1: Detrital zircon populations are shaped by geologic processes and detrital zircon samples are influenced both by these geologic processes and by sampling effects. A sample age distribution can deviate significantly from its parent population distribution, though it is the unknown parent population that is relevant for geological interpretation. Thus, the choice of how to infer parent population characteristics from samples is critical. The population shown is a large detrital zircon dataset (*Pullen et al.*, 2014) and the sample is a random subsample (n = 60) of the dataset. Plots use the kernel density estimation method of *Botev et al.* (2010).

et al., 2003; *Saylor et al.*, 2012, 2013; *Satkoski et al.*, 2013; *Vermeesch*, 2013). The introduction of such quantitative metrics has greatly enhanced the interpretation of detrital zircon age data, facilitating comparison of greater numbers of samples.

Many metrics are used, including quantities associated with the Kolmogorov-Smirnov (K-S) and Kuiper statistical tests (*DeGraaff-Surpless et al.*, 2003; *Lawrence et al.*, 2011; *Vermeesch*, 2013; *Saylor and Sundell*, 2016), and several metrics developed specifically for detrital zircon age distributions, including Similarity (*Gehrels*, 2000), Cross Correlation (*Saylor et al.*, 2012, 2013) and Likeness (*Satkoski et al.*, 2013). Quantitative metrics of correspondence also permit the application of tools such as multi-dimensional scaling (*Vermeesch*, 2013; *Spencer and Kirkland*, 2016) and mixture modeling (e.g., *Amidon et al.*, 2005; *Kimbrough et al.*, 2015; *Sharman and Johnstone*, 2017; *Sundell and Saylor*, 2017) to detrital zircon datasets. However, geological interpretations made from these quantitative metrics are limited by the degree to which detrital zircon samples accurately represent sampled parent populations, and there is reason to believe many samples may not be very representative (e.g., *Andersen*, 2005; *Pullen et al.*, 2014; *Ibañez-Mejia et al.*, 2018). This limitation of existing quantitative metrics is evident in the sample size biasing observed in metric values (*Satkoski et al.*, 2013; *Saylor and Sundell*, 2016). Relatedly, existing metrics do not provide ways to estimate confidence intervals on metric values, and metric behavior is not well understood beyond indicating that some sample pairs are relatively more alike or less alike than other pairs. Given the complexity of detrital zircon age distributions and the limited sampling that characterizes many datasets, there is an ongoing need for new metrics of correspondence that behave in stable and predictable ways and permit robust estimation of metric uncertainty.

Here, we introduce a new method of inferring and comparing zircon age population distributions that formally incorporates the uncertainty inherent in inferring population distributions from detrital zircon samples. Accounting for this uncertainty is important for detrital zircon studies because most parent populations are too complex to be adequately represented by typical sample sizes, and such accounting may also result in a more stable and predictable correspondence metric. Our method infers sets of potential parent populations that are likely to have produced a given sample, which we refer to as probability model ensembles (PMEs; Fig. 2.2). We use a Bayesian framework for this inference because such a framework allows the rigorous quantification of how well any candidate parent population is statistically supported by a given sample. Within this framework, a Markov Chain Monte Carlo (MCMC) procedure is used to aggregate the potential parent populations contained in each PME. PMEs can be plotted to visually assess the level of constraint that a given zircon age sample places on its parent population. PMEs also form the basis

for a new correspondence metric, Bayesian Population Correlation (BPC), which reflects the likelihood that two samples were drawn from the same parent population, as opposed to two distinct parent populations. BPC is the first detrital zircon correspondence metric to display near-complete freedom from sample size bias. In addition, BPC uncertainties can be directly estimated for a specific dataset comparison and BPC results can be predicted from population characteristics using an analytical expression we derive from probability theory. Such predictability permits quantitative interpretations about processes affecting parent populations (e.g., dilution in a sedimentary system). In order to facilitate the use of our methods, we provide MATLAB® scripts (also available as a standalone application) for inferring PMEs and calculating BPC (https://github.com/alextye/BPC).

2.2 A Bayesian method for inferring ensembles of detrital zircon age populations

Earth processes act on populations of detrital zircons, of which measured age samples are subsets (Fig. 2.1). Therefore, making geological interpretations from detrital zircon age data requires using age samples to infer the characteristics of parent population age distributions. Such inference is uncertain because many different parent population age distributions may have produced a given sample set. However, some potential parent populations are far more likely than others. Identifying the set of potential parent populations that are likely to have produced a sample set of observed ages could thus permit more robust geological interpretations of detrital zircon age samples. Here, we present a Bayesian approach for inferring sets of detrital zircon parent populations that are consistent with a set of observed ages. This approach is quantitative and internally consistent, and may lead to more robust interpretation of detrital zircon age samples.

Our method uses Bayes' Theorem to quantify the level of statistical support that a set of zircon ages provides for a candidate parent population. Bayes' Theorem expresses the probability that a particular model, defined by parameters $\boldsymbol{\theta}$, fits a dataset $\boldsymbol{d}$ (*Raftery*, 1995):

$$\mathrm{P}(\boldsymbol{\theta}|\boldsymbol{d}) \propto \mathrm{P}(\boldsymbol{d}|\boldsymbol{\theta})\ \mathrm{P}(\boldsymbol{\theta}) \tag{2.1}$$

with bold symbols indicating vectors. $\mathrm{P}(\boldsymbol{\theta}|\boldsymbol{d})$ is the posterior probability that model $\boldsymbol{\theta}$ accurately describes the process that produced dataset $\boldsymbol{d}$, $\mathrm{P}(\boldsymbol{d}|\boldsymbol{\theta})$ is the likelihood of observing data $\boldsymbol{d}$ given probability model $\boldsymbol{\theta}$, and $\mathrm{P}(\boldsymbol{\theta})$ is the prior probability of $\boldsymbol{\theta}$ based on $a\ priori$ assumptions about the distribution of the model parameters (see Section 2.2.3). For a given dataset $\boldsymbol{d}$, $\mathrm{P}(\boldsymbol{\theta}|\boldsymbol{d})$, $\mathrm{P}(\boldsymbol{d}|\boldsymbol{\theta})$, and $\mathrm{P}(\boldsymbol{\theta})$ are distributions of probability over all

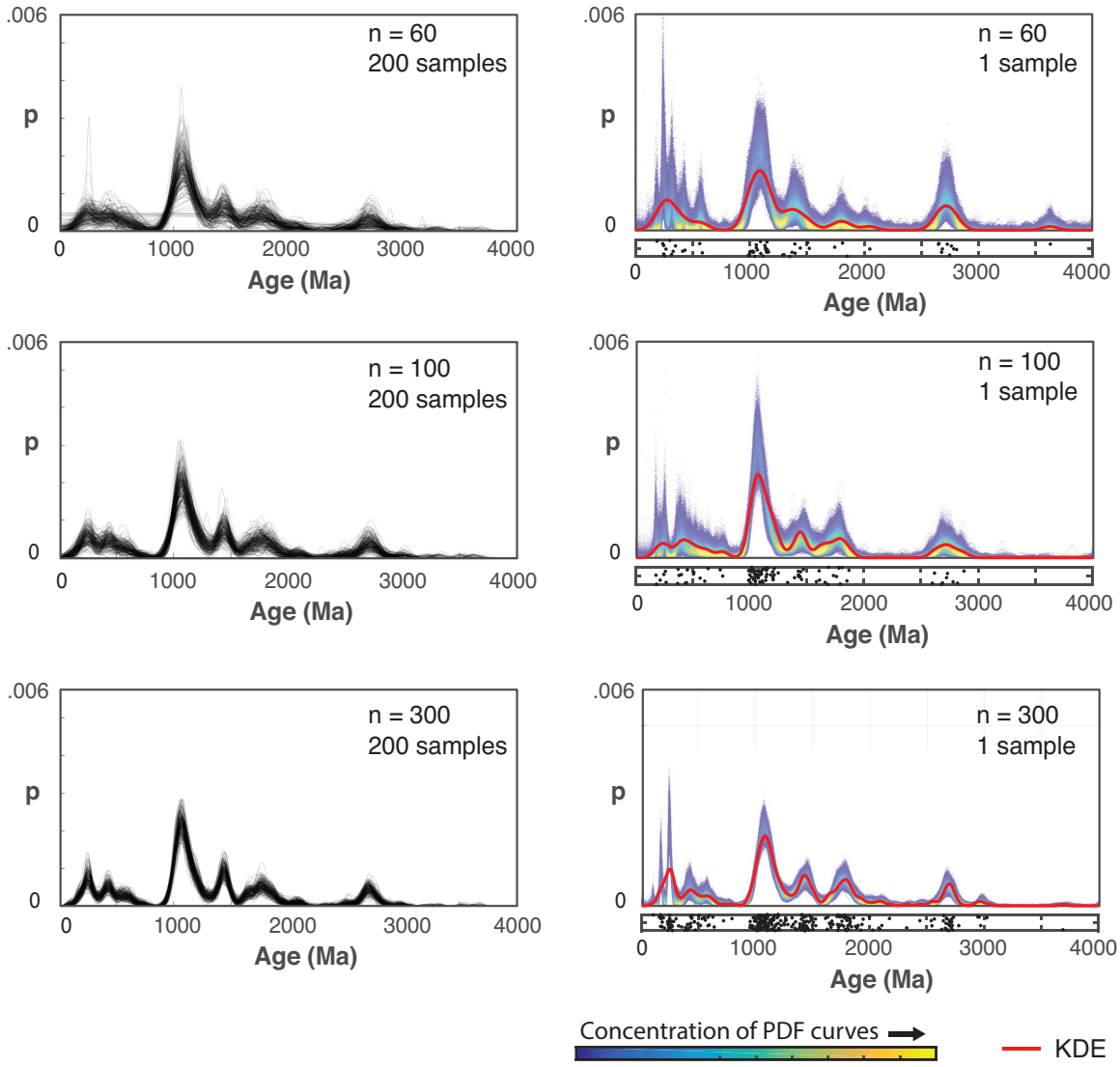

Figure 2.2: The variability of random samples drawn from a population is accurately captured by Probability Model Ensembles (PMEs) inferred from a single sample. (a) Kernel density estimate curves (KDEs, inferred using the method of *Botev et al.*, 2010) of random samples (n = 60, 100, 300) of a population. Samples were drawn directly from the KDE inferred for the complete dataset of *Pullen et al.* (2014). (b) Probability model ensembles (PMEs) inferred for a single sample of varying sample size show an excellent match to the values and variability observed in the subsample KDEs. The KDE curve calculated for each sample is also shown in red, indicating that PMEs capture all major age peaks captured by the KDE. Dot plots underneath each panel show the ages of the single random subsample used to infer each PME (vertical scatter used for visual clarity).

possible model parameters $\boldsymbol{\theta}$. The posterior distribution $\mathrm{P}(\boldsymbol{\theta}|\boldsymbol{d})$ is particularly useful because it quantifies the support that the data provide for various models as parameters vary. Thus, the distribution of $\mathrm{P}(\boldsymbol{\theta}|\boldsymbol{d})$ indicates how tightly or loosely the data constrain each model parameter θ_k, whether the parameters covary, etc. In the detrital zircon application, $\boldsymbol{d}$ is the set of ages and analytical uncertainties of one detrital zircon sample and each model is a potential parent population of the observed sample, defined by parameters $\boldsymbol{\theta}$. Sampling the posterior distribution $\mathrm{P}(\boldsymbol{\theta}|\boldsymbol{d})$ yields a representative set of the potential parent populations likely to have produced the observed sample, which we call a Probability Model Ensemble (PME). Some detrital zircon samples may support a wide variety of candidate population probability models, whereas others support a more constrained set of models (Fig. 2.2). Permissible model variability is reflected in the distribution of inferred model parameters in a PME. This information is lost when only a single kernel density estimator (KDE) curve or probability density plot is used for a given detrital zircon sample.

2.2.1 Representation of detrital zircon age distributions using b-splines

Inferring ensembles of potential parent populations in a Bayesian framework requires an efficient method of representing probability density functions (PDFs) using a set of model parameters $\boldsymbol{\theta}$. Efficient representation is provided by basis-spline or b-spline functions (Fig. 2.3). In b-splining, model curves are generated by summing a series of basis functions $b_1 ... b_n$. Each basis function b_k is a piecewise function with non-zero value over a limited portion of the x axis (Fig. 2.3a), and each basis function has a coefficient θ_k that controls its height. The piecewise function boundaries are called knots, and the shape of each basis function depends on the number of model parameters compared to the number of knots (*De Boor*, 1978). To generate a model curve $s(x|\boldsymbol{\theta})$, the basis functions are multiplied by their respective coefficients and summed (Fig. 2.3b, c). In our method, many basis functions are distributed at fixed, regular intervals over an x axis that corresponds to zircon U-Pb age and basis functions correspond candidate parent population PDFs for a given sample (similar to *Eilers and Marx*, 1996). In order to simplify our modeling, we use splining to model natural log-transformed probabilities, such that each spline curve $s(x|\boldsymbol{\theta})$ is a natural log-transformed probability model (see discussion of the advantages of our approach in Section A.2). Each spline curve $s(x|\boldsymbol{\theta})$ corresponds with a PDF that we define

$$g(x|\boldsymbol{\theta}) = \exp[s(x|\boldsymbol{\theta})] \tag{2.2}$$

Each candidate parent population PDF, $g(x|\boldsymbol{\theta})$, is uniquely identified by its set of basis function coefficients, $\boldsymbol{\theta}$. Sets of likely parent populations aggregated by our method will

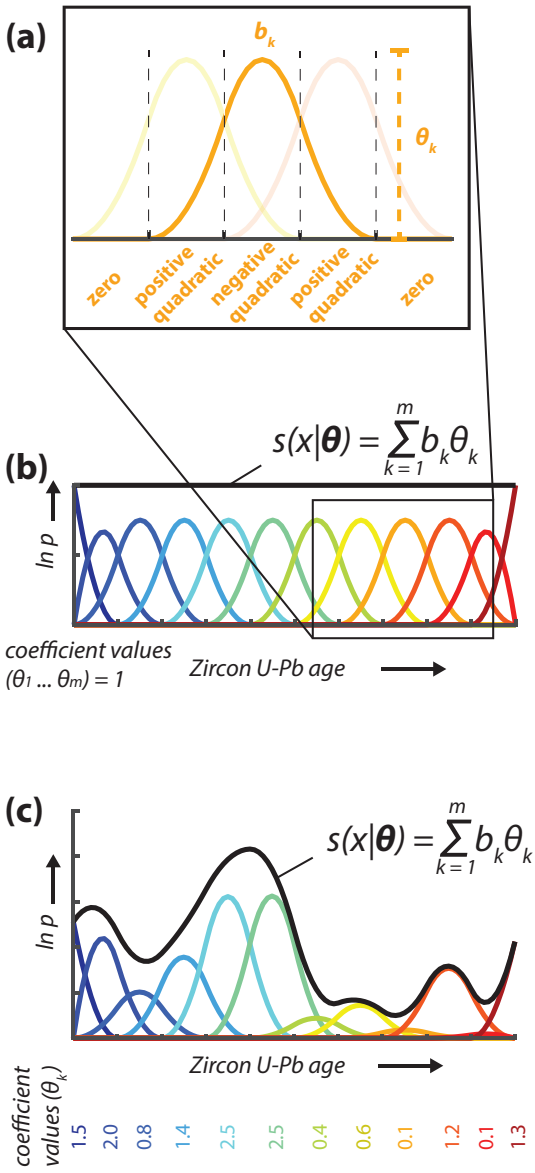

Figure 2.3: Third order basis splines provide an efficient way to represent probability density functions (PDFs) using a finite number of model parameters. (a) Each spline basis function b_k is a piecewise function (boundaries, called knots, shown by dashed lines) that is composed of quadratic pieces and is smooth and differentiable (*De Boor*, 1978). Importantly, each basis function is defined such that it has non-zero value over only a limited region. A coefficient θ_k is multiplied by the basis function to control its height. (b) In our application, third order basis splines, shown in color, are distributed at regular intervals along the x axis, which corresponds to zircon U-Pb age. The resulting modeled curve, s(x), is the sum of all basis functions multiplied by their respective coefficients. This example shows the effect of having the coefficient for each basis function equal to one. (c) This example shows a modeled curve when spline coefficients are varied, with these particular values generated randomly and shown beneath the basis functions. To simplify computation, our application uses these modeled curves as natural log-transformed probability density functions, as discussed in Sections 2.2.1, A.2.

indicate the range of permissible basis function coefficients warranted by a given zircon age dataset, providing a direct estimate of the uncertainty of age peak heights.

The fact that each basis function has non-zero value over a fixed and localized area means that each parameter θ_k has highly localized influence. The localized influence of each θ_k means that the probability of observing a grain of a certain age is a function of a small subset of the model parameters, greatly simplifying the response of model likelihood $\mathrm{P}(\boldsymbol{d}|\boldsymbol{\theta})$ to changes in each model parameter θ_k (see Section A.3 for further discussion). Note that the probability model curves $g(x|\boldsymbol{\theta})$ generated by this b-spline method could potentially have integrated areas that diverge from unity, meaning they are not true PDFs, and we correct for this divergence in the calculation of likelihood $\mathrm{P}(\boldsymbol{d}|\boldsymbol{\theta})$ below. Prior to being plotted or returned to the user, probability model curves $g(x|\boldsymbol{\theta})$ are normalized to integrate to unity for ease of use.

The specifics of our implementation of this spline method are chosen to simplify computation and make efficient use of limited computational resources. Our implementation uses 100 spline basis functions, distributed in a mixed log and linear scheme over zircon U-Pb age space (see further discussion in Section A.2). Our use of a mixed linear and log basis function arrangement is motivated by the systematics of the U-Pb system and the mass ratios measured to calculate U-Pb ages (see *Gehrels*, 2000; *Gehrels et al.*, 2008, for further discussion). For ages $<$1 Ga, the $^{238}\mathrm{U}/^{206}\mathrm{Pb}$ ratio generally yields the most precise age, and the analytical uncertainty of these ages increases proportional to the measured age (*Gehrels*, 2000). The proportionality of analytical uncertainty to age in the $<$1 Ga range suggests that a logarithmic age scale is appropriate in order to capture more precise age peaks at younger ages. For ages $>$1 Ga, the $^{207}\mathrm{Pb}/^{206}\mathrm{Pb}$ ratio generally yields the most precise ages, and analytical uncertainties associated with these ages show an extremely slight, poor negative correlation with age (*Gehrels*, 2000), such that they are effectively uncorrelated. Because of the effective lack of correlation between ages and uncertainties for ages $>$1 Ga, basis functions are deployed on a linear age scale at ages $>$1 Ga, such that basis function width does not change with age. For further discussion of our choice of age scale, see Sections 2.4.4 and A.2.

2.2.2 Quantifying the likelihood

Likelihood indicates the probability of drawing the observed sample from a candidate parent population. The likelihood of a single age, $\mathrm{P}(d_i|\boldsymbol{\theta})$ is determined by evaluating the PDF that corresponds to the coefficients $\boldsymbol{\theta}$ for datapoint d_i (Fig. 2.4). As mentioned above, we use spline curves to represent natural log-transformed probability density functions, which

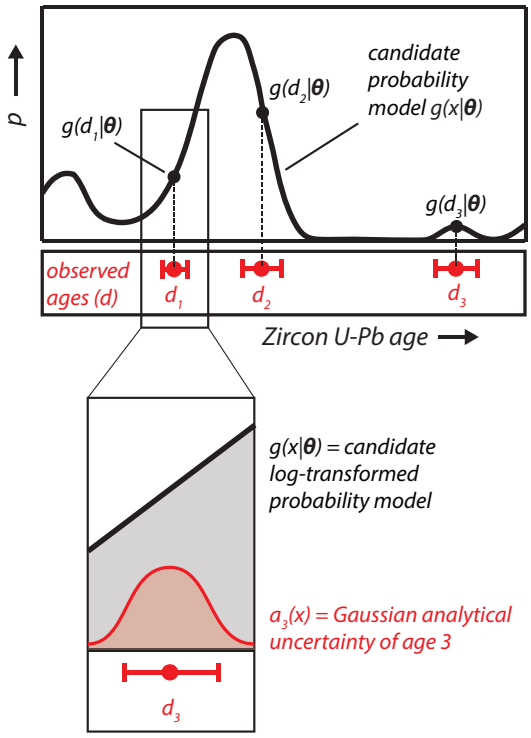

Figure 2.4: Likelihood $\mathrm{P}(d_i|\boldsymbol{\theta})$ is calculated for a candidate parent population model $g(x|\boldsymbol{\theta})$ from the function values of $g(x|\boldsymbol{\theta})$ corresponding to observed zircon U-Pb ages in a sample. Likelihoods are calculated by marginalizing (integrating) over the analytical uncertainty of each observed grain age. See discussion in Section 2.2.2 for more detail.

simplifies our calculations (see further discussion in Section A.2). Thus, each spline curve must be exponentiated to evaluate likelihood. As mentioned above, the curves $g(x|\boldsymbol{\theta})$ that correspond to model parameters $\boldsymbol{\theta}$ may not integrate to 1 (a requirement for a true PDF), so we normalize the likelihood we infer from these curves by the integrated area of the curve. We account for the analytical uncertainties in each measured age by marginalization: rather than evaluate $g(x|\boldsymbol{\theta})$ at a single x value for each datapoint d_i, we evaluate the surrounding area and weigh the function values $g(x|\boldsymbol{\theta})$ by the Gaussian distribution that describes the analytical uncertainty of d_i (Fig. 2.4):

$$\mathrm{P}(d_i|\boldsymbol{\theta}) = \frac{1}{Area\ g(x|\boldsymbol{\theta})} \int g(x|\boldsymbol{\theta}) \cdot a_i(x)\ dx \tag{2.3}$$

where $g(x|\boldsymbol{\theta})$ is the spline function that corresponds to model parameters $\boldsymbol{\theta}$, and $a_i(x)$ is a Gaussian distribution representing the age and analytical uncertainty of d_i. In our implementation, the integration in Eqn. (2.3) is solved numerically using Riemann summation, and the area under $g(x|\boldsymbol{\theta})$ is also calculated by Riemann summation.

Because each zircon age measurement represents an independent draw from its parent population, the likelihood of observing an entire sample $\boldsymbol{d}$ given model $\boldsymbol{\theta}$ is the product of the likelihood of each individual sample age:

$$\mathrm{P}(\boldsymbol{d}|\boldsymbol{\theta}) = \prod_{i=1}^{n} P(d_i|\boldsymbol{\theta}) \tag{2.4}$$

where n is the sample size.

2.2.3 Prior assumptions

Bayesian methods require the explicit statement of prior assumptions, in the form of the probability distribution $\mathrm{P}(\boldsymbol{\theta})$ incorporated into Bayes' Theorem (Eqn. 2.1). Though it may seem generally desirable to make no assumptions, all methods of estimating population probability distributions from finite samples rely on a set of assumptions. Our method uses the prior to enforce the assumption that a distribution should be smooth and uniform in the absence of evidence to the contrary, with peak heights that scale appropriately given the sample size. Such an assumption is an integral part of previous methods to estimate PDFs from finite samples, including kernel density estimation (*Silverman*, 1986; *Botev et al.*, 2010; *Shimazaki and Shinomoto*, 2010), as well as previous use of b-splines for density estimation (*Eilers and Marx*, 1996). We tested three prior distributions to enforce this assumption, including multivariate Gaussian, multivariate Cauchy (*Ferguson*, 1962), and multivariate Student t distributions. Ultimately, we decided to use the multivariate Student

t distribution because of its ease of use and the reasonable behavior of resulting PDFs, as discussed below.

Our first prior assumption is that in the absence of data, any zircon age is as likely as any other within the modeled domain. This assumption is quantified by treating the expected value of each model parameter θ_k as the height of a uniform probability distribution over the domain of x:

$$E(\theta_k) = \frac{1}{range(\text{Zircon U-Pb age})} \tag{2.5}$$

where $range(\text{Zircon U-Pb age})$ here refers to the log-age range over which modeling is conducted, 1 - 4000 Ma in our application. The expected value shown here will yield a uniform distribution over x that integrates to 1. This expected value is the peak of the prior distribution for each parameter.

The second assumption we can reasonably make about a PDF inferred from a finite sample is that if the sample size increases, the height of the age peaks should increase reflecting the increased confidence gained from a larger sample. To form a rough guideline for how much peak height should increase with added sampling, we use the example of a unimodal age distribution. If a unimodal age distribution contains n ages, then the total integrated probability mass away from the lone age peak should equal $\sim \frac{1}{2n}$. This is so because if a second age peak existed in the sampled population and constituted a share of the population of $> \frac{1}{2n}$, then a sample of size n is more likely than not to include at least one zircon age from this second age peak. Conversely, a sample of size n does not provide the statistical power to determine the existence and relative height of age peaks that constitute a share of $< \frac{1}{2n}$ of the population because those peaks are not likely to be included in a sample of size n. Thus, $\sim \frac{1}{2n}$ is a conservative rough estimate of the total probability mass in a given distribution that is not assigned to recognized age peaks in the distribution. The heavy tailed prior distributions that we tested, the Cauchy and multivariate Student t distributions, were able to achieve this desired scaling, whereas the multivariate Gaussian distribution was not. A more detailed and rigorous discussion of this scaling can be found in Section A.4.

Our third consideration for the choice of prior distribution is the ability to choose the degree to which a distribution is smoothed, or equivalently stated, the covariance between adjacent basis functions. The multivariate Student t distribution incorporates a covariance matrix, which makes it easy to specify the covariance between adjacent basis functions, while the multivariate Cauchy distribution does not.

The multivariate Student t prior enforces norms that are common to all methods of in-

ferring continuous PDFs from finite datasets of which we are aware, including those that are commonly used with detrital zircon U-Pb data (e.g., *Botev et al.*, 2010). We parameterize the multivariate Student t distribution using the expected parameter values described by Eqn. (2.5). The covariance matrix we use to parameterize the Student t distribution defines the variability of each basis function coefficient as well as the covariance between the coefficients. Coefficient variance is defined by the diagonal elements of the covariance matrix. Coefficient covariance, which controls the smoothness of modeled PDFs, is defined by the off-diagonal elements of the covariance matrix. The covariance matrix values we use to achieve the desired behavior discussed above are diagonal element values of 13.5^2 and off-diagonal element values that decay away from the diagonal, following the expression $13.5^2\ e^{\frac{-|\,i-j\,|}{100}}$, where i and j are the row and column index of the respective element. The distribution has 5 degrees of freedom (*Lange et al.*, 1989). Despite the performance differences between the multivariate Student t distribution and multivariate Gaussian described here, we found that calculated BPC values (discussed below) were minimally affected by the choice of whether to use a multivariate Gaussian or multivariate Student t prior distribution.

2.2.4 Aggregation of probability model ensembles (PMEs)

Representative PMEs are aggregated for a given sample using a Markov Chain Monte Carlo (MCMC) method, with the Metropolis-Hastings algorithm used to determine whether a potential parent population is added to the PME. In an MCMC method, the unknown posterior distribution $\mathrm{P}(\boldsymbol{\theta}|\boldsymbol{d})$ is explored by a random walker moving through an m-dimensional space, where m is the number of model parameters and each dimension corresponds to a single parameter. In our case, the movement of the walker and the resulting Markov chain (the record of the walker's path through the space) are governed by the Metropolis-Hastings algorithm, resulting in a Markov chain that is a representative sample of the posterior distribution $\mathrm{P}(\boldsymbol{\theta}|\boldsymbol{d})$ (*Gelman et al.*, 2013). In our implementation, the random walker begins at the maximum likelihood model (found by inversion; *Shanno*, 1970) so the walker wastes no steps in reaching the region of high posterior probability. In order to ensure adequate sampling of the posterior distribution $\mathrm{P}(\boldsymbol{\theta}|\boldsymbol{d})$, we require the random walker to run for a greater number of steps if parameter values are highly autocorrelated from one step to the next (*Geyer*, 1992). MCMC convergence is discussed further in Section A.3. The typical number of steps in the Markov chain is 10^4 to 10^5.

Because the Metropolis-Hastings method generates representative samples of the posterior $\mathrm{P}(\boldsymbol{\theta}|\boldsymbol{d})$, models $\boldsymbol{\theta}$ are represented in a PME to the degree that they are supported by

the data. Thus, the permissible variability in models (in this case, parent population PDFs) is represented in this sample of the posterior. Posterior distributions become more tightly clustered the greater the level of constraint the data provide on the model parameters. For instance, when the size of a detrital zircon U-Pb age sample increases, the permissible variability in potential parent populations shrinks (Fig. 2.2).

2.3 Estimating correspondence between PMEs: Bayesian Population Correlation (BPC)

In order to assess the correspondence of two zircon age populations using the robust constraints contained in PMEs, we develop a new comparative metric called Bayesian Population Correlation (BPC). BPC incorporates the uncertainties in parent population inference that are reflected in PMEs. Specifically, BPC compares the probabilistic support for two alternative hypotheses: the joint hypothesis (H_J), in which two observed samples are from one joint parent population, and the separate hypothesis (H_S), in which each sample is drawn from its own, separate parent population. BPC depends on the relative likelihood of the two hypotheses, H_J and H_S, which can vary over many orders of magnitude, so we define the relative likelihood magnitude Λ as the natural log of the relative likelihood of H_J versus H_S:

$$\begin{aligned}\Lambda = \ln\left[\frac{\mathrm{P}(H_J)}{\mathrm{P}(H_S)}\right] &= \left\langle \ln\left[\frac{\mathrm{P}(\boldsymbol{d}_J|\{\boldsymbol{\theta}_J\})}{\mathrm{P}(\boldsymbol{d}_1|\{\boldsymbol{\theta}_1\})\ \mathrm{P}(\boldsymbol{d}_2|\{\boldsymbol{\theta}_2\})}\right]\right\rangle \\ &= \langle \ln \mathrm{P}(\boldsymbol{d}_J|\{\boldsymbol{\theta}_J\})\rangle\ -\ \langle \ln \mathrm{P}(\boldsymbol{d}_1|\{\boldsymbol{\theta}_1\})\rangle\ -\ \langle \ln \mathrm{P}(\boldsymbol{d}_2|\{\boldsymbol{\theta}_2\})\rangle\end{aligned} \tag{2.6}$$

where $\boldsymbol{d}_1$ and $\boldsymbol{d}_2$ are the age data of sample 1 and sample 2, and $\boldsymbol{d}_J$ is the union of $\boldsymbol{d}_1$ and $\boldsymbol{d}_2$, representing the combined data of samples 1 and 2. We refer to $\boldsymbol{d}_J$ as the hypothetical joint sample. $\{\boldsymbol{\theta}_1\}$, $\{\boldsymbol{\theta}_2\}$, and $\{\boldsymbol{\theta}_J\}$ are the PMEs of samples 1 and 2 and the hypothetical joint sample, inferred using the MCMC method described above. Here and in subsequent expressions, angular brackets indicate the mean ensemble natural log likelihood, which is calculated by taking the mean of natural log likelihood values of the full PME. In general, $\mathrm{P}(\boldsymbol{d}_J|\{\boldsymbol{\theta}_J\}) = \mathrm{P}(\boldsymbol{d}_1|\{\boldsymbol{\theta}_J\}) \cdot \mathrm{P}(\boldsymbol{d}_2|\{\boldsymbol{\theta}_J\})$ because $\boldsymbol{d}_J$ is composed of $\boldsymbol{d}_1$ and $\boldsymbol{d}_2$ and zircon ages d_i are independent draws from a population so their probabilities are multiplicative. Substituting this result into Eqn. (2.6) yields

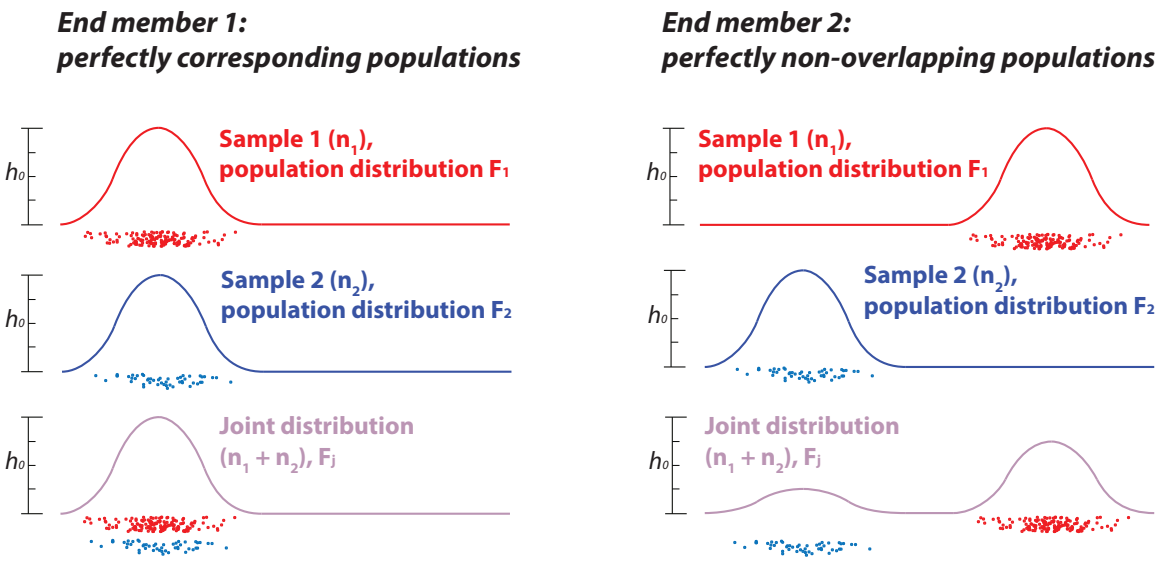

Figure 2.5: Two idealized end member scenarios (perfectly corresponding populations and perfectly non-overlapping populations) assist with the calculation of upper and lower bounds of the relative likelihood magnitude Λ. Scale bar shows h_0, the height of the age peak of the unimodal samples (see Section 2.3).

$$\Lambda = \langle \ln \mathrm{P}(\boldsymbol{d}_1|\{\boldsymbol{\theta}_J\})\rangle \; + \langle \ln \mathrm{P}(\boldsymbol{d}_2|\{\boldsymbol{\theta}_J\})\rangle \; - \; \langle \ln \mathrm{P}(\boldsymbol{d}_1|\{\boldsymbol{\theta}_1\})\rangle \; - \; \langle \ln \mathrm{P}(\boldsymbol{d}_2|\{\boldsymbol{\theta}_2\})\rangle \quad (2.7)$$

For ease of interpretation, we seek to scale Λ to occupy the range between 0 and 1. Such scaling can be accomplished by normalizing Λ with respect to two end member scenarios: (1) identical parent populations, which will produce the maximum Λ value and (2) parent populations with no shared ages, which will produce the minimum Λ value. Here, we calculate these end member results analytically, making the simplifying assumption that samples are large enough to accurately represent parent population PDFs (Fig. 2.5). Following from Eqns. (2.6, 2.7), the expected value of Λ, Λ_{ideal}, is defined as

$$\Lambda_{ideal} = \ln \left[\frac{\mathrm{P}(H_J)}{\mathrm{P}(H_S)} \right] = \ln \left[\frac{\mathrm{P}(\boldsymbol{d}_1|F_J)\ \mathrm{P}(\boldsymbol{d}_2|F_J)}{\mathrm{P}(\boldsymbol{d}_1|F_1)\ \mathrm{P}(\boldsymbol{d}_2|F_2)} \right] \quad (2.8)$$

where F_1, F_2, and F_J are well characterized parent population PDFs and the data are assumed to be independent observations such that $\mathrm{P}(\boldsymbol{d}_J) = \mathrm{P}(\boldsymbol{d}_1) \cdot \mathrm{P}(\boldsymbol{d}_2)$. In the first endmember case, where samples are drawn from identical parent populations, $F_1 = F_2 = F_J$, so Eqn. (2.8) shows that $\Lambda_{ideal} = 0$. In the second endmember case, where parent populations are perfectly non-overlapping, the probability mass of F_J must be spread out in order to accommodate samples from both populations. In this case, F_J is the sum of F_1 and F_2 each

weighted by the proportion of total data that comes from their respective samples:

$$F_J = \frac{n_1}{n_1 + n_2} F_1 + \frac{n_2}{n_1 + n_2} F_2 \tag{2.9}$$

where n_1 and n_2 are the sample sizes of the two samples. This definition of F_J maximizes the likelihood of observing $\boldsymbol{d}_J$, which is the union of $\boldsymbol{d}_1$ and $\boldsymbol{d}_2$. In order to find the minimum Λ value using Eqn. (2.8), we must relate the likelihood of observing a given zircon age d_i under F_J, $\mathrm{P}(d_i|F_J)$, to the likelihood of observing the same age under F_1 and F_2, $\mathrm{P}(d_i|F_1)$ and $\mathrm{P}(d_i|F_2)$. Eqn. (2.3) shows that multiplying F by a constant will also scale $\mathrm{P}(d_i|F)$ by the same constant. Therefore, $\mathrm{P}(d_i|F_J)$ can be calculated from $\mathrm{P}(d_i|F_1)$ and $\mathrm{P}(d_i|F_2)$ as follows:

$$\mathrm{P}(d_i|F_J) = \frac{n_1}{n_1 + n_2} \mathrm{P}(d_i|F_1) + \frac{n_2}{n_1 + n_2} \mathrm{P}(d_i|F_2) \tag{2.10}$$

Considering first the case of d_i taken from sample 1, we assert that because populations 1 and 2 are perfectly non-overlapping, $\mathrm{P}(d_{i,1}|F_2) = 0$, which allows eliminating the second term of Eqn. (2.10). Because the likelihood of observing sample $\boldsymbol{d}_1$ is the product of the likelihood of each individual age in the sample $d_{i,1}$ (Eqn. 2.4) and because $\mathrm{P}(d_{i,1}|F_2) = 0$, it follows from Eqn. (2.10) that

$$\mathrm{P}(\boldsymbol{d}_1|F_J) = \left(\frac{n_1}{n_1 + n_2} \right)^{n_1} \mathrm{P}(\boldsymbol{d}_1|F_1) \tag{2.11}$$

By the same reasoning presented above, $\mathrm{P}(d_{i,2}|F_1) = 0$, so Eqn. (2.11) applies when the subscripts 1 and 2 are swapped, as well. When this result is substituted into Eqn. (2.8), numerator and denominator terms cancel, revealing the expression for Λ_{ideal} when there is no population overlap, which we term Λ_{min}:

$$\Lambda_{min} = \ln \left[\left(\frac{n_1}{n_1 + n_2} \right)^{n_1} \left(\frac{n_2}{n_1 + n_2} \right)^{n_2} \right] \tag{2.12}$$

We define Bayesian Population Correlation as a remapping of Λ onto the range of 0 to 1, which we accomplish using the two endmember cases described above:

$$BPC = 1 - \left(\frac{\Lambda}{\Lambda_{min}} \right) \tag{2.13}$$

Because Λ_{min} accounts for the sizes of each sample, expected BPC values should remain insensitive to sample size, (though BPC uncertainties vary with sample size, see Section 2.5). Two samples drawn from identical parent populations should produce a BPC value

of 1, whereas two samples drawn from completely distinct populations should yield a BPC value of 0. The variation of this metric between 0 and 1, with higher values indicating increasingly similar populations, motivates our use of the word 'correlation' in its name. We note that BPC is similar to the Bayes factor of *Jeffreys* (1998), though the Bayes factor is based on comparison of posterior values rather than likelihood values.

We note that BPC occasionally exceeds 1 for two very similar samples, which can be explained by the fact that both priors and likelihood influence the construction of PMEs, but BPC is based solely on likelihood. Consider the example of a sample being compared against itself, such that to construct the hypothetical joint PME, all observed zircon ages in the sample are doubled. Our priors are tuned such that larger sample sizes will increase age peak heights (see discussion in Section 2.2.3). Thus, in the case of two identical samples, the joint PME will have taller age peaks than the two identical separate PMEs. These taller peaks result in higher likelihoods for each zircon age than the age peaks of the PME inferred for the sample by itself. The higher likelihood of each sample age under the joint PME results in a BPC value slightly greater than 1 (Eqns. 2.6, 2.13). This same phenomenon can occur for two nearly identical samples. Despite this undesired behavior, we believe the use of a likelihood ratio is justified because of its well understood behavior. When BPC is greater than 1, estimated uncertainty (see Section 2.5) typically includes 1.

2.4 Testing the behavior of BPC

We conduct a suite of resampling experiments to test the behavior of BPC. First, a simple experiment involving unimodal populations with variable overlap tests the basic functioning of BPC. Then, the effect of changing sample size on BPC is tested using resampling experiments conducted with published detrital zircon datasets. Finally, we also conduct experiments to assess the effect on BPC of varying the proportion of shared ages in two compared parent populations.

2.4.1 BPC behavior in a simple case

In order to verify that BPC behaves as intended in a simple case, BPC was evaluated for samples of two synthetic, Gaussian parent populations that are systematically displaced relative to one another (Fig. 2.6). For this experiment, PMEs were modeled over an x value domain of 0 to 6.9, which corresponds to the natural logarithmic transformation of the age range 1 - 1000 Ma, thus paralleling our modeling procedure for zircon U-Pb age data $<$1 Ga. One Gaussian parent is centered on 2.5 and a second Gaussian parent of equal

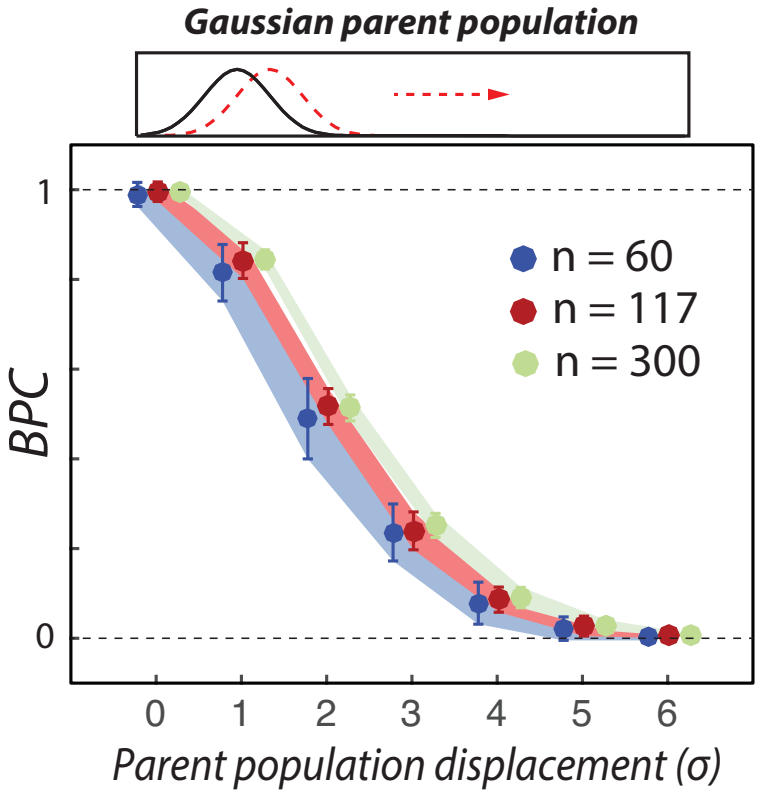

Figure 2.6: Experiments with a range of partially overlapping Gaussian parent populations show that BPC inhabits the full metric range between 0 and 1 and returns consistent values for all tested sample sizes. Two Gaussian parent populations are systematically displaced from one another (expressed in terms of peak-width units σ) and sampled randomly at sample sizes n = 60, 117, 300. Resulting samples are compared using BPC. Each symbol represents the mean and standard deviation of metric values across twenty experiments and symbols are plotted with small horizontal offsets for visual clarity.

width is defined with its center located at 3, 3.5, 4, etc. The standard deviation of each Gaussian parent population is 0.5. Random values are drawn from these Gaussian parent populations and compared to one another using BPC (Fig. 2.6). The analytical uncertainty ascribed to each log-age was ∼0.01, which equates to 1% of its value in linear space. The results of this experiment show that BPC varies smoothly between 0 and 1 with increasing population overlap independent of sample size, as expected.

2.4.2 Independence from sample size bias

To assess the effects of sample size on BPC for realistic samples, BPC is tested on samples drawn from existing detrital zircon datasets (*Pullen et al.*, 2014; *Thomson et al.*, 2017) with variable sample size (Fig. 2.7). The synthetic subsamples used for testing are drawn directly from the KDEs inferred for the large datasets of (*Pullen et al.*, 2014; *Thomson et al.*, 2017), which mirrors the process of sampling a population. Cases of identical parent populations (two samples drawn from the dataset of *Pullen et al.* (2014)) and different parent populations (one sample drawn from the dataset of *Pullen et al.* (2014), one sample drawn from the dataset of *Thomson et al.* (2017)) are both tested, and in each case sample sizes between n = 60 and n = 400 are used. BPC values calculated between random subsamples of identical populations cluster around 1, with decreasing scatter as sample size increases (Fig. 2.7b). When BPC is calculated between random subsamples of two different parent populations, it demonstrates a consistent value across a range of tested sample sizes (Fig. 2.7c), again with decreasing scatter as sample size increases.

The consistent behavior of BPC and lack of sample size biasing contrasts with the behavior of published metrics for detrital zircon correspondence (Fig. 2.7) including Similarity (*Gehrels*, 2000), Cross Correlation (*Saylor et al.*, 2012, 2013) and Likeness (*Satkoski et al.*, 2013). These published metrics are functions of KDE curves inferred for samples, and the values of these metrics are dependent on both sample size and KDE method chosen (*Saylor and Sundell*, 2016, review and test these metrics). Both of these dependencies are problematic because they indicate that metric value is not solely a function of differences between detrital zircon populations, and therefore that these metrics do not solely reflect geologic processes. For comparison with BPC, Figure 2.7 shows values of Similarity, Likeness, and Cross Correlation calculated using the KDE method of *Botev et al.* (2010), which is widely used and implemented in the `DensityPlotter` software of *Vermeesch* (2012). It can be seen that the mean values of Similarity, Likeness, and Cross Correlation are each systematically related to sample size in at least one of the two cases. In addition, of these three metrics, there is no single metric that minimizes sample size bias in the cases of both

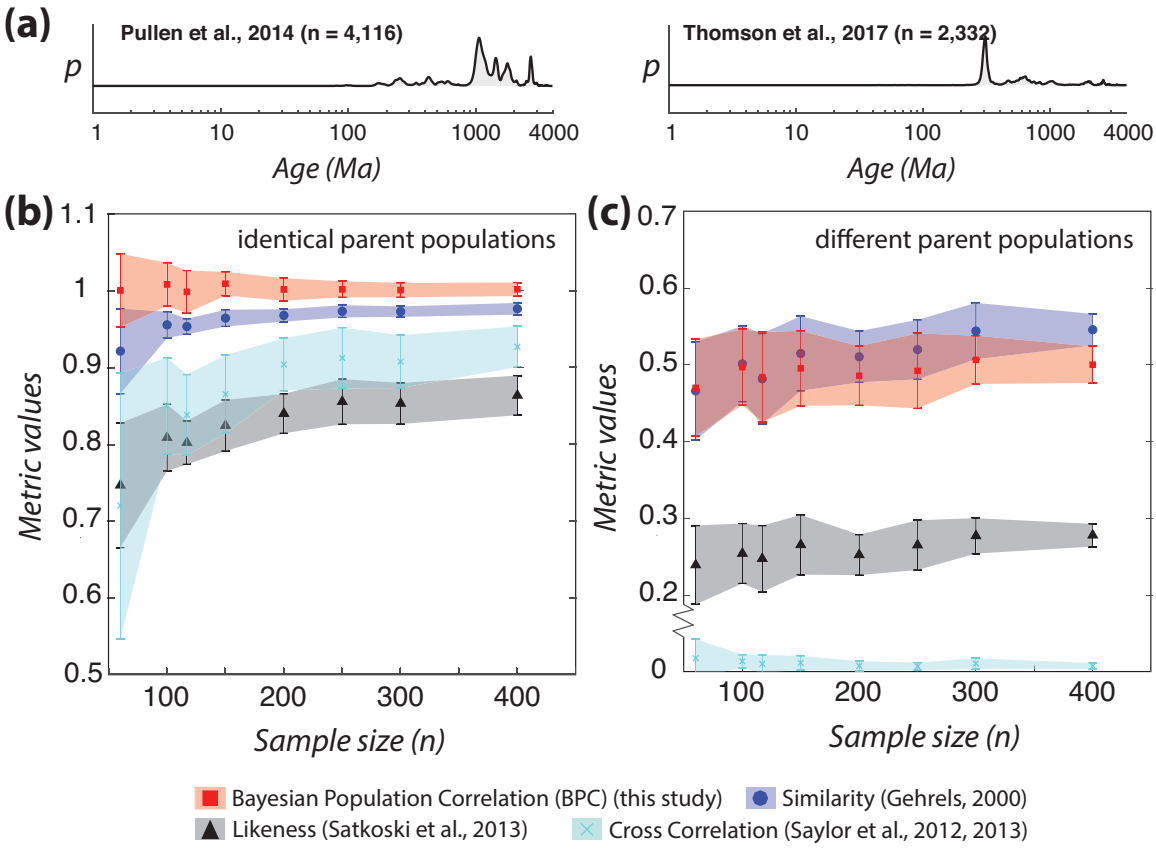

Figure 2.7: BPC calculated from random subsamples of two large detrital zircon datasets are unbiased with respect to sample size, in contrast to existing detrital zircon correspondence metrics. (a) Datasets of *Pullen et al.* (2014); *Thomson et al.* (2017) were resampled by drawing ages directly from the KDE (*Botev et al.*, 2010) calculated for each dataset. (b) Metric results are shown for when two subsamples of a single population (the dataset of *Pullen et al.*, 2014) are compared. (c) Results are shown for when subsamples are drawn from two different populations (the datasets of *Pullen et al.*, 2014; *Thomson et al.*, 2017). The key shows the plotted metrics, and previously published metrics were calculated using KDE curves estimated using the method of *Botev et al.* (2010). BPC is not based on a KDE method. In (c), note the broken vertical axis.

identical and different parent populations. In the case of identical parent populations, Similarity shows the smallest change in value from n = 60 to n = 400, whereas in the case of different parent populations, Similarity shows a greater change in value than Likeness or Cross Correlation. Additional testing using other KDE methods documents changes in metric behavior when different KDE methods are used (see Section A.5, Fig. A.5). In addition, we also find that the test statistics and p-values associated with the Kolmogorov-Smirnov and Kuiper tests, which have been used to assess detrital zircon correspondence, are biased according to sample size for our resampling experiments (Fig. A.4). The sample size biasing and dependence on KDE method of these previously published metrics is explored in more detail elsewhere (*Saylor and Sundell*, 2016). BPC, which shows minimal or no sample size biasing and is not based on kernel density estimation, avoids these issues.

2.4.3 Interpreting the meaning of BPC values

Quantitative interpretation of existing metrics is currently limited to determining whether one pair of samples is more or less alike than another pair of samples. For a metric to have direct implications for earth processes, the metric would need to directly constrain parent population characteristics such as the proportion of ages in one population that are shared with another population. If a metric were to display a robust functional relationship between the shared proportions of populations and metric value, then the metric could be used to provide novel quantitative constraints on processes that affect detrital zircon populations. BPC has the potential to display such a functional relationship, in large part due to its grounding in probability theory. We have already demonstrated the use of probability theory to derive accurate expected BPC values for the cases of identical parent populations and parent populations with no shared ages (Section 2.3). Therefore, it stands to reason that expected BPC values derived analytically in a similar fashion could potentially predict experimental BPC values for partially overlapping parent populations, as well.

We derive an equation for expected BPC value as a function of the proportion of shared ages of two detrital zircon populations (Section A.6) and test it against BPC values from resampling experiments (Fig. 2.8). If these expected values are accurate predictions of BPC values calculated between pairs of detrital zircon samples, then BPC has a functional relationship to the shared proportions of two populations. Such a relationship would permit quantitative interpretations of the effects of earth processes on detrital zircon populations directly from metric value. In order to test whether measured BPC values conform to the predictions derived from probability theory, we devised additional resampling experiments where the proportion of ages shared between two populations is systematically varied (Fig.

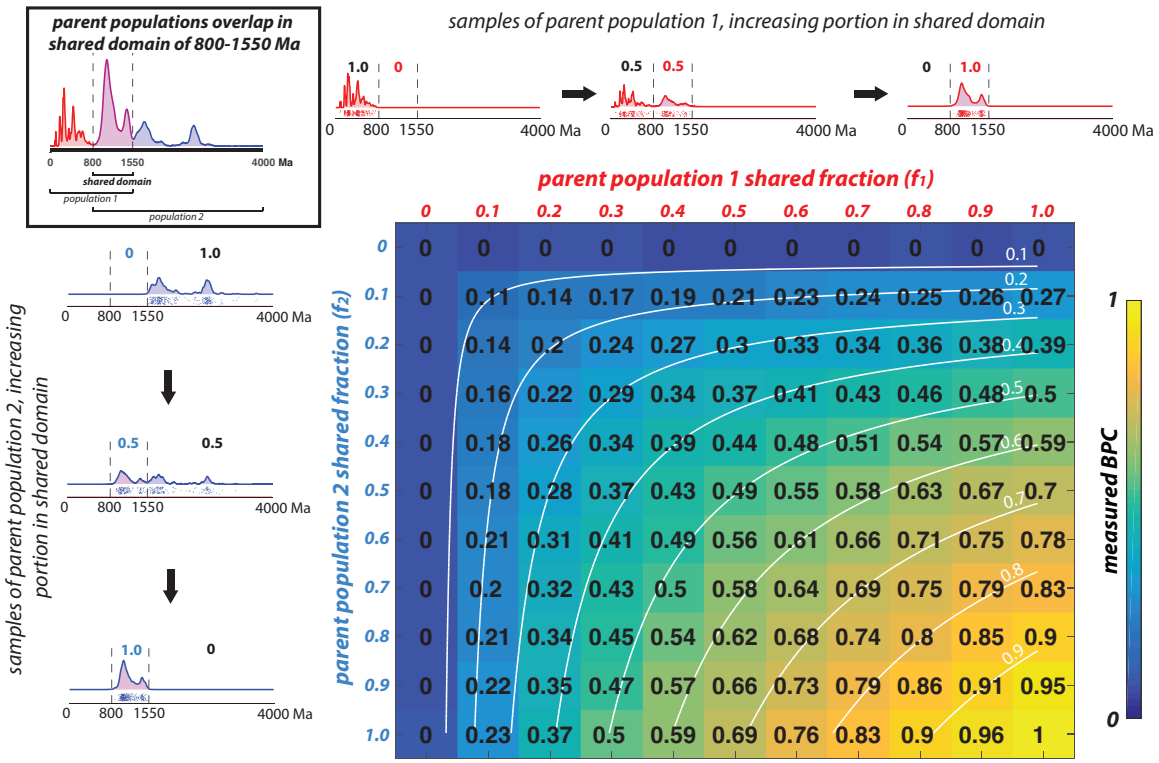

Figure 2.8: Comparison of numerical experiments to analytical predictions indicates that BPC is well described as a function of the proportions of zircon age groups that are shared between two samples. To model the effects of partially overlapping zircon age samples, the dataset of *Pullen et al.* (2014), is divided into three subgroups, 0-800 Ma, 800-1550 Ma, and 1550-4000 Ma (see upper left panel). These subgroups are used to generate synthetic zircon parent populations with variable proportions of shared ages (see description in Section 2.4). Upper and lefthand margins show typical samples drawn from synthetic populations so generated. The greater the proportion of each synthetic population that lies in the shared subgroup, the greater the expected correspondence. The shared fractions of each synthetic parent population are represented by two independent variables, f_1 and f_2, which vary between 0 and 1. f_1 and f_2 form the x and y axes of the table (note that f_2 increases from top to bottom). In the main plot, colors and black numbers correspond to mean BPC values from four experiments for each coordinate pair (f_1, f_2). In each experiment, samples of size n = 300 were drawn from parent populations 1 and 2. White contours show analytically predicted BPC_{ideal} values, given by Eqn. A.10 in Section A.6, which show an excellent match with observed results. The uncertainty of each experimental BPC value shown is 0.02.

2.8). The dataset of *Pullen et al.* (2014) is divided into three broad subgroups (young, 0-800 Ma; middle, 800-1550 Ma; and old, 1550-4000 Ma) and synthetic parent populations are constructed using various mixtures of these subgroups. The subgroup boundaries are chosen to fall between coherent age peaks in the data. For each experiment, two synthetic parent populations are defined as follows: parent 1 includes grains of the young and middle subgroups and parent 2 includes grains of the middle and old subgroups. Thus, a portion of each synthetic parent population consists of grains of the shared middle age domain. The proportion of each parent population that belongs to the shared domain is independently varied from 0 (no middle aged grains) to 1 (entirely middle aged grains) and these proportions are represented as f_1 and f_2. The synthetic parent populations are then sampled and BPC is calculated; this procedure is repeated 4 times for each coordinate pair (f_1, f_2) with sample size n = 300 and results are shown in black in Figure 2.8.

The results of these experimental results show that BPC varies smoothly between zero and one as a function of the shared proportions of detrital zircon populations. BPC values of zero indicate no shared ages between two detrital zircon populations, whereas values of 1 indicate that the samples are likely to have been drawn from identical parent populations. BPC values between 0 and 1 indicate partial overlap of the ages contained in the two populations. We also compare the results of these numerical experiments to expected BPC values derived analytically for variable f_1 and f_2 (see Section A.6, Eqn. A.10). Expected BPC values are shown in white contours in Figure 2.8. BPC results from the resampling experiments conform almost perfectly to the expected values, indicating that BPC values can be accurately predicted from probability theory.

In order to ensure this correspondence between measured and expected BPC values is robust under a variety of realistic conditions, we performed two additional variants of the experiment described above. First, we divide the *Pullen et al.* (2014) dataset into 20 natural age peaks and then assign each of those age peaks to one of three subgroups such that the age peaks of each subgroup are interspersed across the full range of ages present in the dataset. Random subsamples are drawn with replacement from the subgroups and BPC calculated as above. The results of this experimental scheme are indistinguishable from the results when the three subgroups are defined as 0-800 Ma, 800-1550 Ma, and 1550-4000 Ma (Fig. 2.8). Thus, BPC values can be accurately predicted even when the shared and unshared age peaks of two populations are dispersed throughout the range of age values present. In order to test the effect of varying sample size on the predictability of BPC values, the sizes of compared samples were systematically varied for selected combinations of (f_1, f_2). BPC values were within uncertainty of expected values (see below for estimation of BPC uncertainties) for all tested cases, including when sample sizes differ by up to an

order of magnitude. The results of these additional experiments show that BPC values can be accurately predicted from (f_1, f_2) over a variety of sample sizes and in situations where shared and unshared age peaks are interspersed in compared populations.

The functional relationship between BPC and shared population proportions can be inverted, meaning that a BPC value found for two real detrital zircon samples can be used to constrain the shared proportions of the sampled parent populations, which are unknown for natural samples. The shared proportions of two detrital zircon populations (f_1, f_2) are directly affected by geologic processes such as sediment mixing (see *Niemi*, 2013, and Section A.6 for further discussion). Thus, the ability to infer the shared proportions of two detrital zircon populations permits quantitative interpretations of geologic processes from detrital zircon age samples that were not previously possible. The near perfect conformity of BPC values to theoretical expectations for partially overlapping parent populations suggests that expected BPC values could be derived for other more complicated scenarios as well, such as multiple partially overlapping age categories.

2.4.4 Limitations of our implementation of BPC

The fixed location and width of b-spline basis functions suggests that if age peaks are narrow and closely spaced enough, then these age peaks might not be differentiated in PMEs. To quantitatively assess the effect of resolution issues on PME inference and BPC, we performed repeated experiments using synthetic Gaussian parent populations (similar to Fig. 2.6) with variable widths. As might be expected, these experiments indicated that our PME inference method cannot resolve age peaks that are narrower than a single spline basis function. If the major differences between two populations are defined by small offsets between such narrow age peaks, calculated BPC values may be too high. Our mixed log and linear age scale (Section 2.2.1) results in the following minimum widths for age peaks to be fully resolved by our method. Spline basis functions are distributed on a logarithmic age scale at ages $<$1 Ga, and an age peak $<$1 Ga must have a standard deviation of at least 3.5% of its age value to be fully resolved. For instance, a 100 Ma peak must have a standard deviation of at least 3.5 Ma. An age peak $>$1 Ga must have a standard deviation of at least 35 Ma to be fully resolved. We note that these required widths are somewhat greater than the analytical uncertainty of a typical detrital zircon age measurement. However, we suspect that they will be adequate for most detrital zircon age populations, and Figure 2.2 shows that our implementation completely recovers the age peaks revealed by a popular KDE method (*Botev et al.*, 2010).

Computational constraints are the only limitation on the number of basis functions the

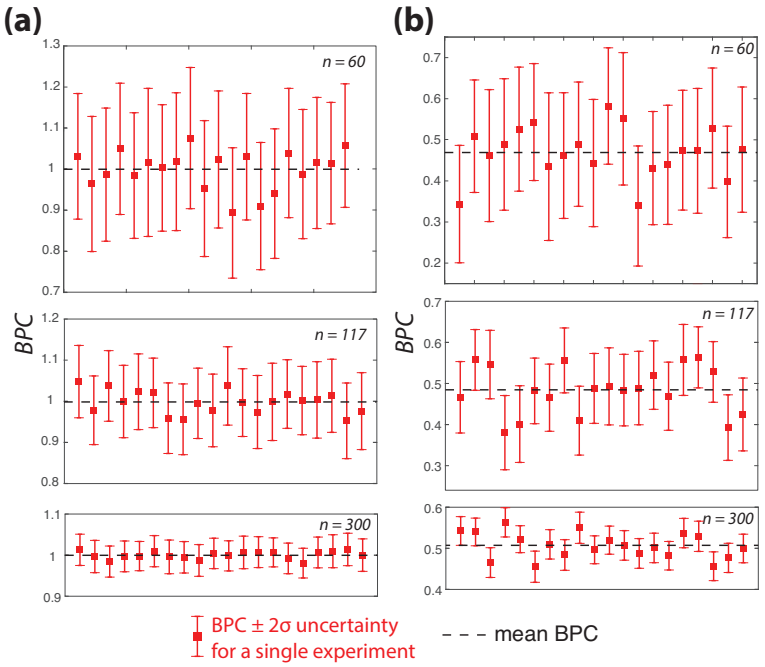

Figure 2.9: Resampling experiments show that the variation of models within PMEs permits estimation of robust BPC uncertainties. (a) BPC with uncertainties for 20 experiments with random subsamples drawn from identical parent populations (*Pullen et al.*, 2014) and compared against one another. Points show BPC values calculated for two synthetic detrital zircon samples and error bars show uncertainty inferred for that particular pair of samples using the method discussed in Section 2.5. (b) BPC with estimated uncertainties for 20 experiments where random subsamples were drawn from two different parent populations (*Pullen et al.*, 2014; *Thomson et al.*, 2017). Black dashed line indicates mean BPC value for each panel, taken as an estimate of the expected BPC value. Uncertainties are calculated from the variation in PMEs (see Section 2.5).

method uses. The current default of 100 basis functions distributed on a hybrid log-linear zircon U-Pb age axis results in manageable runtimes on a personal computer and resampling experiments suggest that for realistically complex samples (drawn from *Pullen et al.*, 2014), PMEs are not affected by resolution issues. If additional computing power is available, our procedure can easily be altered to use more basis functions and thus resolve narrower and more closely spaced age peaks.

2.5 Estimation of BPC uncertainties

Given the uncertainty inherent in inferring parent population age distributions from detrital zircon samples (Figs. 2.1, 2.2), an ideal comparative metric would provide a robust estimate of uncertainty of the metric itself. PMEs contain a large number of potential parent

population PDFs, and the variation within PMEs provides a means to estimate BPC uncertainty. In order to estimate BPC uncertainty, we randomly select models from the joint and separate PMEs and compare their likelihood values following Eqn. (2.6) to calculate a representative set of individual Λ values, which we refer to as Λ_i:

$$\Lambda_i = \ln \mathrm{P}(\boldsymbol{d}_J|\boldsymbol{\theta}_{J,i}) \; - \; \ln \mathrm{P}(\boldsymbol{d}_1|\boldsymbol{\theta}_{1,i}) \; - \; \ln \mathrm{P}(\boldsymbol{d}_2|\boldsymbol{\theta}_{2,i}) \tag{2.14}$$

where $\boldsymbol{\theta}_{J,i}$, $\boldsymbol{\theta}_{1,i}$, and $\boldsymbol{\theta}_{2,i}$ are models randomly drawn from their respective PMEs. The set of Λ_i values is then propagated through Eqn. (2.13) to yield a distribution of BPC values for two samples. The 1σ confidence interval of this distribution is the BPC uncertainty σ_{BPC}. A similar approach to uncertainty estimation in a Bayesian framework is taken by *Kruschke* (2013).

In order to test the reliability of σ_{BPC}, we apply it to the synthetic samples used in the previous section (Fig. 2.9). We calculate σ_{BPC} for random subsamples from two well resolved, real detrital zircon age distributions (*Pullen et al.*, 2014; *Thomson et al.*, 2017) at sample sizes of n = 60, 117, and 300 (the same subsamples as shown in Fig. 2.7). For samples drawn from identical parent populations (Fig. 2.9a), σ_{BPC} proves to be a conservative estimate of uncertainty, with calculated BPC values always lying well within $2\sigma_{BPC}$ of the mean value calculated for each sample size. For samples drawn from two different parent populations (Fig. 2.9b), σ_{BPC} is a roughly appropriate estimate of scatter of BPC values about the mean for a given sample size. In this case, for n = 60, all samples fall within $2\sigma_{BPC}$ of the mean. For n = 117, 85% of BPC values fall within $2\sigma_{BPC}$ of the mean. For n = 300, 75% of BPC values fall within $2\sigma_{BPC}$ of the mean. Even for those samples further than $2\sigma_{BPC}$ from the mean, the mean is typically just beyond their $2\sigma_{BPC}$ error envelope, and σ_{BPC} seems to provide a sensible estimate of the scatter in BPC values for a given sample size. Therefore, we regard σ_{BPC} as a useful indicator of BPC uncertainty that reflects the inherent uncertainty in sampling from an unknown parent population.

2.6 Implications of PMEs and BPC for analysis of detrital geochronology data

We have shown that BPC is a correspondence metric that varies predictably between 0 and 1, shows minimal or no sample size biasing (Fig. 2.7), and for which uncertainties can be readily estimated (Fig. 2.9). These features indicate that BPC is potentially a more reliable metric of correspondence between detrital zircon populations than other metrics currently available.

We have shown that the functional relationship between BPC and the proportions (f_1, f_2) of ages that are shared between two populations can be derived analytically from probability theory (Fig. 2.8, also see Section A.6). This relationship between BPC and the shared proportions of the two populations can be inverted, so that a BPC value calculated for a pair of detrital zircon samples can be used to constrain the shared proportions of their respective parent populations. Because BPC is a function of two independent variables (f_1, f_2; see Fig. 2.8), a BPC value produces nonunique solutions for f_1 and f_2. However, if the value of f_1 or f_2 can be assumed, then a unique solution for the other is possible. Such an assumption might be able to be made given prior knowledge of the sedimentary system in which the zircons were deposited. For instance, if one sample is collected from a location upstream of another sample, it can be assumed that the entirety of the upstream population is shared with the downstream population, i.e., that it is theoretically possible for any age present in the upstream population to also be present in the downstream population. In such a case, f_1 can be assumed to equal 1, permitting the BPC calculated for the two samples to yield a unique solution for f_2, which constrains the proportion of grains in the downstream population that originated in the catchment of the upstream population. Such a constraint could potentially be used, in combination with data on stream length, catchment area, and erosion rate, and under a set of assumptions, to investigate dilution of zircon age populations in sedimentary systems (see, for example, *Niemi*, 2013, and Section A.6 for further discussion).

We have also shown that a PME is a representative set of the possible parent populations that are likely to have produced a given detrital zircon sample (Section 2.2). The diversity of PMEs mirrors the diversity of samples of a certain size obtained from a population (Fig. 2.2). Thus, PMEs may prove useful for the visual assessment of statistical confidence in a detrital zircon sample age distribution. In addition, other types of quantitative analyses besides BPC may be made possible or made more robust through the use of PMEs.

2.7 Conclusions

We develop a metric for comparing two detrital zircon samples—Bayesian Population Correlation (BPC)—that is unbiased with respect to sample size, permits robust estimation of uncertainty, and behaves in a consistent and mathematically predictable manner. Much of the success of this metric depends on the use of a probability model ensemble (PME), rather than a single PDF, to characterize the age distribution of a detrital zircon population. A PME is generated by a Markov Chain Monte Carlo algorithm and is a probabilistically representative set of the potential parent populations consistent with an observed detrital

zircon age sample.

Because of the grounding of BPC in probability theory, the shared proportions of two detrital zircon populations can be directly inferred from calculated BPC values. Such inference, along with the ability to estimate robust uncertainties, may permit new quantitative interpretations of detrital zircon age data. In addition, BPC may be applicable beyond detrital zircon data, such as to other types of detrital geochronology or thermochronology data. As shown here, multi-modal datasets with limited sample sizes may not be well-described by existing widely-used statistical methods—in general, these datasets could benefit from BPC analysis.

Acknowledgments

This work was partially supported by NSF grants EAR-1151247 and EAR-1524304 (NAN). The Turner Fund from the Department of Earth and Environmental Sciences at the University of Michigan supported this work through a postdoctoral fellowship to A. S. Wolf and research grant to A. R. Tye. N. Niemi also acknowledges a CIRES Sabbatical Fellowship from the University of Colorado and colleagues from that institution who stimulated the early seeds of this research. We also acknowledge many helpful conversations with Eric Hetland. Scripts for using our procedure can be found at https://github.com/alextye/BPC.

CHAPTER 3

Quantifying the Effects of Sediment Sorting, Transport, and Sequestration on Detrital Zircon U-Pb Age Populations Using Bayesian Population Correlation

Abstract

Bayesian Population Correlation (BPC) is a comparative metric for detrital geochronology datasets that has quantifiable uncertainties, is insensitive to the variable sample sizes of many detrital geochronology datasets, and has a functional relationship with the proportion of zircon ages that are shared between two sampled populations. Here, we test the potential of BPC as an interpretive tool for detrital geochronology. We apply the metric to three previously published cases in which detrital geochronology data were used to investigate the effects of sedimentary sorting, transport, and sequestration on detrital mineral age populations. The original authors of these three cases used statistical methods such as the Kolmogorov-Smirnov (K-S) test and interpretive methods such as binning zircon ages and calculating changes in bin concentrations between samples. In each case, we find that the new BPC-based analysis yields results consistent with prior methods and statistical techniques. BPC offers several advantages over the previously used methods, such as quantification of the degree of correspondence between two detrital geochronology age populations, rather than a binary test of whether two populations are the same or different. In addition, BPC permits calculation of the proportion of shared ages between any two detrital geochronology age populations, and it may therefore enhance the interpretation of detrital geochronology datasets.

3.1 Introduction

The population of zircon ages in a sedimentary rock or modern sedimentary environment depends on the ages and zircon concentration of sedimentary sources, spatial and temporal variations in erosion, and sediment transport processes in the catchment (e.g., *Gehrels*, 2012; *Satkoski et al.*, 2013; *Dickinson*, 2008; *Tranel et al.*, 2011; *Garçon and Chauvel*, 2014). Because zircons are physically and chemically robust to Earth surface conditions (e.g., *Fedo et al.*, 2003), zircon ages are robust tracers of sediment transport in modern and ancient depositional systems. Thus, detrital zircon age samples can be used to investigate hydraulic sorting, dilution during downstream transport, differential erosion, and sediment storage (*Link et al.*, 2005; *Lawrence et al.*, 2011; *Hietpas et al.*, 2011; *Niemi*, 2013; *Saylor et al.*, 2013; *Stevens et al.*, 2013; *Kimbrough et al.*, 2015; *Nie et al.*, 2015).

Previous authors have attempted to quantify sedimentary processes using multiple detrital zircon samples arrayed within a single depositional system (e.g., *Lawrence et al.*, 2011; *Hietpas et al.*, 2011; *Niemi*, 2013; *Nie et al.*, 2015). However, these attempts were limited due to the complex and multi-modal nature of detrital zircon U-Pb age datasets, which inhibits the inference of detrital zircon population characteristics from samples (*Andersen*, 2005; *Tye et al.*, 2019). Detrital zircon U-Pb age datasets commonly consist of 100 - 300 U-Pb ages, with associated analytical uncertainties, that cluster around one to many age peaks, the shapes of which are highly variable and not easily fit using standard probability distributions (e.g., *Fedo et al.*, 2003; *Gehrels*, 2012; *Vermeesch*, 2012). The complex nature of these distributions has generated controversy about how to model and compare datasets, with many comparisons limited to semiquantitative methods created especially for comparing detrital zircon U-Pb age distributions (*Gehrels*, 2000; *Saylor et al.*, 2012; *Satkoski et al.*, 2013; *Saylor et al.*, 2013), which are significantly biased by the size of compared samples and have significant, but unquantifiable, uncertainties (*Saylor and Sundell*, 2016; *Tye et al.*, 2019). Other authors (e.g., *DeGraaff-Surpless et al.*, 2003; *Lawrence et al.*, 2011) compare samples using general statistical tests such as the Kolmogorov-Smirnov (K-S) test (*Kolmogorov*, 1933; *Smirnov*, 1948), which has been shown in some common cases to yield spurious results for detrital zircon U-Pb age datasets (*Saylor et al.*, 2013; *Vermeesch*, 2013). Specifically, the K-S test is more sensitive to differences in some parts of the range of possible detrital zircon U-Pb ages than others (*Saylor et al.*, 2013). Thus, authors using detrital zircons to analyze sediment transport processes have been limited to qualitative interpretations of the data (e.g., *Lawrence et al.*, 2011; *Hietpas et al.*, 2011; *Nie et al.*, 2015), or quantitative analysis of binned data (*Niemi*, 2013), which loses some information contained in these complicated age distributions.

Tye et al. (2019) present a new quantitative comparative metric, Bayesian Population Correlation (BPC), for which many of the problems associated with other comparative metrics are eliminated or ameliorated. BPC allows the calculation of metric uncertainty and is unbiased with respect to sample size. Of particular importance for investigating the effects of erosion, sediment sorting, transport, and dilution in depositional systems is the fact that BPC values show a predictable relationship to the proportion of shared ages in two compared detrital zircon populations (*Tye et al.*, 2019). Constraining the proportion of shared ages between sampled detrital zircon age populations within a depositional system is the key to quantifying the effects of sediment transport processes, and BPC permits the straightforward calculation of this proportion.

In this paper, we use three published datasets to test the use of BPC for comparing detrital zircon U-Pb age samples and quantitatively inferring the effects of sediment sorting, transport, and sequestration on detrital zircon U-Pb age populations. First, we derive a set of relations between erosion, catchment area, zircon concentration, and the expected dilution of zircon age populations that are propagated downstream between two samples from the same depositional system. We then discuss how BPC values calculated between two samples can be used to infer the proportion of zircon ages in one population that are shared with the other sampled population, which means that BPC values can be used to quantitatively assess zircon dilution in sedimentary systems (*Tye et al.*, 2019). Finally, we use new BPC analyses of three published sets of detrital zircon U-Pb age samples (*Lawrence et al.*, 2011; *Niemi*, 2013; *Nie et al.*, 2015) to quantify the downstream dilution of zircon ages in these datasets. We explore the constraints that these new analyses provide on the catchment areas, sediment sequestration rates, and other parameters of the sampled depositional systems. In doing so, we find that the new BPC analyses enhance the original interpretations of these datasets or broaden the set of circumstances in which similar studies could be conducted.

3.2 Methods

Determining how zircon age populations change downstream in a modern or ancient sedimentary system can reveal where and how sediment from a particular source is sorted, stored, and diluted by input from other sources. Detrital zircon U-Pb ages have become widely used to assess the effects of sediment transport processes on zircon populations moving through depositional systems, where zircon ages are used as fingerprints of source regions found in different parts of the catchment (e.g., *Link et al.*, 2005; *Hietpas et al.*, 2011; *Niemi*, 2013; *Saylor et al.*, 2013; *Stevens et al.*, 2013; *Kimbrough et al.*, 2015; *Nie et al.*,

2015). If two detrital zircon samples are collected such that the catchment of one completely includes the catchment of the other, then the portion of zircons in the downstream sample that originated in the upstream sample's catchment, here termed $\mathrm{zr_d}$, depends on (1) the areas of the two catchments, (2) spatial variability in erosion rates, (3) the location of any sediment traps and the rate at which they remove sediment from the system, and (4) the zircon concentration of potential sources. Studies of other detrital heavy minerals show that in many cases spatially uniform erosion and insignificant sediment storage can be assumed (*Stock et al.*, 2006; *Avdeev et al.*, 2011; *Duvall et al.*, 2012; *Tranel et al.*, 2011), leaving only factors (1) and (4) to influence the downstream evolution of a detrital zircon population. Thus, estimates of $\mathrm{zr_d}$ from detrital zircon ages yield constraints on these factors. Previous studies calculated $\mathrm{zr_d}$ by evaluating the proportion of zircons in a specific age bin for a given sample (*Niemi*, 2013). We demonstrate that $\mathrm{zr_d}$ values can also be derived through BPC, which provides a $\mathrm{zr_d}$ estimate that is more sensitive to subtle differences in zircon age distribution shape and can be used in a wider variety of circumstances than the binned calculation method.

3.2.1 Relation of BPC to $\mathrm{zr_d}$

BPC can be related to the value of $\mathrm{zr_d}$ via its relation to the shared portions of two detrital zircon populations, f_1 and f_2 (Fig. 3.1; Eqn. A.10, A.11 of *Tye et al.*, 2019). In the general case of two detrital zircon age populations being compared, the populations can be divided into age peaks that are shared in common between the two populations and age peaks that are unique to their respective population (Fig. 3.1a). f_1 is defined as the proportion of ages in population 1 that fall within shared age peaks, such that if f_1 equals 0, none of the age peaks in population 1 are present in population 2 (Fig. 3.1a). At the opposite extreme, if f_1 equals 1, then all of the age peaks in population 1 are present in population 2 (Fig. 3.1a). f_2 is defined in the same way for population 2 (Fig. 3.1a). In this general case, BPC values can be accurately modeled as a function of f_1 and f_2 (*Tye et al.*, 2019) such that a BPC result yields a set of permissible (f_1, f_2) pairs that characterize the two compared populations, though neither f_1 nor f_2 can be uniquely identified using a single BPC value. However, in the special case that the two compared populations are known to have been collected from the same depositional system such that the catchment of the upstream population was completely contained within the catchment of the downstream population, then additional assumptions about the values of f_1 and f_2 can be made (Fig. 3.1b). Because the catchment that contributes sediment to population 1, the upstream population, is entirely contained within the catchment that contributes sediment to population 2, the downstream population

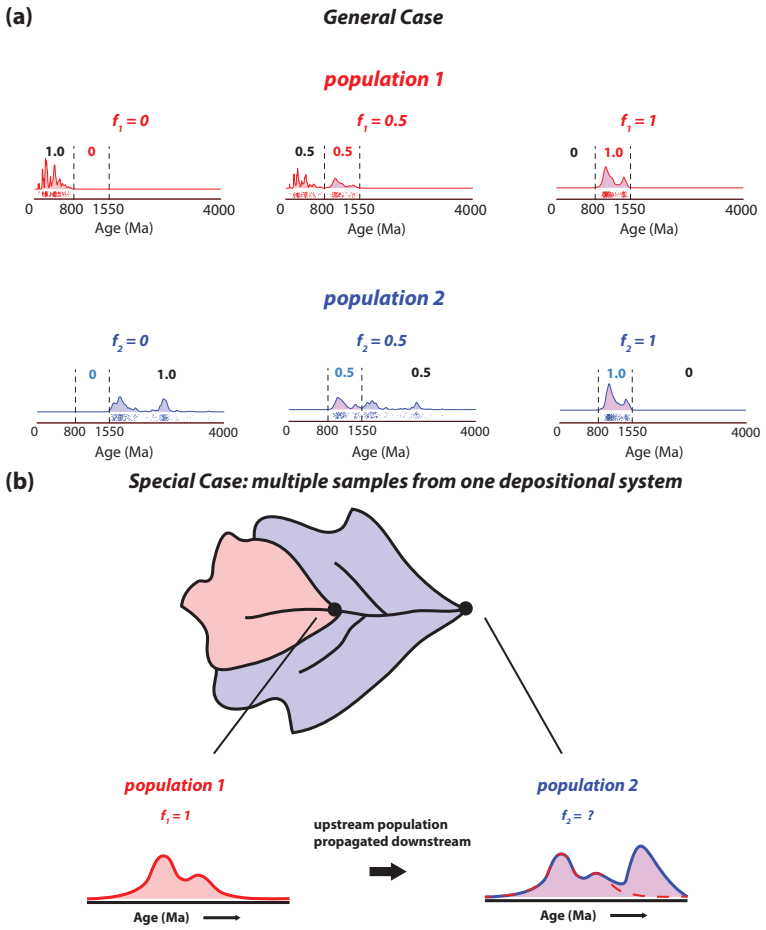

Figure 3.1: Illustration of the shared proportions of two sampled populations, which BPC can be used to estimate. (a) An example shows the general case, in which two detrital zircon age populations have some age peaks shared in common with one another (800-1550 Ma domain) and some age peaks unique to each population (ages <800 Ma for population 1, ages >1550 Ma for population 2). We define f_1 and f_2 as the respective proportions of populations 1 and 2 that fall into the shared 800-1550 Ma domain. (b) In the special case where two sampled populations are located within the same depositional system such that the catchment of one of the two populations entirely contains the catchment of the other sample, multiple assumptions can be made. The panel shows a cartoon map view of a catchment with two sample locations indicated by black dots. The zircon age distributions of the two sampled populations are shown below, and the red portion of the catchment corresponds to the area upstream of population 1 whereas the blue portion of the catchment corresponds to the area upstream of population 2, but not population 1. Because the catchment of population 2 entirely contains the catchment of population 1, all sources that contribute sediment to population 1 also contribute sediment to population 2 and all ages in population 1 are shared with population 2, meaning that f_1 equals 1. f_2 is unknown.

(Fig. 3.1b), all potential sources for population 1 are also potential sources for population 2, meaning that f_1 equals 1 (Fig. 3.1b). Because f_1 can be assumed to be 1, then a BPC value can be used to uniquely calculate f_2, the portion of ages in the downstream population that are shared with the upstream population (Eqn. A.10 of *Tye et al.*, 2019).

In the case where two populations are compared using BPC and one population is located downstream within the same depositional system as the other population (Fig. 3.1b), f_2 is equivalent to $\mathrm{zr_d}$, the proportion of zircons in the downstream population that originated in the catchment of the upstream population. If the catchment of the upstream population contains a set of source zircon ages entirely unique from the downstream catchment, then all zircon ages contained in the downstream population that match ages in the upstream population must have originated within the upstream catchment, and f_2 is therefore the proportion of zircons in the downstream population that originated in the upstream catchment, identical to $\mathrm{zr_d}$. More commonly, some source ages may be shared between the upstream catchment and the downstream catchment, such that zircon ages in the downstream population that match ages in the upstream population may not have originated in the upstream catchment. In such a case, f_2 is greater than the proportion of zircons in the downstream population that originated in the upstream catchment ($f_2 > \mathrm{zr_d}$). Thus, in general $f_2 \geq \mathrm{zr_d}$, or equivalently stated, f_2 is an upper bound on $\mathrm{zr_d}$.

3.2.2 Using BPC-derived $\mathrm{zr_d}$ values to constrain catchment size, transport distance, and sediment transport processes

Within a single depositional system, the transmission of zircon ages from populations located upstream to populations located downstream depends on the relative size of the catchments of the upstream and downstream populations, spatial and temporal variation in erosion rates, sediment storage within the system, and zircon concentrations of sources. If some of these parameters are known or can be assumed for a given depositional system, then $\mathrm{zr_d}$ values can be used to constrain others. As discussed above, detrital heavy mineral studies have shown that for many catchments it can be assumed that erosion is uniform and sediment is not stored (*Stock et al.*, 2006; *Avdeev et al.*, 2011; *Duvall et al.*, 2012; *Tranel et al.*, 2011). If spatially uniform erosion rates and no sediment storage are assumed, then the expected $\mathrm{zr_d}$, referred to as $\mathrm{zr_d}^{\mathrm{pred}}$, depends on catchment areas and zircon concentrations:

$$\mathrm{zr_d}^{\mathrm{pred}} = \frac{A_u}{A_t} \cdot \frac{c_u}{c_t}, \tag{3.1}$$

where A_u & A_t are the areas, and c_u & c_t are the average source zircon concentrations (per unit area) of the upper and total catchments. Here the total catchment refers to the entire catchment contributing sediment to the downstream sample. c_t is itself a function of c_u and c_l (the average zircon concentration of the lower catchment, which is defined to exclude the upper catchment):

$$c_t = \frac{A_u}{A_t} c_u + \left(1 - \frac{A_u}{A_t}\right) c_l \tag{3.2}$$

Under these assumptions, detrital zircon populations are proportionally representative of their catchment areas. Deviation of observed $\mathrm{zr_d}$ values ($\mathrm{zr_d}^{\mathrm{obs}}$; based on BPC) from their predicted values ($\mathrm{zr_d}^{\mathrm{pred}}$; Eqn. 3.1) indicates that the sampled zircon populations are not proportionally representative of their catchment areas, possibly resulting from spatially variable erosion rates or sediment storage.

The relation between $\mathrm{zr_d}$ and catchment area (Eqn. 3.1) can be combined with the power-law relationship between catchment area and fluvial transport distance (*Hack*, 1957) in order to relate $\mathrm{zr_d}$ to fluvial transport distance (*Niemi*, 2013). Hack's Law for the relation between channel length and catchment area (*Hack*, 1957) states that

$$L = CA^h, \tag{3.3}$$

where L is channel length, C is an empirical constant with typical values near 1.5 (*Hack*, 1957; *Montgomery and Dietrich*, 1992), A is catchment area, and h is a constant with typical values near 0.6 (*Hack*, 1957; *Montgomery and Dietrich*, 1992). For two sampled detrital zircon populations within a depositional system with unknown transport distance between them, the transport distance can be calculated by subtracting the length of the upper catchment stream from the length of the lower catchment stream:

$$L_t = CA_t^h - CA_u^h, \tag{3.4}$$

where A_t and A_u are defined as above. Using Eqn. (3.1) to relate A_t to $\mathrm{zr_d}$ reveals that

$$L_t = C\ A_u^h \left(\left(\frac{c_u}{c_t\ \mathrm{zr_d}} \right)^h - 1 \right), \tag{3.5}$$

where c_u and c_t are defined as above (*Niemi*, 2013).

The equations presented in this section represent a small selection of relations between $\mathrm{zr_d}$ and parameters of depositional systems. Because of the relation between BPC and $\mathrm{zr_d}$ (see Section 3.2.1), comparison of detrital zircon U-Pb age distributions using BPC

can provide new constraints on parameters such as stream length, catchment area, zircon fertility, and relative erosion rates in different parts of a given catchment. The constraints provided by BPC have the potential to facilitate new quantitative investigations of ancient and modern sedimentary systems. In the next section, we apply BPC to several published datasets from ancient and modern depositional systems to test the reliability and utility of BPC interpretations.

3.3 BPC results and interpretation

Existing detrital zircon comparative metrics have been used with numerous detrital zircon datasets to assess the effects of fluvial transport (e.g., *Niemi*, 2013), sediment storage (e.g., *Nie et al.*, 2015), sediment sorting (e.g., *Lawrence et al.*, 2011) and mixing (e.g., *Sickmann et al.*, 2016), as well as continent-scale provenance differences (e.g., *Gehrels*, 2000). Here, we present BPC results from three examples that document how the metric is affected by differences in detrital zircon age distributions and the advantages of BPC over other metrics in quantifying the effects of sedimentary processes.

3.3.1 Hydraulic sorting of detrital zircon populations in river microenvironments

A persistent question in detrital geochronology is the degree to which populations of detrital geochronology ages are affected by the energy level of their depositional microenvironment (e.g., *Lawrence et al.*, 2011; *Malusa et al.*, 2016; *Ibañez-Mejia et al.*, 2018). Because greater hydraulic energy is required to move larger and denser sediment grains, sediment is sorted by size and density in depositional microenvironments (e.g., the stoss and lee slopes of a dune), such that grain-size distributions can vary significantly over small spatial scales (*Dietrich*, 1982; *Garzanti et al.*, 2008; *Le Roux*, 2005). If a relationship exists between age and grain size of a mineral used for detrital geochronology in a given depositional system, then geochronological age distributions may vary significantly between microenvironments. Because most applications of detrital geochronology assume that a detrital geochronology dataset is a representative sample of the geochronological ages present in the catchment from which it was collected, local sorting effects within the depositional system are undesirable (e.g., *Ibañez-Mejia et al.*, 2018).

Lawrence et al. (2011) investigate the effect of hydrodynamic fractionation on detrital zircon populations of five depositional microenvironments associated with dunes in the Amazon River (Fig. 3.2). Five sand samples were collected from a dune $\sim$1.25 m high

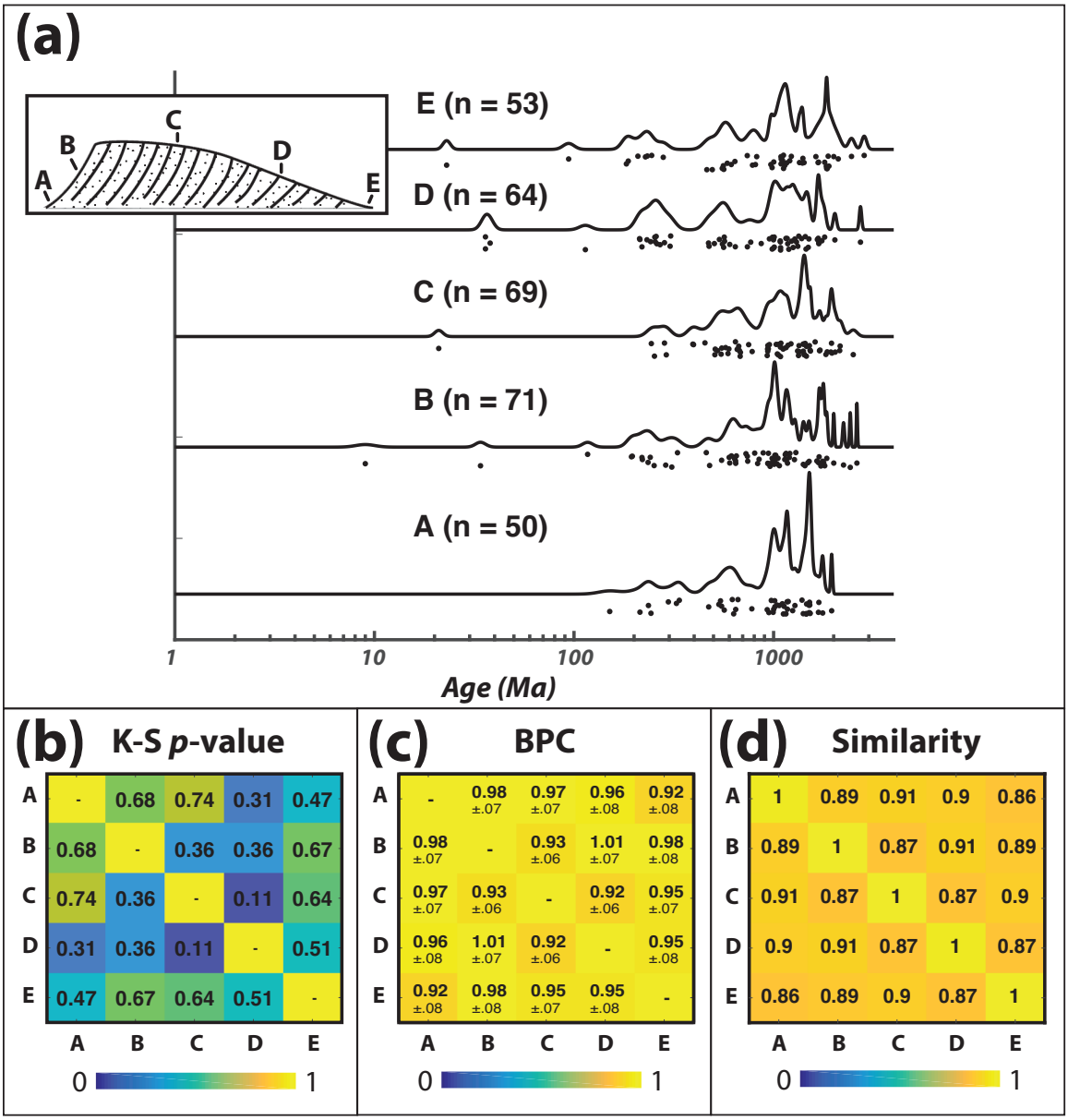

Figure 3.2: BPC indicates that detrital zircon populations of sedimentary microenvironments of a dune bedform (*Lawrence et al.*, 2011) are statistically indistinguishable. (a) Detrital zircon sample microenvironments and ages are shown, using probability density plots (*Hurford et al.*, 1984) for ages. (b) Kolmogorov-Smirnov (K-S) test p-values (taken from *Lawrence et al.*, 2011), (c) BPC (*Tye et al.*, 2019), and (d) Similarity (*Gehrels*, 2000) were calculated for all possible intersample comparisons of the five samples. BPC uncertainties displayed are 1σ. The uncertainty of the other metrics is not readily quantifiable. (Inset of (a) modified from *Lawrence et al.* (2011).)

and ∼20 m long at the edge of a scroll-bar system (*Lawrence et al.*, 2011). *Lawrence et al.* (2011) demonstrate that an age-grain size relationship exists within their sample set of zircons and use statistical methods to test whether the zircon age samples from different dune microenvironments exhibit significant differences due to hydraulic sorting.

Lawrence et al. (2011) assess population differences between the microenvironments using p-values of the Kolmogorov-Smirnov (K-S) test (*Kolmogorov*, 1933; *Smirnov*, 1948), and we use BPC (*Tye et al.*, 2019) and Similarity (*Gehrels*, 2000) to analyze the dune samples they report. All three metrics were calculated for each possible intersample comparison of the five samples (Fig. 3.2). All p-values for sample comparisons reported by *Lawrence et al.* (2011) are above 0.05, indicating that none of the five populations are distinguishable from one another at the 95% confidence level (Fig. 3.2b). The BPC metric (Fig. 3.2c) yields a similar result: all intersample comparisons have BPC values within 2σ uncertainty of 1, meaning that for each comparison the possibility that the sampled populations are identical cannot be rejected at the 95% confidence level. The Similarity values for the sample pairs (Fig. 3.2c) yield the qualitative interpretation that all the samples are quite similar to one another, but no further conclusions can be drawn regarding whether the samples represent statistically distinct populations, or to what degree the populations differ from one another.

The BPC values support the interpretation that hydrodynamic fractionation has not resulted in statistically distinguishable age distributions of the zircon populations for these microenvironments, in agreement with previous analysis using the K-S test. The agreement of BPC with the results of the K-S test is promising because the K-S test is a standard statistical test of equality of two nonparametric probability distributions and is commonly used for detrital zircon data (*DeGraaff-Surpless et al.*, 2003; *Lawrence et al.*, 2011; *Saylor and Sundell*, 2016).

3.3.2 Inferring sediment transport distance from zircon age group dilution

Niemi (2013) uses the sedimentary dilution of detrital zircon populations to constrain the fluvial transport distance between two Miocene sandstones in the Death Valley region. Much of the present distance between the two sampling locations (80 km) has been ascribed to tectonic extension after deposition of the sampled sandstones (*Niemi et al.*, 2001; *McQuarrie and Wernicke*, 2005). Inferring the fluvial transport distance between the samples yields a new constraint on the magnitude of tectonic transport required to achieve the present distance between the samples. *Niemi* (2013) used Jurassic-aged zircons as a tracer

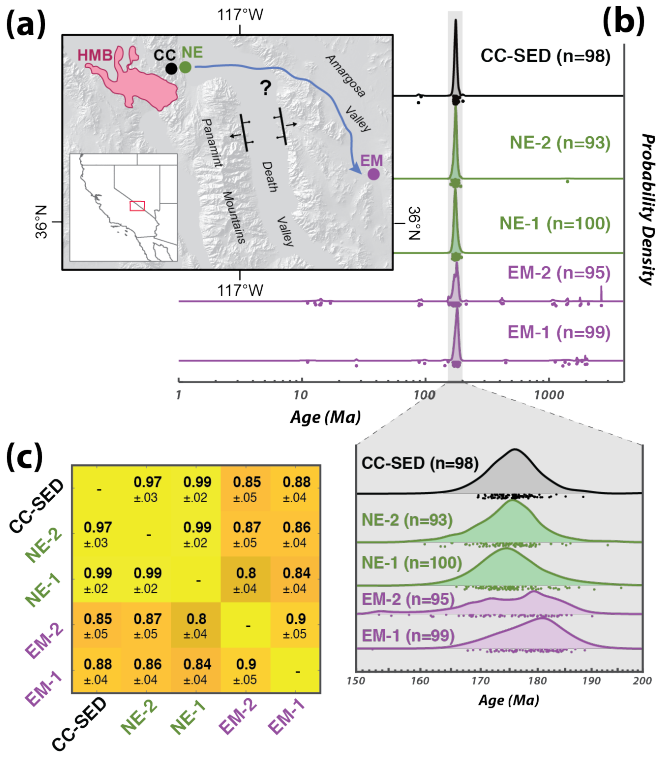

Figure 3.3: Modern and sandstone samples were analyzed in order to understand sedimentary dilution and fluvial transport in a Miocene depositional system in the region of Death Valley, California. (a) location map with current extent of the Hunter Mountain Batholith (HMB), a regionally unique source of Jurassic zircons, outlined in pink, modern sample locality Cottonwood Canyon (CC) marked in black, and locations of samples from the Miocene Navadu Formation (NE) and the Miocene Eagle Mountain Formation (EM) marked in green and purple, respectively. The present distance between the NE and EM sampling localities is ∼80 km. The Miocene fluvial transport distance between the sampling localities may have been less than the present distance, with the remainder due to subsequent extension. (b) detrital zircon probability density plots and dot plots of one modern sample collected at CC and four Miocene sandstone samples collected from sites NE and EM. Inset in light grey focuses on the 150 - 200 Ma age range. (c) BPC is calculated for all possible sample pairs with labeling and color-coding as in Fig. 3.2.

of sediment transport from the Hunter Mountain batholith (HMB) west of Death Valley, which is a unique source of Jurassic zircons in the region (*Niemi*, 2013). Zircons of this age are found in the middle Miocene Navadu Formation immediately adjacent to the HMB, as well as in strata of the equivalently-aged Eagle Mountain Formation currently located ∼100 km ESE of the the batholith (Fig. 3.3). Sedimentologic arguments had previously been put forward to argue that much of the present-day distance between the HMB and the Eagle Mountain Formation is tectonic in origin (*Niemi et al.*, 2001), but quantification of the proportion of sedimentologic and tectonic transport of the Eagle Mountain Formation from its source is problematic (*Renik et al.*, 2008). By measuring the dilution of the diagnostic Jurassic age peak from the HMB, *Niemi* (2013) attempted to ascertain the fluvial transport distance between the Eagle Mountain Formation and the HMB in the middle Miocene.

Detrital zircon samples were collected and analyzed from modern stream sediment that drains the batholith, the middle Miocene Navadu Formation, which was deposited adjacent to the batholith, and the middle Miocene Eagle Mountain Formation. The Navadu Formation has a nearly-identical detrital zircon age distribution to modern river sand sourced from the HMB (Fig. 3.3). The Eagle Mountain Formation has a detrital zircon age distribution similar to the Navadu Formation and modern sand, but with a greater diversity of both older and younger zircon ages. *Niemi* (2013)'s postulate is that the Jurassic detrital zircon age peak in sediment derived from the HMB can be treated as a unique point source that decreases in magnitude with increasing distance of sedimentary transport as the drainage area supplying sediment to the fluvial system increases (*Hack*, 1957). This postulate assumes that both erosion rates and zircon concentrations in eroding bedrock sources throughout the catchment are spatially and temporally uniform, or that variations in these parameters can be quantified.

We review how *Niemi* (2013) calculates $\mathrm{zr_d}$, the dilution of a distinct zircon age population, and then demonstrate the application of BPC to this same problem. *Niemi* (2013) calculates the value of $\mathrm{zr_d}$ by binning the zircon ages from each sample and comparing the proportion of Early Jurassic zircons in the upstream samples (NE-1, NE-2, from the Navadu Formation) to the proportion of Early Jurassic zircons in the downstream samples (EM-1, EM-2, from the Eagle Mountain Formation) using Eqn. (3.5). The upstream Navadu Formation samples have nearly unimodal zircon age distributions dominated by ages associated with the Early Jurassic HMB (Fig. 3.3). The greater diversity of ages present in the downstream Eagle Mountain Formation samples (Fig. 3.3) requires input from non-HMB sources, which were likely located mostly outside the catchment area of the Navadu Formation samples. Samples EM-1 and EM-2 are composed of 86% and 76%

Early Jurassic grains, respectively, equivalent to $\mathrm{zr_d}$ estimates of 0.86 and 0.76. Niemi treats the catchment area of the Navadu Formation as 400 km^2, the present exposure area of the HMB, and defines a $\frac{c_u}{c_l}$ ratio of 3.5, meaning that the HMB produces 3.5 times as many zircons as other sources in the catchments of the Navadu and Eagle Mountain Formation samples. These values are chosen to be upper bounds for the respective parameters in order to yield an upper bound on the fluvial transport distance between the Navadu and Eagle Mountain Formation samples, resulting in a conservative estimate of the tectonic transport distance between the samples. Using these parameter values, *Niemi* (2013) finds the sedimentary transport distance between samples of the Navadu Formation and the Eagle Mountain Formation to be $\sim$20 km, with 60 km of tectonic transport required to achieve the present offset of 80 km between the Navadu Formation and Eagle Mountain Formation samples, consistent with palinspastic reconstructions (*McQuarrie and Wernicke*, 2005).

Alternatively, instead of binning the zircon age populations, BPC can be applied to this problem. BPC values (Fig. 3.3c) calculated between the EM samples and sample NE-1, composed entirely of zircons from the HMB, are 0.84 $\pm$ 0.04 (NE-1 and EM-1) and 0.80 $\pm$ 0.04 (NE-1 and EM-2). By numerical solution of Eqn. A.11 of *Tye et al.* (2019) for $\mathrm{zr_d}$, these BPC values indicate $\mathrm{zr_d}$ values of 0.71 $\pm$ 0.07 and 0.66 $\pm$ 0.06, respectively. The $\mathrm{zr_d}$ values indicated by BPC are $\sim 2\sigma$ less than the original values calculated by *Niemi* (2013). The differences between $\mathrm{zr_d}$ values estimated from the BPC method and the binned-calculation method of *Niemi* (2013) reflect the different sensitivities of the two methods. The binning method employed by *Niemi* (2013) is insensitive to the distribution of zircon ages within the Early Jurassic age bin. The BPC method, however, is sensitive to such distributions and the lower $\mathrm{zr_d}$ value resulting from the BPC approach reflects differences of central age and shape of the Early Jurassic age peak of the Eagle Mountain Formation and the equivalent peak in the Navadu Formation (Fig. 3.3b). The observed differences in the Early Jurassic age peaks require greater dilution of the upstream Navadu Formation population in the downstream Eagle Mountain population than is inferred from the binning method of *Niemi* (2013), which treats all Early Jurassic zircon ages as equivalent. The sensitivity of BPC to the observed differences in age peak shape cause the $\mathrm{zr_d}$ value calculated from BPC to be lower than the $\mathrm{zr_d}$ value calculated from binning.

The differences between the Jurassic age peaks of the Navadu Formation and Eagle Mountain Formation (Fig. 3.3b) have implications for the upstream catchment area and therefore the fluvial transport distance inferred from BPC (Eqn. 3.5). *Niemi* (2013) assumed the upstream catchment area to be the present exposure area of the Hunter Mountain Batholith. If the entire HMB was within the catchment that included the Navadu Formation and Eagle Mountain Formation sample locations, then the Early Jurassic age detrital zircon

age peaks observed within the Navadu Formation and Eagle Mountain Formation should mirror the distribution of ages present in the HMB. The Early Jurassic zircon age peak of the upstream Navadu Formation is centered on ∼178 Ma and the equivalent age peak in the downstream Eagle Mountain Formation is centered on ∼183 Ma (Fig. 3.3b). The HMB has concentrically-zoned crystallization ages, ranging from ∼180 Ma at the edge to ∼155 Ma at the center (*Niemi et al.*, 2001), so the fact that Early Jurassic zircons of the Navadu Formation and the Eagle Mountain Formation are centered on ∼178 Ma and ∼183 Ma respectively indicates derivation primarily from the outer margin of the HMB. Thus, it is unlikely that the catchment that included the Navadu Formation and Eagle Mountain Formation samples contained the entire HMB. Based on the observed ages, it is likely that this catchment included only a moderate portion of the HMB within its boundaries. If the Navadu Formation and Eagle Mountain Formation sandstones only included $\sim \frac{1}{3}$ of the HMB within their catchment areas, the inferred fluvial transport distance inferred between the two formations would be 18 ± 4 km (Eqn. 3.5), requiring 58 - 66 km tectonic transport between the two formations required to account for the present offset of 80 km (*Niemi*, 2013). Such a catchment area is reasonable given the inferred sourcing of Navadu Formation and Eagle Mountain Formation detrital zircons largely from the margin of the HMB, and the resulting fluvial transport distance is also consistent with available constraints on the magnitude of tectonic transport between the Navadu and Eagle Mountain Formations (*McQuarrie and Wernicke*, 2005; *Niemi*, 2013). This example demonstrates that $\mathrm{zr_d}$ values derived from BPC more accurately reflect the differences in compared zircon age populations than $\mathrm{zr_d}$ values calculated from binning detrital zircon samples.

A significant advantage of BPC over a binned calculation approach is that a binned calculation approach depends on the presence of a unique age signal produced by a single source in a depositional system, such as the HMB and the Jurassic zircons eroded from it (*Niemi*, 2013). In contrast, BPC is generalizable and can be applied in situations where an age signal of interest is more complex or overlaps with other detrital zircon ages present in the system. In such cases, BPC presents a source of robust constraints on dilution that is subject to fewer assumptions than a method similar to that of *Niemi* (2013).

3.3.3 Detrital zircon evidence for sediment sequestration in a fluvial system

Nie et al. (2015) use detrital zircons from Quaternary to modern deposits of the Yellow River, Mu Us Desert, and Chinese Loess Plateau to investigate sediment dispersal across the Yellow River drainage and formation of the Chinese Loess Plateau. Based on the similar

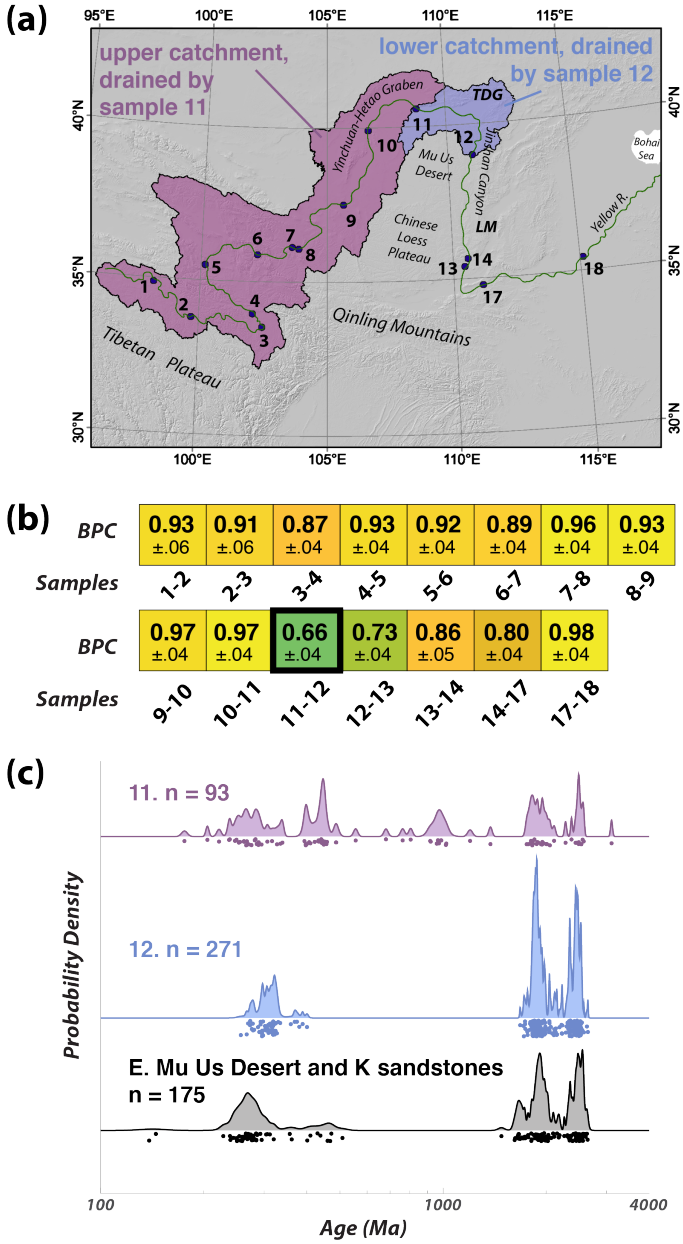

Figure 3.4: Effects of sediment storage and spatially variable erosion on modern detrital zircon populations are assessed using BPC. (a) modern samples (*Yang et al.*, 2009; *Kong et al.*, 2014; *Stevens et al.*, 2013; *Nie et al.*, 2015) were analyzed from along the Yellow River. Outlines show the catchment areas of samples 11 and 12, which have the lowest BPC value of any pair of adjacent samples. Samples are labeled with their number (as *Nie et al.*, 2015). (b) BPC is calculated between adjacent sample pairs, with the lowest value occurring between samples 11 and 12, indicated by the black box, using the same color scale as in Figure 3.2. Detrital zircon spectra are relatively uniform upstream of sample 11. (c) probability density plots are shown for samples 11 and 12 and samples from modern eastern Mu Us Desert sands and Cretaceous sandstones that overlie the Chinese craton.

detrital zircon age spectra they find in the Yellow River, Mu Us Desert, and Loess Plateau deposits, *Nie et al.* (2015) argue that sediment is sequestered in terrestrial basins along the Yellow River and transported by wind to the western Mu Us Desert and the Chinese Loess Plateau (Fig. 3.4). Here, we use BPC to quantitatively assess the effects of sediment sequestration on the downstream propagation of detrital zircon age spectra in modern sediment along the Yellow River.

Eighteen modern detrital zircon samples (*Yang et al.*, 2009; *Kong et al.*, 2014; *Stevens et al.*, 2013; *Nie et al.*, 2015) were examined from the Yellow River, which have been interpreted as being dominated by input from the northeastern Tibetan Plateau and Qingling Mountains (*Nie et al.*, 2015, Fig. 3.4). The location of primary sediment sequestration is determined by *Nie et al.* (2015) to be the Yinchuan-Hetao Graben (Fig. 3.4a).

If sediment storage in the Yinchuan-Hetao Graben significantly reduces the number of zircons transported downstream, then such storage should be reflected in BPC-derived $\mathrm{zr_d}$ values. Specifically, Eqn. (3.1) describes the predicted portion of a downstream detrital zircon population that originated in an upstream catchment, $\mathrm{zr_d}^{\mathrm{pred}}$, based on catchment geometry and zircon concentration, assuming that sediment storage is negligible. In a case where significant sediment storage occurs (*Nie et al.*, 2015), a $\mathrm{zr_d}$ value inferred from a BPC comparison between two samples (here termed $\mathrm{zr_d}^{\mathrm{obs}}$) should be less than the $\mathrm{zr_d}^{\mathrm{pred}}$ value calculated for the given catchment geometry and zircon concentrations. Samples 11 and 12, which bracket the downstream extent of the Yinchuan-Hetao Graben, yield the lowest BPC value of any pair of adjacent samples, 0.66 ± 0.04 (Fig. 3.4b), which corresponds to a $\mathrm{zr_d}^{\mathrm{obs}}$ of 0.39 ± 0.05 by Eqn. A.11 of *Tye et al.* (2019). This BPC-derived $\mathrm{zr_d}^{\mathrm{obs}}$ value means that at least $\sim$60% of the zircons in sample 12 originated from the lower catchment area below sample 11. In contrast, measurement of the catchment areas of the samples indicates that the total catchment of sample 12 is only $\sim$14% larger than sample 11. Solution of Eqn. (3.1) with Eqn. (3.2) reveals that a $\frac{c_l}{c_u}$ ratio of $\sim 11 \pm 2$ would be required for $\mathrm{zr_d}^{\mathrm{pred}}$ to equal $\mathrm{zr_d}^{\mathrm{obs}}$, given the assumptions of spatially constant erosion and no sediment storage. Existing estimates of the range of zircon concentrations in igneous and sedimentary rocks (e.g., *Dickinson*, 2008; *Niemi*, 2013) suggest that such a ratio is unrealistically high, implying sediment storage in the system.

Two additional arguments support the hypothesis that sediment storage is significantly altering the detrital zircon age populations of the modern Yellow River. First, the sources for sample 12—the eastern Mu Us Desert and Cretaceous sandstones overlying the Chinese craton—show significant detrital zircon age distribution overlap with upstream sources (sample 11 in Fig. 3.4c), indicating that $\mathrm{zr_d}^{\mathrm{obs}}$ values based on BPC derived from comparing samples 11 and 12 are overestimated. The overestimation of $\mathrm{zr_d}^{\mathrm{obs}}$ indicates that

fewer of the zircons present in sample 12 would have originated upstream of the sample 11 location than is indicated by our analysis above, lending further support to the hypothesis that much sediment from upstream of sample 11 is sequestered upstream of the sample 12 location. Second, as discussed by *Nie et al.* (2015), at least one major age peak from sample 11 is absent in sample 12, implying extreme dilution or removal of many of those zircons from sedimentary transport. More detailed knowledge of the spatial variability of zircon concentrations and erosion rates in the Yellow River catchment would refine BPC-derived estimates of the proportion of zircons propagated through the Yellow River depositional system.

3.4 Conclusions

BPC is a comparative metric for detrital geochronology datasets which has readily quantifiable uncertainties, no sample size biasing, and values that vary systematically with the proportion of zircon ages shared between two parent populations (*Tye et al.*, 2019). The quantitative interpretation permitted by BPC is shown to support prior conclusions regarding several existing detrital zircon datasets and offers a new method of investigation into how sediment sorting, transport, and storage affect detrital zircon populations.

In one case, we use BPC to show that detrital zircon populations in several sedimentary micro-environments of varying energy level (*Lawrence et al.*, 2011) are indistinguishable from one another. The interpretation from BPC matches the interpretation from the K-S test (*Lawrence et al.*, 2011). The compatible results from BPC and the K-S test are significant because the K-S test is an established statistical test, and these results suggest that BPC values are probabilistically meaningful.

One advantage of BPC over many statistical tests, including the K-S test, is that it is not only a binary test of statistical equivalence of two populations, but it also reflects the degree of correspondence between two populations (*Tye et al.*, 2019). When applied to two samples that are part of the same catchment with one located downstream of the other, BPC can be used to estimate the proportion of the downstream detrital zircon population that is likely to have been derived from the upstream population. In a case involving Miocene sandstones in Death Valley, detrital zircon age population dilution inferred from BPC constrains the fluvial transport distance of the sandstones and yields similar results to an analysis of binned ages (*Niemi*, 2013). This case suggests that BPC may be generally useful for analyzing zircon dilution in sedimentary systems, proving especially advantageous in cases where complex age distributions prevent the use of binned calculations such as that employed by *Niemi* (2013).

BPC can also be used to estimate the effects of processes like sediment storage on the detrital zircon age signal being propagated through a depositional system. BPC values provide constraints on the dilution of zircon populations in depositional systems, and downstream rates of dilution can be compared against the rate of catchment addition in order to assess where zircons are being disproportionately added or removed from the system. In the case of the Yellow River, BPC results suggest the disproportionate dilution of a signal associated with source areas in the upper reaches of the river, providing evidence to support the hypothesis that sediment is sequestered along the course of the river (*Nie et al.*, 2015).

Acknowledgments

This work was partially supported by NSF grants EAR-1151247 and EAR-1524304 (NAN). The Turner Fund from the Department of Earth and Environmental Sciences at the University of Michigan supported this work through a postdoctoral fellowship to A. S. Wolf and research grant to A. R. Tye. N. Niemi also acknowledges a CIRES Sabbatical Fellowship from the University of Colorado and colleagues from that institution who stimulated the early seeds of this research.

CHAPTER 4

Field Estimate of Paleoseismic Slip on a Normal Fault Using the Schmidt Hammer and Terrestrial LiDAR: Methods and Application to the Hebgen Fault (Montana, USA) *

Abstract

The weathering characteristics of bedrock fault scarps provide relative age constraints that can be used to determine fault displacements. Here, we report Schmidt hammer rebound values (R-values) for a limestone fault scarp that was last exposed in the 1959 Mw 7.3 Hebgen Lake, Montana earthquake. Results show that some R-value indices, related to the difference between minimum and maximum R-values in repeated impacts at a point, increase upward along the scarp, which we propose is due to progressive exposure of the scarp in earthquakes. An objective method is developed for fitting slip histories to the Schmidt hammer data and produces the best model fit (using the Bayesian Information Criterion) of three earthquakes with single event displacements of $\geq$ 1.20 m, 3.75 m, and c. 4.80 m. The same fitting method is also applied to new terrestrial LiDAR data of the scarp, though the LiDAR results may be more influenced by macro-scale structure of the outcrop than by differential weathering. We suggest the use of this fitting procedure to define single event displacements on other bedrock fault scarps using other dating techniques. Our preliminary findings demonstrate that the Schmidt hammer, combined with other methods, may provide useful constraints on single event displacements on exposed bedrock fault scarps.

*Chapter 4 is published in *Earth Surface Processes and Landforms*: Tye, A., and Stahl, T. (2018). Field estimate of paleoseismic slip on a normal fault using the Schmidt hammer and terrestrial LiDAR: Methods and application to the Hebgen fault. Earth Surface Processes and Landforms 43, 2397 - 2408.

4.1 Introduction

Exposed rock surfaces weather via physical and chemical processes that change rock mass and surface properties through time (cf. *Birkeland and Noller*, 2000). Depending on the lithology and climate conditions, this weathering usually degrades the mechanical integrity of the rock and increases surface roughness through time (*Benedict*, 1985; *Crook and Gillespie*, 1986; *Maizels*, 1989; *McCarroll*, 1991; *Stewart*, 1996). Relative exposure age dating techniques were developed on the premise that these weathering-related changes can be quantified and used to compare the ages of rocks and landforms, and are usually supported empirically via calibration on surfaces of known age (*Colman and Dethier*, 1986, and references cited therein). Relative and calibrated exposure dating techniques applied to rock surfaces have been used to date moraines (*Matthews and Shakesby*, 1984; *Winkler*, 2005), rock glaciers (*Laustela et al.*, 2003; *Aa et al.*, 2007), snow avalanche ramparts (*Matthews et al.*, 2015), bedrock surfaces (*Gupta et al.*, 2009; *Matthews and Owen*, 2010), fluvial terraces (*Stahl et al.*, 2013), patterned ground (*Winkler et al.*, 2016), and erratic boulder trains (*Darvill et al.*, 2015), among others. They have also been used in the field of paleoseismology to date coseismic rock avalanche deposits (e.g., *Bull*, 1996), correlate deformed river terraces (*Stahl et al.*, 2016), and identify displacement patterns on bedrock normal fault scarps (*Stewart*, 1996; *Tucker et al.*, 2011; *He et al.*, 2016).

Bedrock scarps can be progressively exposed in repeated earthquakes along a normal-slip fault (*Bosi et al.*, 1993). If the scarp face is preserved over several earthquake cycles, as is commonly the case in indurated limestones, several episodes of displacement may be preserved along the face. Previous researchers have performed terrestrial cosmogenic nuclide dating (TCND) transects along scarp faces, using chlorine-36 (^{36}Cl) in limestone, to date the timing of earthquakes and demarcate single event displacements (SEDs) that scale with earthquake magnitudes (e.g., *Wells and Coppersmith*, 1994). Some have observed that the different 'slip patches' have distinguishing weathering characteristics that can be used to delineate SEDs independently of absolute ages (*Stewart*, 1996), or that could assist in choosing sample locations for TCND and/or with the final interpretation of ages (*Zreda and Noller*, 1998). For example, Terrestrial LiDAR scanning (TLS) has been used to investigate the microtopographic expression of these slip patches (*Giaccio et al.*, 2003; *Wei et al.*, 2013; *Wiatr et al.*, 2015; *He et al.*, 2016).

Here, we test the applicability of using TLS and the Schmidt hammer to quantitatively distinguish weathering zones and slip patches on the Hebgen fault in Montana, USA. The interpretation of this scarp as being related to progressive exposure in earthquakes has been questioned due to discrepant paleoseismic histories in nearby records (e.g., *Pierce et al.*,

2000). Therefore, we propose that our approach could be used to clarify the exposure history of this scarp by assessing variations in time-dependent rock weathering properties along the scarp face and estimate the SEDs of past earthquakes. In our analysis, we use curve-fitting techniques that can be used to assess the appropriate form of the weathering index versus scarp height curve, which could be used to objectively identify SEDs using other relative-age dating techniques.

4.2 Background

4.2.1 Significance of single-event displacements in paleoseismology

Determining the surface displacements of past earthquakes on faults is an essential component of paleoseismology. Fault SEDs scale with the magnitude of an earthquake (e.g., *Wells and Coppersmith*, 1994), are used to define fault avoidance zones in seismic hazard assessments (e.g., *Boncio et al.*, 2012; *Villamor et al.*, 2012), and can be used to estimate average earthquake recurrence intervals if long-term fault slip rates are available. Paleoseismic trenching can be used to determine SEDs where a fault has ruptured through unconsolidated sediments, but is not typically feasible across bedrock scarps. TCND along normal-slip bedrock scarps can be used to directly date and measure displacements of multiple paleo-earthquakes (*Benedetti et al.*, 2002; *Benedetti and van Der Woerd*, 2014; *Carcaillet et al.*, 2008; *Mitchell et al.*, 2001; *Zreda and Noller*, 1998). Accurate reconstructions of slip histories in these studies usually rely on several closely spaced samples from the scarp face, numerical modeling (e.g., *Schlagenhauf et al.*, 2010), and/or secondary scarp weathering evidence to corroborate the interpretation of modeled ages.

4.2.2 Geomorphic framework for relative dating of SEDs

Method	Technique	Description/utility	Practical and theoretical limitations	References
Surface roughness	Micro-roughness meter	Can distinguish most recent event in some circumstances	One-dimensional (1D) (transect-based), but can be applied in two dimensions (2D) if scarp is accessible	(*Stewart*, 1996; *Giaccio et al.*, 2003)
	Terrestrial LiDAR	High-resolution, three-dimensional (3D) topography of fault scarp; can distinguish between Holocene-aged events	Equipment is expensive and requires significant data processing	(*Wei et al.*, 2013; *Wiatr et al.*, 2015; *He et al.*, 2016, this study)
	Pit depth	Pit depths increase up-scarp	Requires manual measurement (transect-based), but can be applied in two dimensions	(*Tucker et al.*, 2011)
Image analysis	Color	Identification of paleo bedrock-soil boundary	Some subjectivity in manipulation of color; time-independent color changes	(*Giaccio et al.*, 2003)

Geochemical	Rare earth element (REE) and yttrium	Previous contact with soil enriches fault plane in REE prior to exposure; concentrations can be measured on exposed fault scarp	Requires rock sampling equipment and subsequent laboratory work	(*Carcaillet et al.*, 2008; *Manighetti et al.*, 2010; *Mouslopoulou et al.*, 2011)
Descriptive	Adjusted Geological Strength Index (AGSI)	Incorporates numerous weathering properties of rocks	Some subjectivity in assigning Geological Strength Index (GSI) values; metrics depend on geomorphic framework	This study
Schmidt hammer	Rebound values	Incorporates numerous mechanical properties of rock into R-value measurement	1D (transect-based), but can be applied in 2D if scarp is accessible	This study

Table 4.1: Overview of methods for distinguishing weathering zones on fault scarps.

Surface-rupturing normal faults accumulate displacement episodically in earthquakes or via continuous creep. In the absence of near-surface creep and significant erosion, bedrock fault scarps can record several meters of cumulative displacement over many earthquake cycles. Under ideal circumstances, each earthquake brings a previously unexposed, relatively unweathered, slip patch up to the surface and raises the previously exposed patches from older earthquakes higher along the scarp. Thus, from the bottom to the top of a normal fault scarp (i.e., moving up-dip), there should be progressively more weathered slip patches. This framework assumes that (i) that fault colluvium does not bury the newly exposed slip patch inhibiting subaerial weathering, and (ii) no external processes, besides weathering, significantly alter the scarp after it is exposed (e.g., stream modification of the base of the scarp, removal of rock mass via slope processes, biological weathering due to lichen or vegetation cover, remineralization of calcite lower on limestone scarps) (e.g., *Kastelic et al.*, 2017). These assumptions are not always valid and limit the applicability of all scarp dating techniques at some sites.

Numerous studies have outlined methods for identifying SEDs independently of cosmogenic exposure ages on bedrock scarps and typically focus on differing degrees of rock weathering. In the first TCND study of a bedrock scarp, *Zreda and Noller* (1998) used qualitative metrics of rock weathering (e.g., roughness, preservation of slickensides, pitting, and discoloration) as corroborative evidence of their preferred slip history. Measurements of surface roughness using a microroughness meter (*Stewart*, 1996) and TLS (*Giaccio et al.*, 2003; *Wei et al.*, 2013; *Wiatr et al.*, 2015), pit depth measurements (*Tucker et al.*, 2011), image analysis (*Giaccio et al.*, 2003), and geochemical signature (*Carcaillet et al.*, 2008; *Manighetti et al.*, 2010; *Mouslopoulou et al.*, 2011) have yielded promising results that can assist in interpreting scarp exposure and weathering histories. Other relative dating techniques that measure rock weathering grade are useful in reconnassiance and assessment of bedrock fault scarps (Table 4.1).

4.2.3 The Schmidt hammer in rock weathering and relative-age dating studies

The Schmidt hammer tests rock hardness by measuring the rebound of a spring-loaded piston in a controlled impact against the rock surface, yielding a rebound value (R-value) (*Day*, 1980). The technique has been used in geomorphology for over 40 years (*Day and Goudie*, 1977; *Goudie*, 2006) and has been applied to rapidly assess rock strength in the field and as a relative exposure-age dating tool to distinguish landforms of different ages (*Goudie*, 2006; *Shakesby et al.*, 2011). The latter application operates on the assumption

that rock surface compressional strength and/or mechanical integrity decreases with time. Calibration with rock surfaces of known age allows this assumption to be tested and in some cases, enables researchers to establish chronofunctions that can be used to date rock surfaces or landforms over 10^2 - 10^4 year timescales (e.g., *Stahl et al.*, 2013).

In order to use the Schmidt hammer as a relative dating tool, controls must be emplaced to ensure that exposure age is the dominant, if not the only, variable that affects R-values. Previous researchers have investigated the relationship between R-value and time-independent variables that affect R-values like lithology (e.g., *Goudie*, 2006; *Török et al.*, 2007), sample dimensions (*Sumner and Nel*, 2002; *Aydin*, 2008; *Demirdag et al.*, 2009), number of samples (*Niedzielski et al.*, 2009), operator bias (*Shakesby et al.*, 2006), instrument degradation (*McCarroll*, 1987), biological weathering (*Matthews and Owen*, 2008), moisture content (*Sumner and Nel*, 2002), and spatially-variable weathering rates (*Stahl et al.*, 2013). If these variables are known and adequately controlled, the Schmidt hammer can be used to distinguish rock surfaces with different exposure ages (*Shakesby et al.*, 2006, 2011; *Stahl et al.*, 2013).

The difference between Schmidt hammer R-values in successive impacts at the same location increases with increasing weathering grade (*Aydin and Basu*, 2005; *Nicholson*, 2009; *Matthews et al.*, 2016). Using this differencing approach allows detection of and control for small-scale lithologic, rock mass, or surface roughness variations that lead to time-independent variability in single impact R-values. This effect is partially due to a decrease in surface roughness after the first impact, and subsequent pulverization of the outer weathered zone, leading to higher R-values in successive impacts. *Matthews et al.* (2016) showed that this effect becomes insigificant after the fifth impact in a range of metamorphic and igneous lithologies.

4.2.4 Identification of bedrock fault scarp slip patches using microtopography

Microtopography data acquired using TLS have been combined with surface roughness metrics to investigate fault processes (e.g., *Sagy et al.*, 2007; *Candela et al.*, 2009) and to investigate the weathering of bedrock fault scarps (*Giaccio et al.*, 2003; *Wei et al.*, 2013; *Wiatr et al.*, 2015; *He et al.*, 2016). Most of these approaches use fractal parameters as roughness proxies. Fractal parameter-based methods exploit the fact that on natural surfaces, the magnitude of relief is related to the interval over which it is measured by a power law (e.g., *Ahnert*, 1984). The exponent of this power law reflects how relief changes with scale. For instance, *He et al.* (2016) used the best-fit value of this exponent over the surface

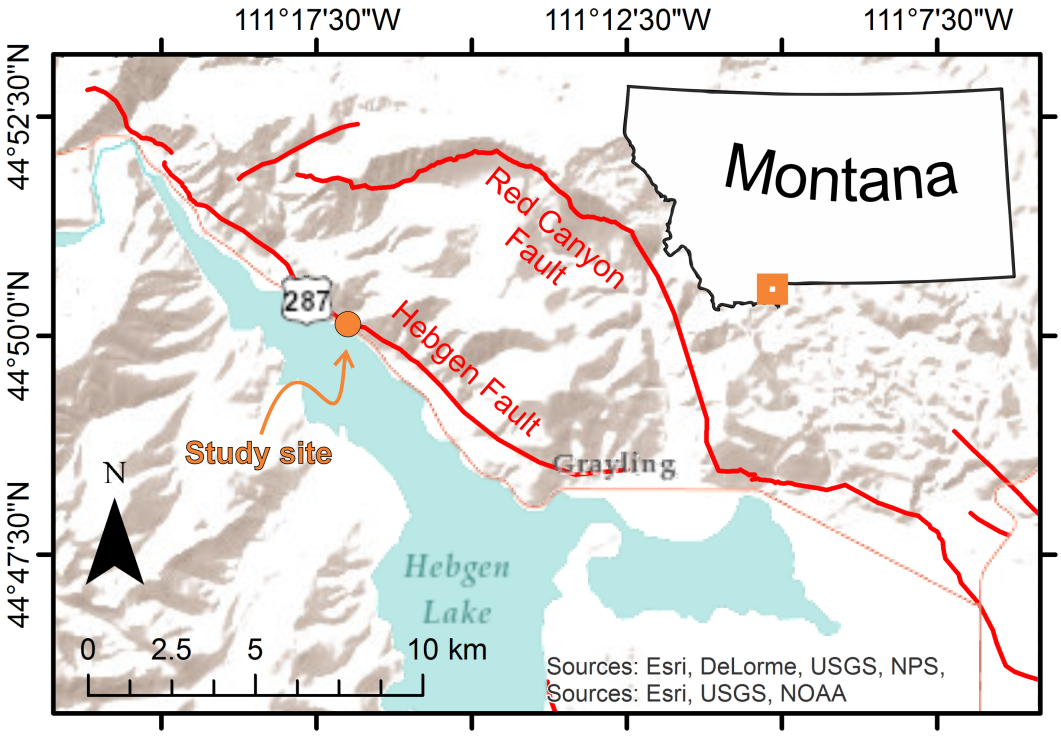

Figure 4.1: Location and fault trace map of the Hebgen and Red Canyon faults in southwestern Montana. Fault traces are from the US Geological Survey Quaternary Fault and Fold database.

of a bedrock fault scarp to identify slip patches on limestone fault scarps. *Wei et al.* (2013) use fractal-based methods to show that on limestone fault scarps, weathering effects are typically expressed on scales of several centimeters and less.

4.2.5 Study site

The ideal study site for testing Schmidt hammer and TLS approaches should have (i) some evidence of multiple slip events exposed along a bedrock fault scarp, (ii) homogenous lithology along the scarp, and (iii) good scarp preservation with subaerial weathering being the predominant mode of postexposure alteration. We selected a site along an exposed section of the Hebgen fault on the northern shore of Hebgen Lake in Montana (Figure 4.1). The lake has an elevation of c. 2000m above sea level. The region is cold and dry, with mean annual temperature of 2.8 °C and mean annual precipitation of c. 500 mm. Mean monthly temperatures range from 8 to 16 °C; monthly precipitation is relatively constant at between 30 and 50 mm. The area of Hebgen Lake was periglacial during the last glacial

maximum (LGM, ∼21 ka BP Pinedale Glaciation) but not occupied by ice and may have been even drier than present day climate (*Licciardi and Pierce*, 2008). Terminal moraines and glacial till from the penultimate Bull Lake glaciation (∼130-160 ka BP) indicate that the valley was occupied by ice in earlier Pleistocene glaciations (*Licciardi and Pierce*, 2008; *Pierce*, 2003).

Hebgen Lake is manmade, created by damming the Madison River in 1914, and is located within the intermontane Madison Valley. The region is currently undergoing northeast-southwest (NE-SW) directed Basin and Range extension and is also at the western flank of Yellowstone hotspot-related deformation (*Wicks et al.*, 2006). The 1959 Mw 7.3 Hebgen Lake earthquake produced surface rupture along the Hebgen and Red Canyon faults (*Witkind et al.*, 1962) which led to NE-directed subsidence, lake-level rise on the northern shore of Hebgen Lake, and subsequent inundation of the old route US-287 (Figure 4.1). The new road was established ∼20m higher, at the base of the c. 250 m-long outcrop considered in this study.

The limestone that comprises the scarp face is mapped as middle Cambrian Meagher Formation (*Zreda and Noller*, 1998; *O'Neill and Christiansen*, 2004). It is finely crystalline and appears massively bedded at the transect site though it is commonly thinly to medium bedded and oolitic in other areas (*O'Neill and Christiansen*, 2004). Fresh faces of the limestone appear grayish tan; weathered faces, in general, are light to dark gray, with some darker staining and pitting evident on some faces. Meter-scale joints are present at some locations along the cliff exposure. No obvious variability in limestone sedimentology was observed along preserved sections of the scarp and no fault breccia or gouge was observed.

Our transect coincides with the study site of *Zreda and Noller* (1998), who used in situ cosmogenic ^{36}Cl to obtain exposure ages of sections of the limestone scarp and model earthquake ages. The remainder of the roadside outcrop is unsuitable for absolute- or relative-age dating as the limestone scarp above the 1959 slip patch has been subject to rockfall and is therefore discontinuous up-dip. *Zreda and Noller* (1998) interpreted the lowest portion of the scarp at our site to have been exposed in 1959 Mw 7.3 Hebgen Lake earthquake, which caused up to c. 6m vertical displacement along the fault. They inferred a total of six earthquakes at this site since 24 ka (four since 7 ka). Their data show that SEDs vary from c. 1-2 m per event, with 2.1 m of slip at the study site in the 1959 earthquake. Nearby trenching studies and mapping of *Hecker et al.* (2000, 2002) and *Pierce et al.* (2000) revealed similar >1.2-3.1 m SEDs, but found evidence of only one Holocene earthquake prior to the 1959 event (c. 1-3 ka) and one latest Pleistocene earthquake (c. 10-15 ka; *Schwartz et al.*, 2009). The nearest trench to the study site revealed a cumulative 2-3 m vertical displacement in the 1959 and penultimate events, and 5-6 m cumulative vertical

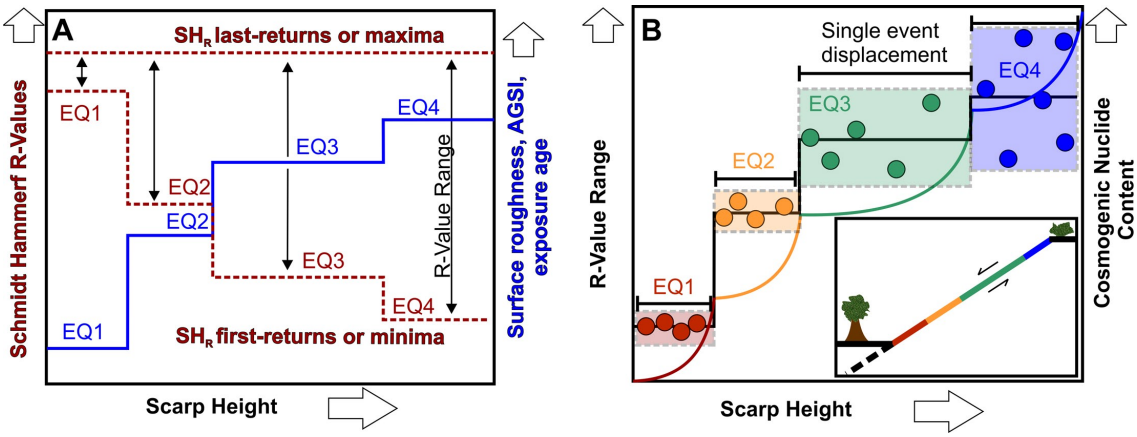

Figure 4.2: Expected relationships between Schmidt hammer R-value, cosmogenic nuclide content, Geologic Strength Index (GSI), surface roughness, scarp height, and relative earthquake age (e.g., EQ1, EQ2, etc.). (A) The R-value range (ΔR) and *I5 index should increase in discrete steps along scarp height that correspond to single event displacements (SEDs) in paleo-earthquakes. (B) SEDs are defined by the distance along scarp height that ΔR are constant, with the expectation that older earthquakes show more scatter in ΔR.

displacement over the last three events (*Schwartz et al.*, 2009). The discord between slip histories in TCND and paleoseismic trenching have led some to question the interpretation of event ages from the cosmogenic transect (e.g., *Pierce et al.*, 2000) or even that the scarp was rejuvenated in the 1959 earthquake. Regarding the latter question, however, *Johnson* (2017) has shown with airborne LiDAR that this trace did indeed rupture in the 1959 earthquake, supporting the interpretation of *Zreda and Noller* (1998) that this site is a bedrock fault scarp.

4.3 Methods

4.3.1 Schmidt hammer framework and field protocol

We used a Proceq mechanical N-type Schmidt hammer with an impact energy of 2.207 Nm. For each sample location spaced 0.25m along the direction of slip on the scarp face (Supporting Information, Figure B.1), we recorded both the first impact R-value and the subsequent four values at the same point of impact. This sample spacing is considered reasonable given the fault's dip-slip motion and all previously reported values of SEDs along the fault (*Zreda and Noller*, 1998; *Hecker et al.*, 2000, 2002; *Pierce et al.*, 2000; *Schwartz et al.*, 2009; *Johnson*, 2017), though centimeter-scale displacements in smaller surface rupturing earthquakes would be unlikely to be detected at this resolution.

The approach of collecting five impacts at the same location allowed us to assess a

'time-series' of R-values and examine various R-value metrics: first-impact (R_1), R-value range (ΔR), *I5 index (after *Matthews et al.*, 2016), and *Imax index (this study). The latter three are defined as

$$\Delta R = R_{max} - R_{min} \tag{4.1}$$

$$^{*}I5 = 100 \times (Ru_5 - R_1)/Ru_5 \tag{4.2}$$

$$^{*}Imax = 100 \times (Ru_{max} - R_{min})/Ru_{max} \tag{4.3}$$

where R_{max} and R_{min} are the highest and lowest R-values of the five successive impacts at a single location, respectively, Ru_5 is the average fifth impact R-value of unweathered rock, and R_1 is the first impact at a single location, and Ru_{max} is the average of maximum R-values on unweathered rock. These unweathered rock R-values come from a single impact site for each distinct rock type and are assumed to be uniform for a given rock type.

For application to fault scarps, the area of scarp exposed in the most recent earthquake should be the least weathered, and thus yield the smallest values for all indices (Eqs. 4.1-4.3; Figure 4.2). In the absence of other modifying geomorphic processes (e.g., scarp renewal by landsliding or by stream abrasion) and complicating variables (non-uniform lithology or non-uniform weathering processes), R-value indices should increase in discrete steps along the scarp with increasing weathering grade (Figure 4.2). Additionally, we propose that older slip patches should display larger variance in R-value indices (i.e., heteroscedasticity) due to small heterogeneities in weathering rates on older surfaces (*Shakesby et al.*, 2011) (Figure 4.2B).

During sampling, first return R-values were recorded if (i) the rock mass did not move or chipwhile sampling and (ii) the sound was resonant rather than hollow, the latter of which is indicative of a shallow discontinuity (e.g., *Stahl et al.*, 2013). If these criteria were met, four additional R-values were recorded at the same location. Lichen were avoided and all measurements were taken in dry conditions over the course of one day by a single operator to avoid operator bias. Sample locations were not abraded or otherwise prepared prior to impacts so as to preserve the original surface roughness. Sampling was limited to a single transect where the scarp was continuous along-dip; other transects along the outcrop were not feasible because slope failures have made identification of the original, continuous scarp face unreliable. Sample vertical locations were adjusted for fault dip (65°). The R-values were not corrected for angle of incidence as all tests were conducted in the same orientation. The Schmidt hammer was calibrated on a test anvil before and after sampling

to ensure no instrument degradation.

We also defined and recorded an Adjusted Geologic Strength Index (AGSI) (e.g., *Marinos et al.*, 2005) to semi-quantitatively describe variations in surface weathering and ensure no major variability in the structural integrity of the limestone scarp. In doing so, we re-defined some criteria from the original Geologic Strength Index (GSI) 'surface quality' scale specifically for quantifying the surface weathering of limestone fault scarps: more weathered surfaces are rougher, more pitted, more stained/discolored, and have degraded and poorly preserved slickensides (*Stewart*, 1996; *Zreda and Noller*, 1998).

4.3.2 Terrestrial LiDAR scanning (TLS) and roughness analysis

To supplement our Schmidt hammer data, we acquired TLS microtopography on a portion of the bedrock fault scarp at Hebgen Lake at a resolution of 1 to 2 mm using a Riegl VZ-2000. The scan area coincides with the scarp above the 1959 slip patch. Plants and artifacts were removed from the dataset manually. Coordinates were transformed such that one coordinate dimension represented the distance from the measured fault surface to the best-fit plane for the entire scarp. As a measure of surface roughness at the scale of interest, we calculated the variance of this fault plane normal distance in a square moving window of size $\sim$20 cm $\times$ 20 cm. The mechanics of our moving window procedure are identical to those in *He et al.* (2016) though the method of analysis of the data within each window is different than their fractal-based method. Given the restricted scale over which weathering effects are topographically expressed (*Wei et al.*, 2013), the topographic variance within a 20 cm window should capture the scale over which the desired signal should exist. *Wiatr et al.* (2015) use a similar window size.

4.3.3 Curve-fitting and SED determination

A determination of event-by-event SEDs depends on (i) assessing whether R-value indices and surface roughness are adequately characterized by discrete steps along the scarp (e.g., Figure 4.2) and (ii) identifying the best-fit locations of those steps along the scarp. If (i) is assumed, then (ii) needs to be conducted in such a way that avoids bias from user input.We developed a maximum likelihood approach that determines the number of steps (i.e., number of earthquakes) and their locations (SEDs) for the observed data. For between n = 1 and n = 6 steps (full range of possible steps given previously reported earthquake histories), a model fit is generated for every possible location of the step(s) along the scarp. The mean (μ) and standard deviation (σ) of observed indices are calculated over all of those steps and the output is the model that maximizes the likelihood function for the index

relative to μ and σ. SEDs are then determined by the width of the steps along the x-axis. Maximum likelihood models were calculated for different functions using the natural logarithm of the R-value index, since a natural logarithmic transformation should reduce the heteroscedasticity inherent in the indices (Figure 4.2). All errors were assumed to be normally-distributed on the natural logarithmic scale.

The same fitting method was also conducted on the TLS-derived surface roughness using microtopographic variance. We use the natural log transform of variance because it eliminates heteroscedasticity and is consistent with previous approaches to the same data (e.g., *Sagy et al.*, 2007; *Candela et al.*, 2009; *Wei et al.*, 2013; *He et al.*, 2016). Our moving window approach results in a two-dimensional grid of topographic variance measurements that covers the measured portion of the fault scarp. To analyze the topographic variance as a function of scarp height, we use the mean log variance of each row of the grid (rows are perpendicular to fault dip). In addition, we use the standard deviation of each row as an independent estimate of uncertainty.

4.3.4 Model selection

If a stepwise fit is not assumed, then the model selection method must be able to accommodate the different functional forms of all candidate models. One such method is the Bayesian Information Criterion (BIC; *Schwarz et al.*, 1978), which quantifies the goodness-of-fit with penalties imposed for additional model parameters:

$$\mathrm{BIC} = \ln(n)k - 2\ln\left(\hat{L}\right) \tag{4.4}$$

where k is the number of free parameters to be estimated, n is the sample size, and $\hat{L}$ is the maximized value of the log likelihood function of the model. Lower BIC values indicate more preferable models. While the stepwise model fits our and others' geologic interpretation of the site as a scarp exposed in episodic earthquakes, we used the BIC to determine if this model is statistically superior to linear and power law fits, and to determine the optimal number of steps for the stepwise model (see Supporting Information).

For calculating the BIC, linear and power law models have three parameters each: two corresponding to the function parameters (slope and intercept, and constant and exponent, respectively) and one corresponding to the standard deviation of the model residuals (*Burnham and Anderson*, 2004). Stepwise models have two parameters (for no steps, y = constant), plus two more for each step. These parameters are the constant y value of each step (e.g., R-value metric or topographic variance), the x values of the break points between steps, and the standard deviation of the model residuals. Linear and power law maxi-

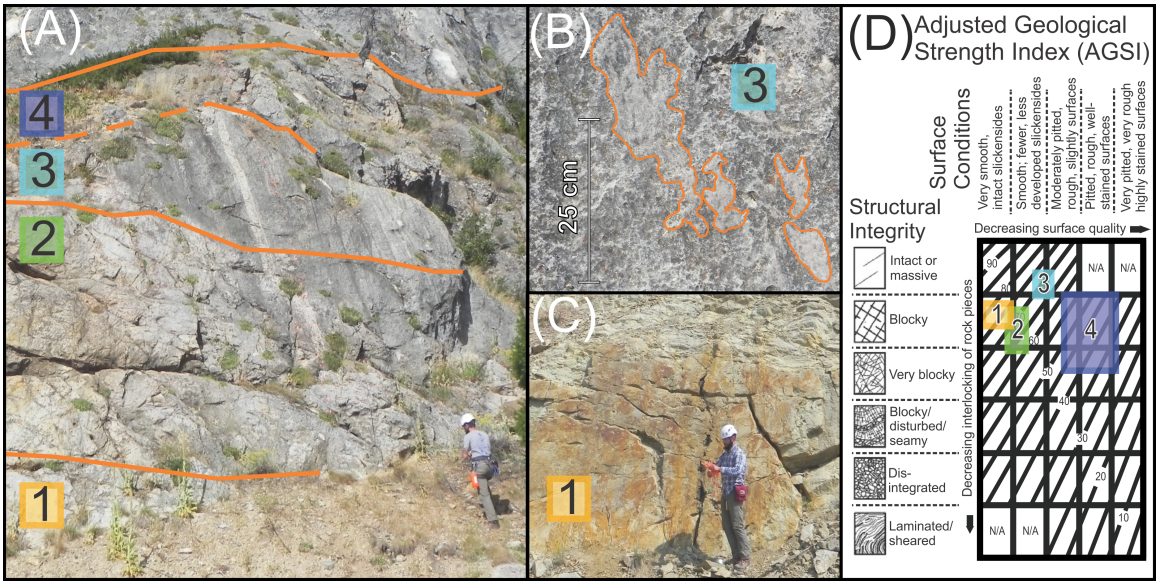

Figure 4.3: (A) Photograph of the scarp in this study and that of *Zreda and Noller* (1998) (location in Figure 4.1). (B) Photograph of slickensides near the top of the scarp in (A). Slickensides become more poorly preserved up-fault. (C) Photograph of scarp section produced in the 1959 Hebgen Lake earthquake. The section is marked by a smooth, striated plane with few weathering pits or staining. (D) Estimations of Adjusted Geologic Strength Index (AGSI) for the scarp. Surface conditions degrade up-scarp (lower values and shifted to the right on the top axis) while variability in structural integrity is less pronounced.

mum likelihood parameters were determined by pattern search (*Hooke and Jeeves*, 1961), whereas stepwise maximum likelihood models were determined using brute force.

4.4 Results

4.4.1 Adjusted Geologic Strength Index (AGSI)

AGSI values generally decrease with increasing scarp height (Figure 4.3) and permit discrimination of three loosely-defined weathering zones over the c. 10 m scarp height. The limestone was observed to have only small variations in structural integrity along the scarp, ranging from Blocky to Intact/Massive (Figure 4.3D). Larger variations were observed in surface quality of the limestone (top axis, Figure 4.3D). Zone I (AGSI = 73-83, c. 0-1.25 m vertical) corresponds to the 1959 slip surface, which has well-preserved slickensides on a smooth, planar and unstained surface (Figure 4.3C). Zone II (AGSI = 60-75; c. 1.25-5 m vertical) is characterized by a slight decrease in structural integrity (Very Blocky to Blocky) but marked decrease in smoothness, slickenside preservation, and increase in discoloration/staining (Figure 4.3A). Zone III (AGSI = 65-75; c. 5-10 m vertical) has the

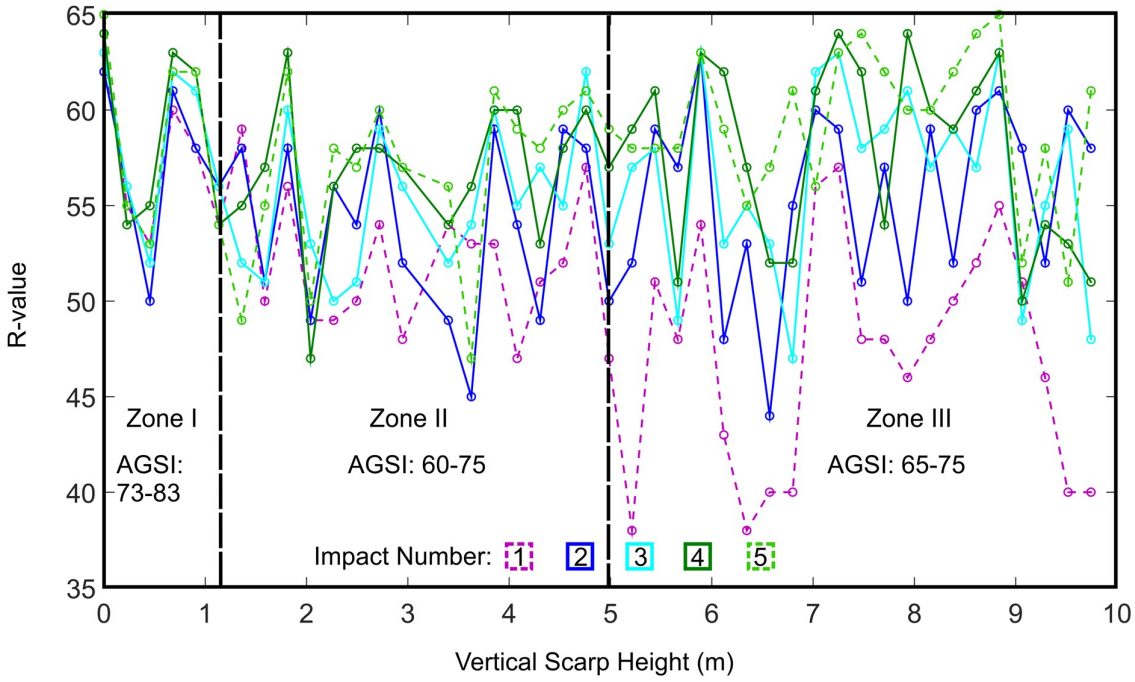

Figure 4.4: Schmidt hammer R-value versus scarp height for all impacts. Adjusted Geologic Strength Index (AGSI) results are shown for three weathering zones (Zones I-III) and correspond to discrete changes in ΔR (the distance between lowest and highest R-values at each point, colored series).

highest structural integrity of the three zones (Intact/Massive) but is again characterized by a decrease in smoothness and slickenside preservation (Figure 4.3B) and an increase in discoloration and pitting (Figure 4.3A) from Zone II. We demarcated one additional zone Zone IV (AGSI = 30-60; $>$ 10m vertical) above the transect that is marked by a decrease in both structural integrity and surface quality, but it is not clear that this zone is a continuation of the planar fault scarp from below (*van der Woerd et al.*, 2000, Figures 4.3A and 4.3D) and is thus not included in further analyses.

4.4.2 Schmidt hammer R-values

The R-value minima (first or second impact in $\sim$90% of sample locations, Figure 4.4) show an overall decreasing trend with increasing scarp height, while R-value maxima (fourth or fifth impact in $\sim$80% of sample locations, Figure 4.4) show less variability with scarp height. From one sample location to the next (i.e., every 0.25m along the scarp) there can be significant variability in R-values. These variations typically affect all of the impacts at a given location, causing some alignment of 'peaks' and 'troughs' in the different impact

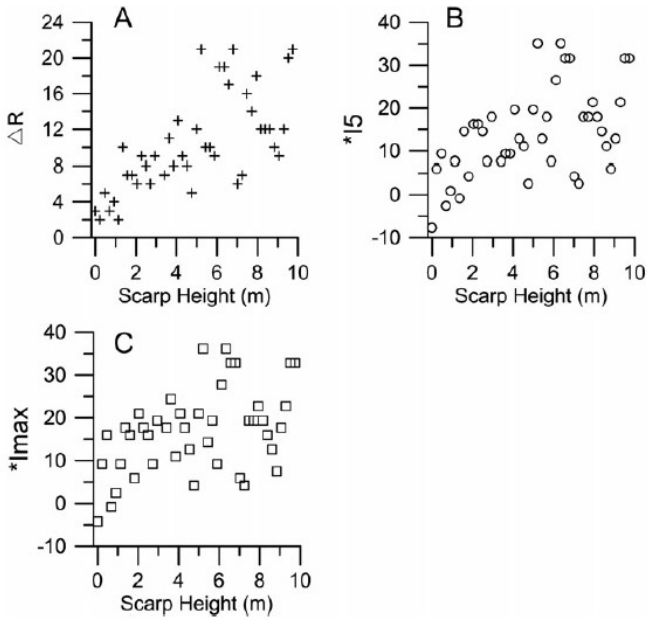

Figure 4.5: Positive correlation of Schmidt hammer R-value range (ΔR), *I5, and *Imax with scarp height. See text for discussion.

series (Figure 4.4). Thus, ΔR remains relatively unchanged over short length scales despite the large fluctuations in individual readings.

The R-value range (ΔR) and *I indices (Eqs 4.2 and 4.3) increase with scarp height (Figure 4.5). For our application, the ΔR metric is preferred over the *I5 and *Imax. The *I metrics (*Matthews et al.*, 2016, and this study) rely on an R-value measurement of unweathered rock, which is then assumed to be constant for that rock type. The entire Hebgen Lake fault scarp is limestone, and lithologic variations that might be expected to affect R-values were not observed during visits to the site. Thus, the use of *I metrics would assume a single, characteristic unweathered R-value for the entire dataset, which conflicts with our data: R-values for repeated impacts at different sites on the 1959 slip patch (Zone I in Figures 4.3 and 4.4) converge on values that differ by up to ∼10, more than a third of the total spread in R-values observed across our dataset. This difference suggests that, at the Hebgen Lake site, non-weathering factors besides general rock type have a significant effect on the R-values of unweathered rock, invalidating the assumption of *I metrics. In contrast, the ΔR values for these impact sites are relatively consistent (Figures 4.4 and 4.5). As such, we conduct further analysis only on ΔR.

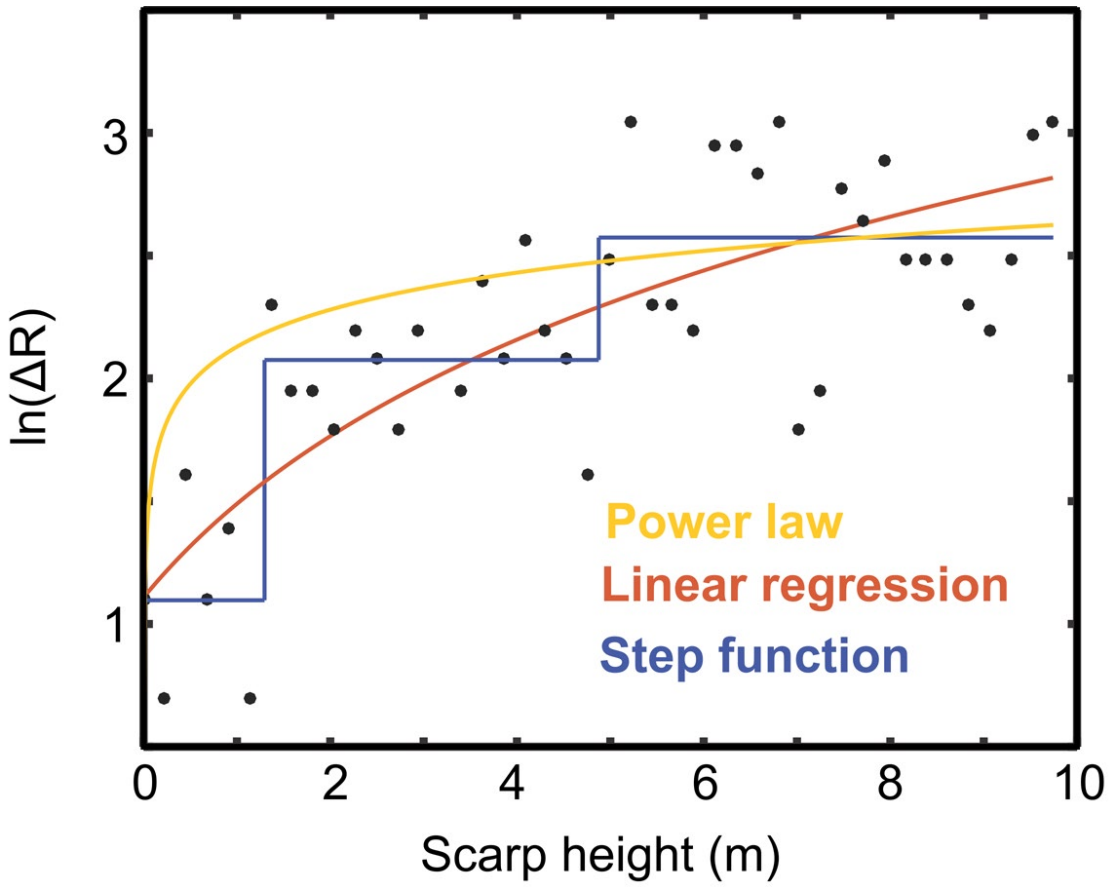

Figure 4.6: Model fitting to Schmidt hammer data in ln(ΔR) space. Using a natural logarithmic ΔR scale reduces the heteroscedasticity observed in ΔR values simplifying model fitting and selection. Only the best-fitting step model (blue, Table 4.2) is shown here, which has a lower Bayesian Information Criterion (BIC) than linear (red) and power law (yellow) model fits.

4.4.3 Model comparison of ΔR

The maximum likelihood models for linear, power law, and stepwise relationships between ΔR and scarp height are shown in Figure 4.6. The values of BIC indicate that a stepwise model with two break points is preferred, corresponding to three distinct patches of ΔR moving up the scarp (Table 4.2, Figure 4.6). It can be seen that the support from BIC for the stepwise model with two breaks over the linear model and stepwise models with more breaks is not overwhelming; however, under the classification scheme of *Kass and Raftery* (1995), the preference of the two-step model over the linear and three-step models should be considered 'positive', and is 'very strong' when compared to power law and one-step models (Table 4.2).

Model	BIC
Linear	49.14
Power law	63.95
Stepwise (one break)	56.72
Stepwise (two breaks)	**46.77**
Stepwise (three breaks)	49.80

Table 4.2: Bayesian Information Criterion (BIC) values for various functional forms of log ΔR versus location on scarp (lower values indicate better fits). The preferred model (stepwise with two breaks) is shown in bold typeface.

4.4.4 TLS-derived surface roughness

The TLS data above the 1959 slip patch assist in interpreting the AGSI values and Schmidt hammer data in that part of the transect. The surface roughness (i.e., topographic variance) decreases as scarp height increases (Figure 4.7). It can be seen that there is significant scatter to the topographic variance data. High and low variance values are not randomly distributed on the fault scarp, but rather form numerous clusters (Figure 4.7B). Natural log transformed topographic variance values can be seen to be homoscedastic (Figure 4.7C). Fits of log transformed topographic variance versus scarp height were conducted on a subset of the total scan, using the same set of functional forms as for R-value range. BIC values indicate a slight preference for a stepwise model with one break over an exponential function (Table 4.3, Figure 4.7C shows the one break step function and the power law function).

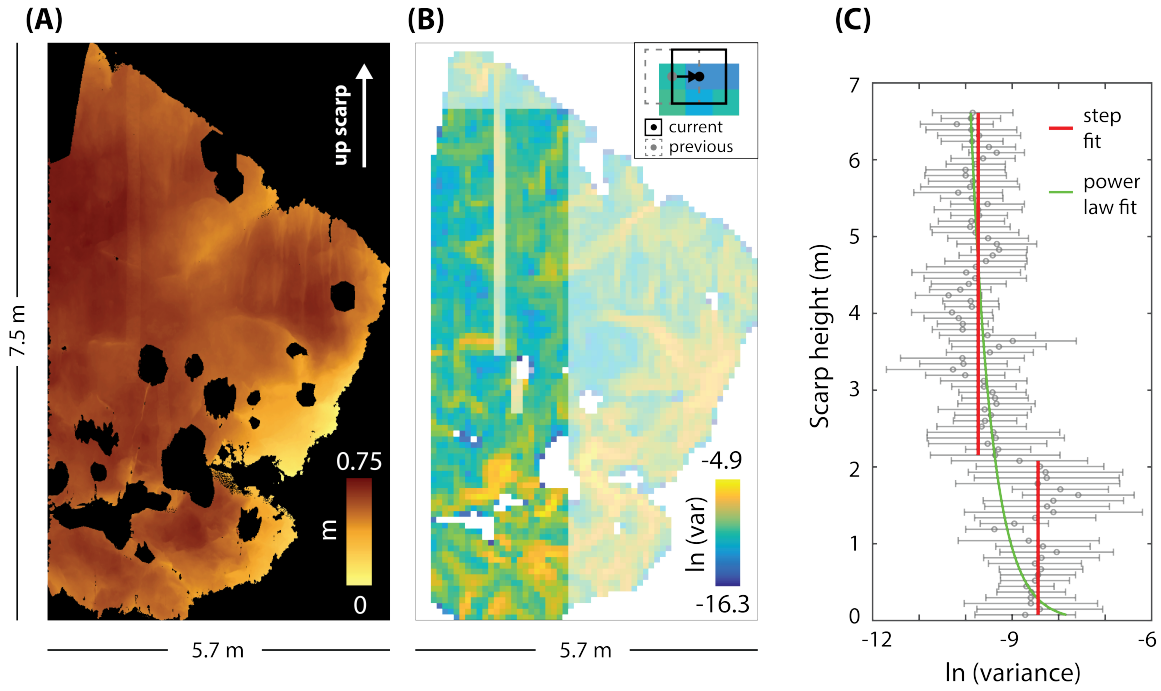

Figure 4.7: Microtopographic analysis from terrestrial LiDAR scanning (TLS) data. (A) Hebgen lake fault scarp TLS dataset has been fit with a plane, and values indicate the distance of each point from the best-fit plane. A cosmogenic nuclide sample transect is visible and provides a common reference to Figure 4.4. The 7.5 m measurement indicates vertical height. (B) Variance of topography calculated over the fault scarp using a moving window. The slightly grayed out region is the full scan, and the fully opaque region is that used for the subsequent analysis. Inset shows mechanics of the moving window. The center of each cell corresponds to the center of one location of the moving window, which is actually twice as wide and twice as tall as the cells shown. Thus, adjacent cells in the main portion cover some of the same topography. (C) Mean and standard deviation topographic variance for each row of the moving window analysis. A step function fit (red) is barely preferred over a power law fit (green; see Table 4.3). LiDAR data is available via UNAVCO with https://doi.org/10.7283/R3HH44.

4.5 Discussion

4.5.1 Use of ΔR as preferred Schmidt hammer metric

On length scales greater than 0.25 m, the change in ΔR is predominantly controlled by decreasing R_{min} (Figure 4.4). Values of R_{max} remain approximately the same (60 ± 3, 1σ) over the scarp and are interpreted to reflect the underlying structural integrity of the rock mass. It is thought that R_{min} varies with surface conditions, like ∼1 cm scale surface roughness, (top row of AGSI, Figure 4.3) and R_{max} remains comparatively stable with structural integrity (left column of AGSI, Figure 4.3). The small drop in R_{max} across weathering Zone II compared to Zone III (Figure 4.4) is reflected by the slight decrease in AGSI structural integrity of Zone II (Figure 4.3). Because of the covariance of R_{max} and R_{min} values (Figure 4.4), ΔR is a more stable metric for weathering duration than a single-impact R-value. The reduced noise of ΔR relative to single impact R-values is important for model selection. Conducting multiple impacts at a single location also yields important information on the underlying conditions of seemingly homogeneous bedrock not obtained by taking a single impact at each location.

There is much greater scatter in both *I metrics than in ΔR (Figure 4.5). This can be attributed to two separate causes. For the *I5 value, the fifth impact does not necessarily yield the highest R-value in our tests, and therefore it is not the best indicator of unweathered rock. This contrasts with the findings of *Matthews et al.* (2016) and could be due to their use in relatively competent rock compared to limestone. The Ru_{max} value might be considered to be a better indicator of unweathered rock in limestone, and therefore *Imax should yield a more useful relationship with exposure age. However, as discussed earlier, the range of R_{max} values within the 1959 slip patch, from which Ru_{max} is calculated, vary significantly. This could be due to non-weathering related variables within the rock and make ΔR more suitable measure of weathering degree.

4.5.2 Apparent steps and SEDs of the Hebgen fault

A step pattern of ΔR is expected on a fault scarp that has been progressively exposed in surface rupturing earthquakes (Figure 4.2). The width of the steps (change in scarp height, Δx) should define the SEDs in these earthquakes. Our preferred model for the Hebgen fault distinguishes the area of scarp exposed in the 1959 Hebgen Lake earthquake and two other slip patches (Figure 4.6). The 1959 slip patch extends from 0.00 to 1.25 m vertical; a second section extends from c. 1.25 to 5.00 m; and a third section is interpreted from c. 5.00 to 9.80 m. We note that the vertical displacement for the 1959 patch is a minimum

because our transect did not extend to the base of the 1959 scarp (which was observed along strike). If interpreted as vertical displacements, these ranges translate to >1.25, 3.75, and 4.80 m vertical slip in past earthquakes. It is unknown if the length of the final step (4.8 m) represents a larger SED or the failure of the Schmidt hammer to discriminate two or more older earthquakes in this age range due to the high variance (Figures 4.5 and 4.6). In any case, these displacements are considered reasonable given the maximum displacements reported along all faults in the 1959 earthquake (c. 3-6 m; *Witkind et al.*, 1962; *Schwartz et al.*, 2009) and the range reported in trenching investigations along the fault (1-3 m).

Model	BIC
Power law	179.89
Stepwise (one break)	**178.34**
Stepwise (two breaks)	185.64

Table 4.3: Bayesian Information Criterion (BIC) values for various functional forms of log topographic variance versus location on scarp. The preferred model is shown in bold typeface.

Like the Schmidt hammer results, TLS-derived topographic variance results from TLS above the 1959 slip patch are best fit with stepwise function (Figure 4.7). It should be noted that the stepwise relationship is only barely preferred over a power law relationship according to the BIC values (Table 4.3), which is due to the high scatter. Some warping is observed between the reliable scarp height values of the TLS data and the height estimates of the Schmidt hammer data, which are estimated using tape measurements and the measured dip of the scarp. However, scarp features such as plants and the track of a past TCND transect provide tiepoints between the TLS data, Schmidt hammer data, and AGSI interpretations. These tiepoints reveal that the location of the step in topographic variance corresponds to within ∼1m with the boundary between Zone II and Zone III in AGSI (Figures 4.3 and 4.4), and the upper break revealed by the R-values (Figure 4.6).

The TLS data is somewhat counterintuitive, however, in that it shows topographic variance decreasing towards the upper part of the scarp. This means that slip patches exposed by older earthquakes have smoother surfaces, at the scales investigated, than those exposed by younger earthquakes. The trend we observe is the opposite of the relationship between variance and scarp height observed by other studies on limestone normal fault scarps (*Wei et al.*, 2013; *Wiatr et al.*, 2015) for length scales similar to our ∼20 cm window. In addition to the results shown in Figure 4.7, we performed the variance analysis with a ∼5 cm moving window, which produced nearly identical results to the ∼20 cm window. In an-

other analysis, we attempted to compensate for some non-planar topography observed on the scarp at small spatial scales with a local best-fit plane within each window. This procedure was undertaken using both ∼5 cm and ∼20 cm moving windows, and the relationship between variance and scarp height was virtually identical to that depicted in Figure 4.7 in both cases.

We interpret the unexpected relationship between topographic variance and scarp height that we observe as a product of jointing in the lower part of the scarp (Figure 4.3). This is mirrored by the lower value of AGSI Structural Integrity for Zone II than for Zone III in Figure 4.3. Thus, our results suggest that variations in macro-structural features such as joints may obscure the effects of weathering in roughness analyses of fault scarps. Our findings from the Hebgen scarp suggest no relationship between the development of macro-scale structural features such as joints and the age of a paleoseismic slip patch (Figure 4.4), which implies that topographic variance due to jointing is not useful for identifying slip patches. It is possible that a method for filtering out features like joints could mitigate this problem.

4.5.3 Reconciling SEDs with other records

Our results based on Schmidt hammer are at odds with the SEDs previously interpreted for this specific site from TCND (*Zreda and Noller*, 1998). We propose that the interpretation of more events with smaller displacements delineated by *Zreda and Noller* (1998) could be due to the methods they used to group samples. Setting aside the six sample groupings based on weathering characteristics presented in *Zreda and Noller* (1998), we fit stepwise exponential functions to the ^{36}Cl apparent ages using a procedure similar to the stepwise fitting presented earlier (Figure 4.8; Supporting Information). The objective of this fitting is not to redefine the absolute ages of events, as could be accomplished with full elemental analysis of the samples and well-established, robust modeling routines for determining the exposure histories of faults (*Schlagenhauf et al.*, 2010). Rather, we aim to find the locations and number of events for which there are statistical support. Each stepwise piece can be expressed as

$$y = y_0 + Ae^{\lambda x}, x_{lb} < x \leq x_{ub} \tag{4.5}$$

where y is the predicted cosmogenic apparent age, y_0 is the age offset of the current step, A is the exponential coefficient, λ is the attenuation length, and x_{lb} and x_{ub} are the lower and upper bounds of x for the current step. The age offset y_0 is not a standard term of the exponential function, but is necessary here and reflects the uniform exposure to cosmic ray

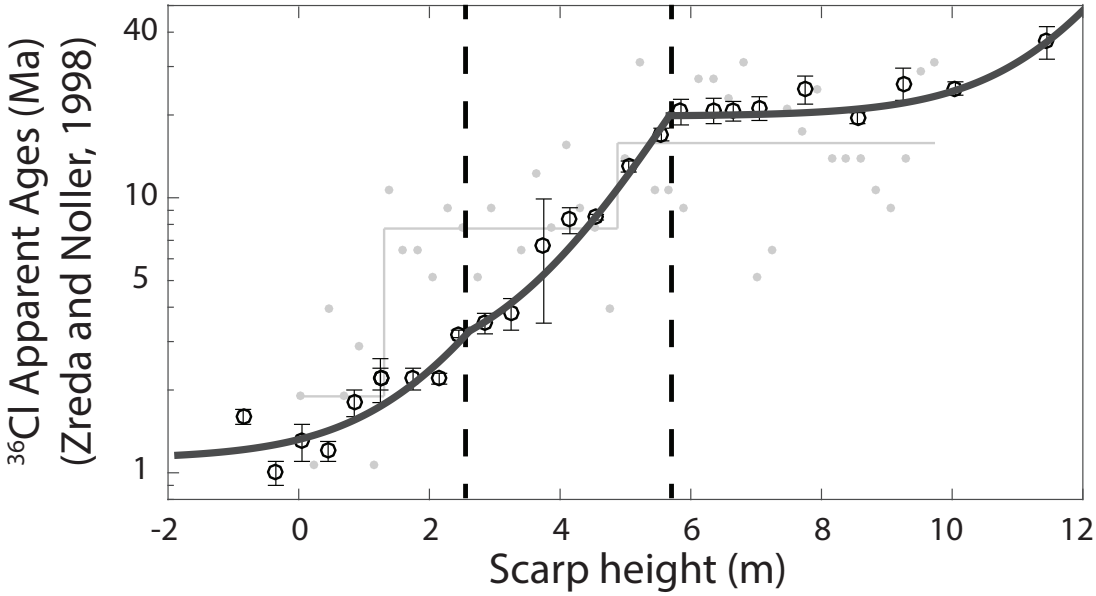

Figure 4.8: Correspondence of discrete breaks in Schmidt hammer data (grey filled circles) and apparent cosmogenic exposure ages of *Zreda and Noller* (1998). The scarp locations of the cosmogenic ages have been shifted using the top of the 1959 slip patch as a common datum between the two datasets, though some uncertainty exists in the co-registration of the two datasets. The highly variable uncertainty in reported apparent cosmogenic ages results in some data having a much greater influence on the fit than other data and introduces uncertainty in the location of the steps.

spallation that a given slip patch undergoes once it is exhumed. Details of the parameters and assumptions used in this fitting are listed in the Supporting Information. Figure 4.8 shows our model fits to *Zreda and Noller* (1998) data, revealing that the data only support a model of the scarp that includes three slip patches (using BIC, shown in Figure 4.8). The locations of the slip patch boundaries inferred from the Schmidt hammer and cosmogenic exposure age data are somewhat offset from one another, though we stress that the co-registration between the two datasets is not robust.

While further testing is required to resolve the debate between paleoseismic trenching and TCND of the Hebgen fault, we consider a three event history, as evinced in the Schmidt hammer data, re-analysis of apparent cosmogenic exposure ages, and late Pleistocene record of events in trenches, to be a plausible outcome. The differences in displacements between trenching and the study site here are not unexpected due to along-strike differences in fault kinematics and distributed (i.e., off-fault) deformation in unconsolidated sediments.

There are two alternative interpretations that our data cannot resolve. The first is that both trenching and the Schmidt hammer miss smaller events that are recorded by the original cosmogenic exposure ages of *Zreda and Noller* (1998). The second is that progressive exposure at this scarp could be assisted by non-tectonic, continuous or diffusive lowering of the colluvial cover at the base of the scarp. *Kastelic et al.* (2017) observed exposure rates due to non-tectonic erosion or deposition of colluvial material at the base of normal faults in Italy, and concluded that exposure rates could outpace fault slip by orders of magnitude. If this was the only process operating on the Hebgen fault, the linear or power-law models for progressive exposure (Figure 4.6) could be the most appropriate curve fits. While our BIC models show favorability for the step-function over these other fits, and there is good evidence for discrete displacements, we consider that the non-tectonic contribution of scarp exposure could lead to the large amount of noise for older events and potentially limit the applicability of using the Schmidt hammer beyond the last $\sim$2 events.

4.5.4 Practical considerations of Schmidt hammer methodology

This study was limited to a single transect along the Hebgen fault, and so further testing should be conducted on other faults in different climates to confirm the utility of the Schmidt hammer in these studies. The technique seems most promising for distinguishing between the most recent event and penultimate event slip patches, as *Stewart* (1996) observed using measurements of surface roughness on limestone faults. In fact, we suggest that the main attribute of the rock weathering being measured by the Schmidt hammer is

the variable centimeterscale surface roughness of different slip patches. Since R-values are relatively simple to obtain in the field, the Schmidt hammer could be used as an auxiliary dataset in conjunction with other techniques (Table 4.1).

Other recommendations for future use are discussed below. Where possible, R-values should be collected in two dimensions along the scarp with their locations surveyed using a string grid or laser-based ranging. This approach would allow for more rigorous spatial and statistical analysis of the data. As with any measurement of paleoseismic slip at a point, care should be taken in applying the derived value of SED (or set of SEDs) to other positions along the fault, as these are likely to vary along-strike and between earthquakes. If a bedrock scarp is exposed in several places along strike, the Schmidt hammer may be a useful tool for providing rapid, preliminary assessment of this slip variability.

In practice, we found that field investigations of steep bedrock scarps using the Schmidt hammer are likely to be limited by along-strike alteration of the scarp and/or the location of sites to set up a rope or ladder to reach sample locations. Care should be taken to avoid areas of visible scarp modification by processes other than weathering. Operating the Schmidt hammer while suspended by a rope is challenging and requires a second person to record values (for non-digitally recording hammers). Even so, it is not always possible to get reliable impacts at every planned sample location due to the geometry and relief of the fault scarp.

For future studies, our approach can be adapted to distinguish SEDs on fault scarps provided that (i) lithology does not change over the fault scarp, (ii) the fault scarp has not been significantly eroded in older events and can be traced as a single, continuous plane over the sample transect, (iii) there are no significant variations in weathering processes and rates through time (e.g., case hardening of older exposed sections), and (iv) non-tectonic exposure of the fault plane does not outpace the rate of exposure in earthquakes.

Faults with higher slip rates, smaller SEDs, and/or shorter recurrence intervals may not show enough inter-event ΔR variability to discriminate displacements (numerically or otherwise). Similarly, faults with much slower slip rates and longer recurrence intervals may have uniform weathering characteristics and therefore ΔR over the exposed scarp. We anticipate that faults with several thousand-year recurrence intervals will yield enough variability in R-values to delineate weathering zones and SEDs. Additionally, with calibration on scarp sections of known age, chronofunctions could be developed that yield numerical paleo-earthquake ages from Schmidt hammer measurements.

4.5.5 Applicability of step function fitting to SED identification

The step function fitting presented in this paper requires little user input, incorporates the effects of heteroscedasticity, and requires few initial assumptions. For other paleoseismic data that are expected to show monotonically increasing, stepwise behavior, but do not have constraints on the absolute location or number of events, this approach is useful in identifying SEDs. Other approaches using regression trees or the sliding window Student's t-test of *He et al.* (2016) are promising, but require more user input and could introduce user bias in defining SEDs.

The assessment of models using the BIC should be used with an understanding of what the BIC represents. This BIC penalizes additional parameters in curve fitting, so it is ideal for avoiding over-fitting slip histories and interpreting too many earthquakes. However, for long-lived bedrock scarps with many small displacements, the BIC may prefer functions with only a few steps or continuous models over a 'true' but complex slip history, thus under-representing the earthquake hazard of a fault. As such, user-discretion is still advisable for selecting the most appropriate model from information criteria.

4.6 Conclusions

The major conclusions of this preliminary study are summarized here:

(1) We have presented the first application of Schmidt hammer testing in resolving single event displacements (SEDs) on bedrock fault scarps. A geomorphic framework and best practice field methods are also provided.

(2) SEDs can be identified by fitting step-functions and other models to the R-value range over five impacts at a point (ΔR) and assessing the model fits using the BIC. We propose that this approach is applicable to other scarp dating techniques (Table 4.1).

(3) For the Hebgen fault, the best-fitting model is a stepwise, three-event model. The resulting SEDs are generally consistent with several meter-scale displacements of the fault in three recent events as proposed by trenching studies and by re-analysis of cosmogenic exposure ages for the same scarp. The exact lengths of these displacements are not resolved, but they probably represent a maximum of c. 4.8 m.

(4) The Schmidt hammer should be used in conjunction with other absolute and relative-age dating techniques to further explore its utility in assessing fault slip in paleo-earthquakes.

The promising results presented in this study could facilitate rapid field assessment of SEDs along active normal faults.

Acknowledgments

This research was supported by the National Science Foundation (NSF) EAR-1451466. This material is based in part on TLS data services provided by the UNAVCO Facility with support from the NSF and National Aeronautics and Space Administration (NASA) under NSF Cooperative Agreement No. EAR-0735156. The authors thank Chris Crosby and William Medwedeff for assistance in the field and are grateful to Kendra Murray and Eric Portenga for providing constructive reviews of early versions of this manuscript. The authors are also grateful to Nathan Niemi, Marin Clark, and Eric Hetland for insightful conversations about Schmidt hammers, field sites, and model selection. Two anonymous reviewers greatly improved the quality of this manuscript.

CHAPTER 5

Schmidt Hammer and Terrestrial Laser Scanning (TLS) Used to Detect Single Event Displacements on the Pleasant Valley Fault (Nevada, USA) *

Abstract

The surface roughness of carbonate fault scarps often reflect varying durations of exposure to subaerial weathering. On the Pleasant Valley fault in central Nevada, the documentation of a surface rupture in 1915, a long recurrence interval of faulting, slow weathering rate, and a relatively high (2-3 m) single event displacement make the discrimination of the historical and penultimate slip patches unambiguous. Following from a 2018 study, we used a Schmidt hammer and terrestrial laser scanning (TLS) to further test whether these weathering patterns delineate exposed slip patches on a fault scarp. Results show that Schmidt hammer rebound value ranges (termed ΔR - the difference between minimum and maximum R-values in repeat impacts at a point), increase by $\sim$8-10 points across the historical-penultimate event transition zone in two separate scarp transects. TLS-derived surface roughness also indicates a clear difference between the most recent and penultimate events. The average single event displacement (SED) estimated using the Schmidt hammer and TLS is 2.85 m at two transect sites and is roughly equivalent to the visually estimated 3 m. While this fault is an ideal case where we know some of the slip history, the results demonstrate that these techniques show promise for discriminating slip patches on larger carbonate fault scarps with longer paleoearthquake histories, and could be used alongside ^{36}Cl cosmogenic exposure-age dating to improve paleoseismic records on normal faults.

*Chapter 5 has been accepted for publication in *Earth Surface Processes and Landforms*: Stahl, T. and Tye, A. (In Press). Schmidt hammer and terrestrial laser scanning (TLS) used to detect single event displacements on the Pleasant Valley fault (Nevada, USA). Earth Surface Processes and Landforms.

5.1 Introduction

Surface rupturing normal faults present a unique opportunity for identifying paleoearthquakes. Where normal faults rupture to the surface in bedrock, fault scarps—the surface expression of one or more earthquakes—may be preserved, allowing direct exposure-age dating of the fault surface and modelling of earthquake displacements and recurrence intervals (*Bosi et al.*, 1993; *Zreda and Noller*, 1998). The use of cosmogenic ^{36}Cl on limestone scarps for these objectives is well-established and provides some of the most detailed paleoseismic records, with the best age precision, available on any fault (e.g., *Zreda and Noller*, 1998; *Benedetti et al.*, 2002; *Schlagenhauf et al.*, 2010; *Benedetti and van Der Woerd*, 2014; *Mouslopoulou et al.*, 2014; *Mechernich et al.*, 2018). The difficulties associated with this technique are that it can be prohibitively time consuming and expensive to prepare and analyse samples at more than one scarp transect and at sampling intervals required to resolve event ages.

Relative age dating techniques, based primarily on rock weathering, have been used alongside ^{36}Cl exposure-age dating of fault scarps to corroborate results and guide sampling for cosmogenic nuclide dating (*Stewart*, 1996; *Zreda and Noller*, 1998; *Giaccio et al.*, 2003; *Tucker et al.*, 2011; *Wei et al.*, 2013; *Wiatr et al.*, 2015; *He et al.*, 2016; *Tye and Stahl*, 2018). These techniques work on the premise that slip patches previously exposed in earthquakes have been subjected to a longer duration of subaerial weathering than more recently exposed patches. *Wallace et al.* (1984) was one of the first to recognise the potential for differential weathering and biogenic colonisation to yield relative age information on the Pleasant Valley scarp in central Nevada, USA. Based on relatively fresh limestone surfaces exposed in the moment magnitude (Mw) 6.9-7.0 1915 Pleasant Valley earthquake (*Doser*, 1988) compared to a higher, more deeply pitted patch, *Wallace et al.* (1984) proposed that the weathering pattern could be used to estimate the age of the pre-1915 most recent event (MRE) on the fault.

In this paper, we test the hypothesis of *Wallace et al.* (1984) on the Pleasant Valley fault using two techniques to characterise the differing degrees of weathering between the 1915 and pre-1915 slip patches. We begin first with a brief review of principles of relative-dating as applied to bedrock fault scarps, followed by a discussion of the study site and methods. We analyse Schmidt hammer rebound values (R-values) and terrestrial laser scanning (TLS) point clouds of the scarp face to characterise the near-surface weathering and roughening of the scarp over a single earthquake cycle. In doing so, we build on the methodology and results of *Tye and Stahl* (2018) from the Hebgen fault (Montana, USA) and provide unequivocal evidence that weathering contrasts in limestone slip patches are

quantifiable under certain climatic and fault behaviour conditions (e.g., recurrence interval, RI, and single event displacement, SED). We conclude with recommendations for applying these techniques elsewhere.

5.2 Background

5.2.1 Relative age dating techniques

Relative-dating techniques were developed on the premise that time-dependent changes to rock masses and surfaces are quantifiable. One of the most widely-used applications is in exposure-age dating, where various metrics of surface weathering have been shown to correlate to the duration the rock surface has been exposed at or near the surface. Among other indicators, rock density and P-wave velocity (*Maizels*, 1989; *Crook and Gillespie*, 1986); surface roughness (e.g., *Wiatr et al.*, 2015; *He et al.*, 2016), and pit depths (*Tucker et al.*, 2011); weathering rind thickness and mineralogy (e.g., *Laustela et al.*, 2003; *Sak et al.*, 2004); and degree of lichen colonisation and lichen diameter (e.g., *Benedict*, 1985; *Bull*, 1996) all have been used as indicators of surface exposure age.

The Schmidt hammer tests rock hardness via a controlled impact of a spring-loaded piston against a surface and has been used in relative- and calibrated-age dating for years (c.f. *Goudie*, 2006). The distance that the piston rebounds within the device is measured and used to produce a rebound value (R-value). Larger R-values are generally expected from smoother and harder (or more elastic) rock surfaces. Schmidt hammer R-values have been shown to correlate with physical rock mass characteristics like uniaxial compressive strength (UCS) and Young's modulus of elasticity (E) (c.f. *Goudie*, 2006), as well as with time-dependent surface weathering characteristics like weathering rind thickness (*Laustela et al.*, 2003; *Stahl et al.*, 2013) and surface roughness (*McCarroll*, 1991; *Tye and Stahl*, 2018).

In order to interpret relative exposure ages from R-values, the user must control for other factors that influence R-value. Schmidt hammer R-values have been shown to be sensitive to variations in lithology (e.g., *Goudie*, 2006; *Török et al.*, 2007), rock moisture content (*Sumner and Nel*, 2002), biologic weathering (*Matthews and Owen*, 2008), rock sample dimensions (*Sumner and Nel*, 2002; *Aydin*, 2008; *Demirdag et al.*, 2009), number of samples per surface (*Niedzielski et al.*, 2009), operator bias (*Shakesby et al.*, 2006), and instrument degradation (*McCarroll*, 1987), among other factors. With adequate control for these factors, the largest influence on R-value is the duration of exposure at the surface.

In regions of tectonic extension, normal faults accommodate dilatational strain via brit-

tle and ductile deformation. Under brittle deformation regimes, large earthquakes ($\gtrsim$ Mw 6) rupture normal faults at the ground surface, causing episodic, centimetre- to metre-scale discrete displacements (e.g., *Nicol et al.*, 2006). Fault scarps in unconsolidated material form and subsequently erode, with the net vertical displacement across the degraded scarp indicating the cumulative displacement from all prior surface-rupturing earthquakes (e.g., *Hanks et al.*, 1984). Fault scarps form and degrade in a different manner where normal faults rupture to the surface in competent bedrock (e.g., at range fronts). For example, in competent limestone lithologies, fault planes may be exposed and weather subaerially while maintaining the overall original scarp slope (e.g., *Bosi et al.*, 1993). Limestone fault scarps therefore preserve horizontal (i.e., oriented along-strike) bands, or slip patches, with different exposure-ages corresponding to the timing of past earthquakes (e.g., *Zreda and Noller*, 1998; *Giaccio et al.*, 2003). The different exposure ages may be reflected in rare earth element content (e.g., *Manighetti et al.*, 2010; *Mouslopoulou et al.*, 2011; *Tesson et al.*, 2016) and/or the weathering characteristics of different patches.

Several studies have examined the weathering characteristics of limestone fault scarps. *Wallace et al.* (1984) was one of the first to qualitatively describe weathering differences between two slip patches on a fault scarp. *Wallace et al.* (1984) noted the difference between a lower $\sim$3 m of fresh scarp exposed in the 1915 Pleasant Valley earthquake and that of an upper more lichen-covered, rougher, and more heavily solution-pitted band. *Stewart* (1996) measured the surface roughness of the Kaperelli and Pisia faults in the eastern Gulf of Corinth, both of which ruptured to the surface and exposed fresh scarp faces in the 1981 Corinth earthquakes. The results of *Stewart* (1996) showed that fault surfaces above the 1981 slip patches were generally rougher than the fresh exposure; however, because of the heteroscedasticity in the data, caution was urged in interpreting paleoseismic histories based on surface roughness beyond historical and MRE events. *Mechernich et al.* (2018) revisited this fault using a multi-proxy approach and identified 6-8 weathering bands (or stripes) that could be correlated with earthquakes. *Tucker et al.* (2011) found a positive correlation between pit depths and cosmogenic exposure-ages on the Magnola fault scarp in the central Apennines, Italy. *Giaccio et al.* (2003) used image analysis to identify previous bands of soil-bedrock contact on the Campo Felice fault in the same region. One of the best-established techniques for carbonate fault scarps has been the Rare Earth Element (REE) method. *Manighetti et al.* (2010) developed the technique on a fault of known earthquake history by examining peaks of REE+Y left over by soil weathering within the first 1.5 m of the ground surface. *Mouslopoulou et al.* (2011) and *Mouslopoulou et al.* (2014) were the first study to apply and subsequently confirm the technique on a fault of unknown paleoearthquake history in Crete.

Surface roughness from terrestrial laser scanning (TLS) microtopography data have also been used to investigate many aspects of fault friction (*Sagy et al.*, 2007; *Candela et al.*, 2009; *Brodsky et al.*, 2016) and scarp weathering (*Wei et al.*, 2013; *Wiatr et al.*, 2015; *He et al.*, 2016; *Tye and Stahl*, 2018). Many of these works have investigated the effects of weathering on the fractal distribution of scarp surface relief (*Wei et al.*, 2013; *He et al.*, 2016). The analysis of *Wei et al.* (2013) showed that the effects of weathering on scarp microtopography are most pronounced at spatial scales of several centimeters or less.

Zreda and Noller (1998) presented the first study using ^{36}Cl exposure-age dating on a limestone fault scarp in their research on the Hebgen fault in Montana, USA. In their study, they used relative weathering metrics (e.g. roughness, discoloration, pitting, and preservation of slickensides) as guides in grouping ^{36}Cl sample concentrations and apparent ages. *Tye and Stahl* (2018) re-evaluated the same exposure using the Schmidt hammer, adjusted Geological Strength Index (GSI), and TLS and found that R-values decreased in steps with increasing height on the scarp, which they attributed to incremental exposure of the scarp in 3-4 earthquakes. Interpretations of TLS data, however, were inconclusive, which could be partially attributed to the macro-scale weathering characteristics of the Hebgen fault site (*Tye and Stahl*, 2018). In order to further test the utility of Schmidt hammer and TLS in characterising carbonate fault scarps, we selected a site with less geomorphic and lithologic complexity.

5.3 Methods

5.3.1 Study site

Our study site is located in central Nevada, USA, within the actively extending Basin and Range province (Fig. 5.1). East-west directed extension in the Basin and Range is accommodated by a series of N-S oriented normal faults, forming a series of topographic ranges and adjacent valleys. The site is located on the Pearce section of the Pleasant Valley fault (*Wallace et al.*, 1984) at the southwestern range front of the Tobin Range (Fig. 5.1). The elevation of the site is c. 1490 m; it has a mean annual temperature (30-year normal) of 9.5 °C and mean annual precipitation of 210 mm (data sourced from National Oceanic and Atmospheric Administration 30-year normals between 1981-2010 for Winnemucca Airport climate station, located 75 km to the North along Pleasant Valley). The lithology of the fault scarp is massive, grey dolomitic limestone of the Triassic Natchez Pass Formation (*Page*, 1935; *Stewart and Carlson*, 1976).

The Pleasant Valley fault last ruptured in an earthquake on October 2nd 1915. The

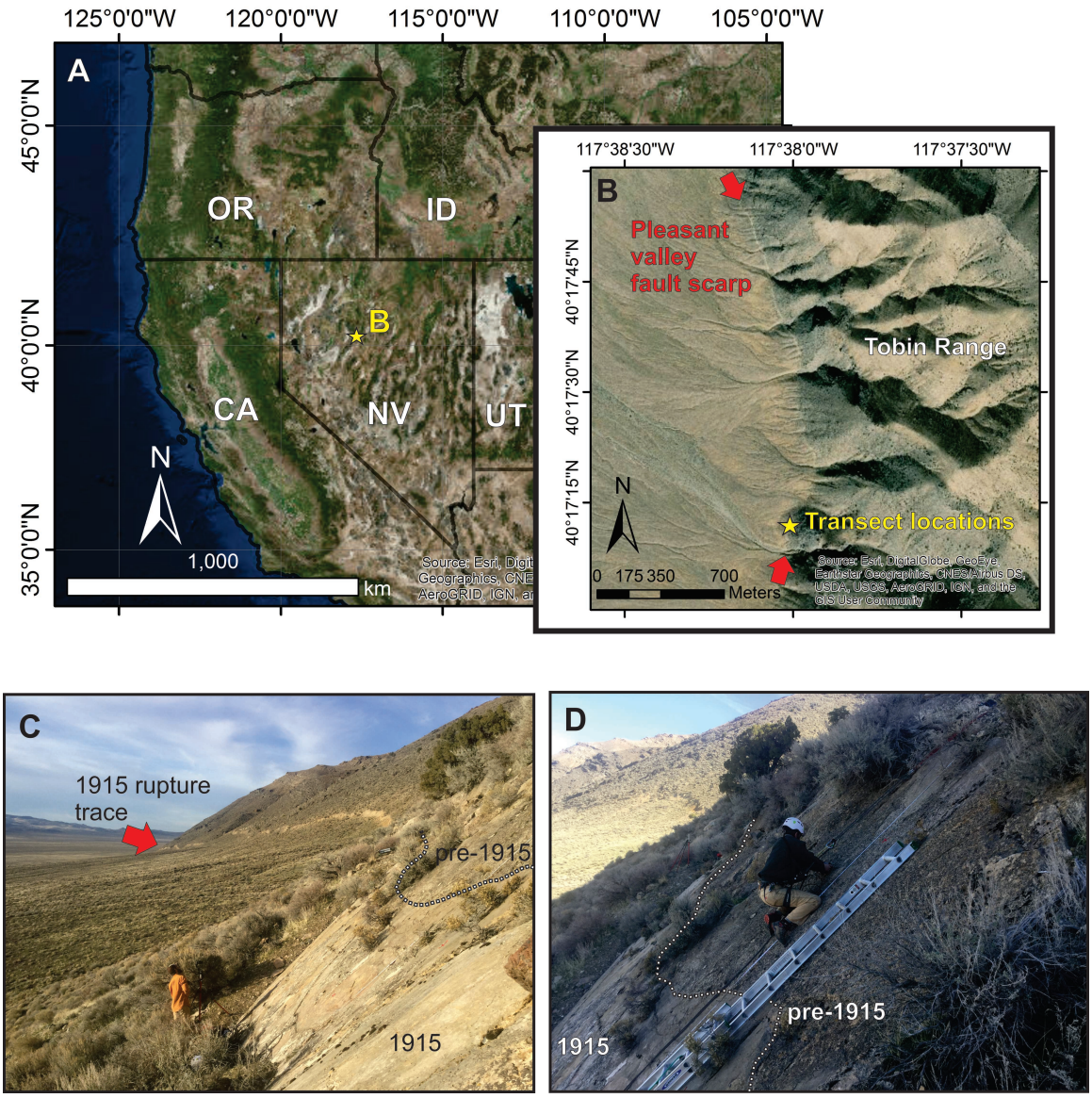

Figure 5.1: Location of the study site within (A) Basin and Range province of Nevada, USA, on the (B) Pearce Section of the Pleasant Valley fault. In (B) the light colored band demarcated by red arrows is the surface rupture of the 1915 Pleasant Valley earthquake. The fault ruptured through both bedrock and unconsolidated alluvial fan gravels (C). The distinction between 1915 and pre-1915 slip patches is primarily color, which is determined by lichen cover (C & D).

seismological moment magnitude (MWs) of the earthquake is estimated to be MWs 6.9-7.0 but is uncertain due to the low number of recording seismograph stations near the epicenter (*Doser*, 1988). The geological moment magnitude (MWg, estimated from field observations of length and displacement) is significantly higher at MWg 7.3-7.5 (*Wallace et al.*, 1984; *Wesnousky*, 2008; *dePolo*, 2013). One potential reason for this discrepancy is that the October 2nd earthquake was preceded, on the same day, by two significant foreshocks that could have caused surface rupture along sections of the Pleasant Valley fault; however, no historical account is definitive in identifying surface rupture from these events (*Wallace et al.*, 1984; *Doser*, 1988; *dePolo*, 2013). Thus, for the purposes of this study, we assume that the observed displacement was accrued during a single event (the 1915 earthquake).

Displacement on the Pleasant Valley fault in 1915 was predominantly dip-slip with a small dextral component. Average net slip was 3.2-3.6 m, with average and maximum dip-slip values of 3 and 6.7 m, respectively (*dePolo*, 2013). Four fault sections have been defined on the basis of local geology, morphology, and trace continuity: (from north to south) the China Mountain, Tobin, Pearce, and Sou Hills sections. The Pearce section is the longest at ∼30 km.

At the study site on the Pearce Section of the fault (Fig. 5.1B), the exposed fault plane strikes 185° and dips 50° to the West, with striae plunging 49° towards 295°, confirming predominantly dip-slip motion with a minor dextral component. The scarp is present as a single exposed fault plane for c. 7.5 m scarp height but becomes progressively covered in vegetation above 5 m. We observed no gouge on the surface. *Wallace et al.* (1984) reported dip-slip of 3 m in the 1915 earthquake at this location and noted bands with different weathering on the limestone scarp, with a transition zone 'a few centimeters wide' (pg. A23). We visually confirmed the observation of this transition zone between 1915 and pre-1915 slip patches, and that the upper patch had 0.5 cm deep and 1-2 cm wide solution pits, more intense lichen cover, and elongate rillenkarren. This upper weathered zone was attributed to a longer duration of weathering on the upper part of the scarp due to one or more pre-1915 earthquakes on the fault by *Wallace et al.* (1984); they proposed an age of several thousand, but less than 12,000 years, for this event.

Paleoseismic studies on the Pleasant Valley fault have not yielded conclusive evidence for the timing or amount of slip in prehistoric earthquakes. An exploratory trench across the scarp in alluvial fan gravels, ∼18 km to the north from our site, found evidence for two or more pre-1915 events that were estimated to be Holocene-late Pleistocene in age (*Bonilla et al.*, 1980). Another unpublished trenching study ∼2.5 km to the south revealed evidence for several faulting events on a ∼13 m high compound scarp, but no dateable material was

recovered (*Anderson and Machette*, 2000).

5.3.2 Schmidt hammer methods

A mechanical N-type Schmidt hammer with an impact energy of 2.207 N m was used to test rebound values of the Pleasant Valley scarp. We followed the sampling protocol of *Tye and Stahl* (2018), whereby we recorded the first impact R-value and four subsequent values at each point along the scarp in order to calculate the R-value range, ΔR. This R-value differencing approach is used to account for small variabilities in rock mass properties that are inherent in any lithology. That is, even if first-impact R-values are significantly different on patches of equivalent exposure-age, ΔR may remain relatively stable (*Tye and Stahl*, 2018). We chose a sampling spacing of 10 cm in two c. 5 m-high scarp transects, as above this scarp height (i) vegetation obscured the upper $\sim$2.5 m and (ii) we had no confidence in a single fault plane continuing beyond that point. The two transects were located approximately 10 m apart along the scarp. All samples were collected over a period of one day in dry conditions by the same operator. We avoided lichen cover and facets that appeared to be more freshly exposed than the surrounding scarp. We also avoided solution pits and attempted to sample on the flattest surface available at that height. Any chipping of the rock surface was noted and a new sample location was chosen at that same scarp height. In doing so, we aimed to test both the near-surface limestone 'hardness' and mm-scale (from the diameter of the contact point) surface roughness. The Schmidt hammer was calibrated on a test anvil before and after the trip to ensure no instrument degradation took place.

5.3.3 Terrestrial Laser Scanning (TLS) methods

In order to quantify cm-scale surface roughness and assess its spatial relationship with rupture patches corresponding to the 1915 and pre-1915 events, we analyzed terrestrial laser scanning (TLS) data collected from the Pleasant Valley scarp. TLS data were collected using a Riegl VZ1000 scanner from four scan positions with average point spacing of $\sim$3 mm in the horizontal and vertical directions on the scarp face. TLS point data were colored using a Nikon D810 Full Frame digital camera mounted on the scanner. One scan position from each of the two study sites (northern and southern) was selected for further analysis and vegetation and irregular erosion features were removed from the data manually. For each scan position, points located on the fault surface were transformed such that the scarp face corresponded with the XY plane. Following this transformation, scarp-normal elevation values of the points were gridded with 3 mm grid resolution.

As a measure of surface roughness, we calculated topographic variance within a square moving window ~5 cm in width (after *Tye and Stahl*, 2018). Within each window, the gridded data were fit to a best-fit fault plane (to account for slight changes in surface orientation across the scarp), and the variance of the residuals were calculated. The ~5 cm moving window moved in ~2.5 cm increments, such that half the gridded data were shared between adjacent windows. Finally, for selected transects at each study site, topographic variance values were horizontally averaged and plotted against scarp height in 2.5 cm increments to visualize any vertical trends within the data.

5.3.4 Curve-fitting

We followed the same procedure outlined in *Tye and Stahl* (2018) for curve-fitting scarp height versus ΔR and TLS-derived roughness data and model selection, and refer the reader there for details of the method. We conducted curve-fitting with natural log-transformed data to reduce effects of heteroscedasticity. Linear, power-law, and step-function models were considered as candidate models. Theoretically, a fault scarp incrementally exposed in earthquakes should have stepped ΔR and roughness versus scarp height relationships, but with unknown amounts and locations of steps. Best-fitting parameters were determined via pattern search for linear and power-law modes (*Hooke and Jeeves*, 1961) and via brute force maximum likelihood for the stepwise models. For the latter, we did not specify the number of steps or their locations, allowing the algorithm to identify these parameters automatically. We used the Bayesian Information Criterion (BIC; *Schwarz et al.*, 1978) to compare model goodness-of-fit while penalising for additional model parameters. The lowest BIC values indicate a balance between model fit and number of parameters, and therefore point towards the preferred model.

5.4 Results

5.4.1 Schmidt hammer

Schmidt hammer R-values generally increase with subsequent impacts in both transects (Fig. 5.2). At 85% of the sample locations, first or second impact R-values (R_1 and R_2) were the lowest, and fourth or fifth impact R-values (R_4 and R_5) were the highest. There is some alignment of 'peaks' and 'troughs' between sample sites that affect all R-values (Fig. 5.2). Minimum and maximum R-values both decrease with increasing height on the scarp, though the decrease is more pronounced in R-value minima (Fig. 5.2). Between ~2.25 m

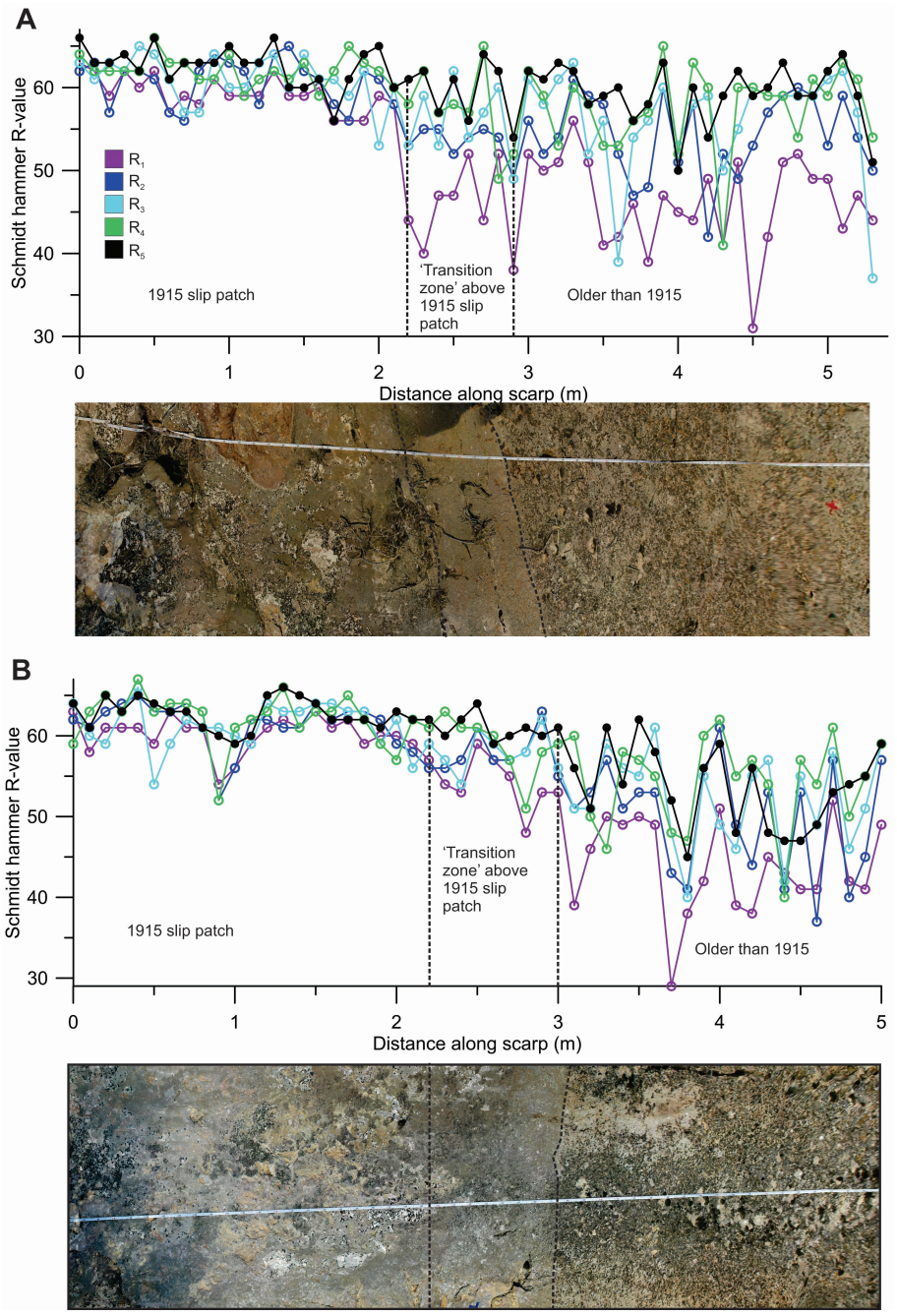

Figure 5.2: Schmidt hammer rebound values (R-values) and orthophotography from the two transects, southern (A) and northern (B). Both transects are approximately 5 m long, measured on the fault plane from the point nearest the ground surface. Rebound values are colored by the order of five impacts (R_1-R_5) at each site spaced 0.1 m on the scarp. The difference between the maximum and minimum R-value at each site is called ΔR (see text for discussion). Striae are well-preserved on the lowest portions of the scarp exposed in the 1915 earthquake, and demonstrate predominantly dip slip motion. The patch above the 1915 rupture is lichen covered, but has small areas of bare rock suitable of Schmidt hammer testing.

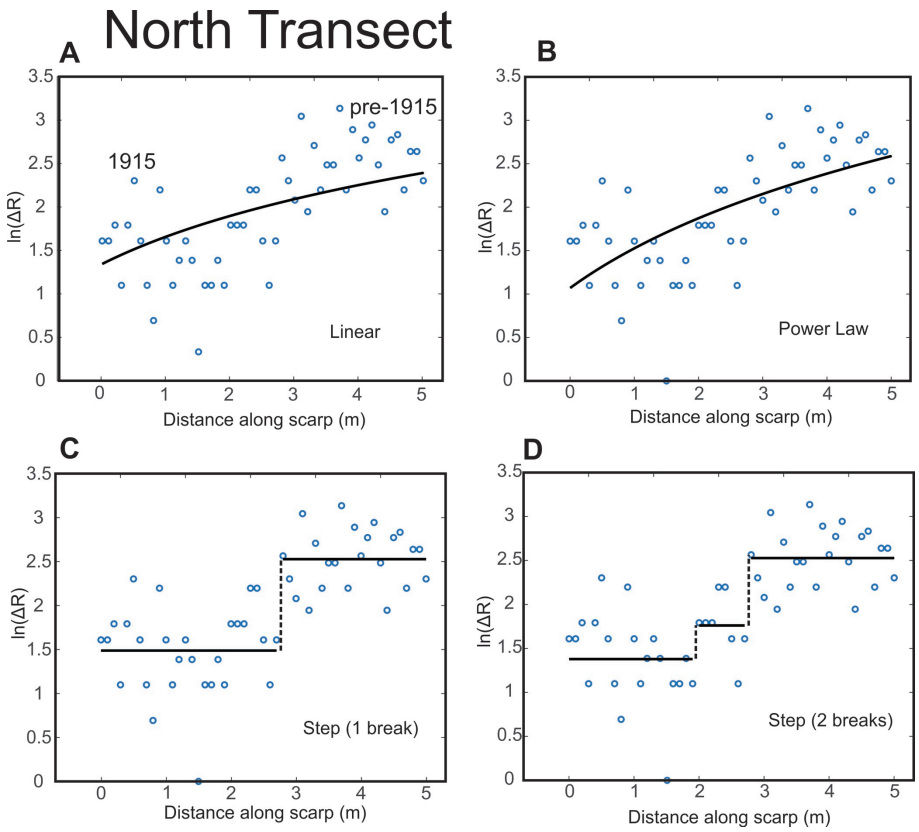

Figure 5.3: The natural logarithm of ΔR plotted against scarp distance shows a general increase in ΔR with increasing height. For the northern transect, the best fitting model based on the Bayesian Information Criterion (BIC) is (C)—the stepwise model with one break at $\sim$3 m.

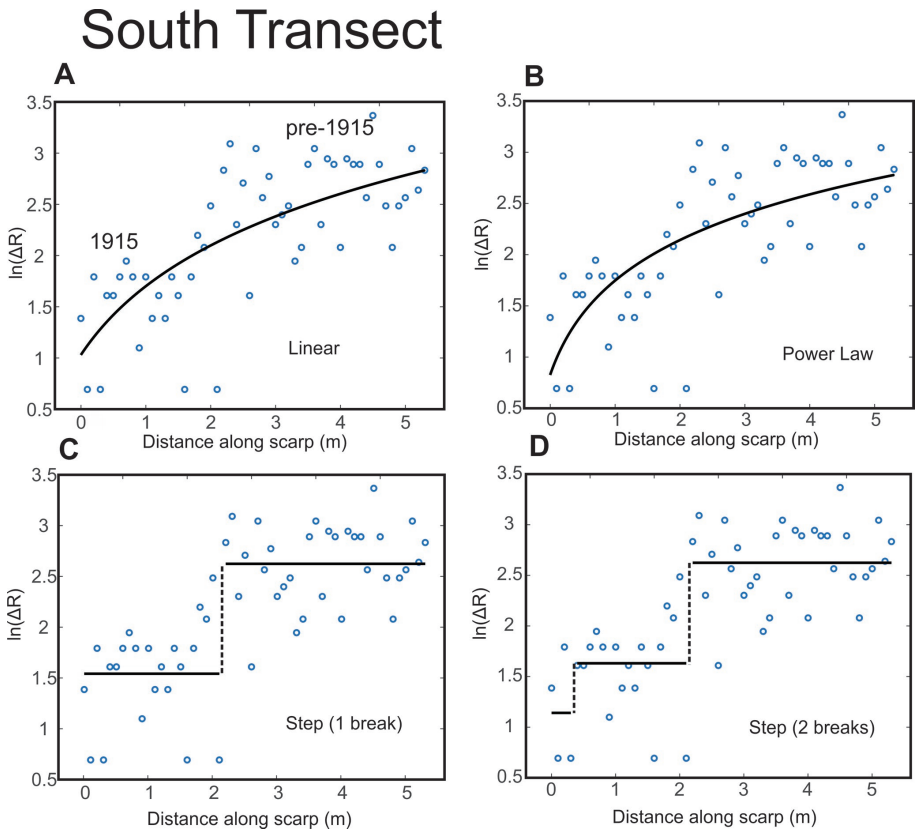

Figure 5.4: The natural logarithm of ΔR plotted against scarp distance shows a general increase in ΔR with increasing height for the southern transect. The best-fitting model is (C)—a stepwise model with one break at $\sim$2 m.

and 3 m in both transects, the difference between R-value minima and maxima (ΔR) starts to become larger by 8-10 points on average. The standard deviation of ΔR also becomes larger above this scarp height, increasing from σ=2.2 to σ=4.8. This area approximately coincides with the transition zone of weathering patterns, identified visually, between 1915 and pre-1915 slip patches (Fig. 5.2).

Modelled ΔR-scarp height relationship	BIC, northern transect	Step location, northern transect	BIC, southern transect	Step location, southern transect
Linear	77.1	–	84.2	–
Power law	92.4	–	92.2	–
Stepwise (one break)	**58.5**	**2.7 m**	**78.5**	**2.2 m**
Stepwise (two breaks)	62.6	2.0 and 2.7 m	81.1	0.4 and 2.2 m

Table 5.1: Model fitting parameters for ln(ΔR) from the two fault transects. Lower values of BIC indicate more preferable models. One outlier ΔR value was removed from the northern transect at height=4.2 m. The preferred model is bolded.

BIC values were calculated using $\sigma_{\ln(\Delta R)}$ = 0.4, which is representative of the scatter of $\ln(\Delta R)$ values within the inferred 1915 and pre-1915 slip patches (Table 5.1). Use of $\sigma_{\ln(\Delta R)}$ values of 0.3 to 0.5, encompassing the full range of local scatter in $\ln(\Delta R)$ values, did not change the preference for a stepwise model. Of the four model fits considered for each transect (Figs. 5.3 and 5.4), the stepwise functions yield the lowest BIC values despite having a larger number of parameters constraining the fit. There is a slight preference for the one-step model in both transects (Table 5.1). The best-fitting step location for the northern transect is at 2.7 m (Table 5.1; Fig. 5.3C), 30 cm below where we had visually identified the cut-off between transition zone and pre-1915 scarp (Fig. 5.2B). The best-fitting step location for the southern transect is located at 2.2 m (Table 5.1; Fig. 5.4C), which is at the boundary of the 1915 slip patch and transition zone above (Fig. 5.2A).

5.4.2 TLS

Our TLS data quantify cm-scale roughness variations over the surface of the fault scarp (Fig. 5.5). Visual distinctions between the 1915 and pre-1915 event rupture patches are present in the colored point clouds (Fig. 5.5 a, d). Though lighting was different between

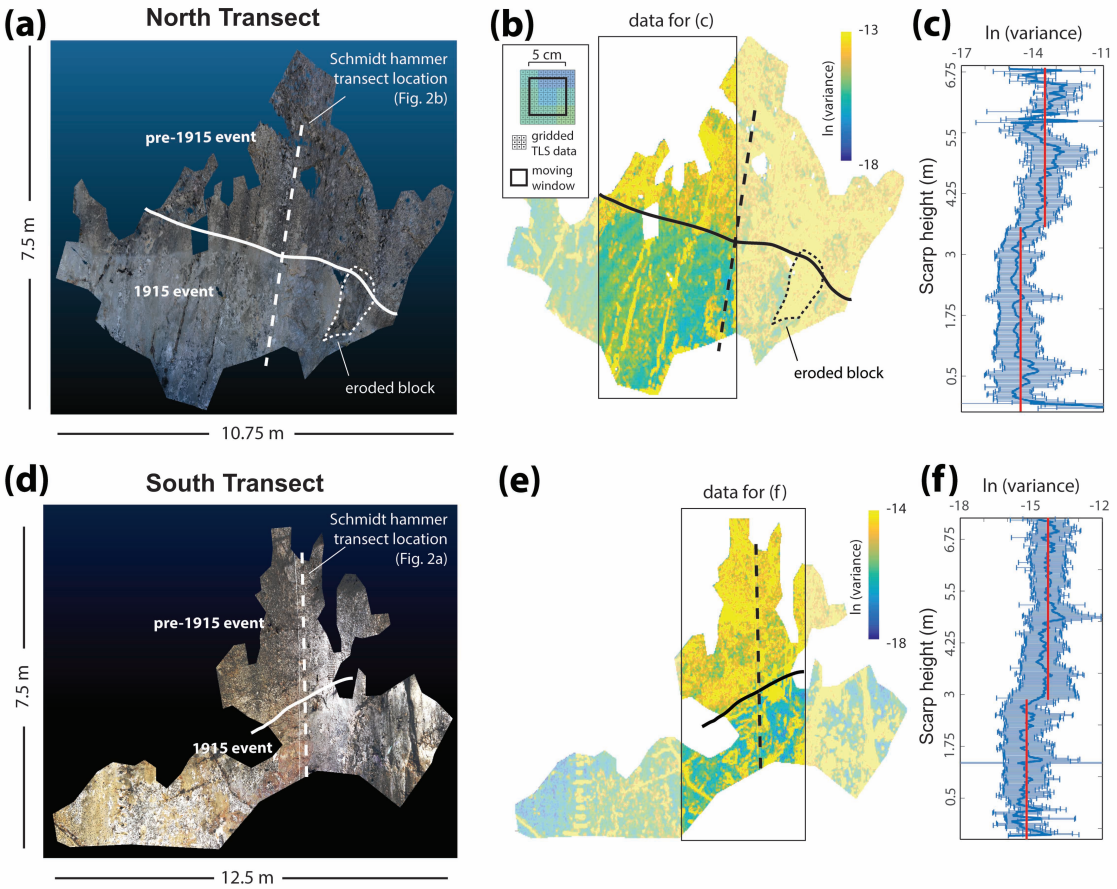

Figure 5.5: Terrestrial laser scanning quantifies the surface roughness of the Pleasant Valley scarp. (a) TLS pointcloud (shown in true color) collected from the northern study location at Pleasant Valley shows a sharp visual distinction between a relatively smooth and light-colored lower portion of the scarp associated with the 1915 event and an upper, relatively rough and darker-colored portion of the scarp. (b) Roughness (topographic variance) analysis was conducted over the entire pointcloud. Inset shows roughness calculation procedure: a moving window moves over gridded TLS data, and within each moving window the variance in plane-normal elevation is calculated and plotted. The moving window is a square of $\sim$5 cm dimension and moves $\sim$2.5 cm between calculations, such that adjacent roughness calculations are based on window locations that share half their area. (c) Vertical variations in horizontally averaged roughness (variance) are plotted for a selected swath of data. Bold blue line indicates the mean ln(variance) for each row within the swath boundaries (shown by the rectangle in b), with error bars reflecting the standard deviation (1σ). Bold red line shows mean topographic variance within the 1915 event patch and the pre-1915 event patch. (d-e) are analogous to (a-c) but show data from the southern Pleasant Valley scarp study location.

the sites, the pre-1915 event rupture patch is darker and appears more pitted than the 1915 event rupture patch at both the northern and southern sites (Fig. 5.5 a, d). Measurements of topographic variance within a ∼5 cm footprint also suggest a measurable difference in surface roughness at this scale between the 1915 and pre-1915 event rupture patches (Fig. 5.5 b, e). The pre-1915 event rupture patch is rougher than the 1915 event patch, and the boundary between the two rupture patches corresponds with the boundary suggested by visual inspection of the scarp point clouds (Fig. 5.5 a, d) and field observations. Horizontally averaged roughness values suggest a stepwise pattern in which the 1915 and pre-1915 event rupture patches have uniform roughness values that are distinct from one another (Fig. 5.5 c, f).

Modelled ln(variance)-scarp height relationship	Northern transect	Southern transect
Linear	577.0	539.2
Power law	758.8	610.0
Constant value	650.5	651.8
Stepwise (one breaks)	**537.0 (step at 3.6 m)**	**535.9 (step at 2.9 m)**

Table 5.2: BIC values for fits of different functional forms to the horizontally-averaged TLS-derived surface roughness data in Figure 5 c, f. The preferred model is bolded.

We use BIC to assess the most appropriate functional form to fit the horizontally averaged roughness data (Table 5.2), using a similar set of functions as tested for the Schmidt hammer data. In the cases of both the northern and southern sites, BIC values indicate that there is a positive to strong preference for a stepwise functional form with one break (Fig. 5.5c, f; Table 5.2). The stepwise model with one break indicates the values of topographic variance that characterize the 1915 and pre-1915 rupture patches at the northern and southern sites. At the northern site (Fig. 5.5 a-c), the pre-1915 rupture patch has a topographic variance value (over a ∼5 cm wavelength) of about $e^{-13.5}$, whereas the 1915 rupture patch has a topographic variance value of about $e^{-14.5}$ (Fig. 5.5c). At the southern site (Fig. 5.5 d-f), the pre-1915 rupture patch has a topographic variance of about $e^{-14.3}$ and the 1915 rupture patch has a value of about $e^{-15.2}$ (Fig. 5.5f). Thus, in both cases, measured roughness values are a factor of $\sim e$ greater in the pre-1915 rupture patch than in the 1915 rupture patch.

5.5 Discussion

5.5.1 Preferred model and demarcation of single event displacements (SEDs)

Visual inspection, Schmidt hammer R-values and topographic variance (henceforth referred to as TLS-derived surface roughness) all detect a contrast between 1915 and pre-1915 slip patches, while the exact characteristics of the transition zone between the two are less clear. Visually (Fig. 5.2), the upper (pre-1915) patch appears rougher, more lichen covered, and 'rustier' in color than the transition zone. The transition zone is lichen free, but rougher and darker in color than the 1915 slip patch (Fig. 5.2).

The difference between R-value minima and maxima, or ΔR, increases from 1915 to pre-1915 patches (Figs. 5.3 and 5.4), which is consistent with previous interpretations that older patches are rougher and softer due to subaerial weathering (*Tye and Stahl*, 2018). The transition zone between the two slip patches has a variable ΔR signature in the two transects. In the northern transect, ΔR values gradually increase up-scarp within the transition zone to 3 m scarp height (Fig. 5.2B). The upper and lower boundaries of the transition zone are in fact approximated in the stepwise model with two steps (Table 5.1; Fig. 5.3D). In the southern transect, the ΔR boundary between 1915 slip patch and the transition zone is more abrupt (Figs. 5.2A & 5.4C). This is where the best-fitting stepwise model (using BIC) places the step (Table 5.1; Fig. 5.3C).

TLS-derived surface roughness has several implications for the processes controlling fault scarp surface roughness at the cm-scale. Horizontally averaged roughness values show a uniform distribution within the 1915 and pre-1915 event rupture patches with a significant difference in roughness between the two rupture patches (Fig. 5.5 c, f). This distribution of roughness indicates that the dominant control on surface roughness of the Pleasant Valley scarp is whether a particular $\sim$5 cm patch of the scarp was exposed during the 1915 or pre-1915 event. The paleoseismic control on surface roughness conforms to field observations from the Pleasant Valley site and prior studies of other bedrock normal fault scarps, which also reveal approximately stepwise surface roughness distributions (*Wiatr et al.*, 2015; *He et al.*, 2016). Overall, our TLS data indicate that the Pleasant Valley scarp contains two regions of distinct roughnesses that in general correspond to the 1915 and pre-1915 event rupture patches.

A gradual transition is observed between the ΔR and TLS-derived roughness 'steps' between the 1915 and pre-1915 event rupture patches (Figs. 5.2 - 5.5). At both sites, the transitions occur over a band of 0.25 - 0.5 m scarp height. The transition is similar to that

observed in other studies of fault scarp surface roughness, which has been hypothesized to reflect weathering within soil at the base of an exposed scarp between earthquakes (discussion below). The interpretation of these transition zones and locations of these steps is significant for estimating single event displacements (SEDs). We consider the transition zone to represent the region where soil or colluvium was in contact with the fault scarp prior to the 1915 earthquake. Identification of similar discolored bands have been identified on other fault scarps (e.g., *Giaccio et al.*, 2003; *Mechernich et al.*, 2018). It follows that these bands will be more weathered than the subsurface fault scarp, and depending on the length of time (i.e., recurrence interval of faulting), soil chemistry, and colluvium or soil density, they will exhibit weathering characteristics consistent with the previously exposed patch (e.g., our southern transect) or transitional between the two patches (e.g., our northern transect). The fact that the zones do not follow one particular ΔR pattern leads to uncertainty in determining how much the fault slipped in previous earthquakes.

Visually, we would estimate an SED of between 2.2-3.0 m of dip slip of the Pleasant Valley in 1915 at the two transect sites, whereas we would estimate between 2.2 (Fig. 5.4C) and 2.9 m (Fig. 5.5f) for the southern transect, and 2.7 and 3.6 m for the northern transect, based on curve fits to ΔR and TLS-derived surface roughness, respectively (step location values from Tables 5.1 and 5.2). The difference between the two sites and the two techniques can be attributed to undulations in the elevation of the colluvium at the base of the scarp, the scale of roughness being measured, and the varying properties of the transition zone. Averaging our four step locations, we would estimate dip slip SED of 2.85 m, which is in decent agreement with the 3 m dip slip previously estimated at the site (*Wallace et al.*, 1984) and our visual inspection. We see no evidence for more than one rupture patch in the 2-3 m of fault scarp preserved above the transition zone, so we would estimate a minimum SED of $\geq$2-3 m for the penultimate event at this site. We cannot rule out small, closely-spaced events older than the 1915 slip patch, but there is no evidence for this in our data or in the historic record.

5.5.2 Sources of uncertainty in determining SEDs

Using this method, sources of uncertainty in determining SEDs include (i) inherent heterogeneity in limestone lithology and surface weathering, leading to natural variability in ΔR or TLS-derived surface roughness values, (ii) natural variability in Schmidt Hammer R-Values due to instrumental error, (iii) epistemic uncertainty regarding small displacement events, events closely spaced in time, or non-tectonic modification to the scarp's exposure history, and (iv) the presence of a 'transition zone' between patches and locations of best-

fitting model step within it. While (i), (ii), and (iii) are unable to be completely eliminated, these forms of uncertainty can be reduced by careful site selection and sampling. Point (iv) warrants further discussion below.

The transition zone can take on weathering characteristics, measured by ΔR values, of the older slip patch or of both patches. In this study, the best-fitting model for Schmidt hammer data either places a step near the top or bottom of this zone. This leads to differences in estimated SED values between transects, using only the Schmidt hammer data, of $\sim$0.5 m and an underestimation of the SED in our curve fitting of between 0.3-0.8 m ($\sim$10-27%) for the most recent event. On other fault scarps, depending on how these transition zones weather, their thicknesses, and whether they are present at all, this effect may lead to over- or underestimation of SEDs on older patches using the Schmidt hammer. There is not a general solution to this problem, as varying weathering rates; soil density, thickness, and chemistry; and limestone properties will influence how these zones weather in different settings. However, TLS-derived surface roughness data place the step higher (i.e., nearer the top of the transition zone) in both transects, therefore providing a counterbalance to the finer-scale surface roughness and/or surface hardness measured by the Schmidt hammer.

5.5.3 Application to other limestone fault scarps—where can this be used and how can it be improved?

This study demonstrates unambiguously that TLS and the Schmidt Hammer are useful for demarcating SEDs associated with the most recent paleoearthquakes on carbonate fault scarps provided certain tectonic, climatic, and lithologic conditions are met. The Pleasant Valley fault is a low slip rate fault with a long recurrence interval of surface rupturing earthquakes, which means that previously exposed slip patches have a long time (10^3-10^4 years) to weather prior to exposure of the next patch. Thus, limestone from the penultimate event patch has time to develop pits, rillenkarren, and surface rinds that will distinguish itfrom the relatively fresh limestone of the most recent event patch. Under similar low weathering rate conditions, differences in ΔR may not be statistically distinguishable if recurrence intervals are shorter than 10^3 years (e.g., *Tye and Stahl*, 2018).

The other factor that influences where this method can be applied is highlighted by the scale of SEDs relative to that of near-surface weathering (i.e., transition zone thickness). The Pleasant Valley fault has 2-3 m scale displacements and a transition zone of $\sim$0.5 m, leading to uncertainties of $\sim$20% in models of SEDs. If the transition zone thickness was smaller, or the displacement larger, this uncertainty would be reduced. Where transition zone locations are unable to be established independently, small ratios of SED to transition

zone thickness will limit the utility of the Schmidt Hammer method.

Weathering rates will also influence where this technique can be applied. Because weathering rates typically decrease with exposure age (e.g., via a power law or similar curvilinear trends; e.g., *Stahl et al.*, 2013), all of the oldest slip patches will have similar weathering characteristics beyond a certain age. Additionally, older slip patches may begin to physically weather such that a continuous fault plane is no longer recognizable; in this instance, the hardness and/or cm-scale roughness may be more indicative of the presence of macro-scale fractures rather than time-dependent chemical and biokarstic weathering (e.g., *Giaccio et al.*, 2003). Significant post-exposure alteration via caliche (or calcrete) development is also likely to affect both Schmidt hammer and TLS-derived surface roughness measurements.

Targeting well-dated faults in different climates, with variable recurrence intervals and/or SEDs, will provide further evidence the Schmidt hammer and TLS can be used to demarcate slip patches. A multi-proxy approach that combines Schmidt hammer, TLS, and other (e.g., REE, photographic, seismic velocity) methods could also be used to reduce the uncertainty associated with any one technique. At present, combined Schmidt hammer and TLS seem to be of use for, at a minimum, characterising mm to cm-scale roughness contrasts between most recent and penultimate events. Further study of larger, multi-event scarps will confirm the climatic, tectonic, and lithologic conditions required for using this method to measure SEDs independently of historical or cosmogenic exposure age-dated events.

5.6 Conclusions

The weathering characteristics of two distinct slip patches on the Pleasant Valley fault scarp are evident in Schmidt hammer and TLS analysis. Our best fitting models to the ΔR and TLS data, using a Bayesian Information Criterion (BIC), place breaks between the 1915 and pre-1915 slip patches at an average of 2.85 m up the scarp, which is consistent with the reported and visually estimated $\sim$3 m SED at the site. The presence of a weathering 'transition zone' between the 1915 and pre-1915 patches is one major source of uncertainty, and handling of this uncertainty in other locations will depend on site-specific climate, lithologic, and soil properties. The penultimate event on the Pleasant Valley fault had an SED of $\geq$2-3 m, since there is no evidence of more than one event preserved above the transition zone in either Schmidt hammer or TLS data. We propose that a multi-proxy approach, incorporating our TLS and Schmidt hammer methods alongside other established techniques, might allow for even more robust SED estimates on multi-event bedrock fault

scarps.

Acknowledgments

The authors would like to thank Nathan Niemi, Marin Clark, Eric Portenga, Kendra Murray and other members of the SCALE Lab at the University of Michigan for providing valuable discussion in developing this method. We would like to thank Proceq USA for kindly allowing us to test the Pundit 200 and Pulse Echo for this purpose. Stahl was supported by NSF EAR Fellowship 1451466. We thank Brendan Hodge for assistance with TLS data collection and reduction. This material is based on data, equipment, and engineering services provided by the UNAVCO Facility with support from the National Science Foundation (NSF) and National Aeronautics and Space Administration (NASA) under NSF Cooperative Agreement No. EAR-0735156. Two anonymous reviewers greatly improved the quality of the manuscript. TLS data is available at https://doi.org/10.7283/jq24-jd07.

CHAPTER 6

Sedimentary Response to Collisional Orogeny Recorded in Detrital Zircon Provenance of Greater Caucasus Foreland Basin Sediments

Abstract

The transition from subduction to collision marks a major change in the force balance on an orogen, and has been linked to changes in plate motion, topography, and climate. However, uncertainty persists in interpreting the timing of collision from sedimentary records in some of the most well-studied collisional orogens. The Caucasus region, in which collision began recently and foreland-basin stratigraphic records are well-preserved and accessible, provides an ideal location in which to investigate the stratigraphic record of collision.

We present new detrital zircon U-Pb age data from the Caucasus region that record changes in sediment routing and source exhumation during the initiation of collision. Combined with published stratigraphy, thermochronology, and paleomagnetic data, our results reveal a timeline of the progression from soft to hard collision in the Caucasus and the resulting sedimentary response. Soft collision is recorded at 15 - 8.5 Ma by the deposition of upper-plate detritus onto a lower-plate sequence inferred to have been located on the lower-plate continental slope. Following soft collision and before hard collision, foreland-basin sedimentation shallowed and coarsened from marine turbidites to terrestrial conglomerates. Finally, hard collision with accelerated exhumation rates and slowed plate convergence began at 5 Ma, coincident with the onset of foreland-basin erosion at the locus of collision and establishment of an axial drainage network within the foreland basin that conveyed sediment from the locus of collision to lower elevation regions along strike. Our results indicate a progression of sedimentary changes that accompany collision, and may permit more accurate recognition and dating of early collision in mature collisional orogens.

Our detrital zircon U-Pb age dataset also constrains the crystallization histories of ter-

ranes accreted to the southern margin of Eurasia that likely guide present deformation in the Arabia-Eurasia collision zone, of which the Caucasus is a part. The Greater Caucasus and the basement of the Scythian platform, located to the north of the Greater Caucasus, have a shared crystallization history that is distinct from that of the East European Craton and the Transcaucasus. The Transcaucasus, Greater Caucasus, and Scythian domains all contain zircons associated with the Gondwanan Pan-African orogeny at 900-600 Ma, indicating that all three domains are exotic to Eurasia. Thus, our data support tectonic reconstructions in which terrane boundaries are located between Scythia and Eurasia and between the Greater Caucasus and Transcaucasus.

6.1 Introduction

The collision of two continents following the closure of an intervening ocean basin has occurred numerous times during Earth's history (e.g., *Nance et al.*, 2014). The transition from subduction to collision constitutes a major change in the balance of forces acting on an orogen (*Duretz et al.*, 2011, 2012) and the mass flux into an orogen (e.g., *Ingalls et al.*, 2016). The initiation of collision affects topography (e.g., *England and Houseman*, 1986), plate kinematics (*Patriat and Achache*, 1984; *Dewey et al.*, 1989), and climate (e.g., *Edmond*, 1992; *Molnar et al.*, 2010; *Jagoutz et al.*, 2016). The transition from subduction to collision is a diachronous process that proceeds from the final consumption of oceanic lithosphere between two continents (often termed "soft" collision; *Klootwijk et al.*, 1985; *Lee and Lawver*, 1995; *Chung et al.*, 2005) until the consumption or deformation of thinned continental to transitional lithosphere is complete ("hard" collision), such that force-balance changes in the orogen result in plate kinematic changes, changes in exhumation rates, or the initiation of far-field deformation (*Lee and Lawver*, 1995; *van Hinsbergen et al.*, 2012; *Cowgill et al.*, 2016). In order to understand orogenic mass balance and the effects of collision on climate, plate kinematics, and ocean circulation, we need highly resolved records of the transition from subduction to collision (e.g., *DeCelles et al.*, 2014; *Zhuang et al.*, 2015, and references therein).

Foreland-basin sediment composition and facies provide insight into collision zone evolution, and stratigraphic records are commonly used to constrain the timing of initial collision in orogens (*Garzanti et al.*, 1987; *Dewey and Mange*, 1999; *Ding et al.*, 2005; *Weislogel et al.*, 2006; *Zagorevski and van Staal*, 2011). Sedimentary records of collision are affected by a complex set of factors, including evolving source areas (*Axen et al.*, 2001), changing topography (*Pusok and Kaus*, 2015), and varying base levels (*Krijgsman et al.*, 1999). Interpreting the sedimentary record of collision is further complicated in

mature collisional orogens by the fact that foreland-basin systems have been disrupted by post-collisional deformation and partially to wholly destroyed by erosion or tectonic burial (e.g., *Hu et al.*, 2015). In the case of one mature collision zone, the India-Asia collision, studies of several different stratigraphic sections thought to record the initiation of collision have led to interpreted collisional ages that differ from one another by up to 10 Myr (e.g., *DeCelles et al.*, 2004; *DeCelles et al.*, 2014; *Hu et al.*, 2012, 2015; *Zhuang et al.*, 2015; *Wu et al.*, 2014). Thus, there is an ongoing need to better understand the stratigraphic record of initial collision and its spatial and temporal variation within a foreland-basin system.

The optimal setting for investigating the sedimentary response to the initiation of collision is an orogen where collision began recently, such that the stratigraphic record of collision initiation is well preserved. Ideally, independent constraints on the timing and progression of collision, such as records of plate motion and exhumation, would also be available. There are several examples of orogens thought to be undergoing the initial stages of collision where the sedimentary effects of collision could be probed, including Taiwan (*Teng*, 1990), Papua New Guinea (*Jaques and Robinson*, 1977), and the Caucasus (*Philip et al.*, 1989; *Mumladze et al.*, 2015). Of these, the Caucasus is unique in that the basin between the two colliding continents is entirely non-marine, permitting ease of access to the foreland-basin strata of interest. In addition, published paleomagnetic, geodetic, and thermochronometric records constrain the kinematics of the Caucasus and the surrounding region during the transition from subduction to collision (*Reilinger et al.*, 2006; *Avdeev and Niemi*, 2011; *Kadirov et al.*, 2012; *Austermann and Iaffaldano*, 2013; *Kadirov et al.*, 2015; *van der Boon et al.*, 2018). The goal of this study is to use the records available in the Caucasus to develop a coupled sedimentary and kinematic framework of collision that may also be applicable to other orogens.

A continental margin subjected to subduction and continental collision will undergo diverse changes in topography and structure that are recorded in its associated foreland basin (Fig. 6.1). Prior to convergence, sediment aprons of the two continents that will ultimately collide are deposited onto opposite-facing passive continental margins (Fig. 6.1a; *Tricart*, 1984). The initiation of convergence causes the growth of an accretionary prism on the basin margin above a new subduction zone (*Karig and Sharman III*, 1975). During this time, marine sedimentation continues in the narrowing ocean basin, and the subduction of the lower plate beneath the accretionary prism causes sediment from the accretionary prism to be deposited onto the lower plate (Fig. 6.1b; *Karig and Sharman III*, 1975). As convergence continues, the basin will continue to narrow and the continental slope of the lower plate will eventually enter the subduction zone, with lower plate sediment becoming incorporated into the accretionary prism (Fig. 6.1c; *DeCelles et al.*, 2014). Because of the

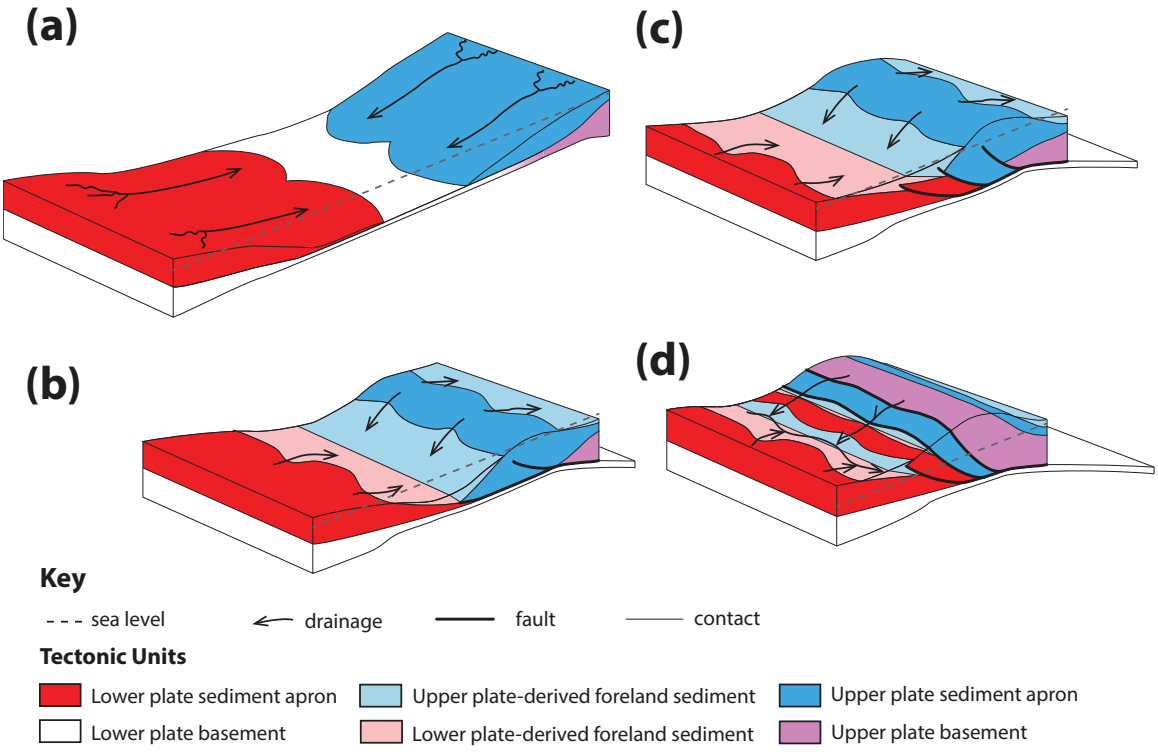

Figure 6.1: Generalized model of the evolution of an orogen during the transition from subduction to collision (see Section 6.1 for complete discussion). (a) Two continents are separated by an ocean basin. (b) Basin closure has begun via subduction beneath the margin of the basin, resulting in the formation and forward growth of an accretionary prism above the subduction zone. (c) Lower plate continental slope enters the subduction zone (soft collision). (d) Further convergence drives jamming of the subduction zone, accelerated exhumation in the orogenic wedge, and foreland basin uplift (hard collision). Foreland basin uplift causes erosion of the foreland basin and sediment evacuation via an axial drainage network. (d) is the current state of the western Caucasus.

increasing mass of sediment being added to the accretionary prism, rock uplift is likely to accelerate in the upper plate (e.g., *Davis et al.*, 1983; *Morley*, 1988). Finally, subducted transitional to continental lithosphere enters the subduction zone (*Cloos*, 1993), concomitantly increasing crustal thickness across the collision zone, accelerating upper plate rock uplift (e.g., *Lallemand et al.*, 1992), and narrowing and uplifting the foreland basin (Fig. 6.1d). The uplift of the foreland basin will decrease accommodation space and ultimately lead to erosional conditions (e.g., *Soria et al.*, 1999).

Along-strike variations in buoyancy, structural style, and topography of an incipient collision zone are controlled by the shape of the lower-plate continent. While the the foreland basin is uplifted at the locus of initial contact between upper- and lower-plate continents, lower elevation marine or non-marine basins are likely to exist along strike where the upper and lower plate continents are not yet in contact (e.g., *Şengör*, 1976). Axial drainages will develop that convey sediment from the uplifted portion of the foreland basin at the locus of collision to lower elevation basins along strike (Fig. 6.1d). As uplift of the foreland basin continues, erosion of foreland basin deposits and continued deformation in the accretionary prism will result in the exposure of the lower portion of the prism, and accelerated upper-plate rock uplift rates will lead to the exposure of deeper crustal levels (Fig. 6.1d; e.g., *Avdeev and Niemi*, 2011).

The predicted response of an orogen to initial collision suggests several consequences for the basin between the two colliding continents. First, shallowing of the basin is predicted to lead to terrestrial and then erosional conditions (Fig. 6.1b-d). Second, basin sediment is expected to be sourced from progressively deeper crustal levels of the orogen as exhumation rates increase in response to the thickness and buoyancy of the lower plate (Fig. 6.1d). Finally, an axial drainage network that includes both upper and lower plate continents within its catchment area is expected to develop in the basin (Fig. 6.1d). The Caucasus provides a natural setting in which to test whether these expected effects are clearly observed and, importantly, to constrain the relative timing of these effects and the stage of the transition from soft to hard collision at which they occur.

The predicted changes in sediment routing and depositional environments can be tested by a combination of stratigraphic facies analysis and sediment provenance. Facies analysis of foreland basin stratigraphic sequences permit inference of changes in basin depth and depositional environment. Sediment provenance can be investigated using U-Pb ages of detrital zircons, which are physically and chemically robust to earth surface conditions (*Gehrels*, 2012). By comparing the zircon age distributions of foreland basin sedimentary strata to the distributions present in potential source areas, changes in sediment routing and source area exposure over time can be inferred (e.g., *Gehrels*, 2000, and many others).

We present a new, comprehensive detrital zircon U-Pb age dataset from the Caucasus to probe the evolution of sediment routing and exhumation of sediment source areas during the transition from subduction to collision. The distinct crystallization histories of key tectonic units in the Caucasus collision zone (e.g., *Cowgill et al.*, 2016, Vasey et al., in review) suggest that detrital zircon U-Pb age data should be useful for discriminating between regional sources. Samples collected from three foreland basin sections distributed along strike of the Caucasus collision zone permit the identification of both temporal and spatial changes in sedimentary routing. By combining this zircon U-Pb age dataset with published stratigraphy for the three sampled sections, we find evidence for coarsening and shallowing foreland basin deposition leading to erosional conditions, derivation of sediment from deeper crustal levels in the orogen, and establishment of an axial drainage network in the foreland basin. We combine the timing of these stratigraphic changes with published thermochronometric (*Avdeev and Niemi*, 2011), geodetic (*Reilinger et al.*, 2006; *Kadirov et al.*, 2012, 2015; *Sokhadze et al.*, 2018), and paleomagnetic (*Austermann and Iaffaldano*, 2013; *van der Boon et al.*, 2018) records to correlate sedimentary changes such as the transition to erosional conditions in the basin with distinct stages of the transition from soft to hard collision (Fig. 6.1). In doing so, we develop a framework for the stratigraphic record of collision that may be applicable to interpreting the stratigraphic archives of other collisional orogens.

In addition to investigating the stratigraphic record of collision, we also explore the implications of our dataset for the distribution of terranes and sutures on the southern margin of Eurasia at the longitude of the Caucasus. Tectonic sutures often guide subsequent strain accommodation (*Jones and Tanner*, 1995; *Rusmore et al.*, 2001; *Fitzgerald et al.*, 2014). However, the distribution of tectonic sutures in the Caucasus region remains controversial (*Şengör*, 1984; *Natal'in and Şengör*, 2005; *Saintot et al.*, 2006a; *Adamia et al.*, 2011a; *Stampfli et al.*, 2013). Our detrital zircon U-Pb age dataset constrains the crystallization history of several basement domains within the Caucasus, which we use to test hypothesized suture locations and the associated tectonic implications. Insight into pre-existing lithospheric boundaries in the Caucasus region may improve our understanding of rheological controls on the spatial distribution of deformation in the Arabia-Eurasia collision zone.

6.2 Geological background

The Caucasus is located on the southern margin of Eurasia, within the Arabia-Eurasia collision zone (Fig. 6.2a). To the immediate north of the Caucasus, within Russia, lies Scythia,

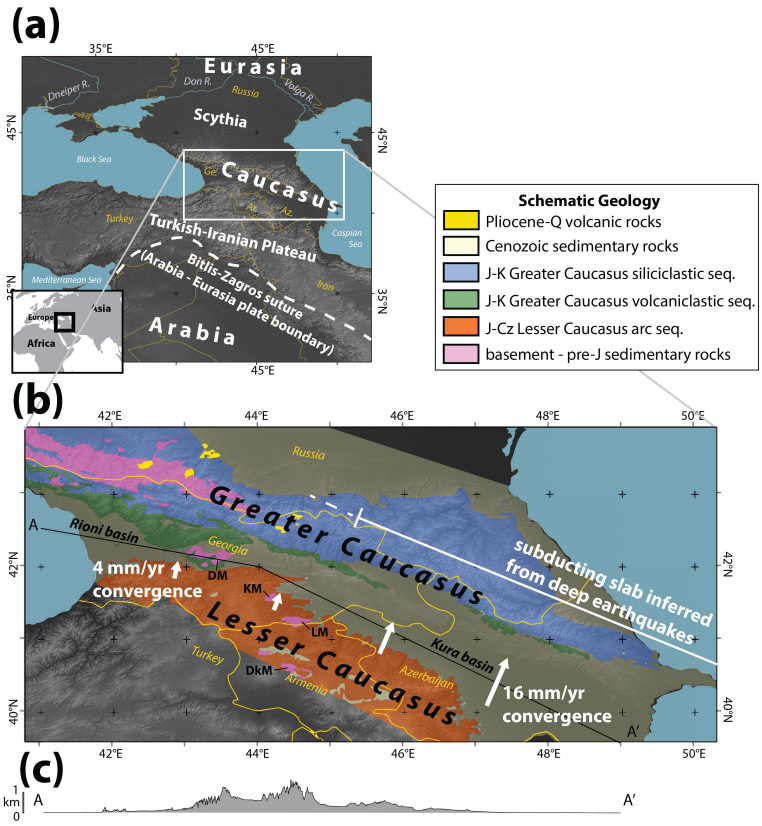

Figure 6.2: Location and tectonic setting of the Caucasus. (a) The Caucasus region is located on the southern margin of Eurasia in the Arabia-Eurasia collision zone. Political boundaries and labels are shown in yellow. (b) The Caucasus consist of the WNW-striking Greater Caucasus and Lesser Caucasus, which are converging toward one another. Schematic GPS convergence rates (*Reilinger et al.*, 2006; *Kadirov et al.*, 2015) between the Greater and Lesser Caucasus and along-strike extent of a north-dipping subducting slab inferred from deep earthquakes (*Mellors et al.*, 2012; *Mumladze et al.*, 2015) are shown in white. Key tectonic units are shown in color with key to the upper right (see further discussion in Section 6.2.2). Abbreviated names of geologic features: DM—Dzirula Massif, KM—Khrami Massif, LM—Loki Massif, DkM—Dzarkuniatz Massif. Black line A - A' shows location of topographic profile below. (c) Foreland-basin topographic profile along strike of the Greater Caucasus along line A - A'.

a tectonic platform (*Natal'in and Şengör*, 2005; *Saintot et al.*, 2006a) that is bordered to its north by stable Eurasia (Fig. 6.2a; e.g., *Allen et al.*, 2006; *Bogdanova et al.*, 2008). To the south of the Caucasus is the Turkish-Iranian plateau, which is separated from stable Arabia to its south by the Bitlis-Zagros suture, the Arabia-Eurasia plate boundary (Fig. 6.2a; e.g., *Şengör and Kidd*, 1979; *Sengör and Yilmaz*, 1981; *Copley and Jackson*, 2006).

The Caucasus region consists of two parallel, WNW-striking mountain ranges, the Greater Caucasus and the Lesser Caucasus (Fig. 6.2b). West of 43° E, the Greater Caucasus is separated from the Lesser Caucasus by the Rioni Basin, which is drained by the Rioni River, a west-flowing river that drains into the Black Sea (Fig. 6.2b, c). Between 43° E and 45 ° E, a contiguous band of elevated topography runs between the Greater and Lesser Caucasus (Fig. 6.2c). East of 45 ° E, the Greater Caucasus is separated from the Lesser Caucasus by the Kura Basin, which is drained by the east-flowing Kura River into the Caspian Sea (Fig. 6.2b, c).

6.2.1 Tectonic setting and history

The present tectonic setting of the Caucasus is constrained by seismic and geodetic data (Fig. 6.2b). Deep earthquakes beneath the eastern Greater Caucasus suggest the presence of a north-dipping, subducting slab beneath the range (*Mellors et al.*, 2012; *Mumladze et al.*, 2015), and GPS convergence rates of ∼15 mm/yr are consistent with inferences that subduction is currently active (*Reilinger et al.*, 2006; *Kadirov et al.*, 2012, 2015). The Kura Basin and the Lesser Caucasus are on the lower plate of this subduction system (Fig. 6.2b). There are no deep earthquakes beneath the western Greater Caucasus (*Mumladze et al.*, 2015) and GPS convergence rates in the western Greater Caucasus are 3-4 mm/yr (*Reilinger et al.*, 2006; *Kadirov et al.*, 2015; *Sokhadze et al.*, 2018), suggesting that subduction in the western part of the range has ceased and this part of the range is colliding with the Lesser Caucasus, which is located immediately to the south. At the locus of collision, elevated topography is contiguous between the Greater and Lesser Caucasus (Fig. 6.2c). The combination of ongoing collision inferred in the western Caucasus and active subduction in the eastern Caucasus suggests that the orogen is transitioning diachronously from subduction to collision, with the western part of the range at a more advanced stage of this transition than the eastern part of the range (Fig. 6.2b; *Mumladze et al.*, 2015).

The Caucasus region has a complex deformation history. The southern Eurasian margin was affected by successive episodes of subduction, terrane accretion, and rifting throughout the Phanerozoic that are thought to have generated significant lithospheric heterogeneity in the region (e.g., *Şengör*, 1984; *Stampfli*, 2013). The regional pre-Jurassic tectonic history

remains uncertain, however, in part due to the lack of exposure of rocks old enough to record this history (e.g., *Natal'in and Şengör*, 2005; *Saintot et al.*, 2006a). Most of the presently exposed bedrock in the Greater and Lesser Caucasus was deposited in an arc- or backarc-basin environment in the Jurassic to Eocene (Fig. 6.2b). During this time, the Lesser Caucasus contained an active volcanic arc that extended west into the Pontides and east into Iran above the north-dipping subducting slab of Neotethys (e.g., *Sosson et al.*, 2010; *Rolland et al.*, 2011; *Adamia et al.*, 2011a). Concomitant with this subduction, a system of backarc basins opened to the north of the arc, including the Black Sea basins, the South Caspian Basin, and the Greater Caucasus Basin, which opened to the north of the Lesser Caucasus and is where most of the sedimentary bedrock presently exposed in the Greater Caucasus was deposited (e.g., *Zonenshain and Le Pichon*, 1986; *Adamia et al.*, 2011a; *Vincent et al.*, 2016). In the latest Eocene or early Oligocene, the Greater Caucasus Basin began to close by northward subduction, leading to the formation of the Greater Caucasus as an accretionary prism (e.g., *Vincent et al.*, 2007; *Adamia et al.*, 2011a; *Forte et al.*, 2014; *Cowgill et al.*, 2016). The complete closure of the backarc basin(s) that separated the Lesser Caucasus from Eurasia was marked by the initiation of collision in the western Greater Caucasus, which has been proposed to have occurred as early as 35 Ma (*Vincent et al.*, 2016) to as late as 5 Ma (*Cowgill et al.*, 2016).

6.2.2 Potential sources of Cenozoic foreland-basin sediment

The Caucasus and surrounding regions contain three distinct domains of igneous and metamorphic basement and four distinct tectonostratigraphic sedimentary sequences that may have contributed sediment to the basin between the Greater and Lesser Caucasus during convergence and collision. Here, we outline these sources and their potential contribution to Caucasus Cenozoic foreland-basin sediment.

Three distinct basement domains may have contributed sediment to Cenozoic Caucasus foreland basins: the Eurasian interior (consisting of the East European Craton and Urals), the Greater Caucasus basement, and the Transcaucasus basement. The Archean to Neoproterozoic crust of the East European Craton (*Bogdanova et al.*, 2008) forms the core of the Eurasian interior at the longitude of the Caucasus and contributes sediment to rivers that drain into the Black and Caspian seas (Fig. 2a; *Allen et al.*, 2006; *Wang et al.*, 2011). The East European Craton may also have contributed sediment to the Cenozoic foreland basin of the Caucasus (*Allen et al.*, 2006). Some rivers that drain the East European Craton also include the Urals in their watershed, so sediment sourced from the Eurasian interior may also include detritus from the Paleozoic Ural orogen (*Allen et al.*, 2006). The second

potential basement source is a predominantly late Paleozoic (Hercynian) arc assemblage that constitutes the basement of the Greater Caucasus (*Adamia et al.*, 2011a; *Somin*, 2011). This arc assemblage is exposed in the core of the western portion of the Greater Caucasus (Fig. 6.2b; *Nalivkin*, 1976). The third basement domain exposed in the Caucasus is the Transcaucasus basement, a set of isolated massifs of Precambrian to Paleozoic crust that lie between the Greater and Lesser Caucasus and within the Lesser Caucasus (the Dzirula, Khrami, Loki, and Dzarkuniatz Massifs; Fig. 6.2b; *Nalivkin*, 1976; *Zakariadze et al.*, 2007; *Gamkrelidze and Shengelia*, 2007; *Mayringer et al.*, 2011; *Rolland et al.*, 2016).

Of the four tectonostratigraphic sequences in the Caucasus that may have contributed sediment to the Cenozoic foreland basin, one is unique in being Paleozoic to Triassic in age, which is older than the other sequences. Marine sedimentary rocks of Paleozoic to Triassic age, dominantly turbidites and carbonates, are locally found in depositional or structural contact with the Transcaucasus basement and the southern margin of the Greater Caucasus basement (see reviews in *Khain*, 1975; *Adamia et al.*, 1981; *Şengör et al.*, 1984). The succession immediately to the south of the Greater Caucasus basement is called the Dizi Series (*Adamia et al.*, 2011a; *Somin*, 2011). These Paleozoic to Triassic successions are exposed only over a minor area within the Caucasus.

The three tectonostratigraphic sequences that constitute the vast majority of exposed bedrock in the Caucasus are age-equivalent sequences of Jurassic to Cretaceous age and younger that are markedly different in their lithologies. These three sequences, which we describe here in order from south to north, are thought to have been deposited on the flanks of the Lesser Caucasus arc and in the Greater Caucasus Basin (e.g., *Nalivkin*, 1976; *Zonenshain and Le Pichon*, 1986; *Saintot et al.*, 2006b; *Sosson et al.*, 2010; *Rolland et al.*, 2011; *Vincent et al.*, 2016). The southernmost of the three sequences, the Jurassic to Eocene Lesser Caucasus arc sequence is exposed in the Lesser Caucasus and includes volcanic, volcaniclastic, and carbonate strata with numerous Jurassic to Eocene intrusions that reflect volcanic-arc activity in the Lesser Caucasus (Fig. 2b; *Nalivkin*, 1976; *Kopp and Shcherba*, 1985; *Sosson et al.*, 2010; *Rolland et al.*, 2011; *Sahakyan et al.*, 2017). Exposed on the southern slope of the Greater Caucasus is the Jurassic to Cretaceous Greater Caucasus volcaniclastic sequence, which includes a thick sequence of mafic to intermediate volcanic and volcaniclastic strata and carbonates with local Jurassic intrusions (Fig. 2b; *Nalivkin*, 1976; *Mengel et al.*, 1987; *Kopp*, 1985). The Greater Caucasus volcaniclastic sequence is thought to have been deposited in the Greater Caucasus Basin (e.g., *Vincent et al.*, 2016). Within the Greater Caucasus, to the north of the volcaniclastic sequence, is a Jurassic to Cretaceous sequence dominated by siliciclastic turbidites and shallow marine sandstones (Fig. 2b; e.g., *Saintot et al.*, 2006b; *Vincent et al.*, 2013). We term this sequence the Greater Caucasus

siliciclastic sequence in order to differentiate it from the Greater Caucasus volcaniclastic sequence, though some carbonates are present in the sequence. The sedimentary architecture of the Greater Caucasus siliciclastic sequence, inferred from seismic data, suggests that the sequence is derived from north of the Greater Caucasus (*Sholpo*, 1978). Because the Lesser Caucasus arc sequence, Greater Caucasus volcaniclastic sequence, and Greater Caucasus siliciclastic sequence together account for the majority of exposed bedrock in the Caucasus today (Fig. 6.2b), they are anticipated to have been sources for Oligocene to Quaternary foreland basin sediment.

6.3 Methods

We report 29 new detrital zircon U-Pb age samples (Table S1) from Cenozoic sandstones and modern river sands comprising 7,090 total ages (Table S2). We collected samples from modern rivers draining the Greater and Lesser Caucasus and from Paleogene to Quaternary foreland-basin stratigraphic sections located along the southern margin of the Greater Caucasus in Georgia and Azerbaijan during three field seasons from 2015 to 2017. Mineral separation was conducted at the University of Michigan. Heavy mineral fractions were mounted in epoxy and polished to expose crystal interiors. Mounts were made of entire heavy-mineral fractions, rather than hand selected individual zircons, in order to ensure that representative random samples of zircons were analyzed. Mount imaging was conducted at the University of Michigan and the University of Arizona Laserchron Center. U-Pb analyses were conducted at the University of Arizona Laserchron Center using a laser-ablation system attached to a Thermo Element 2 single collector ICP-MS (*Gehrels et al.*, 2008; *Pullen et al.*, 2014). Analyses >20% discordant were excluded from further interpretation. Where practical, we analyze at least 300 zircons per sample, which provides more robust characterization of zircon age signatures than analyses with typical (n $\sim$ 100) sample sizes (*Pullen et al.*, 2014).

6.3.1 Sampling

Understanding provenance changes related to the transition of an orogen from subduction to collision (Fig. 6.1) requires characterizing the zircon age signature of potential source areas and quantifying the contribution of those sources to foreland-basin deposits. We use 16 new samples of modern river sands from targeted catchments that contain specific bedrock ages and lithologic types, along with published modern and bedrock detrital zircon samples (*Allen et al.*, 2006; *Wang et al.*, 2011; *Cowgill et al.*, 2016), to characterize the zircon age

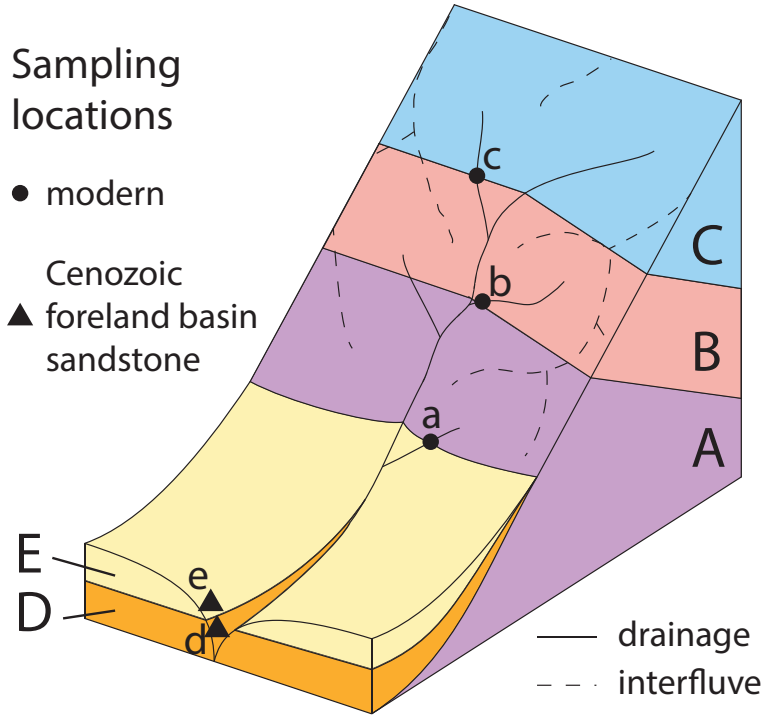

Figure 6.3: We use a two part detrital zircon sampling strategy to understand the evolution of foreland basin sediment provenance. We collect samples of foreland basin strata (rock samples d, e, of foreland basin units D, E), and we use modern samples of targeted catchments to characterize potential sources contributing to the sampled foreland strata (river sands at locations a, b, and c provide detrital zircon age signatures of units A, B, C, respectively).

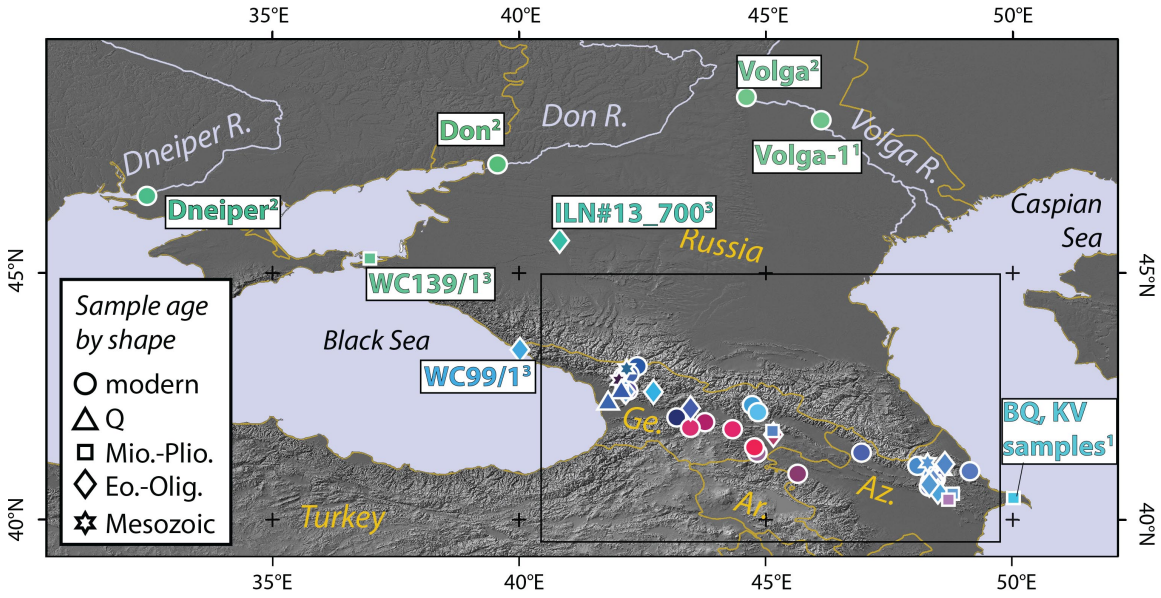

Figure 6.4: New and published sampling covers the Eurasian interior, the Greater Caucasus, and the Lesser Caucasus. Sample colors indicate affinity to the Eurasian interior (green), the Greater Caucasus (blue), or the Lesser Caucasus (red); see Figure 6.7 and Sections 6.3.2, 6.4.2 for details. Black rectangle shows the extent of Figure 6.5a. Samples outside this rectangle have their names displayed and are superscripted according to source publication: 1–*Allen et al.* (2006); 2–*Wang et al.* (2011); 3–*Vincent et al.* (2013). Samples inside the rectangle have their names displayed in Figure 6.5. Country names are abbreviated as follows: Ge.–Georgia, Ar.–Armenia, Az.–Azerbaijan.

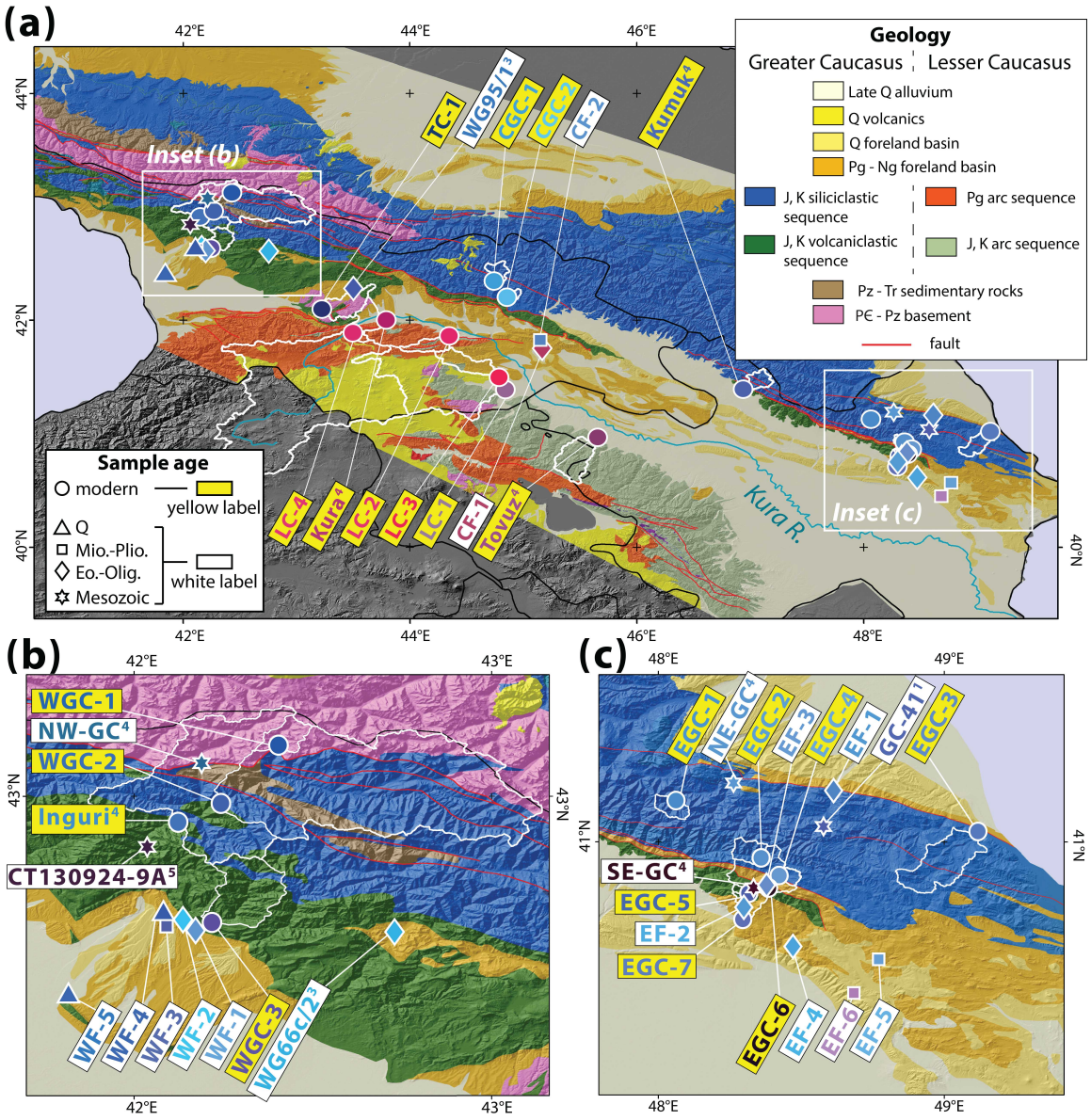

Figure 6.5: Simplified geology and detrital zircon sample locations in the Greater and Lesser Caucasus. Sample names are shown in rectangles and sample colors are as in Figure 6.4. Political boundaries are shown in black and catchment boundaries of modern samples are shown in white. The Kura River is shown in blue in (a). Abbreviations in the geology key are as follows: PЄ–Precambrian, Pz–Paleozoic, Tr–Triassic, J–Jurassic, K–Cretaceous, Pg–Paleogene, Q–Quaternary. For samples not from this study, sample name superscripts reflect source publication as in Figure 6.4 with two additions: 4–*Cowgill et al.* (2016), 5–*Trexler* (2018).

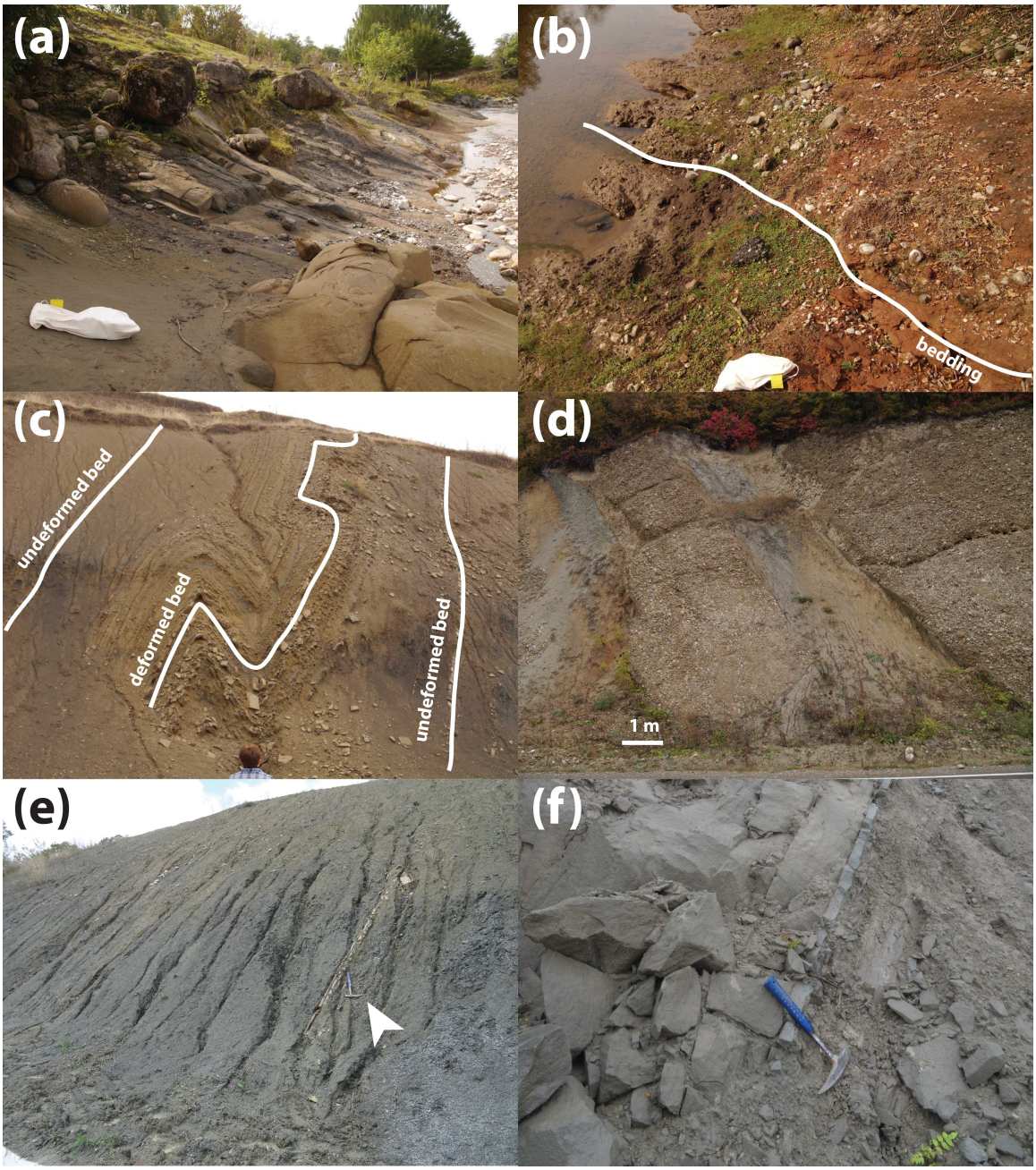

Figure 6.6: Photographs of sampled Cenozoic foreland-basin strata. (a) Oligocene, Early Miocene, or Middle Miocene turbidites of the western foreland-basin section (sample WF-2). (b) Latest Pliocene conglomerate of western section, bedding marked in white (sample WF-3). (c) Middle Miocene turbidite of the central section with bedding of undeformed and deformed horizons marked in white (sample CF-1). (d) Late Miocene conglomerate of the central section (sample CF-2). (e) Oligocene or Early Miocene turbidite of the eastern section with arrow indicating rock hammer for scale (sample EF-4). (f) Pliocene sandstone of the eastern section (sample EF-6).

signatures of the potential source areas described in the previous section (Figs. 6.3, 6.4, 6.5). Using modern river-sand samples to characterize potential sources is an efficient way to capture well-mixed, representative zircon age signals associated with erosion from the source area (Fig. 6.3).

In order to understand the changing sources of foreland-basin sediment over time, we compare the zircon age signatures of potential sources to rock samples from Cenozoic foreland-basin strata (Fig. 3). We report 13 new samples taken from different stratal levels of three Cenozoic foreland-basin sections (western, central, and eastern sections) located on the southern margin of the Greater Caucasus (Figs. 6.4, 6.5, 6.6). Five new samples were analyzed from the western foreland-basin section from rocks of Oligocene to Quaternary age (Fig. 6.5b). Two samples were analyzed from the central foreland-basin section of Middle Miocene and Late Miocene age (Fig. 6.5a). Six samples were analyzed from the eastern foreland-basin section, including rocks of Cretaceous-Paleocene to Pliocene age (Fig. 6.5). In addition to these new samples, our analyses are integrated with five foreland basin samples from the western Greater Caucasus (*Vincent et al.*, 2013) and four samples from a Pliocene section at the far eastern extent of the Greater Caucasus (*Allen et al.*, 2006).

6.3.2 Data visualization

In order to facilitate visualization of the data, we employ a sample coloring scheme throughout the paper in which samples are colored based on their Bayesian Population Correlation (BPC; a metric of detrital zircon sample correspondence that varies between 0 and 1; *Tye et al.*, 2019) to three end-member samples. The three end-member samples were chosen to highlight first-order age distinctions among the potential sources: the Eurasian interior (represented by sample Volga; *Wang et al.*, 2011) is dominated by Proterozoic zircon ages, the Greater Caucasus (represented by sample EGC-4) is predominantly represented by Paleozoic zircon ages (*Adamia et al.*, 2011a; *Somin*, 2011), and the Lesser Caucasus (represented by LC-3) is characterized by Jurassic to Eocene zircon ages (e.g., *Sosson et al.*, 2010). Endmember choice is discussed further in Section 6.4.2. The coloring scheme works as follows: each sample is assigned an RGB triplet whereby the red value is equal to the BPC value of the sample compared to the Lesser Caucasus endmember, the green value comes from comparison to the Eurasian interior endmember, and the blue value comes from comparison to the Greater Caucasus endmember (Fig. 6.7).

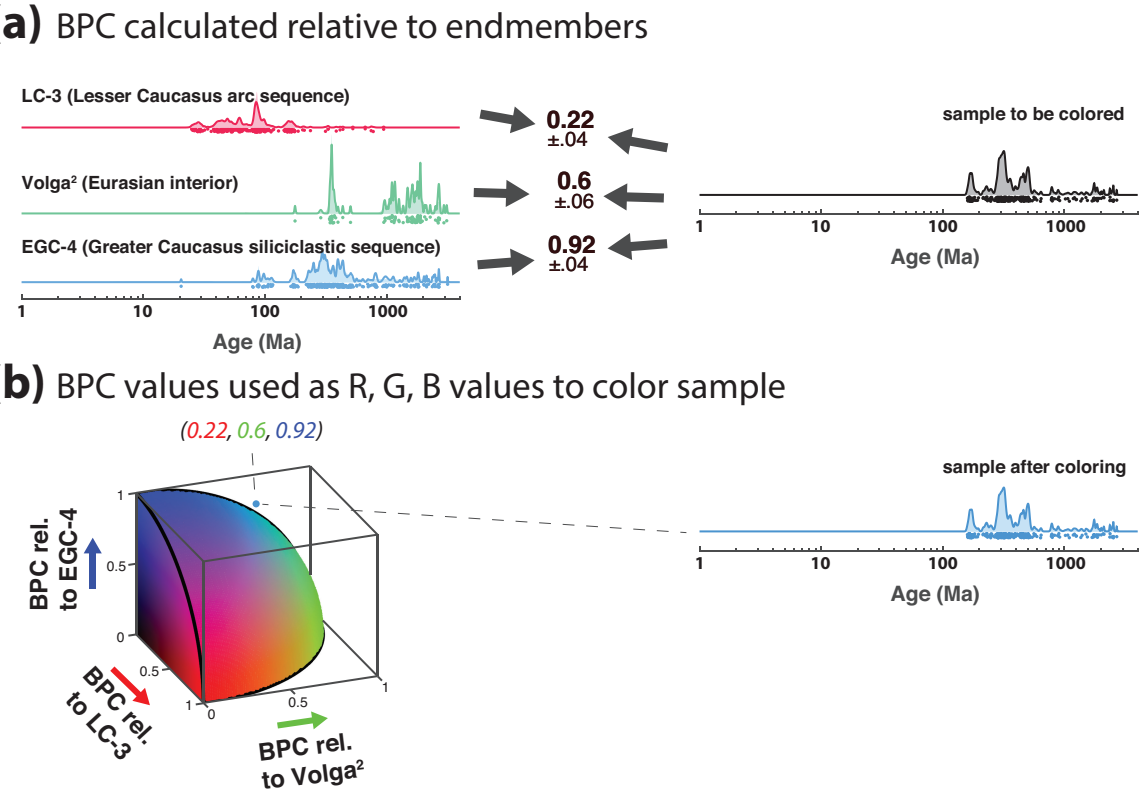

Figure 6.7: Throughout this paper, samples are colored according to their BPC value (*Tye et al.*, 2019) relative to three representative endmembers of the Eurasian interior, Greater Caucasus, and Lesser Caucasus. (a) BPC values are calculated between each sample and the three end member samples. (b) Calculated BPC values are used as R, G, B values for coloring each sample. The colored surface shown is a visual aid; samples do not need to fall on this surface.

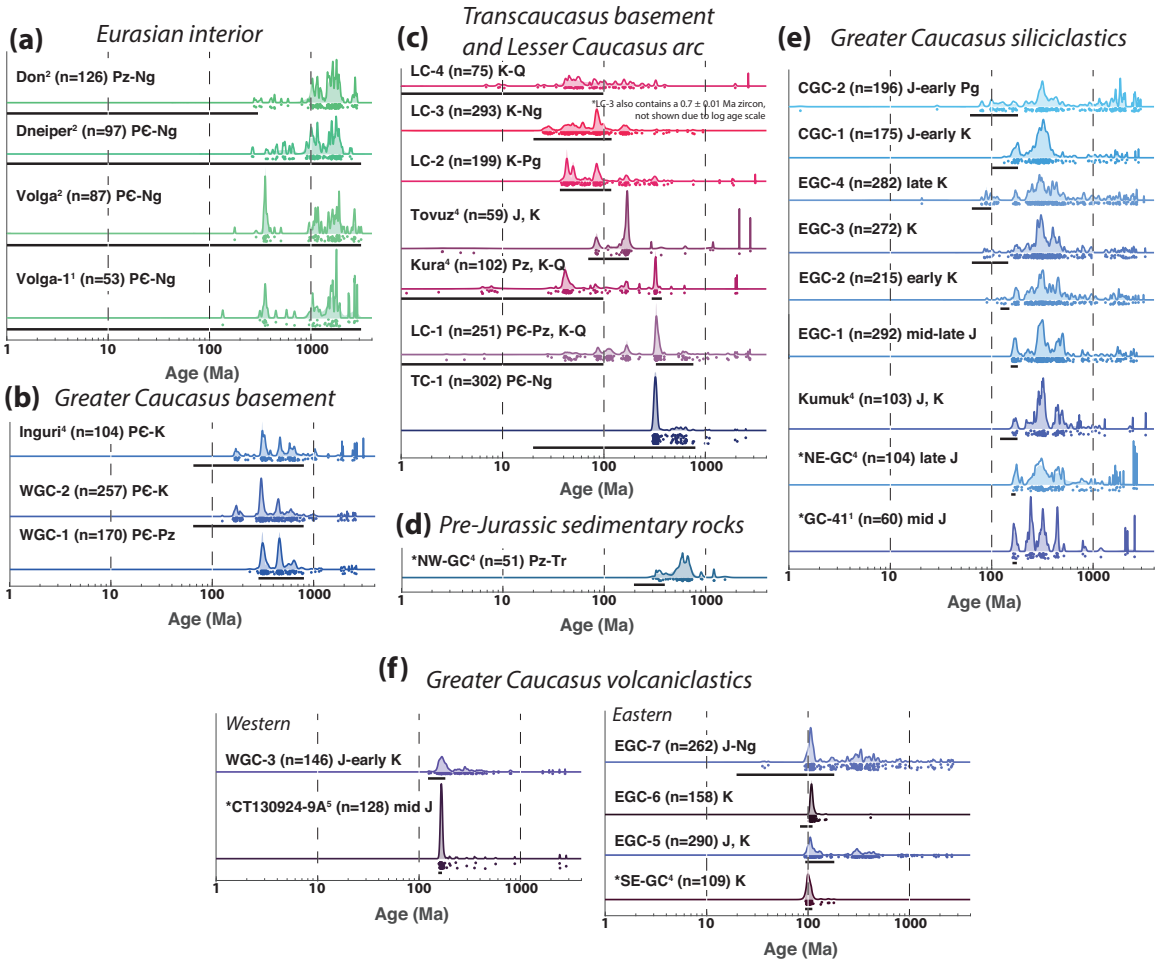

Figure 6.8: Distinct zircon age signatures are observed from (a) the Eurasian interior, (b) the Greater Caucasus basement, (c) the Transcaucasus basement and Lesser Caucasus arc sequence, (d) pre-Jurassic sedimentary rocks, (e) the Greater Caucasus siliciclastic sequence, and (f) the Greater Caucasus volcaniclastic sequence. The Greater Caucasus volcaniclastic sequence is subdivided into a western and eastern portion, with the western portion largely consisting of Jurassic strata and the eastern portion consisting largely of Cretaceous strata. Samples are colored as shown in Figure 6.7, and are arranged by region. The plot of each sample shows a probability density plot (*Hurford et al.*, 1984) as a solid line, a kernel density estimate (*Silverman*, 1986; *Shimazaki and Shinomoto*, 2010; *Vermeesch*, 2012) as a shaded area, age observations ignoring analytical uncertainty as a band of dots beneath the curves (vertical scatter for visual clarity), and a black bar that shows the age of the sample (for bedrock samples) or the ages of bedrock strata within the sampled catchment (for modern samples). Each sample is labeled with its name, sample size, and its age or the ages of strata within the sampled catchment (*Nalivkin*, 1976; *Asch et al.*, 2005). Previously published samples are marked with a superscript, corresponding to references as in Figures 6.4, 6.5. Most samples are from modern river sands, and bedrock samples are marked with an asterisk (*). Age abbreviations are as in Figure 6.5, plus: Ng–Neogene.

6.4 Source-area detrital zircon signatures

6.4.1 Detrital zircon age signatures of potential sources for Caucasus Cenozoic sediment

In order to use detrital zircon data from foreland basin deposits to understand the Cenozoic tectonic history of the Caucasus, we must first characterize the zircon age signatures of potential sediment sources of the foreland basin deposits. In this section, we discuss the zircon age distributions that distinguish seven potential sources (Fig. 6.8) that outcrop within the Caucasus and surrounding region (Figs. 6.4, 6.5). Three of these sources are regional basement domains (the Eurasian interior, the Greater Caucasus basement, and the Transcaucasus basement). One potential source is the pre-Jurassic sedimentary sequences that crop out over small areas adjacent to Greater Caucasus and Transcaucasus basement outcrops. Three sources are Jurassic to Eocene tectonostratigraphic sequences (the Lesser Caucasus arc, Greater Caucasus siliciclastic, and Greater Caucasus volcaniclastic sequences). We first discuss the basement domain sources.

Three distinct basement domain sources can be distinguished by their detrital zircon age signatures: the Eurasian interior (including the East European Craton and Urals; Fig. 6.8a), the crystalline basement exposed in the Greater Caucasus (Fig. 6.8b), and the basement massifs of the Transcaucasus (Fig. 6.8c). Modern samples from rivers that drain the Eurasian interior are composed of at least 70% zircon ages >900 Ma, which are associated with the East European craton (Fig. 6.8a; *Allen et al.*, 2006; *Bogdanova et al.*, 2008). Some samples representing the Eurasian interior also contain a subordinate peak ~360 Ma derived from the Urals (*Allen et al.*, 2006). Rivers that drain the Eurasian interior contain very few Mesozoic zircons and no Cenozoic zircons. Detritus of the Greater Caucasus basement (Fig. 6.8b) is primarily identifiable by narrow age peaks centered on 300 Ma and 450 Ma. Scattered Neoproterozoic to Middle Paleozoic ages are also present in the Greater Caucasus basement rocks, defining a broad age peak centered on 600 Ma (Fig. 6.8b). Transcaucasus basement massifs are targeted by sample TC-1 and are also included in the catchments of samples LC-1 and Kura (Figs. 6.5a; 6.8c). Pre-Mesozoic ages in these samples are dominated by a single peak at ~300 Ma (Fig. 6.8c). Samples derived from Transcaucasus basement massifs also contain scattered Neoproterozoic to Paleozoic ages that define a broad peak near 600 Ma (Fig. 6.8c). The distinguishing detrital zircon age characteristics of the three basement domain sources are that the Eurasian interior is the only source of abundant zircons >900 Ma; the Greater Caucasus basement contains large, subequal zircon age peaks at ~300 Ma and ~450 Ma; and the Transcaucasus basement

massifs contain only one major age peak, at ∼300 Ma (Table 6.1).

One potential sediment source in the Caucasus is a set of Paleozoic to Triassic, fine-grained clastic to carbonate sedimentary sequences exposed over small areas adjacent to the Greater Caucasus basement and Transcaucasus basement massifs (Figs. 6.5b, 6.8d; *Khain*, 1975; *Şengör et al.*, 1984; *Adamia et al.*, 2011a). One of these sequences is the Dizi Series, located directly south of the Greater Caucasus basement (*Khain*, 1975; *Şengör et al.*, 1984; *Adamia et al.*, 2011a). Bedrock sample NW-GC (*Cowgill et al.*, 2016) from the western Greater Caucasus (Fig. 6.5a, b), though mapped as Jurassic in age (*Nalivkin*, 1976), is thought to have been collected from the Paleozoic to Triassic Dizi Series because of its location close to the mapped contact between Jurassic strata and the Dizi Series (*Nalivkin*, 1976), the similarity of lithologies present in the Jurassic strata and Dizi Series (*Khain*, 1975; *Adamia et al.*, 2011a), and the similarity of the age signature of NW-GC to other Dizi Series detrital zircon U-Pb age data (D. Vasey, in review). The detrital zircon age signature of sample NW-GC shows a wide, primary age peak centered on 600 Ma, with a secondary peak centered on 330 Ma (Fig. 6.8d).

The age signature of NW-GC, a bedrock sample, differs markedly from modern samples that include the Dizi Series and other Paleozoic to Triassic sequences within their source catchments (see samples Inguri, WGC-2, and LC-1; Figs. 6.5, 6.8), suggesting that the signature of NW-GC is not effectively propagated through the sedimentary system. The lack of propagation of the NW-GC age signature is likely due to the fine-grained clastic and carbonate lithologies that characterize Paleozoic to Triassic sedimentary sequences on the southern slope of the Greater Caucasus and within the Transcaucasus/Lesser Caucasus (*Khain*, 1975; *Adamia et al.*, 2011a), as well as the small exposure area of these sequences compared to other potential sedimentary sources in the Caucasus. The signature of NW-GC differs from all foreland basin samples, as we later show, suggesting that these pre-Jurassic sedimentary sequences do not contribute meaningful quantities of measurable zircons to regional basins, so we disregard them as a traceable sediment source.

The final three sources we characterize are three Jurassic to Eocene tectonostratigraphic packages that outcrop over large areas in the Caucasus region (Fig. 6.5): the Lesser Caucasus arc sequence (Fig. 6.8c), Greater Caucasus siliciclastic sequence (Fig. 6.8e), and Greater Caucasus volcaniclastic sequence (Fig. 6.8f). Samples derived from the Lesser Caucasus arc sequence can be recognized by the ubiquity of zircons 90 Ma and younger (Fig. 6.8c), which are virtually absent in other potential sources. Lesser Caucasus arc sequence samples also contain an age peak centered on 170 Ma. Samples of the Greater Caucasus siliciclastic sequence (Fig. 6.8e) share two major zircon age peaks with the Greater Caucasus basement (∼300 Ma and ∼450 Ma), though in the Greater Caucasus siliciclastic

sequence these age peaks are wider than in the Greater Caucasus basement. Additional age populations present in some or all Greater Caucasus siliciclastic sequence samples include Permian to Triassic ages, either on the margin of a ∼300 Ma peak or as a separate peak; a ∼170 Ma zircon age peak; scattered Precambrian to Paleozoic ages ranging from 3 Ga to 500 Ma; and small quantities of ∼100 Ma zircons (Fig. 6.8e). The Greater Caucasus volcaniclastic sequence yields largely unimodal detrital zircon age samples, which are centered on 170 Ma in the western Greater Caucasus and 105 Ma in the eastern Greater Caucasus (Fig. 6.8f). Samples that represent the Greater Caucasus volcaniclastic sequence and that also contain appreciable quantities of other age peaks (samples WGC-3, EGC-5, EGC-7) come from catchments that include both Greater Caucasus volcaniclastic strata and Greater Caucasus siliciclastic strata. Detrital zircon age signatures of the three Jurassic to Eocene tectonostratigraphic sequences in the Caucasus can be distinguished by the fact that the Lesser Caucasus arc sequence contains plentiful zircons <90 Ma, the Greater Caucasus siliciclastic sequence contains wide age peaks centered on 300 and 450 Ma, and the Greater Caucasus volcaniclastic sequence yields unimodal zircon U-Pb age peaks at 170 and 105 Ma (Table 6.1).

The zircon age signature characteristics described above permit the discrimination of six potential sources for Caucasus foreland basin sediment (Table 6.1). These sources include the Eurasian interior, Greater Caucasus basement, Transcaucasus basement, the Lesser Caucasus arc sequence, the Greater Caucasus siliciclastic sequence, and the Greater Caucasus volcaniclastic sequences. Because these sources have distinct detrital zircon U-Pb age signatures, their contributions can be tracked in foreland basin sedimentary rock samples.

Potential source	**Diagnostic zircon age signature**
Eurasian interior	Ages >900 Ma
Greater Caucasus basement	Narrow, subequal age peaks at ∼300 Ma and ∼450 Ma
Transcaucasus basement	Narrow age peak at ∼300 Ma, no peak at ∼450 Ma
Paleozoic to Triassic sedimentary sequences*	Wide age peak 500-800 Ma, secondary peak at 330 Ma
Lesser Caucasus arc sequence	Ages <90 Ma
Greater Caucasus siliciclastic sequence	Wide age peaks centered on ∼300 Ma and ∼450 Ma

Greater Caucasus volcaniclastic sequences	Unimodal age peak at ∼170 Ma or ∼105 Ma

Table 6.1: Diagnostic detrital zircon age signatures of seven potential sources of Cenozoic foreland basin strata in the Caucasus. Note that the signature listed for pre-Jurassic sedimentary sequences (marked with an *) is only based on a single bedrock sample, but these locally outcropping sequences likely contribute very few datable zircons to the foreland basin. See text for further discussion.

6.4.2 Defining and representing detrital zircon source endmembers

In order to visually represent the source contributions to samples analyzed in this study, we employ a coloring scheme in which sample R, G, and B values are colored based on their Bayesian Population Correlation values (*Tye et al.*, 2019) when compared to three representative endmember samples (Fig. 6.7; BPC values shown in Tables S3, S4). The color scheme visually communicates the regional reach of sediment from three major crustal domains: the Eurasian interior, Greater Caucasus, and Lesser Caucasus. The Eurasian interior (associated with the color green) sits to the north of the Caucasus and Eurasian interior detritus can be identified primarily by a preponderance of zircons >900 Ma (Fig. 6.8a; Table 6.1). Endmember sample Volga (*Wang et al.*, 2011) is representative of the Eurasian interior because it includes Archaean to Proterozoic zircons from the East European Craton as well as some Paleozoic zircons from the Urals (e.g., *Allen et al.*, 2006; *Wang et al.*, 2011). The Greater Caucasus domain (associated with the color blue) contains several potential sources including basement, siliciclastic strata, and volcaniclastic strata (Fig. 6.8b, e, f; Table 6.1). Endmember sample EGC-4 was chosen to represent the Greater Caucasus because it is a large (n = 282) sample and its ages, dominated by peaks centered approximately on 300 Ma and 450 Ma, are broadly representative of the Greater Caucasus basement and Greater Caucasus siliciclastic sequence. The Lesser Caucasus domain (associated with the color red) is located to the south of the Greater Caucasus and is associated with significant quantities of zircons <90 Ma (Fig. 6.8c; Table 6.1). Endmember sample LC-3 was chosen to represent the Lesser Caucasus, which is largely composed of Jurassic to Eocene volcanic and volcaniclastic rocks (Figs. 6.2, 6.5), because it is a large (n = 293) sample that contains the greatest number of <90 Ma zircons characteristic of the Lesser Caucasus (Fig. 6.8c). The use of this coloring scheme permits the visual differentiation of Eurasian interior, Greater Caucasus, and Lesser Caucasus sources in modern samples and foreland basin sedimentary rock samples (Figs. 6.5, 6.8, 6.9).

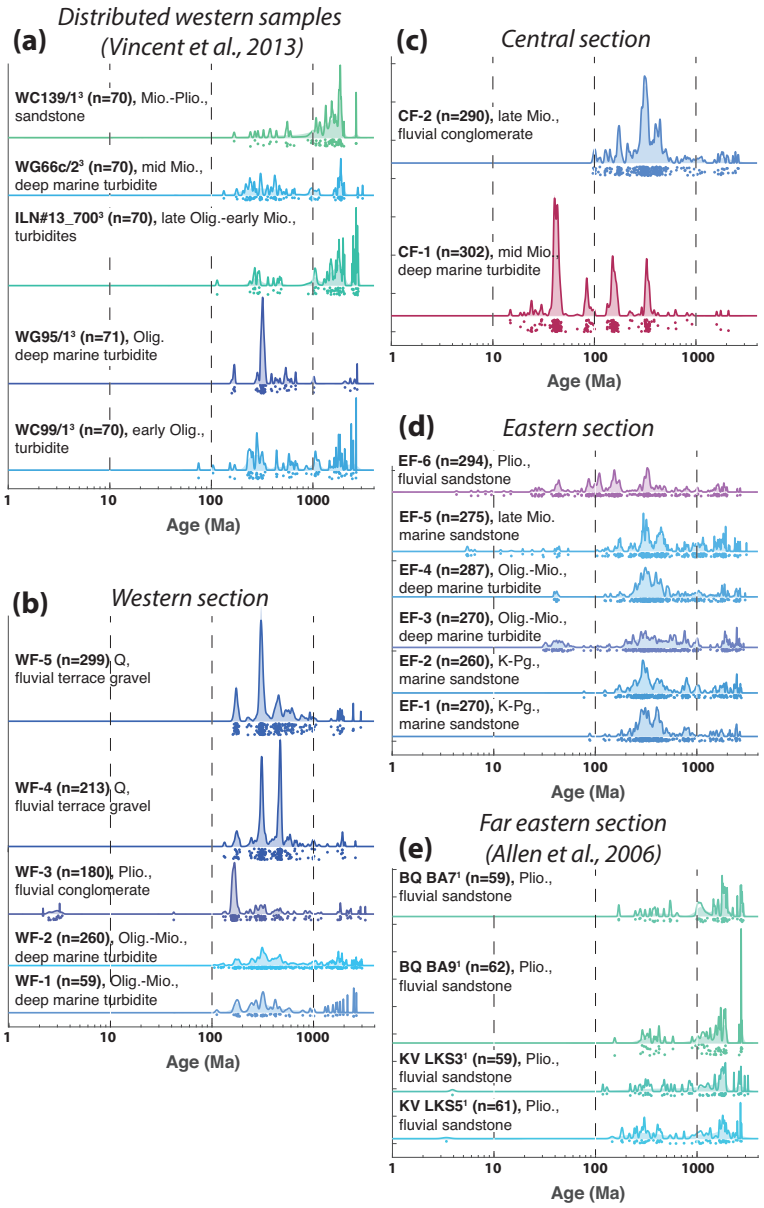

Figure 6.9: Detrital zircon age spectra of foreland basin sedimentary rocks reflect Cenozoic provenance variation over space and time. Previously published samples from distributed locations in the western Greater Caucasus are shown (a; *Vincent et al.*, 2013). New samples were collected from western (b), central (c), and eastern (d) foreland basin sections. Previously published samples from a Pliocene section at the far eastern extent of the range are also reported (e; *Allen et al.*, 2006). Spectra are shown in reverse stratigraphic order in each panel. Symbology is the same as Figure 6.8. Sample ages and rock types are listed, and are shown visually in Figure 6.10. Abbreviations are as in Figure 6.8, plus: Olig.–Oligocene, Mio.–Miocene, Plio.–Pliocene, Pleis.–Pleistocene.

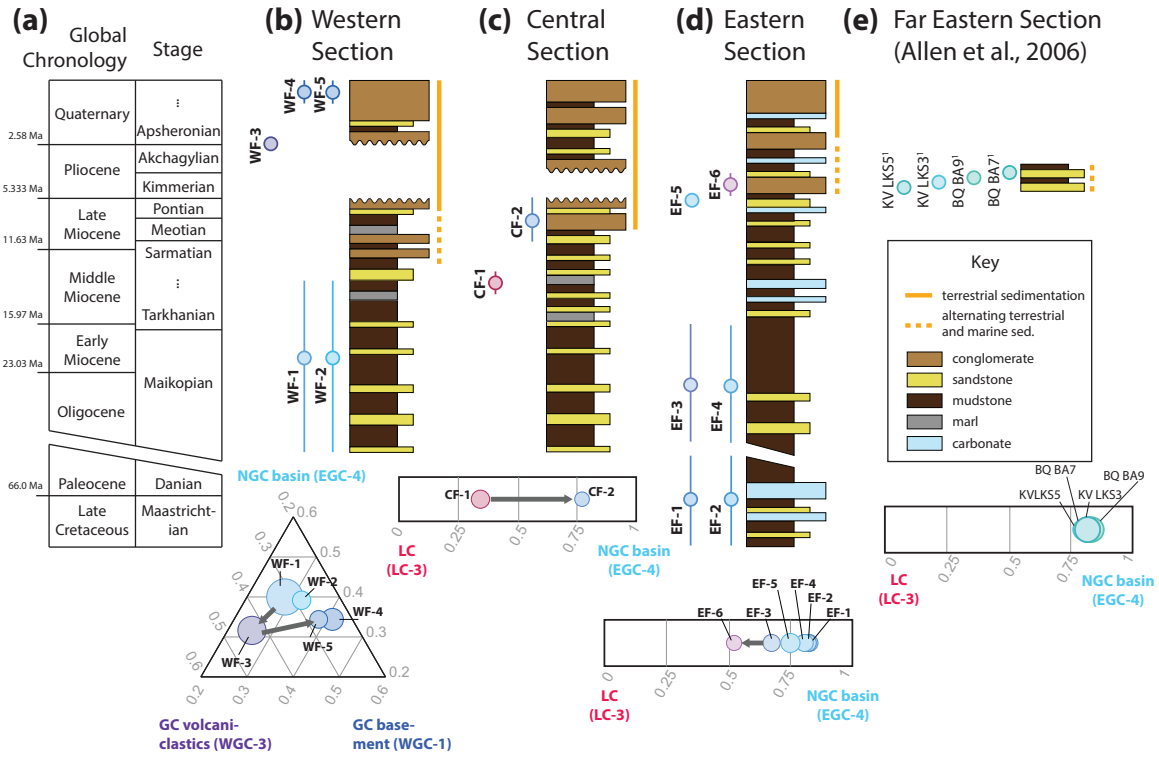

Figure 6.10: Foreland basin samples are shown in stratigraphic context. (a) Global chronology with stratigraphic stage names (Paratethyan stage names are used for the Neogene; *Jones and Simmons*, 1998). (b-e) Western, central, eastern, and far eastern sampled foreland basin sections. Sample ages are depicted with symbols next to each stratigraphic column, with error bars representing the range of possible ages. Symbols are colored using the coloring scheme used throughout this paper (Fig. 6.7). Beneath each section is a plot of normalized BPC of the samples relative to potential sources for the section (source sample numbers shown in parentheses), with arrows indicating trends over time (see Tables S3, S4 for BPC results). Plot symbol size is mean BPC uncertainty (1σ) with respect to the endmember samples, and symbols for the Central and Eastern sections have been doubled in size for visual clarity. Schematic stratigraphy, including interpretation of marine versus terrestrial sedimentation, is compiled from *Edilashvili* (1957); *Dzhanelidze and Kandelaki* (1957); *Gamkrelidze and Kakhazdze* (1959); *Voronin et al.* (1959); *Khain and Shardanov* (1960); *Mekhtiev et al.* (1962); *Hinds et al.* (2004); *Vincent et al.* (2014). Blank space in sections marks missing time due to unconformities. Unconformities without significant missing time are not shown. The distributed western samples of *Vincent et al.* (2013) are not depicted stratigraphically because they are from a variety of locations with variable stratigraphy.

6.5 Foreland basin zircon U-Pb characteristics and provenance interpretation

We use detrital zircon U-Pb age distributions from foreland basin stratigraphic sections, in combination with the source signatures outlined above, to infer the sources of foreland basin sediment and changes in provenance over time. Here, we describe the zircon age distributions of new and previously published samples from foreland basin sedimentary strata deposited during the Cenozoic in the basin between the Greater and Lesser Caucasus (Fig. 6.9). In describing these age distributions, we discuss sample lithologies (Fig. 6.6 shows photos of selected sampled lithologies) and the stratigraphic context of samples (Fig. 6.10). We also compare foreland basin zircon age signatures with the sources discussed above and published datasets in order to discuss the implications for source exposure and sediment routing systems. In following sections, we discuss the tectonic implications of the sediment routing systems and sources implied by our data. New foreland samples were collected from three stratigraphic sections (western, central, and eastern) and were deposited in Paleogene to Quaternary time (Figs. 6.5, 6.9). We also discuss published samples from a Pliocene section at the far eastern extent of the range (*Allen et al.*, 2006), as well as a set of previously published samples that were collected over a wide area of the western Greater Caucasus (*Vincent et al.*, 2013). Age constraints for our samples are based on published geologic mapping (*Edilashvili*, 1957; *Dzhanelidze and Kandelaki*, 1957; *Gamkrelidze and Kakhazdze*, 1959; *Voronin et al.*, 1959; *Khain and Shardanov*, 1960; *Mekhtiev et al.*, 1962; *Nalivkin*, 1976) unless otherwise noted, and published age constraints are used for previously published samples. The zircon age distributions are discussed roughly in order from west to east, beginning with the previously published distributed samples in the western portion of the range (*Vincent et al.*, 2013) and proceeding with our new western, central, and eastern sampled sections, followed by the published far eastern section (*Allen et al.*, 2006, Fig. 6.9).

6.5.1 Distributed foreland basin samples of the western Greater Caucasus

Previously published distributed Cenozoic samples from the western Greater Caucasus include five samples from early Oligocene to latest Miocene/earliest Pliocene time (Fig. 6.9a; *Vincent et al.*, 2013). This group of five samples includes two samples that lie to the northwest of the range (samples ILN#13_700 and WC139/1; Fig. 6.4), and three samples located on the southern margin of the range (samples WC99/1, WG66c/2, and WG95/1; Figs. 6.4,

6.5). The two samples northwest of the Greater Caucasus, late Oligocene to early Miocene sample ILN#13_700 and Miocene to Pliocene sample WC139/1, are composed mostly of zircons >900 Ma (Fig. 6.9a) with some scattered Neoproterozoic and Paleozoic ages. Overall these two samples show a clear affinity to the Eurasian interior (Fig. 6.8a). Early Oligocene sample WC99/1, an Oligocene turbidite sample from the south side of the westernmost Greater Caucasus, contains ∼40% zircons >900 Ma, as well as a 230-360 Ma age peak (Fig. 6.8a). This sample shows a partial affinity to the Eurasian interior, with the 230-360 Ma age peak suggesting a partial affinity to the Greater Caucasus siliciclastic sequence. Middle Miocene turbidite sample WG66c/2 was collected from near our western section (Fig. 6.5b), and contains scattered Paleozoic to Triassic ages that coalesce around two broad age peaks at 450 and 300 Ma, as well as ∼35% ages >900 Ma (Fig. 6.8a). These ages indicate that WG66c/2 was likely derived predominantly from the Greater Caucasus siliciclastic sequence. Sample WG95/1 was collected from an Oligocene turbidite in close proximity to the Dzirula Massif (Fig. 6.5a), a Transcaucasus basement massif, and has a detrital zircon age distribution dominated by a narrow ∼300 Ma age peak (Fig. 6.9a) that closely matches that of modern detritus from the Dzirula Massif (sample TC-1, Fig. 6.8b).

The spatial distribution of source affinities within these samples has implications for the late Cenozoic depositional system of the Caucasus. The fact that samples on the northern slope and near the western margin of the Greater Caucasus (ILN#13_700 and WC139/1; Fig. 6.9a) have a close affinity to samples of the Eurasian interior (Fig. 6.8a) suggests that detritus from the Eurasian interior was deposited to the north of the Greater Caucasus and also to the south of the westernmost portion of the range (Fig. 6.4). In contrast, the detrital zircon age distribution of sample WG66c/2 (Fig. 6.9a) shows a near perfect resemblance to the Greater Caucasus siliciclastic sequence (Fig. 6.8e), suggesting that at the longitude at which it was deposited, sediment was sourced primarily from the Greater Caucasus (Fig. 6.5b). Sample WC99/1 (Fig. 6.9a), deposited on the southern slope of the Greater Caucasus at an intermediate longitude between WC139/1 and WG66c/2 (Fig. 6.4) shows a hybrid detrital zircon age signature suggesting mixing of the Eurasian interior and Greater Caucasus siliciclastic sequence sources. Together, these samples define a spatial mixing trend where the Eurasian interior is the dominant detrital zircon source affinity of Neogene sediment on the north side of the Greater Caucasus and in the far western portion of the basin to the south of the Greater Caucasus, whereas the Greater Caucasus siliciclastic sequence is the dominant source affinity of Neogene deposits on the southern margin of the central to western Greater Caucasus (Figs. 6.4, 6.5).

The spatial distribution of affinities to the Eurasian interior and Greater Caucasus siliciclastic sequence mirrors the distribution of quartzose and lithic-rich sandstones in Oligocene

to Pliocene deposits on the northeastern margin of the Black Sea (*Vincent et al.*, 2013, 2014). Quartzose sand is observed in Neogene sedimentary rocks to the north of the Greater Caucasus and in the far western portion of Neogene sedimentary rocks on the south side of the range (west of 40° E; *Vincent et al.*, 2013, 2014). The distribution of quartzose sand corresponds spatially with detrital zircon age signatures of Eurasian affinity (Fig. 6.4; samples ILN#13_700 and WC139/1 in Fig. 6.9a). In contrast, lithic-rich sand is observed in Neogene sedimentary rocks from the western Greater Caucasus (east of 40° E; *Vincent et al.*, 2013, 2014), in the same region where Oligocene to Miocene sandstones reveal a detrital zircon age signature similar to the Greater Caucasus siliciclastic sequence (Fig. 6.4; samples WC99/1 and WG66c/2 in Fig. 6.9a). The correspondence of quartzose Neogene sandstones with zircons of Eurasian affinity and of lithic-rich Neogene sandstones with zircons of Greater Caucasus siliciclastic affinity suggest that quartzose Neogene sandstones may be derived from the Eurasian interior and lithic-rich sandstones may largely be derived from the Greater Caucasus siliciclastic sequence.

6.5.2 Western foreland basin section

Our western foreland basin section contains five samples spanning Oligocene to Quaternary age (Fig. 6.9b) that were collected from a ∼2.3 km thick stratigraphic section exposed along the Chanistskali River near Jvari, Georgia (Fig. 6.5b; *Dzhanelidze and Kandelaki*, 1957). Within the section, sedimentation is largely turbiditic in nature from the Oligocene to the Middle Miocene (*Dzhanelidze and Kandelaki*, 1957). From the latest Miocene through the Quaternary, sedimentation is largely terrestrial and conglomeratic, with a period of erosion or non-deposition during the latest Miocene to Pliocene (Fig. 6.10b; *Dzhanelidze and Kandelaki*, 1957; *Vincent et al.*, 2014). The two oldest samples from the section, WF-1 and WF-2, were collected from Oligocene or Miocene turbidites (Fig. 6.6a shows sample location of WF-2) and show dispersed Proterozoic to Triassic ages with wide peaks centered on 450 Ma and 300 Ma (Fig. 6.9b) and ∼25% of ages >900 Ma. WF-1 and WF-2 have a zircon age peak at 170 Ma, as well. These two samples show an almost perfect resemblance to samples of the Greater Caucasus siliciclastic sequence (Fig. 6.8e). The three youngest samples collected from the section, samples WF-3, WF-4, and WF-5, were collected from latest Pliocene to Quaternary fluvial conglomerates (Fig. 6.6b shows sample location of WF-3). Sample WF-3 is dominated by a 170 Ma peak, along with small, wide peaks at ∼300 Ma and ∼450 Ma (Fig. 6.9b). In the dominance of the 170 Ma age peak, sample WF-3 shows a close similarity to the zircon age signature of the western portion of the Greater Caucasus volcaniclastic sequence (samples CT130924-9A,

WGC-3 in Fig. 6.8f). Sample WF-3 also shows a concentration of zircon ages between 3.0 and 2.5 Ma, which likely originate from the eruption of the Chegem caldera in the northern Greater Caucasus at ∼2.8 Ma (*Lipman et al.*, 1993). Samples WF-4 and WF-5 have tightly clustered ∼300 Ma and ∼450 Ma age peaks, and have 7-8% zircons >900 Ma, significantly fewer than stratigraphically lower samples WF-1 and WF-2 (Fig. 6.9b). The tight clustering of the ∼300 Ma and ∼450 Ma age peaks and smaller proportion of ages >900 Ma in samples WF-4 and WF-5 differentiate these samples from WF-1 and WF-2, and suggest that WF-4 and WF-5 have an affinity to the Greater Caucasus basement, rather than to the Greater Caucasus siliciclastic sequence.

The three sources most similar to the age spectra observed in the western section are the Greater Caucasus siliciclastic sequence (Fig. 6.8e), Greater Caucasus volcaniclastic sequence (Fig. 6.8f), and the Greater Caucasus basement (Fig. 6.8b), all of which are located to the north of the section, so the observed provenance changes likely reflect changing exposure within the sediment source area. Therefore, we regard the provenance changes in the western section as recording the exposure of the volcaniclastic strata and the basement of the Greater Caucasus as a result of progressive deformation, unroofing, and erosion of the range. The age of first exposure of the Greater Caucasus volcaniclastic strata is uncertain, but is bracketed by Middle Miocene sample WG66c/2 (*Vincent et al.*, 2013), which is located near our sampled section and which shows no evidence of derivation from the volcaniclastic strata, and late Pliocene sample WF-3, which is dominated by ∼170 Ma ages. Samples WF-4 and WF-5 record initial exposure of the Greater Caucasus basement during the latest Pliocene to Quaternary. Combining the detrital zircon age data with stratigraphic interpretations (Fig. 6.10b; *Dzhanelidze and Kandelaki*, 1957; *Gamkrelidze and Kakhazdze*, 1959; *Vincent et al.*, 2014) reveals that the initial exposure of basement, and potentially the initial exposure of the Greater Caucasus volcaniclastic strata, followed the transition to terrestrial sedimentation within the western Caucasus. In addition, derivation of sediment from the Greater Caucasus basement accompanied the re-establishment of deposition after a period of erosion or non-deposition (Fig. 6.10b).

A published analysis of recycled palynomorphs sampled from the same section also constrains the unroofing history of the western Greater Caucasus (*Vincent et al.*, 2014). Successively older palynomorphs are found stratigraphically higher in the section, which suggests the exhumation of progressively deeper strata over time in the source area (*Vincent et al.*, 2014). In Early Oligocene strata, the oldest palynomorphs observed are of Eocene age. Beginning in the Late Oligocene, palynomorph assemblages imply source ages as old as Early Cretaceous, with a significant portion of Eocene palynomorphs also present. In Early Miocene strata, the prevalence of Eocene palynomorphs decreases and recycled paly-

nomorphs transition to predominantly Cretaceous age. A small number of palynomorphs in Early Miocene strata imply Middle Jurassic source ages (*Vincent et al.*, 2014). Though no samples younger than Early Miocene were analyzed (*Vincent et al.*, 2014), the exhumation history implied by these samples is consistent with exposure of basement in the Pliocene to Quaternary.

6.5.3 Central foreland basin section

Our central foreland basin section contains two samples of Middle and Late Miocene age, collected from a 5 - 8 km thick Oligocene to Quaternary succession 30 km northeast of Tbilisi, Georgia (Fig. 6.5a; *Edilashvili*, 1957). In the sampled section, terrestrial emergence and a transition from turbiditic to largely conglomeratic deposits occurred in the Late Miocene (Fig. 6.10c; *Edilashvili*, 1957). Sample CF-1 was taken from a Middle Miocene turbidite (Fig. 6.6c). CF-1 contains zircon ages $<$90 Ma and age peaks centered on 300 Ma and 170 Ma (Fig. 6.9c), a very similar age distribution to modern samples of the Lesser Caucasus (Fig. 6.8b). Sample CF-1 also contains two $\sim$15 Ma zircons, which constrain its depositional age. A depositional age of $\sim$15 Ma is broadly consistent with previously reported biostratigraphic age constraints for the sampled strata (*Nalivkin*, 1976). Upsection, Late Miocene fluvial conglomerate sample CF-2 (Fig. 6.6d) has dispersed Proterozoic to Mesozoic zircon ages with wide peaks centered on 450-400, 300, and 170 Ma (Fig. 6.9c), indicating a close similarity to samples of the Greater Caucasus siliciclastic sequence (Fig. 6.8e).

The transition of sediment source from the Lesser Caucasus to the Greater Caucasus observed in the central foreland basin section is most simply explained by northward translation of the section toward the Greater Caucasus on the lower plate of the Greater Caucasus subduction system. At the outcrop from which CF-1 was collected, folding within isolated strata between undeformed stratigraphic packages suggests that syn-sedimentary slumping occurred (Fig. 6.6c), likely on a paleoslope. Given the Lesser Caucasus provenance of CF-1 (Fig. 6.9c) and the shale-rich lithology and syn-sedimentary deformation of the outcrop from which it was collected, CF-1 was likely deposited on the distal continental margin of the Lesser Caucasus. The transition from Lesser to Greater Caucasus provenance, which occurred sometime in the Middle to Late Miocene, was roughly coeval with the transition of the section to terrestrial, largely conglomeratic deposits in the Late Miocene (Fig. 6.10c). The central section also contains a Pliocene hiatus of similar timing and duration to that observed in the western section (Fig. 6.10).

6.5.4 Eastern foreland basin section

Samples from the eastern section (Fig. 6.9d, 6.10d) span almost the entire Cenozoic, from the latest Cretaceous or Paleocene until the Pliocene, and were collected from a 6 - 8 km thick composite section (Fig. 6.5c; *Khain and Shardanov*, 1960). Within this section, a transition to largely terrestrial, conglomeratic sedimentation occurred in the latest Miocene to earliest Pliocene (*Khain and Shardanov*, 1960). Most samples of the section (EF-2 through EF-6) were collected near Lahij and Shamakhi, Azerbaijan. Late Cretaceous to early Paleocene sample EF-1 was collected from the north side of the Greater Caucasus, near the village of Afurgha, Azerbaijan, though it was deposited prior to shortening and topographic development in the Greater Caucasus (which began in the late Eocene to Oligocene; *Vincent et al.*, 2007; *Adamia et al.*, 2011b), and is thus inferred to have been deposited in the same basin as samples EF-2 through EF-6. Samples EF-1 to EF-5 were collected from turbiditic to shallow marine sandstones of Late Cretaceous/Paleocene through Late Miocene age (Fig. 6.6e shows turbiditic strata sampled for EF-4). Samples EF-1 through EF-5 reveal a stable detrital zircon age signature featuring dispersed Proterozoic to Triassic ages, typically with peaks centered on 400-450 Ma and 300 Ma (Fig. 6.9d). Age peaks centered on 170 Ma are sometimes present, and Oligocene to late Miocene samples in this section also show some ages from 60 to 30 Ma. Overall, samples EF-1 to EF-5 show a strong similarity to modern samples of the Greater Caucasus siliciclastic sequence (Fig. 6.8e). The Cenozoic grains in samples EF-3, EF-4, and EF-5 are likely to have originated in Cenozoic volcanic centers of the Lesser Caucasus and neighboring Talysh mountain ranges (*Allen and Armstrong*, 2008; *Verdel et al.*, 2011; *van Der Boon et al.*, 2017). These Cenozoic zircons could have been transported by turbidity currents and mixed with Greater Caucasus-derived sediment within the basin, or they could have been deposited in the basin as volcanic airfall and subsequently reworked. We tentatively favor the latter interpretation because samples EF-3, EF-4, and EF-5 lack the major Jurassic and Cretaceous age peaks that characterize modern and foreland-basin samples derived from the Lesser Caucasus (samples LC-1 to LC-4, Fig. 6.8c; CF-1, Fig. 6.9c). Together, samples EF-1 to EF-5 indicate derivation from the Greater Caucasus siliciclastic sequence from the Late Cretaceous or Paleocene until the Late Miocene.

In contrast to samples EF-1 to EF-5, Pliocene sample EF-6 (Fig. 6.6f; from the Productive Series sandstone, interpreted to be fluviolacustrine by *Hinds et al.*, 2004) shows scattered Proterozoic to Cenozoic zircon ages with peaks centered on $\sim$300 Ma, 160 Ma, 105 Ma, and 85 Ma, with many additional ages $<$85 Ma (Fig. 6.9d). The distribution of zircon ages in EF-6 contains several peaks that indicate similarity to the Lesser Caucasus arc sequence (Fig. 6.8c). However, EF-6 also contains a number of Precambrian zircons

and a wide ∼450 Ma age peak, indicating affinity to both the Greater Caucasus siliciclastic sequence (Fig. 6.8e) and the Lesser Caucasus arc sequence (Fig. 6.8c).

The fluvio-lacustrine depositional environment of sample EF-6 and its shared affinity to the Greater Caucasus siliciclastic and Lesser Caucasus arc sequences requires fluvial mixing of detritus of the two sources, which has implications for the evolution of the foreland basin drainage network. Range-perpendicular drainage networks, which likely dominated the pre-collisional depositional systems of the Greater Caucasus and Lesser Caucasus (Fig. 6.1a-c) would only transport detritus of either the Lesser Caucasus or the Greater Caucasus. All foreland basin samples in this study except EF-6 show detrital zircon age signatures suggesting derivation from either the Lesser Caucasus or the Greater Caucasus/Eurasia, consistent with deposition in range-perpendicular drainage networks (Fig. 6.9). On the other hand, an axial drainage network in the basin between the Greater and Lesser Caucasus would contain sediments from both Greater and Lesser Caucasus sources within its catchment area (Fig. 6.1d), providing a mechanism for fluvial mixing of the sources in sample EF-6. Thus, we interpret the mixing of Greater and Lesser Caucasus sources in sample EF-6 as evidence of the establishment of an axial drainage network between the Greater and Lesser Caucasus in latest Miocene to earliest Pliocene time. The existence of an axial drainage network in the Pliocene is also implied by the non-deposition or erosion occurring in the western and central foreland basin sections at this time (Fig. 6.10b-d), which requires sediment transport away from the western and central portions of the foreland basin. Because of the confinement of the foreland basin between the Greater and Lesser Caucasus mountain belts, sediment transported away from the western and central portions of the foreland basin must have been transported along strike in an axial drainage network. The existence of such an axial drainage at this time has been previously hypothesized (e.g., *Kroonenberg et al.*, 2005), and such a drainage configuration is similar to the modern Kura River (shown in Fig. 6.5a). The establishment of an axial drainage network within the foreland basin indicates that at the longitude where the Greater and Lesser Caucasus were closest to one another, the foreland basin became unable to accommodate the total flux of sediment from the two mountain belts during the latest Miocene to earliest Pliocene, at which point along-strike sediment transport within the foreland basin began.

6.5.5 Far eastern foreland basin section

The far eastern section consists of previously published samples from the Pliocene Productive Series sandstones on the Apsheron Peninsula in easternmost Azerbaijan (Figs. 6.4, 6.9e, 6.10e; *Allen et al.*, 2006). This section covers a smaller range of geologic time than the

western, central, and eastern sections discussed above (Fig. 6.10). These samples show a virtually constant detrital zircon age signature through time that features a majority of ages >900 Ma, with scattered Neoproterozoic to Mesozoic ages that coalesce around ∼300 Ma and 400-450 Ma age peaks in some samples (Fig. 6.9e). A subsequent detrital zircon study with greater sampling resolution of this section revealed similar age signatures (*Abdullayev et al.*, 2018). The concentration of zircons >900 Ma in these samples indicates affinity to the age signatures of the Eurasian interior (Fig. 6.8a), with the wide ∼300 Ma and 400-450 Ma age peaks of some samples suggesting affinity to the Greater Caucasus siliciclastic strata (Fig. 6.8e), as well.

6.6 Tectonic context of observed zircon crystallization ages

The detrital zircon U-Pb ages observed in our samples reflect the crystallization history of the Caucasus and surrounding regions. Here, we discuss the probable regional sources of observed zircon ages, roughly in order from youngest to oldest.

6.6.1 Cenozoic zircon crystallization

Cenozoic zircon ages are found primarily in samples derived from the Lesser Caucasus (Fig. 6.8c), and they are also present in small quantities in several samples that otherwise appear to be derived from Greater Caucasus sources (samples WF-3, EF-3, EF-4, EF-5; Fig. 6.9). The Lesser Caucasus was the site of a Mesozoic to Eocene arc, as well as subsequent volcanism that spanned the Oligocene to Quaternary (*Nalivkin*, 1976; *Dilek et al.*, 2010; *Adamia et al.*, 2011a; *Sahakyan et al.*, 2017). The western Greater Caucasus hosts Pliocene to Quaternary volcanic centers (*Lipman et al.*, 1993), and small, poorly studied intrusions of pre-Pliocene age have also been mapped (*Nalivkin*, 1976). Given the close age correspondence between late Cenozoic zircons in sample WF-3 (Fig. 6.9b) and the eruption of Chegem caldera in the western Greater Caucasus (2.8 Ma; *Lipman et al.*, 1993), Chegem is a likely source for the young detrital zircons of WF-3. No Cenozoic volcanic centers are known in the eastern Greater Caucasus, so we attribute Cenozoic zircons in eastern foreland-basin samples EF-3, EF-4, and EF-5 (Fig. 6.9d) to volcanic airfall from the Lesser Caucasus and neighboring Talysh.

6.6.2 Permian to Mesozoic zircon crystallization

Cretaceous zircons are found in samples from the Lesser Caucasus (Fig. 6.8c), the Greater Caucasus siliciclastic sequence (Fig. 6.8e), and the Greater Caucasus volcaniclastic se-

quence (Fig. 6.8f). In the Lesser Caucasus arc sequence (Fig. 6.8c), Cretaceous zircons are common and likely were crystallized during Mesozoic arc volcanism (e.g., *Sosson et al.*, 2010; *Adamia et al.*, 2011a; *Rolland et al.*, 2011). In the Greater Caucasus siliciclastic sequence (Fig. 6.8e), Cretaceous zircons are likely derived by volcanic airfall from the Lesser Caucasus, which is the nearest known center of Cretaceous volcanism (e.g., *Sosson et al.*, 2010; *Rolland et al.*, 2011). Cretaceous zircons dominate the eastern Greater Caucasus volcaniclastic sequence (Fig. 6.8f), which is Cretaceous in age (*Nalivkin*, 1976; *Kopp*, 1985), defining a single narrow detrital zircon age peak at 105 Ma (Fig. 6.8f).

Jurassic zircons are observed in appreciable quantities in samples of the Lesser Caucasus arc sequence (Fig. 6.8c), the Greater Caucasus siliciclastic sequence (Fig. 6.8e), and the Greater Caucasus volcaniclastic sequence (Fig. 6.8f). Jurassic intrusive rocks have been recognized in all three sequences (*Nalivkin*, 1976; *Hess et al.*, 1995). The Jurassic marked the initiation of arc volcanism in the Lesser Caucasus and the initial rifting of the Greater Caucasus Basin (*Zonenshain and Le Pichon*, 1986; *Sosson et al.*, 2010; *Vincent et al.*, 2016), so it is unsurprising that Jurassic zircons were generated in association with these settings and are common throughout the region. Because Jurassic zircons are ubiquitous in Jurassic and younger sedimentary sequences throughout the Caucasus, they are not useful for differentiating between potential sediment sources.

Permian to Triassic zircons are observed in significant quantity only in the Greater Caucasus siliciclastic sequence (Fig. 6.8d) and foreland basin sediments inferred to be sourced from it. Such Permian to Triassic grains are likely derived from Permian and Triassic volcanic and volcaniclastic rocks that overlie the Greater Caucasus basement on the northern slope of the range (*Belov*, 1981; *Nazarevich et al.*, 1986).

6.6.3 Precambrian to Carboniferous zircon crystallization

Pre-Permian zircon ages in the Caucasus reflect the crystallization history of regional basement domains. A ~300-360 Ma age peak is ubiquitous in the Greater Caucasus basement (Fig. 6.8b), Transcaucasus basement massifs (Fig. 6.8c), and the Greater Caucasus siliciclastic sequence (Fig. 6.8e), as well as younger sedimentary strata derived from these sources (Figs. 6.9). This age peak reflects crystallization during the Variscan orogeny, which was a period of intense magmatism and high temperature - low pressure metamorphism in the Caucasus region (e.g., *Belov et al.*, 1978; *Somin*, 2011). The Greater Caucasus basement and Greater Caucasus siliciclastic sequence also contain a ~450 Ma age peak, typically in subequal proportion to the ~300 Ma age peak (Fig. 6.8b, e). In our samples from modern rivers that drain the Greater Caucasus basement, this ~450 Ma age peak

is likely sourced from pre-Carboniferous metamorphic complexes that constitute part of the Greater Caucasus basement (*Somin*, 2011). The presence of 300-360 and 450 Ma age peaks in samples of the Greater Caucasus siliciclastic sequence (Fig. 6.8e) indicates that the source region of this sequence may have undergone a history of metamorphism and magmatism similar to that of the Greater Caucasus basement. 600-900 Ma zircons are observed in minor proportions in many samples of Greater Caucasus basement (Fig. 6.8b), Transcaucasus basement massifs (Fig. 6.8c), and Greater Caucasus siliciclastic sequence (Fig. 6.8e). The ages of these zircons suggest an affinity to the Pan-African orogeny, which occurred on Gondwana (e.g., *Johnson and Woldehaimanot*, 2003; *Horton et al.*, 2008). Pre-900 Ma zircons are present in our study mostly in the modern detritus of the Eurasian interior as well as sedimentary strata likely derived in part from the Eurasian interior. Zircons of this age are associated with the East European Craton (*Allen et al.*, 2006; *Bogdanova et al.*, 2008).

6.7 Implications of Caucasus detrital zircon U-Pb age data for terrane boundaries and Tethyan tectonics

Sutures formed between two colliding terranes are planes or zones of weakness that deform more easily than intact lithosphere and therefore may influence the spatial distribution of subsequent tectonic strain (*Jones and Tanner*, 1995; *Rusmore et al.*, 2001; *Fitzgerald et al.*, 2014). The southern margin of Eurasia is composed of accreted terranes that are involved in collision throughout the Alpine-Himalayan system (*Şengör*, 1984; *Stampfli et al.*, 2013). These terranes were emplaced during multiple episodes of ribbon continent or superterrane rifting from Gondwana and accretion to the southern margin of Eurasia throughout the Phanerozoic, concomitant with the formation and subduction of Neotethys, Paleotethys, and one or more precursor oceans (*Şengör*, 1984; *Stampfli et al.*, 2013). These terranes and sutures of these subducted oceans should be present on the southern margin of Eurasia.

At the longitude of the Caucasus, the number and location of terrane boundaries along the southern Eurasian margin remain uncertain. A Paleozoic suture has been proposed between Scythia and the East European Craton (*Natal'in and Şengör*, 2005, Fig. 6.2), though available evidence is also consistent with the hypothesis that Scythia is the extended margin of the East European Craton, and thus would not be separated from the craton by a suture (*Saintot et al.*, 2006a). Several authors have identified an ophiolite emplaced during the Carboniferous at the northern margin of the Greater Caucasus basement (*Adamia et al.*, 1981; *Somin*, 2011), suggesting a suture between the Greater Caucasus and Scythia.

However, *Natal'in and Şengör* (2005) argue that the Greater Caucasus basement is part of Scythia and that the present location of the ophiolite between the Greater Caucasus basement and the rest of Scythia is due to Triassic strike-slip fault displacement. Several reconstructions place a suture between the Greater Caucasus and Transcaucasus basement domains (*Şengör*, 1984; *Stampfli*, 2013), although other authors have noted petrologic and age similarities between the Transcaucasus basement and Greater Caucasus basement (e.g., *Zakariadze et al.*, 2007; *Mayringer et al.*, 2011). South of the Transcaucasus, terrane boundary locations are less ambiguous because of the presence of ophiolites along the Sevan-Akera suture zone (e.g., *Khain*, 1975; *Galoyan et al.*, 2009) and the Bitlis-Zagros suture zone (e.g., *Sengör and Yilmaz*, 1981).

Our detrital zircon age data constrain the timing and approximate magnitude of magmatic and metamorphic episodes affecting basement domains of the East European Craton, Scythia, the Greater Caucasus, and the Transcaucasus, which should add evidence for or against proposed sutures between these domains. Our modern samples directly characterize the crystallization histories of the Greater Caucasus basement (Fig. 6.8b) and Transcaucasus basement (Fig. 6.8c), and published samples reflect the crystallization history of the Eurasian interior (*Allen et al.*, 2006; *Wang et al.*, 2011, Fig. 6.8a). Sedimentary architecture (*Sholpo*, 1978) and field observations (*Vincent et al.*, 2013) indicate that the Greater Caucasus siliciclastic sequence was derived from the north, suggesting that our samples from this sequence (Fig. 6.8e) constrain the crystallization history of the Eurasian interior and/or Scythia. Unlike the Eurasian interior, detrital zircon age signatures from the Greater Caucasus siliciclastic sequence contain a majority of ages $<$900 Ma, typically with peaks at 300 Ma and 450 Ma (Fig. 6.8e). Because zircons of age $<$900 Ma are comparatively rare in samples of the Eurasian interior and do not cluster in clear age peaks at 300 Ma and 450 Ma (Fig. 6.8a), it is likely that the $<$900 Ma detrital zircons of the Greater Caucasus siliciclastic sequence are derived from Scythia (Fig. 6.2a). The scattered ages $>$900 Ma present in Greater Caucasus siliciclastic sequence samples (Fig. 6.8e) may be derived from the Eurasian interior. Because the crystallization ages indicated by these detrital zircons constrain the tectonic histories of the East European Craton (*Allen et al.*, 2006; *Wang et al.*, 2011), Scythia, the Greater Caucasus basement, and the Transcaucasus basement, they are likely to yield new insight into the locations of sutures on the southern margin of Eurasia and their role in guiding tectonic deformation on this complex plate margin.

6.7.1 Detrital zircon U-Pb age constraints on the original locations of Scythia, Greater Caucasus basement, and Transcaucasus basement domains

Central to locating terrane boundaries on the southern margin of Eurasia is determining whether Scythia, Greater Caucasus, and Transcaucasus basement domains formed in situ on the Eurasian margin or whether they originated on Gondwana or as intra-oceanic island arcs. Past work has identified zircons of age 600-900 Ma as diagnostic of crystallization during the Pan-African orogeny, which occurred on Gondwana (*Johnson and Woldehaimanot*, 2003; *Horton et al.*, 2008). Zircons of this age are virtually absent from samples containing detritus from the East European Craton (Fig. 6.8a). Our detrital zircon U-Pb ages from the Greater Caucasus siliciclastic sequence (Scythia), Greater Caucasus basement, and the Transcaucasus basement indicate that significant quantities of 600-900 Ma ages are present in all three domains, suggesting that they all originated on Gondwana (Fig. 6.8b, c, e). Whereas previously available data from Scythian basement were unable to resolve whether Scythia was exotic to Eurasia (e.g., *Saintot et al.*, 2006a), our data (see below) support the hypothesis that a suture divides Scythia from Eurasia (*Natal'in and Şengör*, 2005). Our findings are consistent with the common view that the Transcaucasus and Greater Caucasus basement domains are exotic to Eurasia (e.g., *Adamia et al.*, 2011a, and many others). The age of accretion of Scythia, the Greater Caucasus, and Transcaucasus basement domains to Eurasia is bounded by the age of the Pan-African orogeny to be ¡600 Ma.

6.7.2 Detrital zircon age constraints on the relationship between Greater Caucasus basement and Scythia

A suture between the Greater Caucasus basement and Scythia is suggested by ophiolites in the northern Greater Caucasus that divide the two domains and that were emplaced in the Carboniferous (*Adamia et al.*, 1981; *Somin*, 2011). However, the Greater Caucasus and Scythia have also been proposed to constitute a single terrane disrupted and duplicated by Triassic strike-slip faulting (*Natal'in and Şengör*, 2005). If the Greater Caucasus basement and Scythia constitute a single terrane, then the two domains would be expected to generally share the same crystallization and metamorphic history. If the Greater Caucasus basement is a separate terrane from Scythia, it is less likely (though still possible) that the Greater Caucasus basement would share the crystallization history of Scythia. Detrital zircon ages from the Greater Caucasus basement cluster around age peaks at 300 Ma and

450 Ma (Fig. 6.8b). Detrital zircon ages from the Greater Caucasus siliciclastic sequence, which we infer to be derived largely from Scythia, also cluster around age peaks at 300 Ma and 450 Ma (Fig. 6.8e). The major difference between the age signatures of the Greater Caucasus basement and Greater Caucasus siliciclastic sequence is that the 300 Ma and 450 Ma age peaks are wider in the siliciclastic sequence samples (Fig. 6.8e) than in the basement samples (Fig. 6.8b). Assuming that the Greater Caucasus siliciclastic sequence was derived from a large region or regions of Scythia, this difference may reflect somewhat diachronous crystallization across Scythia, of which only a small portion is exposed in the Greater Caucasus basement. Overall, our detrital zircon ages show that the Greater Caucasus basement has a very similar crystallization history to Scythia, lending support to the hypothesis that the Greater Caucasus basement is part of Scythia (*Natal'in and Şengör*, 2005). We hypothesize that the apparent terrane boundary between the Greater Caucasus basement and Scythia may be a result of strike-slip duplication of a single terrane and an adjacent suture zone.

6.7.3 Detrital zircon age constraints on the similarities and differences between Greater Caucasus basement and Transcaucasus basement

While several authors have proposed the existence of a suture between the Greater Caucasus and Transcaucasus basement (*Şengör*, 1984; *Adamia et al.*, 2011a; *Stampfli*, 2013), others have noted age and compositional similarity between the Transcaucasus and Greater Caucasus (*Zakariadze et al.*, 2007; *Mayringer et al.*, 2011), suggesting a shared tectonic history between the two domains. The presence or absence of a suture here is important because the Jurassic to Eocene opening of the Greater Caucasus Basin occurred between the Greater Caucasus basement and Transcaucasus basement (*Zonenshain and Le Pichon*, 1986; *Vincent et al.*, 2016). Thus, the opening of the Greater Caucasus Basin may have been guided by a pre-existing structure between the Greater Caucasus and Transcaucasus. Our detrital zircon ages show that while the Greater Caucasus basement contains subequal age peaks at 300 Ma and 450 Ma (Fig. 6.8b), the Transcaucasus basement contains a 300 Ma age peak but does not contain a 450 Ma age peak (Fig. 6.8c). Our samples of the Greater Caucasus siliciclastic sequence (representing Scythia) indicate that 300 Ma and 450 Ma age peaks are subequal in size across much of Scythia (Figs. 6.8e), in addition to within the Greater Caucasus basement (Fig. 6.8b). The fact that the Transcaucasus basement lacks such a pervasive and significant age peak compared to the Greater Caucasus and Scythia lends support to the hypothesis that a terrane boundary may separate the Greater

Caucasus and Transcaucasus (e.g., *Stampfli*, 2013).

6.7.4 Constraints on the timing of accretion of Scythia, Greater Caucasus basement, and Transcaucasus basement to Eurasia

While our data cannot directly constrain the timing of terrane movement and accretion, the crystallization histories recorded in our detrital zircon ages can be used to test hypothesized tectonic histories of the southern Eurasian margin. Our data are broadly consistent with the tectonic reconstruction of *Stampfli* (2013) for the Greater Caucasus and Transcaucasus during the Paleozoic (Fig. 6.11a, b). In the model of *Stampfli* (2013), the Greater Caucasus is translated from Gondwana to Laurussia in the Ordovician to Silurian as part of the Hunia superterrane, with accretion to Laurussia complete by 420 Ma (Fig. 6.11a). The translation of the Hunia superterrane is accomplished by south-directed subduction of the Qaidam ocean, which occupied the area between Hunia and Laurussia, and spreading of the Rheic ocean between Hunia and Gondwana (*Stampfli*, 2013, Fig. 6.11a). The subduction of the Qaidam ocean beneath Hunia provides a mechanism for crystallization of zircons in the Greater Caucasus basement that broadly cluster around 450 Ma. Subsequently in the *Stampfli* (2013) model, the Transcaucasus terrane was translated from Gondwana toward Laurussia as part of the Galatia superterrane during the late Devonian to Carboniferous (Fig. 6.11b). The northward translation of Galatia was accomplished by north and south vergent subduction of the Rheic ocean beneath the Galatia and Hunia superterranes and spreading of Paleotethys between Galatia and Gondwana. Following the collision of the Galatia and Hunia superterranes, northward subduction of Paleotethys beneath Galatia and Hunia began immediately (Fig. 6.11b). The bivergent subduction of the Rheic ocean followed by the northward subduction of Paleotethys provides a mechanism for the crystallization of zircons in the Greater Caucasus and Transcaucasus basement domains that cluster around 330-300 Ma. Thus, the tectonic model of *Stampfli* (2013) is consistent with observed zircon age distributions present in the Greater Caucasus and Transcaucasus basement domains (Fig. 6.11).

Natal'in and Şengör (2005) hypothesize that Scythia was formed by Triassic to Early Jurassic duplication of an extensive arc terrane by strike-slip faulting. This hypothesis can account for the similar crystallization histories we observe in the Greater Caucasus basement and in Scythia (Fig. 6.8b, e). The hypothesis of *Natal'in and Şengör* (2005) is also compatible with the reconstruction of *Stampfli* (2013) because the proposed Triassic formation of Scythia (*Natal'in and Şengör*, 2005) postdates the reconstruction of *Stampfli* (2013) (Fig. 6.11c). The similarity of detrital zircon age signatures from the Greater Cau-

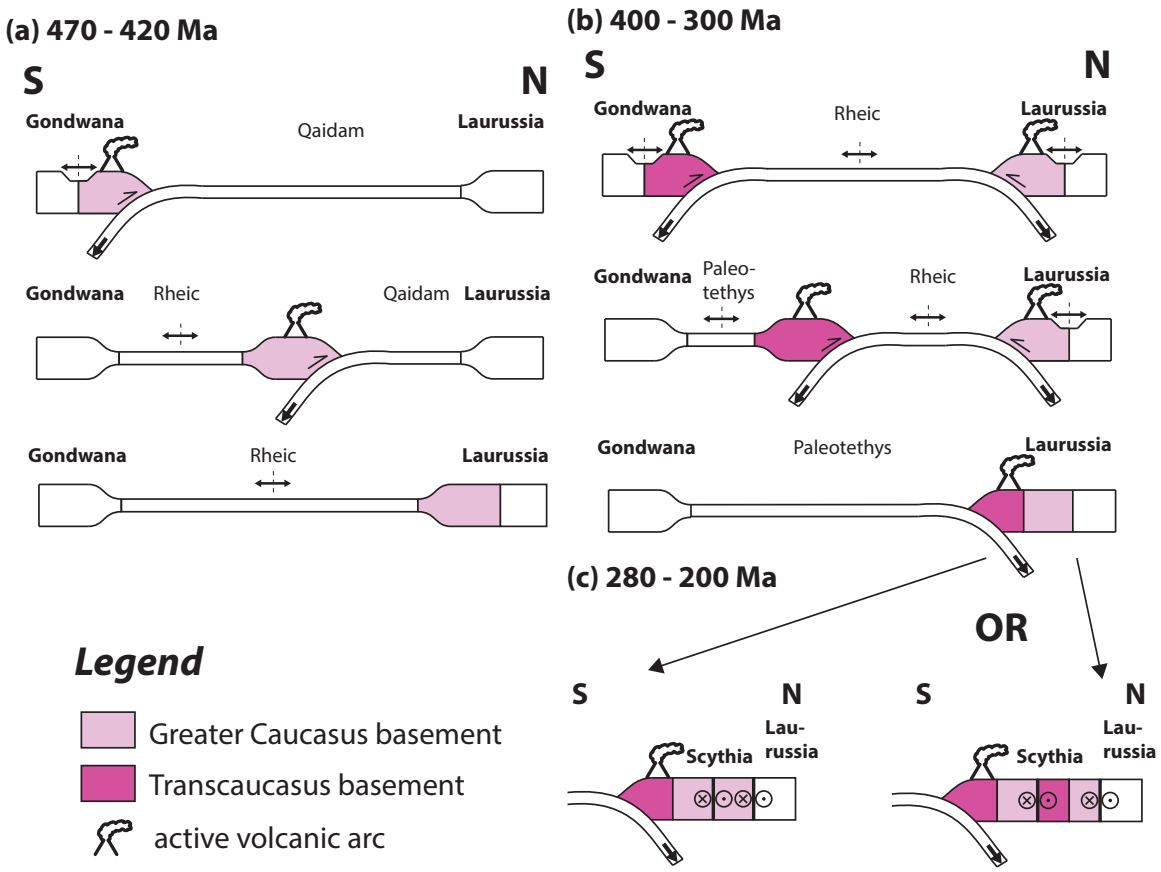

Figure 6.11: Crystallization histories of the East European Craton, Scythia, the Greater Caucasus basement, and the Transcaucasus basement (Fig. 6.8) have implications for Paleozoic to Triassic terrane accretion and broadly support the tectonic models of *Stampfli* (2013) and *Natal'in and Şengör* (2005). (a) Differences in crystallization history between the Greater Caucasus basement and East European Craton suggest that the Greater Caucasus is exotic to Eurasia, and a major Greater Caucasus age peak centered on 450 Ma is consistent with an active arc at that time (*Stampfli*, 2013). (b) The lack of 450 Ma zircons in the Transcaucasus (Fig. 6.8b) suggests that the Transcaucasus did not undergo the Ordovician to Silurian arc volcanism that likely affected the Greater Caucasus. However, a shared 300 Ma age peak is consistent with bivergent subduction underneath both domains resulting in their convergence (*Stampfli*, 2013). (c) The similarities between Greater Caucasus and Scythia crystallization histories supports the hypothesis that Scythia is composed of slivers of the Greater Caucasus arc that were duplicated by strike slip faulting (*Natal'in and Şengör*, 2005). Scythia may also contain slivers of Transcaucasus basement. See Section 6.7 for further discussion.

casus basement and Scythia (Figs. 6.8b, e) suggests that the Greater Caucasus terrane was involved in the Triassic strike-slip faulting that formed Scythia, though it is unclear whether the Transcaucasus terrane was involved as well. If accretion of the Transcaucasus to the Greater Caucasus occurred prior to the Triassic (as proposed by *Stampfli*, 2013), then Scythia may include tectonic slivers of the Transcaucasus/Galatia terrane, in addition to slivers of the Greater Caucasus/Hunia terrane (Fig. 6.11c). Given the fact that our detrital zircon samples inferred to represent Scythia are from Jurassic-Cretaceous catchments of unknown dimension, our data are not adequate to determine whether Scythia contains slivers of the Transcaucasus/Galatia terrane.

6.7.5 Suture locations

Overall, our data are consistent with the Paleozoic tectonic model of *Stampfli* (2013) and strike-slip deformation and duplication of Scythia/Greater Caucasus basement in the Triassic to Early Jurassic (*Natal'in and Şengör*, 2005, Fig. 6.11). Assuming the tectonic model outlined here, remnants of the Qaidam ocean would be located between Scythia and the East European Craton and potentially duplicated within Scythia. The Paleozoic, eclogite-bearing blueschists (*Perchuk and Philippot*, 1997; *Philippot et al.*, 2001) and ophiolite (*Adamia et al.*, 1981) observed on the northern slope of the Greater Caucasus, which were previously interpreted as a suture between the Greater Caucasus and Scythia, are likely to be a tectonic sliver of the Qaidam ocean suture. Remnants of the Rheic ocean would be located between Greater Caucasus basement and Transcaucasus basement and potentially duplicated in Scythia (Fig. 6.11c). The number and ages of sutures implied by our data are inconsistent with the hypothesis that the Paleotethys suture is located between the Greater Caucasus and Transcaucasus basement (*Şengör*, 1984). Remnants of Paleotethys would be located at the Sevan-Akera suture zone south of the Transcaucasus/Lesser Caucasus (as suggested by *Adamia et al.*, 2011a, among others; Fig. 6.11c).

6.8 Implications for stratigraphic records of collision

Understanding how foreland basin sedimentation evolves over the transition from subduction to collision will permit more accurate reconstructions of ancient continental collisions and their effects on plate kinematics, topography, and exhumation. In this section, we first review and synthesize the sediment provenance and facies changes observed in the Caucasus during the initiation of collision and discuss the drivers of the observed changes. We then compare the timing of changing sedimentation patterns to records of plate kine-

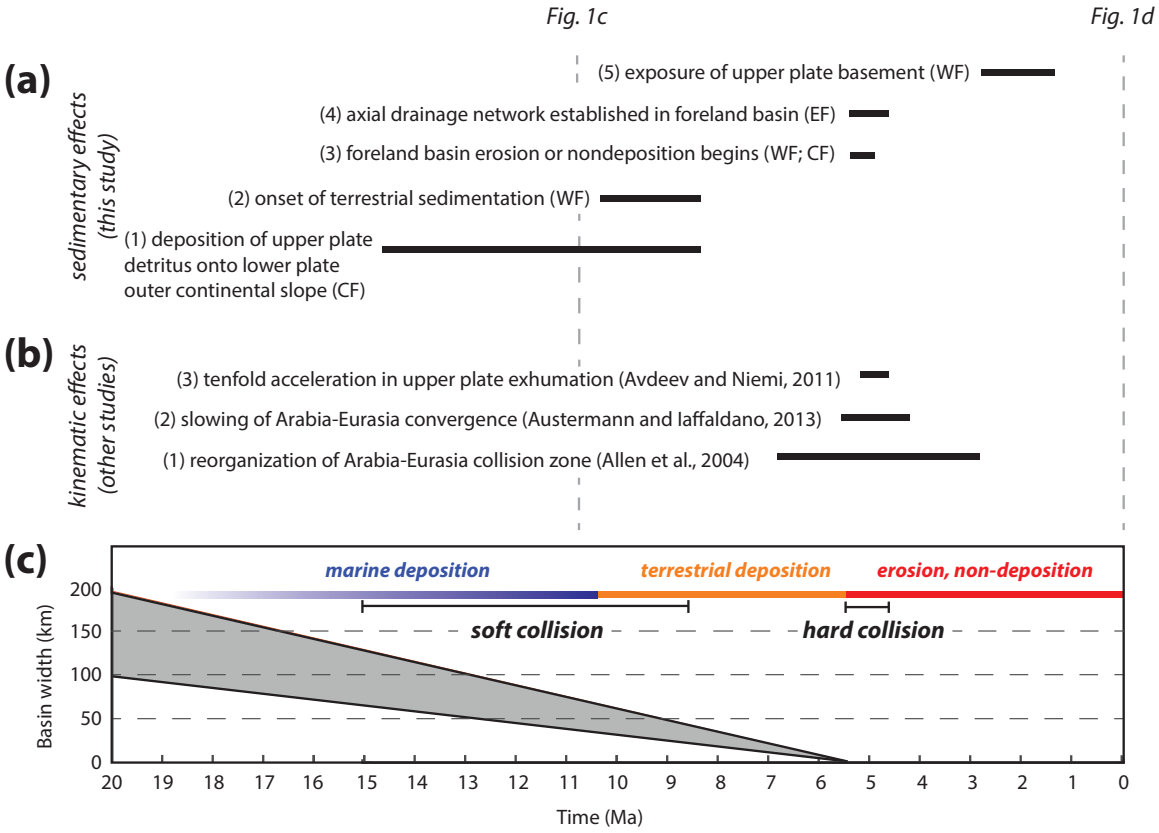

Figure 6.12: A generalized timeline of sedimentary and plate kinematic effects is developed from observations in the Caucasus. (a) Effects of the initiation of collision on foreland basin sedimentation are inferred from our detrital zircon sediment provenance interpretations and published stratigraphy. Each event is numbered for reference in the text and labeled parenthetically with the foreland basin section from which it was inferred (WF—western, CF—central, EF—eastern). (b) Kinematic effects of collision are reported from other studies, numbered and labeled with references for further discussion in the text. (c) Basin width, foreland sedimentation style, and phase of collision are plotted against time. Basin width is inferred using timing estimates of Greater and Lesser Caucasus convergence and width estimates of the intervening basin (see Section 6.8.3 for further discussion). The gray shaded region indicates an uncertainty envelope based on variability in basin width estimates. Colored bars indicate three periods of sedimentation in the Caucasus foreland basin during the initiation of collision, summarized from the sedimentary events listed above. Phases of collision are inferred from stratigraphy, provenance, and kinematic observations, as discussed in the text. Bars represent the range of ages within which the initiation of soft and hard collision could have occurred, based on available data. Vertical dashed lines indicate the ages associated with the time steps of collision shown in Figure 6.1.

matics and exhumation in the Caucasus in order to correlate the stratigraphic record with the transition from subduction to collision. Finally, we develop a generalized timeline of the sedimentary and kinematic effects of collision observed in the Caucasus that can be exported to other orogens.

6.8.1 Late Cenozoic provenance and facies changes of Caucasus foreland basin sediment

The western, central, and eastern foreland basin sections on the south side of the Greater Caucasus record several changes in provenance and facies during the Miocene to Quaternary (Figs. 6.9, 6.10). The western section reveals a Middle to Late Miocene transition from organic-rich marine turbidites to terrestrial deposition of predominantly conglomerates and sandstones, as well as an erosional hiatus from latest Miocene to late Pliocene (Fig. 6.10b). Detrital zircons from the western section reveal Oligocene to Miocene derivation of sediments from the Greater Caucasus siliciclastic sequence, with derivation from the Greater Caucasus volcaniclastic sequence and finally the Greater Caucasus basement during the latest Pliocene to Quaternary (Fig. 6.9b). The central section reveals a Late Miocene transition from turbiditic marine sediments to largely conglomeratic terrestrial sediments, with an erosional hiatus during the early to middle Pliocene (Fig. 6.10c). Detrital zircons from the central foreland basin section reveal a transition in source from the Lesser Caucasus to the Greater Caucasus, preceding or approximately coinciding with the coarsening of sediments and terrestrial emergence of the sequence (Fig. 6.9c). The Lesser Caucasus provenance, apparent slumping, thin bedding, and shale-rich lithology of the Middle Miocene strata from which CF-1 was collected (Fig. 6.6c) suggest that the central section was located toward the distal margin of the lower plate continental slope during the Middle Miocene. The eastern foreland basin section reveals a Pliocene transition from marine turbiditic sedimentation to conglomeratic and sand-rich sedimentation in a predominantly terrestrial environment (Fig. 6.10d). Detrital zircons from the eastern section show consistent derivation from the Greater Caucasus siliciclastic sequence until Pliocene conglomerates and sandstones are deposited, which are derived from both the Greater and Lesser Caucasus, likely signaling the integration of an axial drainage network parallel to the Greater and Lesser Caucasus (Fig. 6.9d).

Together, the lithologies and provenance observations from these three sections reflect a set of changes to the sedimentary system between two converging continents during the transition from subduction to collision (Fig. 6.12). Detrital zircon provenance of the central section reveals that upper-plate detritus was deposited on the lower plate continental slope

sometime between ∼15 Ma and 8.5 Ma (Fig. 6.9c; event 1 in Fig. 6.12a). Facies of the western and central sections, which lie broadly within the western Greater Caucasus where collision likely began in the latest Miocene to Pliocene (*Philip et al.*, 1989; *Avdeev and Niemi*, 2011; *Cowgill et al.*, 2016), indicate a transition to terrestrial and largely conglomeratic sediments in the late Middle to Late Miocene, around 10.5 to 8.5 Ma (Fig. 6.10b, c; event 2 in Fig. 6.12a). In the latest Miocene to early Pliocene (∼5.5 Ma), an erosional hiatus begins in the western and central sections (6.10b, c; event 3 in Fig. 6.12a), coeval with the integration of an axial drainage network in the foreland basin (Figs. 6.9d, 6.10d; event 4 in Fig. 6.12). Finally, in the latest Pliocene or Quaternary (¡2.8 Ma), the first sediment derived from Greater Caucasus basement is deposited in the western foreland basin (Fig. 6.9b; event 5 in Fig. 6.12a). These events outline three broad periods of foreland basin sedimentation (depicted in Fig. 6.12c). In the first period, deposition between the Greater and Lesser Caucasus occurs in a marine setting until ∼10 Ma. In the second period, the basin between the Greater and Lesser Caucasus occurs predominantly in a terrestrial setting from ∼10 Ma until ∼5.5 Ma. In the final period, the basin between the Greater and Lesser Caucasus is largely erosional or non-depositional after ∼5.5 Ma.

6.8.2 Drivers of observed facies and provenance changes

In order to assess whether collision is a primary driver of the observed late Cenozoic sedimentary changes in the Caucasus, we compare the timing of observed sedimentary changes with the timing of Caucasus collision and the timing of late Cenozoic regional base-level changes, a potential alternative driver of changing sedimentation patterns. First, we outline the stratigraphic, kinematic, and thermochronometric constraints on the timing of collision in the Caucasus and discuss whether the inferred collisional history can account for the changes in sedimentation that are documented by our data. Second, we discuss the timing of late Cenozoic base-level changes in the Paratethyan system (of which the Black Sea, Caspian Sea, and the Caucasus foreland basin were parts), and consider whether documented base-level variations can explain stratigraphic observations and provenance data from the Caucasus. Finally, we discuss whether the patterns of late Cenozoic Caucasus sedimentation we infer from stratigraphy and provenance data are consistent with predictions made from a generalized model of collision (Fig. 6.1).

Many workers divide collision into a soft phase and hard phase (*Klootwijk et al.*, 1985; *Lee and Lawver*, 1995; *Chung et al.*, 2005; *van Hinsbergen et al.*, 2012; *Cowgill et al.*, 2016). Soft collision is understood as the initial entrance of a thinned continental margin, composed of lithosphere that is transitional between continental and oceanic, into a sub-

duction zone (*Lee and Lawver*, 1995; *Chung et al.*, 2005). The age of soft collision can be bracketed from the stratigraphic record if a stratigraphic sequence shows evidence of a transition from lower plate-derived sediment deposited in a continental-slope environment to upper plate-derived sediment (*DeCelles et al.*, 2014; *Hu et al.*, 2015). Our central foreland basin section shows such a transition, from Lesser Caucasus-derived turbidites that underwent soft sediment deformation likely on the lower plate continental slope (Fig. 6.6c) to Greater Caucasus-derived conglomerates upsection (Figs. 6.9c, 6.10c). Soft collision began prior to the deposition of the upper sample (CF-2) at $\geq$8.5 Ma and likely after deposition of the lower sample (CF-1) around 15 Ma, as the thin bedding and dominantly fine grain size of the sampled turbidites suggest deposition near the distal edge of the continental slope (Fig. 6.12a). The wide range in the age of soft collision is partly a result of samples available from the section and could potentially be refined in the future.

Hard collision is marked by changes in plate kinematics, exhumation rates, and/or initiation of far-field deformation in response to the stress changes associated with subduction of continental lithosphere (*Lee and Lawver*, 1995; *van Hinsbergen et al.*, 2012; *Cowgill et al.*, 2016). Several lines of evidence can be used to determine the timing of hard collision in the Caucasus, including exhumation rates derived from thermochronometry (*Avdeev and Niemi*, 2011), plate velocities derived from paleomagnetic and geodetic data (*Austermann and Iaffaldano*, 2013), and fault kinematic reconstructions (*Allen et al.*, 2004). Within the upper plate of the Caucasus collision zone, a tenfold increase in upper-plate cooling rates is documented to have occurred at 5 Ma, which is most reasonably explained by a rapid increase in exhumation rate (Fig. 6.12b; *Avdeev and Niemi*, 2011). Within the Arabia-Eurasia collision zone, of which the Caucasus is a part, a regional compilation of paleomagnetic and GPS data indicate a slowing of convergence at 5 Ma (Fig. 6.12b *Austermann and Iaffaldano*, 2013). Finally, retrodeforming many structures in the Arabia-Eurasia collision zone indicates that only 3-7 Ma of slip at current rates is required to account for their net offset, suggesting a major plate kinematic reorganization at this time potentially related to collision (Fig. 6.12b *Allen et al.*, 2004). Together, these three lines of evidence indicate that kinematic reorganization, plate slowing, and increased exhumation rates occurred within the Caucasus and surrounding region at 5 Ma, consistent with 5 Ma marking the beginning of hard collision in the western Caucasus (*Cowgill et al.*, 2016). Thus, the available sedimentary, paleomagnetic, thermochronometric, and fault kinematic data from the region are consistent with a progression from soft to hard collision occurring during the period from >8.5 Ma to 5 Ma, the time frame for most of the changes we infer in foreland basin sedimentation (Fig. 6.12).

While the sedimentary changes observed overlap in time with the initiation of collision

in the Greater Caucasus (e.g., *Cowgill et al.*, 2016), Miocene to Pliocene sedimentation was also affected by rapid base-level change in the Paratethyan basin system of which the Caucasus foreland basin was part (e.g., *Forte and Cowgill*, 2013; *van Baak et al.*, 2015). Disconnection of the Mediterranean from the Atlantic drove base-level falls of >1 km in Black and Caspian Seas at 5.59 Ma (*Krijgsman et al.*, 1999; *Zubakov*, 2001; *Krijgsman et al.*, 2010; *Vasiliev et al.*, 2013; *Forte and Cowgill*, 2013). This base-level fall would have also reduced base level in the basin between the Greater and Lesser Caucasus, which served as a connection between the Black and Caspian seas (*Zonenshain and Le Pichon*, 1986). Black and Mediterranean Sea base levels were restored by 5.33 Ma following reconnection with the Atlantic (*Krijgsman et al.*, 1999; *Garcia-Castellanos et al.*, 2009; *van Baak et al.*, 2015). Unlike in the Black Sea, low base levels in the Caspian appear to have persisted until 4.0 - 2.7 Ma (*Forte and Cowgill*, 2013; *van Baak et al.*, 2019). The persistent low base levels of the Caspian Sea following base level rebound in the Black Sea indicates that a Pre-Messinian marine gateway between the Black and Caspian seas had been closed by the earliest Pliocene, likely as a result of ongoing convergence and collision in the Caucasus. Because low Paratethyan base levels associated with disconnection from the Atlantic Ocean persisted only from 5.59 Ma to ∼5.33 Ma (*Krijgsman et al.*, 1999; *Garcia-Castellanos et al.*, 2009; *van Baak et al.*, 2015), these base level changes cannot by themselves account for the basin shallowing, terrestrial sedimentation, and erosion/non-deposition observed in Caucasus foreland basin sections from the Late Miocene to the present. In contrast, the initiation of collision in the Caucasus would have caused permanent changes in lithospheric buoyancy and topography that can account for the observed changes in sedimentation.

In addition to assessing the temporal correspondence of collision with inferred late Cenozoic changes in foreland basin sedimentation in the Caucasus, we compare the inferred changes to predictions from the generalized model of collision discussed in Section 6.1 (Fig. 6.1). These predictions include shallowing of the foreland basin leading ultimately to erosional conditions (Fig. 6.1b-d), sourcing of sediment from deeper crustal levels of the orogen (Fig. 6.1d), and development of an axial drainage network in the basin (Fig. 6.1d). Stratigraphic facies changes and detrital zircon provenance data indicate that during the Late Miocene to Quaternary, the foreland basin shallowed and became erosional (Fig. 6.10; events 2, 3 in Fig. 6.12a), an axial drainage network was developed (Fig. 6.10d; event 4 in Fig. 6.12a), and sediment was sourced from the basement of the orogen for the first time (Fig. 6.10b; event 5 in Fig. 6.12a). Thus, the changes in sediment provenance, lithology, and drainage pattern inferred from the Caucasus foreland basin conform well to the predictions developed from a general model of collision (Fig. 6.1).

6.8.3 Correlating basin width with facies and provenance changes

Because Paratethyan base-level changes alone cannot account for the Miocene to present sedimentary changes observed in the Caucasus, convergence and collision of the Greater and Lesser Caucasus must be the primary driver influencing foreland basin facies and provenance. Thus, the width of the basin between two converging continents may influence facies and provenance in pre-collisional to collisional basins, and stratigraphic records may be able to be used to infer the width of these closing basins at different points in time. We use a simple calculation to estimate the width of the closing basin at the time these changes occurred (Fig. 6.12c). Width estimates of the basin between the Lesser and Greater Caucasus range from 200 - 280 km from kinematic reconstructions using paleomagnetic data (*van der Boon et al.*, 2018) to 350 - 400 km from interpretation of sedimentary facies (*Cowgill et al.*, 2016). The basin is thought to have closed from 35 Ma (*Adamia et al.*, 2011b) until 5.5 Ma, when the basin became dominantly erosional and no longer accommodated sediment (Fig. 6.10). For simplicity, we assume a constant convergence rate between 35 and 5.5 Ma. We plot basin width over time assuming a range of pre-convergence widths from 200 - 400 km and a constant convergence rate from 35 Ma until 5.5 Ma, which equates to convergence rates of 7 - 13 mm/yr. Such rates are comparable to modern convergence rates in the eastern Greater Caucasus where subduction is still active (*Reilinger et al.*, 2006; *Kadirov et al.*, 2012, 2015). Using this basin-width reconstruction, we find that when upper plate detritus was deposited on the lower plate continental slope in the central section (15 - 8.5 Ma), defined as the initiation of soft collision, the basin was between 20 and 125 km wide (Fig. 6.12c). When the basin transitioned to terrestrial sedimentation (10.5 - 8.5 Ma), the basin was between 20 and 70 km wide (Fig. 6.12c). When the basin became largely erosional (5.5 Ma), by definition the basin width was reduced to zero (Fig. 6.12c). This basin width reconstruction serves as a starting point for determining how the width of a converging basin can be inferred from the stratigraphic record. Ultimately, such a reconstruction may serve as an interpretive tool for constraining the width of pre-collisional basins based on changes in sedimentary facies and provenance.

6.8.4 Temporal links between collisional and sedimentary processes in the Caucasus

Caucasus foreland basin stratigraphy, as well as thermochronometric, paleomagnetic, and fault kinematic data constrain the progression from soft to hard collision and the sedimentary response to the initiation of collision (Fig. 6.12). The timing of soft collision is constrained by the stratigraphic record of the distal continental margin of the lower plate

having upper plate detritus deposited onto it (e.g., *DeCelles et al.*, 2014) as is observed in our central foreland basin section, where soft collision is inferred to have occurred between 15 Ma and 8.5 Ma (Fig. 6.9c, 6.10c). Hard collision at ∼5 Ma in the Caucasus is supported by an increase in upper plate exhumation (*Avdeev and Niemi*, 2011), a decrease in convergence rate (*Austermann and Iaffaldano*, 2013), and a kinematic reorganization with the initiation of many faults throughout the Arabia-Eurasia collision zone (*Allen et al.*, 2004, Fig. 6.12b). Comparison of the timing of facies and provenance transitions (Section 6.8.1, Fig. 6.12a) with the ages of soft and hard collision yields several insights. Soft collision (event 1 in Fig. 6.12a) coincides with or is followed by shallowing and a transition to terrestrial sedimentation (event 2 in Fig. 6.12a; Fig. 6.12c). Hard collision (events 1-3 in Fig. 6.12b) follows soft collision by 3.5 - 10 Myr. Hard collision coincides with the establishment of erosional or non-depositional conditions in the foreland basin (event 3 in Fig. 6.12a) and the development of an axial drainage network in the foreland basin (event 4 in Fig. 6.12a; Fig. 6.12c). Finally, hard collision is followed after 2 - 3 Myr by exposure of upper-plate basement (event 5 in Fig. 6.12a).

The coincidence of hard collision with the establishment of erosional or non-depositional conditions in the foreland basin and integration of an axial drainage network is striking. Assuming that hard collision is most precisely dated using the thermochronometric record of upper plate exhumation in the Greater Caucasus (*Avdeev and Niemi*, 2011, 5 Ma), then the establishment of erosional foreland basin conditions and a foreland axial drainage network (5.5 Ma) occurred within 0.5 Myr of hard collision. A more conservative view is that hard collision occurred 5 $\pm$ 2 Ma, the time frame over which a kinematic reorganization occurred over the entire Arabia-Eurasia collision zone in which slip on many presently active faults within the collision zone began (*Allen et al.*, 2004). If it is assumed that hard collision began sometime within the age range 5 $\pm$ 2 Ma, then the temporal offset between hard collision and foreland basin erosion/non-deposition is less than or approximately equal to the range of uncertainty in the age of hard collision.

6.8.5 Implications for other collisional orogens

The provenance and lithology of Caucasus foreland-basin sediments are temporally correlated with changes in basin width and the initiation of collision (Fig. 6.12), and these correlations can potentially be used predictively in other orogens. The transition from subduction to collision initiates a series of sedimentary responses (Fig. 6.12) that occur in a specific order, consistent with predictions based on a generalized model of collision (Fig. 6.1). Earliest deposition of upper plate detritus onto the lower plate continental margin (soft

collision) occurs before or synchronously with the arrival of coarse detritus and a transition to nonmarine conditions, when the basin is 20 - 125 km wide, 3.5 - 10 Myr before hard collision. The exact timing of the delay between soft and hard collision is likely to vary with convergence rate and geometry of transitional lithosphere in the collision zone (e.g., *van Hinsbergen et al.*, 2012). Hard collision (events 1-3 in Fig. 6.12b) can be identified by the transition to erosional conditions in the foreland basin between two converging continents (event 3 in Fig. 6.12a), together with the formation of an axial drainage network in the foreland basin (event 4 in Fig. 6.12a), which can be recognized by a mixture of sediments sourced from both the upper plate and lower plate. Detritus from deeper crustal levels of the upper plate reaches the foreland basin several million years after hard collision (event 5 in Fig. 6.12a), likely reflecting increasing upper plate exhumation rates following hard collision (e.g., *Avdeev and Niemi*, 2011). The compositional effects of accelerated upper plate erosion on foreland basin sediment will vary based on the crustal structure and lithology of the orogen. Perhaps the most important implication of our analysis is the close temporal correspondence between hard collision, the establishment of erosional foreland basin conditions, and formation of axial drainage networks in the foreland basin, which should permit more accurate dating of hard collision in mature collisional orogens.

Accurately dating the transition from soft to hard collision in mature orogens is critically important for crustal mass balance and for understanding how collision affects plate kinematics, topography, climate, ocean circulation, and other aspects of the Earth system (*Patriat and Achache*, 1984; *England and Houseman*, 1986; *Edmond*, 1992; *Molnar et al.*, 2010; *DeCelles et al.*, 2014; *Zhuang et al.*, 2015; *Ingalls et al.*, 2016). For instance, the India-Asia collision has been hypothesized to have caused changes in topography (*England and Houseman*, 1986; *Dupont-Nivet et al.*, 2008), global climate (*Raymo and Ruddiman*, 1992), and species dispersal (*Jaeger et al.*, 1989). Testing these hypotheses requires accurate estimates of the timing of collision, but there has thus far been significant disagreement between such estimates (e.g., *DeCelles et al.*, 2004; *Hu et al.*, 2012; *van Hinsbergen et al.*, 2012; *DeCelles et al.*, 2014; *Wu et al.*, 2014; *Hu et al.*, 2015; *Zhuang et al.*, 2015). In addition, shortening reconstructions of orogens depend significantly on the mass flux into the orogen, which is strongly affected by the timing of the transition from oceanic lithosphere subduction to collision with the lower plate continent (*van Hinsbergen et al.*, 2012; *Cowgill et al.*, 2016). Our observations of the sedimentary response to soft and hard collision in the Caucasus may provide new insight into the collisional histories of mature orogens, permitting more accurate tectonic reconstructions and tests of hypothesized effects of collision.

6.9 Conclusions

We present new detrital zircon U-Pb age data from the Caucasus that grant insight into the sedimentary response to initial collision, which began recently and is ongoing. By combining new detrital zircon sediment provenance with published stratigraphy, thermochronometric, paleomagnetic, and fault-kinematic data from the Caucasus and surrounding regions, we construct a timeline of the transition from subduction to collision and its stratigraphic record. We find evidence of soft collision in the form of deposition of upper-plate detritus onto the lower plate continental margin at 15 - 8.5 Ma. Hard collision with accelerated upper plate exhumation and decreasing plate convergence rates at 5 Ma is marked in the stratigraphic record by the establishment of erosional foreland basin conditions and the formation of an axial drainage network in the foreland basin. Our results establish a framework for how the evolution of incipient collision is recorded in stratigraphy. This framework may be useful for more accurately inferring the timing of soft to hard collision in ancient collisional orogens from stratigraphic records.

Our detrital zircon U-Pb data also provide new constraints on the crystallization histories of Scythia, which is inferred to be the source of the Greater Caucasus siliciclastic sequence; the Greater Caucasus basement; and the Transcaucasus basement. Whereas Scythia and the Greater Caucasus basement share major, sub-equal detrital zircon age peaks centered on 450 Ma and 300 Ma, the Transcaucasus basement lacks the 450 Ma age peak. Scythia, the Greater Caucasus basement, and the Transcaucasus basement all contain zircons of 900-600 Ma inferred to reflect crystallization on Gondwana during the Pan-African orogeny, suggesting that all three domains are exotic to Eurasia. Our data support tectonic reconstructions that place terrane boundaries between Scythia and Eurasia and between the Greater Caucasus basement and Transcaucasus basement.

Acknowledgments

We gratefully acknowledge field assistance provided by Eric Cowgill, Chad Trexler, Adam Forte, Luka Tsiskarishvili, Salome Gogoladze, Mamuka Natsvlishvili, and Rafiq Safarov. Tea Godoladze, Fakhraddin Kadirov, and Samir Mammadov graciously arranged field logistics. Assistance with sample preparation was provided by Megan Hendrick, Amanda Maslyn, Will Bender, and Gordon Moore. Zircon U-Pb analysis was conducted at the University of Arizona Laserchron Center, which is supported by NSF EAR-1338583. We thank Heather Kirkpatrick, Lindsey Abdale, and Laserchron Center staff members Mark Pecha, Dominique Geisler, Kojo Plange, Gayland Simpson, Chelsi White, and Dan Al-

berts for help with zircon U-Pb age analyses. This work was supported by the University of Michigan via International Institute and Rackham Graduate School grants (A. Tye) and NSF EAR-1524304 (NAN). Supplemental information including exact sample locations (Table S1), measured detrital zircon U-Pb age data (Table S2), BPC values (Table S3), and BPC uncertainties (Table S4) can be found at https://doi.org/10.7302/xay7-8a71.

CHAPTER 7

Structural and Thermochronometric Data Provide Insight into Strain Accommodation within an Active Accretionary Prism, the Eastern Greater Caucasus

Abstract

Accretionary prisms are ubiquitous at convergent plate margins and deform internally to maintain a critical taper angle. The mechanisms of internal deformation within accretionary prisms remain poorly characterized, however, in part because of the submarine setting of most active accretionary prisms. We present new geologic mapping, structural measurements, and thermochronometry data from transects across an active, sub-aerially exposed accretionary prism, the Eastern Greater Caucasus of western Asia. Folding, small-offset thrust faults, and minor compressional volume loss are inferred to have accommodated all tectonic convergence ($\sim$120 km) across the plate boundary. Cumulative offset on the basal detachment increases from zero at the toe of the prism to 120 km beneath the retro-wedge limit of prism deformation. Our observations document pervasive folding and small-offset thrusting within the turbiditic lithologies at the core of the range, as well as accretion of a tectonic sliver consisting of the entire sedimentary sequence of the lower plate. Thermochronometry data and cross-cutting relationships between major faults and syn-orogenic sediments indicate that this accretion occurred prior to 6 Ma. Deformation of the prism core by folding continued after this accretionary episode and is likely ongoing. Together, our data suggest that out-of-sequence folding accommodates a significant portion of the internal deformation required for an accretionary prism to maintain critical taper.

Our data also have implications for the evolution of the Arabia-Eurasia collision zone. We infer a difference in cumulative shortening between the western to central-eastern seg-

ments of the Greater Caucasus, which has accommodated >200 km shortening and began deforming ~35 Ma, and the Eastern Greater Caucasus, Alborz, and South Caspian Basin, which accommodate ~120 km shortening and began to deform 12-10 Ma. This difference in shortening suggests slip on an orogen-scale, right-lateral strike-slip fault that intersects with the central to eastern segment of the Greater Caucasus and was active from 35 Ma or earlier until 12-10 Ma or later. Candidate structures include the previously described West Caspian Fault and Arax Fault.

7.1 Introduction

Accretionary prisms are deforming wedges of marine sedimentary rocks that accommodate compressional strain above subduction zones and contain important records of convergent tectonic motion (e.g., *Leggett et al.*, 1979; *Sample and Fisher*, 1986; *Ghisetti et al.*, 2016). Because of the brittle rheology of upper crustal rocks, accretionary-prism growth can be modeled as a critically-tapered Coulomb wedge, in which thickening of the prism by internal deformation and growth by accretion of new material act to maintain a constant, critical taper angle in the prism (*Davis et al.*, 1983; *Moore and Silver*, 1987; *Morley*, 1988).

Although accretion of new material to prisms through offscraping and underplating has been well described, the mechanisms of internal prism thickening remain poorly constrained (e.g., *Platt et al.*, 1985; *Sample and Fisher*, 1986; *Moore and Silver*, 1987). Knowing how strain is accommodated within an accretionary prism is vital to understanding how convergent strain is partitioned in convergent plate boundaries (e.g., *Mulugeta and Koyi*, 1992), how tectonic convergence can be inferred from the geologic record, and what hazards that are posed by accretionary prism deformation processes (e.g., *Ito and Obara*, 2006). The submarine setting of most active accretionary prisms (e.g., *Moore and Silver*, 1987; *Moore and Saffer*, 2001; *Ghisetti et al.*, 2016) restricts extensive study of their interiors. On the other hand, accretionary prisms preserved in the geologic record are often deeply exhumed, highly deformed, and/or no longer active (e.g., *Leggett et al.*, 1979; *Sample and Fisher*, 1986; *Pound et al.*, 2014). Thus, studies of well-preserved and active accretionary prisms in which internal deformation can be observed are rare.

Here, we present a structural and thermochronometric study of strain accommodation in the Eastern Greater Caucasus orogen of western Asia, which is inferred to be an active accretionary prism from its setting above a subduction zone accommodating 10-12 mm/yr convergence (Fig. 7.1; e.g., *Reilinger et al.*, 2006; *Kadirov et al.*, 2012; *Mellors et al.*, 2012; *Kadirov et al.*, 2015; *Mumladze et al.*, 2015) and its composition of predominantly marine sedimentary rocks (e.g., *Nalivkin*, 1976; *Bairamov et al.*, 2008). Our dataset

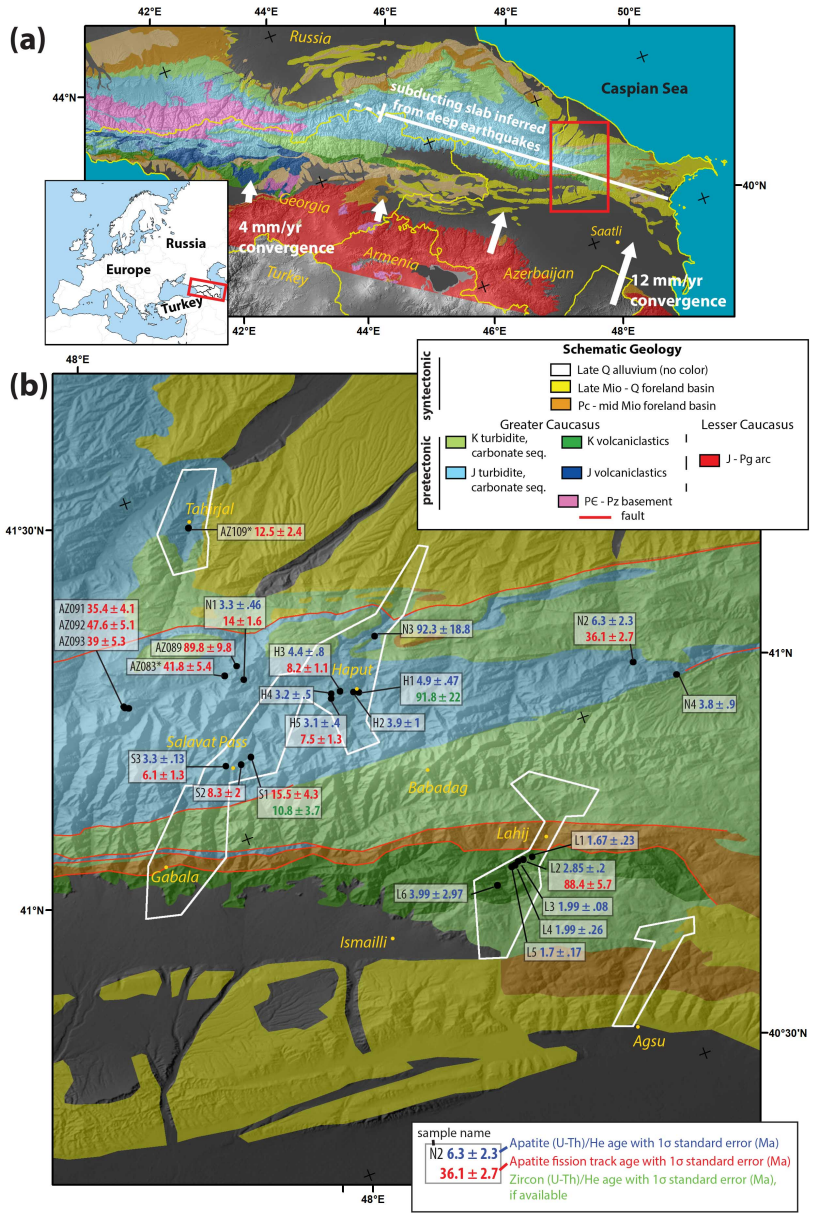

Figure 7.1: (a) The Greater Caucasus is a WNW-trending mountain belt in western Asia that accommodates NNE-directed shortening. Schematic geology is shown following the key in (b). White annotation shows geodetic convergence rates and the along-strike extent of a subducting slab inferred beneath the range from deep earthquakes (*Mumladze et al.*, 2015). Political boundaries and country names are shown in yellow. Inset map shows location of the panel in red. The red box in the panel shows the extent of (b). (b) The study area is located in the Eastern Greater Caucasus. Schematic geology is shown using the same symbology as in (a). White polygons show extents of structural mapping transects (Fig. 7.2). New and existing (*Bochud*, 2011, Avdeev, unpublished) thermochronometric ages are shown using black circles, with ages displayed in text boxes following the legend shown in the lower righthand corner.

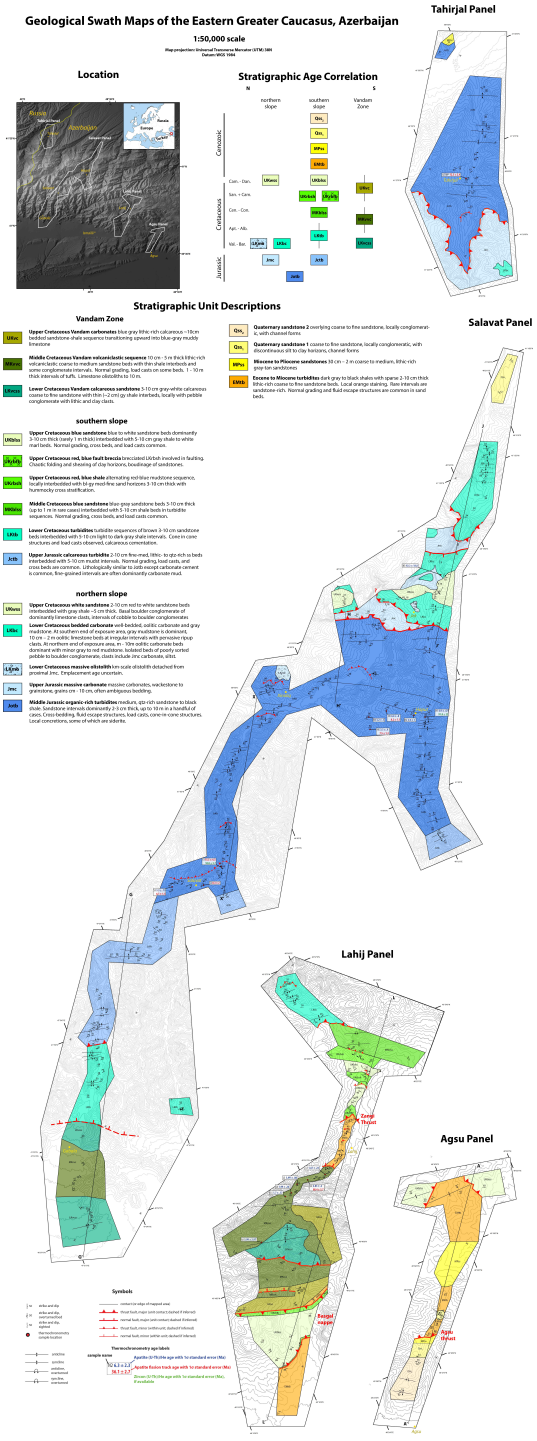

Figure 7.2: New geologic swath maps across the Eastern Greater Caucasus. The full-size version can be accessed at https://doi.org/10.7302/gc06-q290.

consists of multiple structural geologic mapping transects that together traverse the entire orogen across strike, and thermochronometric ages of the apatite and zircon (U-Th)/He systems and the apatite fission track system (Figs. 7.1, 7.2). Using this dataset, we develop a comprehensive structural model of the range that allows us to infer the mechanisms by which strain is accommodated within the Eastern Greater Caucasus accretionary prism. Our thermochronometric data constrain exhumation depth and timing across the range, which we use to infer the temporal evolution of deformation. We use the structural model and the constraints from thermochronometry to address the mechanisms of internal thickening within the prism, the partitioning of strain between the prism interior and the basal detachment (megathrust), and prism growth. The insight provided by our data has implications for deformation processes, recording of convergent strain, and hazards associated with accretionary prisms generally.

7.2 Geological Background

The WNW-striking Greater Caucasus orogen is located within the Arabia-Eurasia collision zone and accommodates convergence between Eurasia to the north and the Lesser Caucasus microcontinent to the south (Fig. 7.1a; *Zonenshain and Le Pichon*, 1986; *Philip et al.*, 1989; *Vincent et al.*, 2007; *Adamia et al.*, 2011a; *Cowgill et al.*, 2016; *Vincent et al.*, 2016). The orogen is inferred from geological and geophysical data to be in the process of transitioning from subduction to collision (*Mumladze et al.*, 2015; *Cowgill et al.*, 2016, Tye et al., submitted). Deep earthquakes suggest the presence of a subducting slab beneath the Eastern Greater Caucasus (Fig. 7.1a; *Mellors et al.*, 2012; *Mumladze et al.*, 2015) and geodetic convergence rates indicate that 10-12 mm/yr of shortening is accommodated in the Eastern Greater Caucasus, while 4 mm/yr is accommodated in the western part of the orogen (Fig. 7.1a; *Reilinger et al.*, 2006; *Kadirov et al.*, 2012, 2015; *Sokhadze et al.*, 2018). These deep earthquakes and geodetic convergence rates have been interpreted to suggest that collision has begun in the western part of the orogen while active subduction continues in the Eastern Greater Cauacasus (*Mumladze et al.*, 2015). Large magnitude (potentially M9) earthquakes with complex ruptures have been inferred from historic records in the Eastern Greater Caucasus, where subduction is inferred to be active (*Nikonov*, 1982; *Berberian*, 1997).

The subject of this study is the Eastern Greater Caucasus at the eastern end of the orogen (Fig. 7.1b). Exposed bedrock of the Eastern Greater Caucasus consists entirely of Middle Jurassic and younger sedimentary rocks (e.g., *Nalivkin*, 1976). The exposed lithologies include (1) a broadly regressive Cenozoic sequence exposed on the margins of the range

that transitions from Eocene to Miocene turbidites to Pliocene to Quaternary sandstones and conglomerates; (2) the Mesozoic Vandam Zone sequence, which outcrops along the southern margin of the orogen and contains a highly competent series of volcaniclastic sandstone beds; (3) a Mesozoic passive margin sequence exposed over the majority of the range that is composed predominantly of thinly-bedded turbidites and also includes a platform carbonate system exposed on the north side of the range toward the interior of the upper plate (Figs. 7.1, 7.2; e.g., *Nalivkin*, 1976; *Bochud*, 2011; *Alizadeh et al.*, 2016). The thinly-bedded turbidites that constitute the bulk of the orogen are lithologically and mechanically typical of the rocks incorporated into accretionary prisms (e.g., *Moore*, 1989). Thus, the Eastern Greater Caucasus is a natural example of an active accretionary prism above a subduction zone.

Several lines of evidence constrain the total magnitude of convergence accommodated within the Eastern Greater Caucasus. Paleomagnetic vertical axis rotations from samples located on the lower plate of the Greater Caucasus subduction system in the Pontides, Lesser Caucasus, Talysh, and Alborz mountains have been interpreted to suggest that a total of $\sim$120 km of across-strike shortening has been accommodated within the Eastern Greater Caucasus (*van der Boon et al.*, 2018). Such a magnitude of convergence is consistent with the down-dip extent of the subducting slab beneath the Apsheron Sill, located along-strike to the east of the Eastern Greater Caucasus inferred from seismic experiments (*Green et al.*, 2009). Deep earthquakes beneath the Eastern Greater Caucasus are confined to $<$60 km depth (*Mumladze et al.*, 2015), which is also broadly consistent with a moderately dipping slab of 120 km down-dip extent. No structural shortening estimates exist for the Eastern Greater Caucasus, and constraining the proportion of inferred tectonic convergence that is accommodated by upper-plate shortening is a goal of this study.

7.3 Methods

In order to constrain the magnitude, style, and timing of deformation within the active accretionary prism of the Eastern Greater Caucasus, this study uses a combination of geologic mapping, construction of balanced geological cross sections, and thermochronometry.

7.3.1 Geologic mapping and cross-section construction

Geologic mapping was conducted from 2016 to 2017 across the range at the $1:50,000$ scale in four swath transects that together span the across-strike extent of the Eastern Greater Caucasus (Figs. 7.1, 7.2). Lithostratigraphic units were defined based on field ob-

servations, and age determinations are based on biostratigraphic ages reported in previous mapping studies of the region (*Golubjatnikov and Dubogryzova*, 1959; *Voronin et al.*, 1959; *Khain and Shardanov*, 1960; *Nalivkin*, 1976; *Bairamov et al.*, 2008). Existing geochronologic results from the region are in agreement with the reported biostratigraphic ages (e.g., *Cowgill et al.*, 2016, Tye et al., submitted). Our mapping effort focuses on structural observations and that can constrain range-scale structural models.

Geologic cross sections were constructed based primarily on field mapping and structural measurements, with reference to prior studies (*Golubjatnikov and Dubogryzova*, 1959; *Voronin et al.*, 1959; *Khain and Shardanov*, 1960; *Nalivkin*, 1976; *Bairamov et al.*, 2008; *Green et al.*, 2009; *Bochud*, 2011; *Cowgill et al.*, 2016). Knowledge of unit thicknesses are of primary importance for constructing cross sections, particularly for inferring the depth of subsurface contacts and structures. We use unit thicknesses inferred from mapped near-surface structural geometry, and our inferred thicknesses are consistent with previously reported thickness constraints (*Golubjatnikov and Dubogryzova*, 1959; *Voronin et al.*, 1959; *Khain and Shardanov*, 1960; *Nalivkin*, 1976; *Bairamov et al.*, 2008; *Green et al.*, 2009; *Bochud*, 2011). However, the lateral thickness and facies variations within the sedimentary rocks that make up the Eastern Greater Caucasus, lack of undeformed sections, and lack of publicly available subsurface data are sources of uncertainty, particularly for the highly-deformed rocks at the core of the range (*Golubjatnikov and Dubogryzova*, 1959; *Voronin et al.*, 1959; *Khain and Shardanov*, 1960; *Bairamov et al.*, 2008; *Green et al.*, 2009; *Bochud*, 2011). For simplicity, unit thicknesses are held constant within our cross sections, except where observations or thermochronometry data require otherwise. Therefore, depths to contacts and structures displayed in the cross sections, particularly in the highly-deformed core of the range, should not be regarded as definitive. Because we use a line balancing approach to calculate horizontal shortening, where the deformed length of individual beds or contacts are used to constrain shortening magnitudes and pre-deformation structure, uncertainties in unit thickness should have minimal impact on estimated shortening.

Our cross sections are balanced using a graphical line-balancing approach whereby the lengths of selected stratigraphic horizons are measured on a two-dimensional cross section and all such measured horizons must be of equal length in the pre-deformation geometry of the orogen (e.g., *Dahlstrom*, 1969; *Suppe*, 1983; *Woodward et al.*, 1989; *Suppe*, 1990). Because of the significant variability and uncertainty in thicknesses of deformed lithostratigraphic packages of the Eastern Greater Caucasus, line balancing of cross sections is likely to yield more accurate and precise shortening estimates than area balancing of cross sections, which relies on accurate knowledge of unit thicknesses (e.g., *Judge and*

Allmendinger, 2011).

7.3.2 Thermochronometry

We use a combination of new and existing (*Bochud*, 2011, Avdeev, unpublished) thermochronometry data to constrain the deformational history of the Eastern Greater Caucasus. New analyses are presented from thermochronometry samples that we collected throughout the Eastern Greater Caucasus (Figs. 7.1, 7.2; Tables 7.1, 7.2, 7.3, 7.4). Thermochronometric systems analyzed include (U-Th)/He in apatite (AHe; e.g., *Farley*, 2002; *Ehlers and Farley*, 2003) and zircon (ZHe; e.g., *Reiners et al.*, 2004; *Reiners*, 2005), as well as fission track in apatite (AFT; *Donelick et al.*, 2005). Nominal closure temperatures for these systems range from ∼60 °C for the AHe system to ∼110 °C for the AFT system and ∼180 °C for the ZHe system (e.g., *Reiners and Brandon*, 2006), which together permit inference of detailed cooling and exhumation histories. We present a total of 18 individual samples (Table 7.1), eight of which are from two vertical transects, comprising 62 AHe analyses (Table 7.2), 8 AFT analyses (Table 7.4), and 6 ZHe analyses (Table 7.3). Mineral separations were performed using standard mechanical, magnetic, and density separation techniques at the University of Michigan. New AHe and ZHe analyses were conducted at the University of Michigan (He analyses) and the University of Arizona (ICP-MS analyses), and AFT data were collected at the University of Arizona. Pre-existing AHe and AFT data (Avdeev, unpublished) were collected at Caltech and Apatite to Zircon, Inc., respectively.

In order to enhance interpretation of the thermochronometry data, two modeling approaches are applied to the data. For selected samples, we use a Bayesian inverse thermal modeling method, implemented in the program 'QTQt', to determine permissible cooling histories consistent with measured ages from multiple thermochronometric systems (*Gallagher*, 2012). In addition, we find evidence of post-cooling folding in strata from which we collected two vertical transects in the Eastern Greater Caucasus, and we use a simple model to investigate the effects of post-cooling rotation of sampled strata on the apparent age-elevation relationship of the samples. In the model, the samples are treated as being attached to a rigid block that has been rotated about a horizontal axis parallel to range strike by an unknown angle following complete closure (cooling) of all thermochronometric systems. Different candidate rotation angles yield different slopes of the relationship between age and present (post-rotation) elevation of the samples. Because the slope of the age-elevation relationship is mathematically equivalent to a vertical exhumation rate (e.g., *Brandon et al.*, 1998; *Farley et al.*, 2001), we are able to use independent constraints on exhumation rate to constrain the post-cooling rotation undergone by the sampled rocks and

assess the significance of this post-cooling rotation for deformation processes within the range.

Sample Name	longitude	latitude	elevation (m)	Rock type	Collection Name
H5	48.17775937	41.1447223	2806	Turbidite ss	17HAP02
H4	48.18026187	41.15102436	2539	Turbidite ss	17HAP03
H3	48.1932959	41.15053457	2284	Turbidite ss	17HAP04
H2	48.21016171	41.14282649	1964	Turbidite ss	17HAP05
H1	48.21690897	41.1397564	1796	Turbidite ss	17HAP06
S1	48.04431427	41.10641537	2556	Turbidite ss	16XIN04
S3	48.00682881	41.10642568	3251	Turbidite ss	16XIN07
S2	48.02790326	41.10100003	3017	Turbidite ss	16XIN08
L1	48.366586	40.84032	1173	Volcaniclastic ss	AB0867
L2	48.353808	40.841153	1188	Volcaniclastic ss	AZ0605
L3	48.345823	40.841128	1098	Volcaniclastic ss	AB0866
L4	48.339746	40.838003	1101	Volcaniclastic ss	AB0855
L5	48.334866	40.837371	1138	Volcaniclastic ss	AB0862
L6	48.307258	40.819571	1082	Volcaniclastic ss	AB0856
N1	48.071838	41.21152	2558	Turbidite ss	AB0890
N2	48.592548	41.048605	1176	Turbidite ss	AZ0619
N3	48.265042	41.206848	1622	Turbidite ss	AZ0620
N4	48.643753	41.011043	1259	Turbidite ss	AB0888

Table 7.1: Names and locations of thermochronometry samples. Sample name is how the sample is referred to in figures and discussion here, whereas collection ID is the original name designated upon field collection. Positive longitudes are east and positive latitudes are north. ss stands for sandstone.

Name	U (ppm)	Th (ppm)	Sm (ppm)	He (ncc)	Radius (um)	Length (um)	FT	Uncorrected Age (Ma)	Age (Ma)	Age Error (Ma)
H5b	28.07	60.56	75.31	0.017	41.7	86.1	0.70	2.33	3.33	0.03
H5c	15.59	65.82	335.77	0.013	47.9	88.3	0.73	1.76	2.41	0.03
H5e	136.88	146.20	294.53	0.090	40.4	123.7	0.71	2.62	3.70	0.03
H4b	30.32	76.39	144.02	0.025	46.4	106.9	0.73	2.15	2.93	0.03
H4c	3.19	9.12	180.42	0.011	57.0	132.5	0.78	3.68	4.71	0.06
H4d	3.66	87.54	316.53	0.013	44.6	110.9	0.73	1.97	2.71	0.03
H4e	3.50	30.79	257.77	0.011	58.5	115.7	0.78	2.02	2.58	0.03
H3d	2.84	47.12	119.48	0.018	47.9	120.1	0.75	4.29	5.76	0.06
H3e	16.99	49.03	194.67	0.036	48.6	100.7	0.74	5.07	6.84	0.06
H3f	12.21	53.74	502.64	0.015	44.2	97.2	0.72	2.72	3.77	0.05
H3g	16.43	34.49	185.95	0.013	44.2	121.9	0.73	1.85	2.54	0.03
H3h	5.13	27.39	185.96	0.011	47.1	150.6	0.75	2.19	2.92	0.03
H2d	109.92	327.59	160.27	0.037	40.2	87.9	0.69	1.34	1.93	0.02
H2e	26.04	52.25	142.82	0.050	51.9	143.1	0.77	3.31	4.31	0.04
H2j	5.96	17.23	232.17	0.010	46.4	90.1	0.73	3.99	5.50	0.06
H1b	1.14	11.48	23.82	0.010	51.9	159.5	0.77	4.82	6.26	0.08
H1c	9.06	40.84	29.33	0.035	66.9	120.1	0.81	3.33	4.14	0.04
H1d	5.69	19.88	247.64	0.021	54.1	170.5	0.78	3.73	4.78	0.05
H1e	1.00	36.99	203.89	0.022	60.1	164.3	0.80	3.50	4.39	0.05
S3a	44.09	92.69	257.36	0.038	43.3	129.0	0.73	2.31	3.18	0.09
S3c	13.44	45.40	342.67	0.029	55.4	156.8	0.78	2.36	3.02	0.06
S3d	9.14	75.92	520.77	0.015	43.5	106.4	0.72	2.36	3.28	0.04

S3f	72.47	115.92	409.11	0.046	39.5	113.7	0.70	2.54	3.64	0.03
L1a*	8.41	31.13	47.79	0.172	90.50	315.00	0.83	2.00	2.40	0.06
L1b*	7.08	26.80	64.86	0.130	73.50	300.00	0.80	1.77	2.21	0.06
L1c*	6.33	24.03	75.19	0.076	74.50	257.00	0.80	1.16	1.45	0.04
L1d*	6.63	38.76	108.85	0.083	48.50	158.00	0.69	0.95	1.38	0.08
L1e*	4.80	30.32	130.86	0.077	53.50	129.00	0.70	1.16	1.66	0.10
L1f*	7.46	47.23	134.06	0.061	41.00	149.00	0.65	0.59	0.92	0.07
L2a*	2.68	6.70	-	0.056	52	268.5	0.74	2.44	3.30	-
L2b*	3.79	16.89	-	0.087	42	261	0.68	2.05	3.00	-
L2c*	3.73	15.41	-	0.074	62.5	324	0.78	1.86	2.39	-
L2d*	1.95	5.47	-	0.038	73	283.5	0.80	2.15	2.69	-
L3a*	3.91	12.48	68.10	0.055	80.00	156.00	0.79	1.47	1.87	0.07
L3b*	5.15	27.92	93.82	0.098	51.50	167.00	0.71	1.51	2.14	0.10
L3c*	2.18	11.41	120.80	0.040	54.5	166	0.72	1.42	1.98	0.19
L4a*	3.29	25.22	102.89	0.054	53.00	177.00	0.72	1.06	1.48	0.09
L4b*	2.77	16.02	55.70	0.045	49.50	198.00	0.71	1.23	1.74	0.12
L4c*	8.52	40.59	119.69	0.207	65.50	227.00	0.77	2.08	2.70	0.08
L4d*	8.78	58.50	99.56	0.186	55.50	232.00	0.74	1.50	2.03	0.07
L5a*	5.94	38.86	83.04	0.116	56.00	200.00	0.73	1.39	1.90	0.07
L5b*	6.82	34.89	61.17	0.101	51.50	171.00	0.71	1.23	1.73	0.08
L5c*	1.64	7.14	126.30	0.029	64.00	147.00	0.74	1.47	1.98	0.16
L5d*	5.51	24.76	162.39	0.055	61.00	127.00	0.73	0.88	1.21	0.08
L6a*	6.38	38.52	74.86	0.057	42.50	124.00	0.65	0.66	1.03	0.10
L6e*	4.92	27.76	89.61	0.326	66.50	130.00	0.74	5.15	6.96	0.25

N1a*	6.08	139.43	192.91	0.589	40.00	136.00	0.63	2.75	4.40	0.18
N1b*	26.31	217.78	90.02	0.709	37.50	128.00	0.61	1.68	2.73	0.11
N1c*	8.09	222.48	270.78	0.473	41.50	115.00	0.62	1.42	2.29	0.09
N1d*	9.11	211.05	302.89	0.561	39.50	153.00	0.63	1.73	2.75	0.11
N1e*	28.08	192.29	101.03	1.119	38.50	133.00	0.62	2.80	4.48	0.17
N2c*	1.86	53.45	232.4	0.011	50.15	150.6	0.77	1.70	2.20	0.03
N2d*	25.51	219.78	389.14	0.105	41.08	129	0.71	6.20	8.74	0.07
N2e*	5.47	105.51	148.18	0.013	41.73	88	0.70	2.30	3.29	0.04
N2f*	67.93	118.73	314.28	0.260	40.19	169.2	0.72	10.10	14.04	0.11
N2g*	32.37	183.76	210.92	0.029	47.94	71.6	0.71	2.20	3.08	0.03
N3a*	25.41	37.91	-	8.920	55	192	0.74	47.59	64.33	-
N3b*	2.47	13.05	-	1.880	51.5	250.5	0.73	62.32	85.63	-
N3c*	4.83	25.00	-	5.240	45	241.5	0.70	89.32	128.29	-
N4a*	8.65	45.51	79.4	0.009	42.65	105.12	0.72	2.00	2.79	0.04
N4b*	21.69	63.23	363.62	0.026	50.13	115.72	0.75	2.29	3.04	0.03
N4c*	92.27	91.66	337.3	0.099	41.10	128.12	0.71	4.02	5.63	0.05

Table 7.2: Apatite (U-Th)/He results for individual grains. Data collected by Avdeev (unpublished) are marked with an asterisk (*) next to the sample name. For two samples (L2, N3) analyzed in June 2007, Sm concentrations were not measured and U and Th error was not reported, so age uncertainties cannot be calculated, so these quantities are marked with dashes (-). Subsequent analyses from the same instrument in November 2007 have typical age uncertainties of 2-3%.

Name	U (ppm)	Th (ppm)	Sm (ppm)	He (ncc)	Radius (um)	Length (um)	FT	Uncorrected Age (Ma)	Age (Ma)	Age Error (Ma)
H1a	308.20	156.21	0.00	0.00658	39.6	165.6	0.71	58.7	82.55	0.78
H1b	384.47	210.99	0.00	0.01120	41.7	203.6	0.73	85.3	116.92	1.08
H1c	625.99	401.68	0.00	0.00479	41.1	171.8	0.72	54.9	76.06	0.69
S1a	268.62	211.15	0.00	0.00105	40.4	130.8	0.71	10.7	15.04	0.13
S1b	623.22	282.11	0.00	0.00107	41.7	108.2	0.71	6.4	9.02	0.08
S1c	1125.90	552.21	0.00	0.00116	39.1	92.8	0.69	5.7	8.31	0.07

Table 7.3: Zircon (U-Th)/He results for individual grains.

Name	Number of grains	Central Age (Ma)	Error (Ma)	p_{χ^2}	Mean track length (μm)	Standard dev. (μm)
H3	20	8.21	1.08	0.99	-	-
H5	20	7.47	1.29	0.99	-	-
S1	8	15.53	4.27	0.64	-	-
S2	15	8.27	1.98	0.91	-	-
S3	15	6.14	1.33	0.91	-	-
L2	40	88.4	5.7	0.28	12.21	1.5
N1	39	14	1.6	0	12.56	2.23
N2	38	36.1	2.7	0	11.51	2.23

Table 7.4: Apatite fission track pooled sample ages. Individual grain data and track length data is available at https://doi.org/10.7302/gkqx-rc70. p_{χ^2} indicates the probability that individual grain ages of a sample are accurately described by a single age component.

7.4 Structural and thermochronometric results and interpretation

New structural and thermochronometry data from the Eastern Greater Caucasus constrain the timing, magnitude, and means of accommodation of shortening within an active accretionary prism. In describing the data, we proceed from south (the toe of the accretionary prism) to north (the interior of the prism). We proceed in this order because shortening inferred from the deformation of young and comparatively shallow crustal rocks at the toe of the prism constrains the net slip on major structures that underlie the range. Consideration of such constraints on net slip permits more accurate inference of subsurface structural geometries in the interior of the prism. For each of several mapped transects that together span the range across strike (Figs. 7.1, 7.2), we provide geological observations from the range, present new and existing thermochronometry results (*Bochud*, 2011, Avdeev, unpublished), make first-order structural interpretations, and describe the magnitude of horizontal shortening required by our structural interpretations.

The Azerbaijan portion of the Eastern Greater Caucasus has been the subject of several previous geological mapping investigations (e.g., *Golubjatnikov and Dubogryzova*, 1959; *Voronin et al.*, 1959; *Khain and Shardanov*, 1960; *Nalivkin*, 1976; *Bairamov et al.*, 2008). However, significant disagreements exist regarding the structural architecture of the range,

including the locations and slip senses of major and minor faults (*Khain and Shardanov*, 1960; *Nalivkin*, 1976; *Bairamov et al.*, 2008), and structural measurements are often not well-documented. Ages assigned to our mapped lithostratigraphic packages are largely based on biostratigraphic ages reported in prior mapping studies (*Golubjatnikov and Dubogryzova*, 1959; *Voronin et al.*, 1959; *Khain and Shardanov*, 1960; *Nalivkin*, 1976; *Bairamov et al.*, 2008). In some structurally complex areas, ambiguities introduced by differing contact locations and uncertainties in which lithologies were sampled for biostratigraphic dating led to uncertainties in structural interpretations, though such cases are rare and do not affect interpretations of the gross structural geometry of the range.

7.4.1 Agsu transect

The Agsu transect runs from the southern range boundary of the Eastern Greater Caucasus about 15 km northeast into the range (Figs. 7.1, 7.2). Of our four mapping transects, the exhumation depth of the Agsu transect is the least (Fig. 7.2), and the rocks exposed in the transect are dominantly Cenozoic (*Voronin et al.*, 1959; *Khain and Shardanov*, 1960; *Nalivkin*, 1976).

7.4.1.1 Geological description

Several distinct lithologies and structural styles are observed within the transect (Fig. 7.2, Agsu transect). Our observations within the transect are reported from south to north.

Exposed at the southern end of the transect is a sequence of predominantly coarse to medium sandstones, with lenses of conglomerates and siltstones to clays, and channelized bedforms (Fig. 7.2, Agsu transect). This sequence is reported as Pliocene to Quaternary in age and includes sandstones associated with the Pliocene Productive Series, a regionally extensive sandstone to conglomerate unit, (unit MPss; Fig. 7.2), as well as overlying strata deposited during the early Quaternary Akchagylian regional stage (unit Qss_1; Fig. 7.2) and the overlying Apsheronian regional stage (unit Qss_2; Fig. 7.2; *Voronin et al.*, 1959; *Khain and Shardanov*, 1960; *Nalivkin*, 1976). The sequence is dominantly south-younging and overturned, with bedding orientations dipping moderately to steeply northward (Fig. 7.2, Agsu transect). The lack of elevated topography and exposed bedrock to the south of this sequence suggests that foreland basin sedimentary strata are undisturbed to the south and therefore that this overturned sequence is the northern limb of an overturned syncline. An exception to the dominant bedding orientation within this sequence is a small anticline observed in some of the youngest exposed strata, near the southern margin of exposed bedrock of the range (Fig. 7.2, Agsu transect). The location of this small anticline is

consistent with its formation in order to accommodate shortening within the core of the overturned syncline of which these strata are part, potentially above an out-of-the-syncline thrust (*Dahlstrom*, 1970; *Butler*, 1982).

To the north of the overturned, south-younging Pliocene to Quaternary sandstone sequence, the depth of exhumation increases. The Pliocene to Quaternary sequence is bounded to its north by a major thrust fault of which it is the footwall. We call this fault the Agsu thrust for convenience (Fig. 7.2, Agsu transect). In the hanging wall of the Agsu thrust is a sequence of coarse sandstones to shales interpreted to be turbiditic of Eocene to Miocene age, which are associated with the regionally extensive, dominantly flyschoid packages of the Koun Suite and Maikop Series (unit EMtb; e.g., *Voronin et al.*, 1959; *Khain and Shardanov*, 1960; *Nalivkin*, 1976; *Alizadeh et al.*, 2016). This sequence forms a coherent, moderately north-dipping panel immediately to the north of the Agsu thrust, but further to the north, the orientation of bedding planes becomes more variable, ranging between moderate northward dip angles to steep southward dip angles (Fig. 7.2, Agsu transect). Between the Agsu thrust and the northern end of the Agsu transect, this sequence is unconformably overlain by conglomerates and sandstones in two localized areas (Fig. 7.2, Agsu transect). In the southern of these two areas, the overlying deposits are of Quaternary age (Akchagyl regional stage; *Voronin et al.*, 1959; *Nalivkin*, 1976), whereas in the northern area, the overlying deposits are of Late Miocene age (Pontian regional stage; *Voronin et al.*, 1959; *Nalivkin*, 1976). At the northern extent of the Agsu mapping transect, turbidites of the Eocene to Miocene sequence (EMTb) are structurally overlain by thrusted Upper Cretaceous marine sandstones (unit UKblss; Fig. 7.2, Agsu transect).

7.4.1.2 Structural interpretation

This transect permits us to make several first-order structural interpretations, which are aided by a structural cross section constructed from the surface geology (Fig. 7.3). The transect contains two major thrust faults, the Agsu thrust, which juxtaposes an Eocene to Miocene turbidite sequence (EMtb) in the hanging wall against a Pliocene to Quaternary sandstone sequence in the footwall (MPss, Qss_1, Qss_2); and the thrust at the northern end of the transect that places Cretaceous marine sandstones (UKblss) over the Eocene to Miocene shale-rich sequence (Fig. 7.2, Agsu transect; Fig. 7.3). In addition, the variable bedding planes of the Eocene to Miocene turbidite sequence (EMtb) indicates significant deformation confined to this sequence. Here, we discuss the constraints the surface geology places on the two major thrust faults and internal deformation of the Eocene to Miocene turbidite sequence (EMtb).

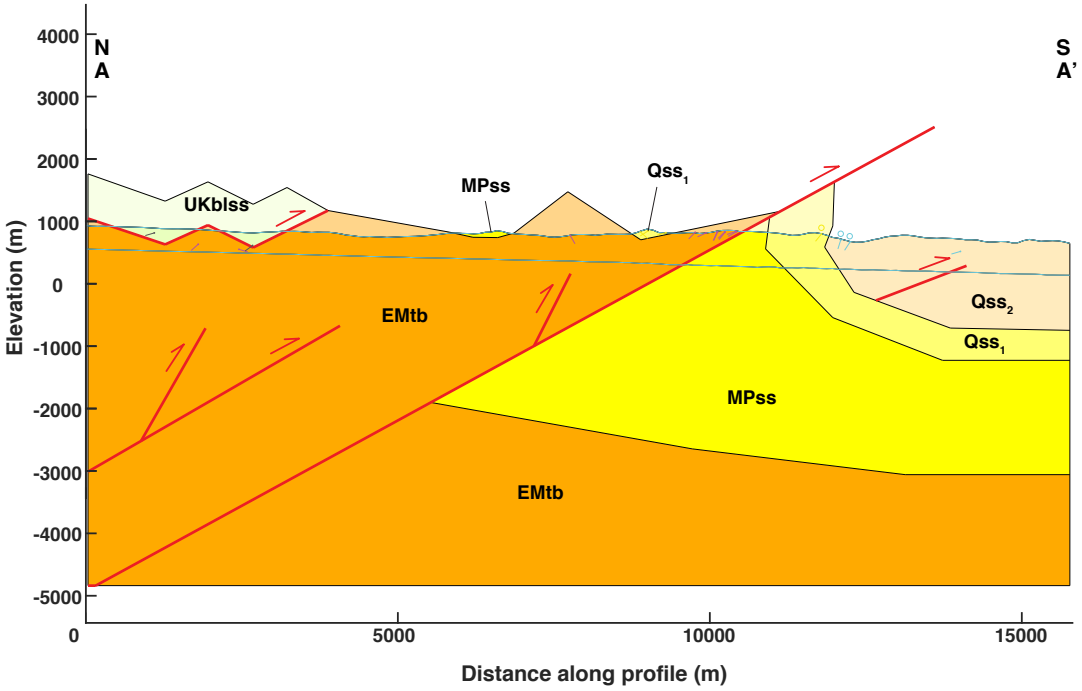

Figure 7.3: Interpretive structural cross section of the Agsu transect (Fig. 7.2, Agsu panel). Geologic units are as depicted in Figure 7.2. Dipticks show measured bedding planes, projected from within 5 km from the line of section. A diptick with an open circle above indicates an overturned bed. The two topographic profiles show the highest and lowest topography within 5 km perpendicular to the line of section.

7.4.1.2.1 Agsu thrust

Because there is no significant topography nor exposed bedrock to the south of the Agsu transect, it is reasonable to conclude that the Agsu thrust, the southernmost major structure of the Eastern Greater Caucasus at this longitude, is the range-bounding thrust. The predominantly moderate north dip (30-50° is typical) of sandstones and shales immediately to the north of the Agsu thrust (Fig. 7.2, Agsu transect) is consistent with a moderate fault dip (30° is depicted in Fig. 7.3). Assuming that the Agsu thrust soles into a subhorizontal detachment at depth and that the Eocene to Miocene turbidite sequence (EMtb) that immediately overlies the fault was deposited on a horizontal or low-gradient surface, the depth to detachment is constrained by the thickness of overlying units preserved to the south to be 4-5 km (*Voronin et al.*, 1959, Fig. 7.3). Such a depth is consistent with the range-bounding structure geometry inferred ∼20 km to the west, where displacement on the structure has caused the formation of a foreland basin fold and thrust belt (*Forte et al.*, 2013, Fig. 7.1). The geometry of the footwall is consistent with fault-propagation folding (*Erslev*, 1991, and references therein), implying that displacement on the Agsu thrust has been limited. Such an inference is supported by the geometries of the younger sandstones that unconformably overlie the Eocene to Miocene shale sequence (Fig. 7.3). Limited displacement on the Agsu thrust is also consistent with the inferred geometry of the range-bounding structure beneath the foreland basin fold and thrust belt to the west, where the fault terminates in fault-propagation folds and does not break the surface (*Forte et al.*, 2013).

7.4.1.2.2 Northern thrust

The second major fault exposed in the Agsu transect is the fault that emplaces Upper Cretaceous marine sandstones (UKblss) over the shale-rich Eocene to Miocene turbidite sequence (EMtb). Vertical relations between these two units indicate unambiguously that the Cretaceous strata are thrust over the younger rocks (Fig. 7.2, Agsu transect; Fig. 7.3). The continuous exposure of Eocene and younger strata to the south of this fault indicates that the transport direction of the fault is to the south. The Agsu transect contains only the southernmost extent of the thrust sheet and the subsurface geometry of this thrust is discussed in conjunction with the Lahij transect, where surface geology constrains the thrust geometry (Fig. 7.2, Agsu transect).

7.4.1.2.3 Internal deformation within the Eocene to Miocene turbidite sequence (EMtb)

The space between the two major faults of the Agsu transect is dominantly occupied by the Eocene to Miocene turbidite sequence (EMtb; Fig. 7.3). The surface exposure of this

sequence in the Agsu transect, combined with the inference that its stratigraphic base is at least as deep as the 4-5 km deep detachment rooted into by the Agsu thrust, indicates that the sequence has been tectonically thickened by a factor of 3-4 north of the Agsu thrust (Fig. 7.3). Given the outcrop pattern observed in the Agsu transect, this thickening must have occurred largely by faults and folds entirely confined to the Eocene to Miocene turbidite sequence (Fig. 7.2, Agsu transect; Fig. 7.3). Figure 7.3 shows a combination of imbricate faults that may have produced the inferred thickening of the sequence, although these faults are not observed to break the surface. These faults are located along strike from an antiformal stack above a decollement located in the same sequence to the west (*Forte et al.*, 2013), and an antiformal stack architecture within our Agsu transect would also be consistent with the constraints from surface geology.

Taken together, several important structural inferences can be made from the Agsu transect. First, hanging-wall and footwall geometries suggest that the range- bounding structure of the Eastern Greater Caucasus terminates in a fault-propagation fold and therefore has not accommodated significant slip relative to the amount of shortening that is likely recorded across the range. Second, the Eocene to Miocene turbidite sequence (EMtb) to the north of the range-bounding fault has been tectonically thickened several times over by folds and faults, though the exact structure is difficult to determine because of the poor exposure and propensity for folding of this shale-rich sequence. Finally, the Eocene to Miocene turbidite sequence is overlain by a thrust sheet transporting Upper Cretaceous marine sandstones (UKblss) from the north.

7.4.1.3 Shortening estimate

We estimate the horizontal shortening required to produce our inferred structural geometry. Because of the lack of consistent exposure of the Eocene to Miocene turbidite sequence (EMtb; Fig. 7.2, Agsu transect), conducting a line-balanced estimate of structural shortening would be extremely difficult on this transect. Instead, for this transect we use an area-balancing approach. Though area balancing carries significant uncertainties where stratigraphic thicknesses are uncertain (e.g., *Judge and Allmendinger*, 2011), we feel that an area-balancing approach is justified for this section because it is not structurally complex (Fig. 7.3) and an independent estimate exists of the shortening accommodated by a structurally analogous portion of the range located nearby along strike (*Forte et al.*, 2013). We perform an area balance on the Eocene to Miocene turbidite sequence (EMtb; Fig. 7.3), finding that the cross sectional area occupied by the sequence is 61 km^2 (Fig. 7.3). Given the section length of 15.75 km (Fig. 7.3) and the reported sequence thickness of $\sim$1.85 km (*Voronin et al.*, 1959), the measured cross sectional area of 61 km^2 implies that at least

$\sim$17 km of horizontal shortening is accommodated within the section. This magnitude is consistent with the 18 km of shortening inferred in the structurally analogous portion of the range 20 km to the west (*Forte et al.*, 2013).

The amount of erosion in the transect is unknown and affects our shortening estimate. The calculated shortening estimate is a minimum, and any eroded material that was removed from the section would imply additional horizontal shortening. However, the fault-propagation fold geometry of the range-bounding Agsu thrust, as well as the presence of Upper Miocene and Lower Quaternary sedimentary deposits overlying deformed Eocene to Miocene turbidites (Fig. 7.3) suggest that the amount of eroded Eocene to Miocene turbiditic material is minor. If the projected extent of EMtb above modern ground level (Fig. 7.3) is added to the area-balancing calculation, then 1 km of additional shortening is implied. Therefore, the cross-sectional area of eroded material may affect our shortening estimate by several km, but likely no more than that.

7.4.2 Lahij transect

The Lahij transect is located about 15 km northwest along strike from the northern extent of the Agsu transect and extends from exposures of the Eocene to Miocene turbidite sequence (EMtb) along strike from the northern Agsu transect into the Mesozoic rocks of the southern slope of the Eastern Greater Caucasus (Fig. 7.1; Fig. 7.2, Lahij transect). The transect includes rocks of Middle Cretaceous to Miocene age (*Khain and Shardanov*, 1960; *Nalivkin*, 1976; *Bairamov et al.*, 2008).

7.4.2.1 Geological description

The Lahij transect contains several lithologically-distinct stratigraphic packages and is structurally complex (Fig. 7.1; Fig. 7.2, Lahij transect). Of particular note within the transect are structurally nearly-adjacent sequences of the same age and very different lithologies, suggesting significant displacement on faults within the transect. Again, we discuss the geologic observations from this transect from south to north.

Proceeding from south to north within the transect, the first sequence encountered is composed of dark gray, thinly bedded sandstones and shales mapped as Eocene to Miocene (*Khain and Shardanov*, 1960; *Nalivkin*, 1976) and inferred to belong to the Eocene to Miocene turbidite sequence (EMtb; Fig. 7.2, Lahij transect). Moving to the north, we observed sandstone to shale and marl lithologies mapped as Upper Cretaceous to earliest Paleogene (Danian stage; *Khain and Shardanov*, 1960; *Nalivkin*, 1976). The observed lithologies include a sequence of red to blue mudstones with 2-4 cm thick white to gray

sandstones that have been chaotically folded and boudinaged, likely reflecting proximity to a fault (UKrbfb), as well as stratigraphically- and structurally-overlying, white to gray sandstone-shale sequences (UKblss; Fig. 7.2, Lahij transect). The fault-related disruption of the stratigraphically lowest portion of this package suggests that the package is tectonically transported along a thrust fault. The southernmost exposures of the Upper Cretaceous to Danian package in the Lahij transect is inferred to represent the southern margin of the hanging wall of this thrust (Fig. 7.2, Lahij transect). This inferred thrust sheet has been previously referred to as the Basgal Nappe (e.g., *Khain*, 2007; *Bochud*, 2011; *Alizadeh et al.*, 2016). Inconsistent bedding geometries within the white to gray sandstone suggest folding on 100 m to 1 km wavelengths (Fig. 7.2, Lahij transect).

Bedding orientations and observed lithologies to the north suggest that the thrust on which the Basgal Nappe is transported breaks the surface to the north of the thrust sheet. The northernmost measured exposure of the white to gray sandstone sequence (UKblss) in this part of the range dips to the south (Fig. 7.2, Lahij transect). To the north of this outcrop, chaotically folded and brecciated red and blue mudstones (UKrbfb) structurally overlie dark gray shales with thin (2-4 cm) sandstone interbeds mapped as Eocene to Miocene (EMtb), suggesting a thrust between the two sequences.

The stratigraphic package north of the Basgal nappe thrust sheet is broadly south dipping and south younging. The Eocene to Miocene turbidite sequence (EMtb) directly beneath the thrust sheet has inconsistent bedding and is poorly exposed (Fig. 7.2, Lahij transect). Directly to the north, a broadly south-dipping, locally folded sequence of thin, blue gray sandstones to muddy carbonates mapped as Upper Cretaceous is exposed (UKvc; *Khain and Shardanov*, 1960; *Nalivkin*, 1976, Fig. 7.2, Lahij transect). Moving to the north within this broadly south-younging stratigraphic package, the next oldest lithology is a sequence of black to brown turbidites, thick bedded (>1 m) volcaniclastic sandstones, and tuffs mapped as Middle Cretaceous (MKvvc; *Khain and Shardanov*, 1960; *Nalivkin*, 1976; *Kopp*, 1985, Fig. 7.2, Lahij transect). This volcaniclastic sequence is bounded on the north side by a fault, to the north of which is the stratigraphically underlying sequence, which is composed of thinly bedded, calcareous gray sandstones and shales mapped as Lower Cretaceous (*Khain and Shardanov*, 1960; *Nalivkin*, 1976, LKvcss). Bedding orientations on both sides of the fault suggest a south directed thrust, in which the Lower Cretaceous sequence constitutes the hanging wall and the Middle Cretaceous sequence is the footwall (Fig. 7.2, Lahij transect), and the small stratigraphic offset across the fault indicates that net displacement can be no more than several kilometers (Fig. 7.2, Lahij transect). Together, these lithologies are referred to as the Vandam Zone (e.g., *Kopp*, 1985; *Khain*, 2007; *Alizadeh et al.*, 2016). The Vandam Zone is a coherent tectonostratigraphic package that

extends along the southern margin of the Eastern Greater Caucasus throughout Azerbaijan (e.g., *Kopp*, 1985; *Khain*, 2007; *Alizadeh et al.*, 2016).

To the north, the Vandam Zone sequences are deformed in an anticline-syncline pair. The Lower Cretaceous calcareous sandstone-shale sequence (LKvcss) sits at the core of a broad anticline, the southern limb of which extends to the Basgal nappe thrust sheet as discussed above (Fig. 7.2, Lahij transect). To the north of the core of this anticline, bedding planes dip to the north and the stratigraphic younging direction is northward. The Lower Cretaceous calcareous sandstone-shale sequence (LKvcss) passes upward into the Middle Cretaceous volcaniclastic sequence (MKvvc). Near the stratigraphic top of the volcaniclastic sequence is the core of a large syncline, to the north of which the volcaniclastic sequence repeats in a subvertically-dipping panel with a southward stratigraphic younging direction (Fig. 7.2, Lahij transect).

The Middle Cretaceous volcaniclastic sequence (MKvvc) is bounded to its north by a fault, which divides this Cretaceous sequence from a thinly bedded sandstone-shale turbidite sequence mapped as Eocene to Miocene (EMtb; Fig. 7.2, Lahij transect, Fig. 7.4a; *Khain and Shardanov*, 1960; *Nalivkin*, 1976). The fault dips to the north, and the Eocene to Miocene turbidite sequence (EMtb) is in the hanging wall and the Middle Cretaceous volcaniclastic sequence (MKvvc) is in the footwall, suggesting that this is a normal fault (Fig. 7.2, Lahij transect, Fig. 7.4a). To the north of this normal fault, the Eocene to Miocene turbidite sequence is deformed in a series of close to isoclinal folds with wavelengths of order 100 m to 1 km (Fig. 7.2, Lahij transect).

The Eocene to Miocene turbidite sequence (EMtb) is bounded on its northern margin by chaotically folded red and blue mudstones with brecciated sandstone interlayers mapped as Upper Cretaceous (UKrbfb; Fig. 7.2, Lahij transect; Fig. 7.4b; *Khain and Shardanov*, 1960; *Nalivkin*, 1976). These intensely deformed rocks are inferred to be proximal to a fault, termed the Zangi thrust in the literature (e.g., *Khain*, 2007; *Alizadeh et al.*, 2016). These intensely deformed rocks are exposed over a band about 0.5 km wide across strike (Fig. 7.2, Lahij transect).

To the north of the intensely deformed band associated with the Zangi thrust is a faulted and folded, broadly south-younging tectonostratigraphic package consisting of sandstones and shales mapped as Cretaceous (Fig. 7.2, Lahij transect; *Khain and Shardanov*, 1960; *Nalivkin*, 1976). To the immediate north of the deformed red and blue mudstones is a sequence of blue to white sandstones with cross bedding and load casts interbedded with gray mudstones mapped as Upper Cretaceous (UKblss; Fig. 7.2, Lahij transect; *Khain and Shardanov*, 1960; *Nalivkin*, 1976). To its north, this sequence is bordered by an interval of chaotically folded red and blue mudstones with brecciated sandstone interlay-

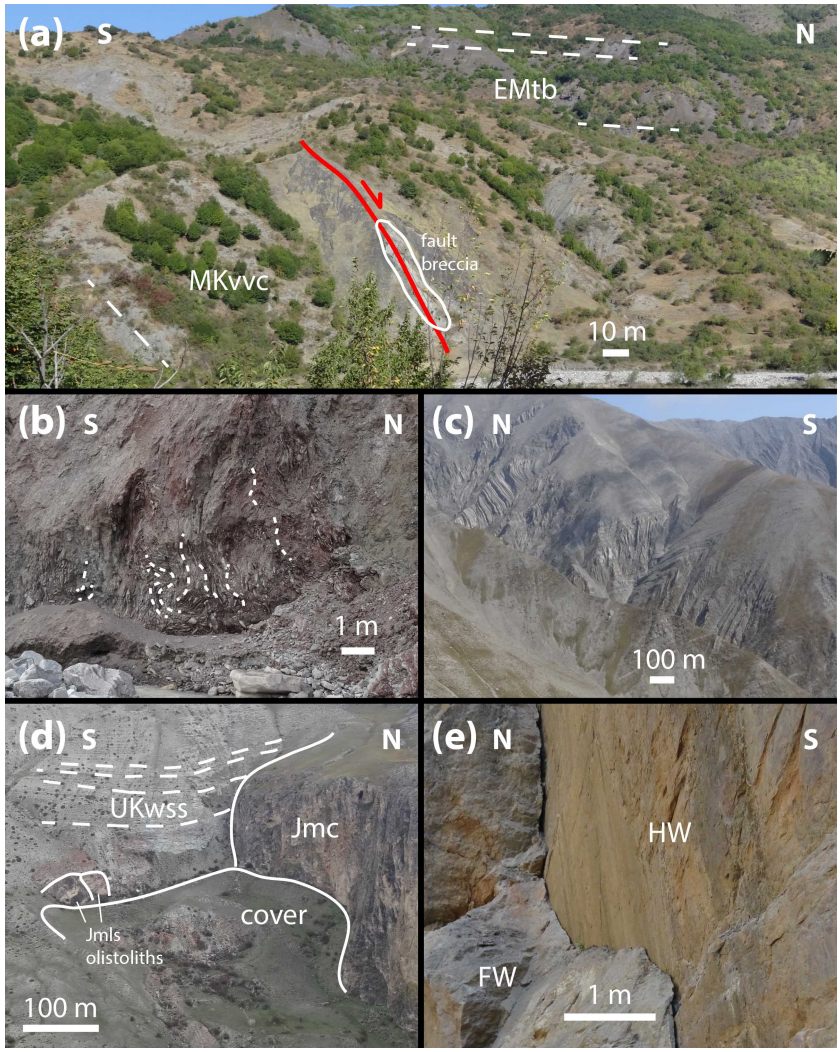

Figure 7.4: Photographs of several important field relations in the Eastern Greater Caucasus. Approximate orientation is depicted in each photo and unit names are as in Figure 7.2. (a) The northern margin of the Vandam Zone tectonostratigraphic package is bounded to the north by a north dipping normal fault near the town of Lahij (Fig. 7.2, Lahij panel). Dashed white lines are bedding planes. (b) Immediately structurally above the Zangi thrust is a $\sim$0.5 – 1 km thick zone of chaotically folded red and blue shales with sandstone interbeds that have been brecciated and boudinaged (Fig. 7.2, Lahij panel). Dashed white lines show bedding planes. (c) Much of the southern slope of the Eastern Greater Caucasus is dominated by close to tight asymmetric folds on 0.5 – 1 km wavelengths. Shown here are folds in Lower Cretaceous turbidites (LKtb) at Babadag. (d) A steep angular unconformity in the northern part of the range where Upper Jurassic massive carbonate (Jmc) is unconformably overlain by Upper Cretaceous white sandstone (UKwss). Dashed lines show bedding planes, solid lines show contacts. (e) A normal fault in the northern part of the range juxtaposes Upper Jurassic massive carbonate (Jmc) in the footwall (FW) against Lower Cretaceous bedded carbonate (LKbc) in the hanging wall (HW).

ers similar to the lithology observed associated with the Zangi thrust (UKrbfb; Fig. 7.2, Lahij transect). Beyond this deformed zone to the north is a broadly north-dipping and north-younging panel consisting of a sequence of red and blue mudstones with thin sandstone interbeds mapped as Upper Cretaceous (UKrbsh; Fig. 7.2, Lahij transect; *Khain and Shardanov*, 1960; *Nalivkin*, 1976) stratigraphically overlain by blue to white sandstones with gray mudstone interlayers (UKblss; Fig. 7.2, Lahij transect; *Khain and Shardanov*, 1960; *Nalivkin*, 1976). To the north of this panel is a broadly south-younging package that comprises from south to north an overturned, south-younging sequence of Upper Cretaceous red and blue mudstones (UKrbsh; Fig. 7.2, Lahij transect; *Khain and Shardanov*, 1960; *Nalivkin*, 1976); a blue to gray sandstone and shale sequence inferred from bedding orientations and contacts to stratigraphically underlie the red and blue mudstones (MKrbsh; Fig. 7.2, Lahij transect; *Khain and Shardanov*, 1960; *Nalivkin*, 1976); and a brown to black turbiditic sandstone-shale sequence mapped as Lower Cretaceous with cross bedding, load casts, and cone-in-cone structures (LKtb; Fig. 7.2, Lahij transect; *Khain and Shardanov*, 1960; *Nalivkin*, 1976). We note that because of the structural complexity of this tectonostratigraphic package and the differing age and structural interpretations depicted on prior geologic maps (e.g., *Khain and Shardanov*, 1960; *Nalivkin*, 1976), our understanding of the stratigraphic order of Middle to Upper Cretaceous lithologies within this package is somewhat uncertain. We address this uncertainty and its implications for deformation in the range in the Structural Interpretation section.

7.4.2.2 Thermochronometric data

Thermochronometric ages are reported from six samples from the Lahij transect (Tables 7.1, 7.2, 7.3, 7.4; Fig. 7.2, Lahij transect; Avdeev, unpublished). All six samples were collected from the Middle Cretaceous volcaniclastic sequence (MKvvc) of the Vandam Zone in the central region of the transect (Fig. 7.2, Lahij transect). Analyzed apatites from this volcaniclastic sequence have euhedral shapes and were likely derived from proximal igneous sources. The AHe system was analyzed in all six samples, yielding sample mean ages ranging between 1.5 and 4.0 Ma (Table 7.2; Fig. 7.2, Lahij transect; Avdeev, unpublished). In sample L2, the AFT system was also analyzed, yielding an age of 88.4 $\pm$ 5.7 Ma (Table 7.4; Fig. 7.2, Lahij transect; Avdeev, unpublished). This age is similar to the mapped Middle Cretaceous (Cenomanian) age of the rock (*Khain and Shardanov*, 1960), as well as the age of detrital zircons derived from the volcaniclastic portions of the Vandam Zone ($\sim$105 Ma; Tye et al., submitted), suggesting the AFT age corresponds to apatite crystallization or cooling shortly thereafter.

We use thermal modeling to infer a set of time-temperature histories that are likely

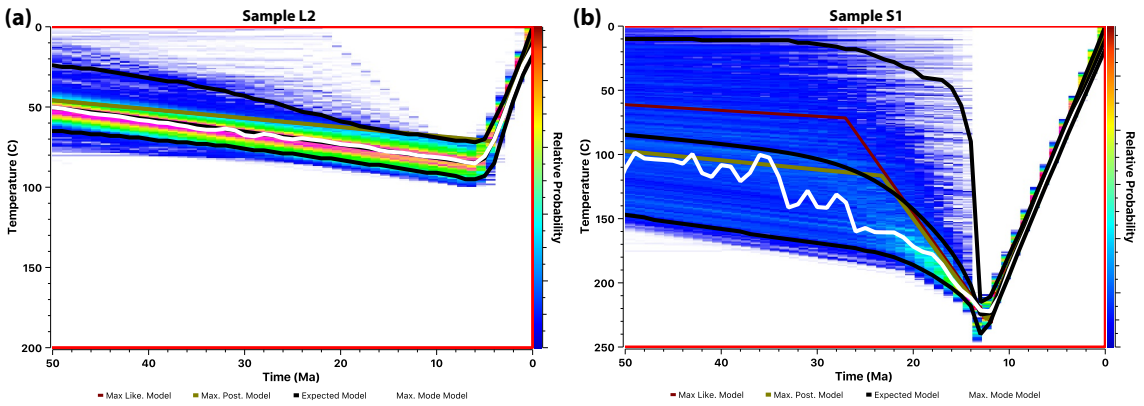

Figure 7.5: Permissible time-temperature histories for thermochronometry samples L2 (Avdeev, unpublished; a) and S1 (b), inferred using the Bayesian inverse thermal modeling software QTQt (*Gallagher*, 2012).

to have produced the observed thermochronometric ages in sample L2 (*Gallagher*, 2012), which has an unreset AFT age and Pliocene to Quaternary AHe ages (Table 7.2; Fig. 7.5a). The likely time-temperature paths indicated by thermal modeling of the sample are well constrained and are characterized by burial from the middle Cretaceous until ∼6 Ma, with subsequent cooling of ∼90° C (Fig. 7.5a). For geothermal gradients of 20 - 30° C, such cooling equates to 3.0 – 4.5 km exhumation at an average rate of 0.50 – 0.75 mm/yr since 6 Ma. The cooling history of this Vandam Zone volcaniclastic (MKvvc) sample provides an important constraint on the structural interpretation of the Lahij transect.

7.4.2.3 Structural interpretation

Several features of the Lahij transect are of significant structural importance. These include the Basgal nappe thrust sheet and the lithologic contrast between the Vandam Zone tectonostratigraphic package and the northern tectonostratigraphic package exposed in the Lahij transect. We first discuss these features, then explore their implications, together with inferences from the Agsu transect, for the subsurface geometry of the Lahij transect (Fig. 7.6).

7.4.2.3.1 Basgal nappe thrust sheet

The Basgal nappe thrust sheet is bounded by a fault or faults that break the surface both to the north and to the south south and juxtapose Upper Cretaceous sedimentary strata in the hanging wall against Eocene to Miocene strata in the footwall (Fig. 7.2, Lahij transect). The southern extent of the Basgal nappe thrust sheet in the Lahij transect is structurally contiguous with the Upper Cretaceous sedimentary rocks observed thrust over Eocene to Miocene

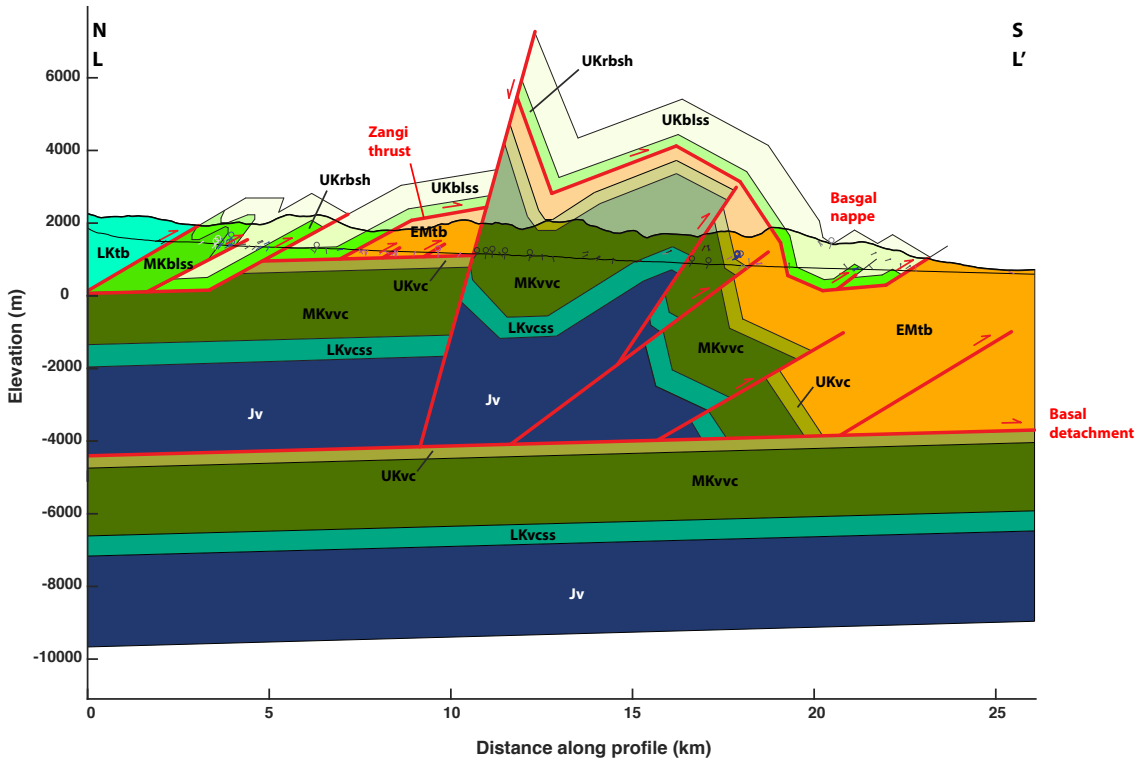

Figure 7.6: Interpretive structural cross section of the Lahij transect (Fig. 7.2, Lahij panel). Geologic units are as depicted in Figure 7.2, with the addition of Jv, the Jurassic sequence of the Vandam Zone, which we did not encounter at the surface. Dipticks indicate measured bedding orientations projected from within 5 km of the line of section, with an open circle over a diptick indicating an overturned bed. The two topographic profiles show the highest and lowest topography within 5 km perpendicular to the line of section.

strata at the northern end of the Agsu transect, indicating that the Basgal Nappe thrust sheet is laterally continuous along strike (Fig. 7.2, Agsu transect; *Khain and Shardanov*, 1960; *Nalivkin*, 1976). The lithologies of the Basgal nappe thrust sheet, which include Upper Cretaceous red and blue mudstones contorted and brecciated by a structurally proximal thrust fault (UKrbfb) and an overlying Upper Cretaceous sandstone-shale sequence (UKblss) correspond with the lithologies of Upper Cretaceous strata in the hanging wall of the Zangi thrust, which also include chaotically deformed red and blue mudstones (UKrbfb) and an overlying sandstone-shale sequence (UKblss; Fig. 7.2, Lahij transect, Fig. 7.4b; Fig. 7.6). Therefore, one reasonable hypothesis is that the Basgal Nappe was transported from the north along the Zangi thrust (Fig. 7.6). On the other hand, if the Basgal nappe thrust sheet were not transported from the north, it would be expected to share the facies of equivalently-aged rocks of the Vandam Zone, with which it is in structural contact. In the Vandam Zone, the Upper Cretaceous is dominated by muddy carbonates (UKvc), and lacks the distinctive red and blue mudstone sequence associated with both the Zangi thrust (Fig. 7.4b) and the Basgal Nappe (Fig. 7.2, Lahij transect). The lithologies of the Basgal Nappe therefore reflect tectonic transport from north of the Vandam Zone sequences, likely along the Zangi thrust (Fig. 7.6).

The structural geometry of the Basgal nappe thrust sheet also suggests derivation from the north. Given the across-strike width of the Basgal nappe thrust sheet (Fig. 7.6) and the structural thickness of the Eocene to Miocene strata it is thrust over (Figs. 7.3, 7.6), unrealistically steep thrust faults ($\sim$80° dip) would be required to uplift the thrust sheet as a pop-up structure (Fig. 7.6). In contrast, the fault geometry implied by exposures in the Agsu transect is largely subhorizontal (Fig. 7.2, Agsu transect; Figs. 7.3, 7.6). The structural geometries and exhumation depth of the Cenozoic strata of the Agsu transect, which can largely be extrapolated along strike to south of the Lahij transect, indicate that the Basgal nappe could not have been transported northward from a location closer to the southern toe of the range (Fig. 7.2, Agsu transect; Fig. 7.3). Thus, tectonic transport of the Basgal nappe thrust sheet from the north is the most likely explanation for our observations, and the basal fault of the thrust sheet is likely the southern extension of the Zangi thrust (Fig. 7.6; e.g., *Khain*, 2007; *Bochud*, 2011; *Alizadeh et al.*, 2016).

7.4.2.3.2 Lithologic contrast and structural relationship between Vandam Zone and northern tectonostratigraphic packages

The broadly south-younging Cretaceous tectonostratigraphic package exposed at the northern end of the Lahij transect is coeval with the Vandam Zone tectonostratigraphic package exposed to the south, though the two tectonostratigraphic packages differ greatly in

lithology and structural style (Fig. 7.2, Lahij transect). The lithology of the northern tectonostratigraphic package is characterized dominantly by thin (<10 cm) bedded turbiditic sandstone-shale sequences, and this tectonostratigraphic package deforms easily, forming close to isoclinal folds of wavelengths ranging from 100m to 1 km and a large number of small-displacement intraformational thrust faults (Fig. 7.2, Lahij transect). In contrast, the Vandam Zone tectonostratigraphic package is cored by a sequence of thick ($\leq$ 5 m) bedded volcaniclastic sandstones and tuffs, and this sequence appears to limit folding of the tectonostratigraphic package to 5 – 10 km wavelengths (Fig. 7.2, Lahij transect; Fig. 7.6). The volcaniclastic strata of the Vandam Zone are lithologically similar to Cretaceous lithologies penetrated by scientific drilling in the Kura basin to the south of the Eastern Greater Caucasus (*Agabekov and Moshashvili*, 1978) and Cretaceous rocks exposed in the Lesser Caucasus (e.g., *Kopp and Shcherba*, 1985; *Nalivkin*, 1976). As will be discussed later, the thin sandstone to mudstone strata exposed in the northern extent of the Lahij transect (Fig. 7.2, Lahij transect) are broadly similar to the lithologies exposed in the core of the Eastern Greater Caucasus. Thus, the Lahij transect contains the contact between two regionally extensive and lithologically distinct stratigraphic packages.

The lithological contrast between the northern tectonostratigraphic package of the Lahij transect and the Vandam Zone tectonostratigraphic package suggests significant slip on one or more of the structures that separate these two tectonostratigraphic packages. Two structures separate the northern tectonostratigraphic package from the Vandam Zone: the Zangi thrust and the normal fault that forms the northern boundary of the Vandam Zone strata. The present distance between the southern margin of the Basgal nappe thrust sheet, which belongs to the northern stratigraphic package, and the main exposure of the Zangi thrust indicates greater than 15 km of slip on the Zangi thrust (Fig. 7.2, Lahij transect, Fig. 7.6). In contrast, the steep dip of the normal fault that bounds the Vandam Zone, combined with map thicknesses of offset units and footwall thermochronometry data that suggest $\sim$3-4 km exhumation, limit net slip to <5 km. Thus, the significant lithologic differences between the northern and Vandam Zone tectonostratigraphic packages can best be explained as a product of the accumulation of significant slip on the Zangi thrust.

7.4.2.3.3 Subsurface structure of the Lahij transect

We infer a hypothesized subsurface structure of the Lahij transect (Fig. 7.6) based on surface geology and constraints from the thermochronometry data presented above and shortening estimates from the Agsu transect (Fig. 7.2, Agsu transect). The locations of surface-breaking faults and surface and near-surface structures are well constrained due to the bedrock exposure in the map area. Here, we discuss our inference of four aspects of

the subsurface structure (Fig. 7.6): the variable thickness of the Eocene to Miocene turbidite sequence (EMtb), the subsurface structure of the normal fault that forms the northern boundary of exposed Vandam Zone, the duplication of the Vandam Zone stratigraphic package, and the location of the footwall ramp beneath the Zangi thrust.

In our reconstruction, the depicted thickness of the Eocene to Miocene turbidite sequence (EMtb) is variable (Fig. 7.6). Inferred thickening of the sequence in the southern portion of the transect is based on the depth to the base of the unit inferred from the Agsu transect (Fig. 7.2, Agsu transect) and is attributed to structural duplication, similarly to the Agsu transect (Fig. 7.3). Prior mapping in the area indicates a variable thickness of the Eocene to Miocene turbidite sequence (EMtb) in the Lahij transect between the Basgal nappe thrust sheet and the structurally underlying Vandam Zone (*Khain and Shardanov*, 1960; *Nalivkin*, 1976). Map thickness estimates of the sequence within our Lahij transect range from 0.5 – 0.75 km at most (as depicted in Fig. 7.6) to complete absence of the sequence in some areas (*Khain and Shardanov*, 1960; *Nalivkin*, 1976). This variation in thickness has been attributed to erosion (e.g., *Alizadeh et al.*, 2016), although an alternative explanation is that the variable thickness is due to the structural removal of the sequence along the thrust that emplaced the Basgal nappe thrust sheet. Whether the removal of some of the Eocene to Miocene turbidite sequence (EMtb) beneath the Basgal nappe thrust sheet is due to erosion or thrusting does not significantly impact our structural reconstruction of the Eastern Greater Caucasus or shortening estimates.

A normal fault marks the northern boundary of surface exposures of the Vandam Zone stratigraphic package (Fig. 7.2, Lahij transect; Fig. 7.6). The footwall of the fault is a vertically-dipping, south-younging fold limb and is part of an asymmetric anticline-syncline pair in which north-younging limbs dip moderately to the north and south-younging limbs dip steeply to the south or are vertical to overturned (Fig. 7.2, Lahij transect; Fig. 7.6). This asymmetric fold geometry suggests generation by fault-propagation folding above north dipping thrust faults (*Suppe*, 1990; *Erslev*, 1991). Thus, the observed north dipping normal fault may be a reactivated thrust. If so, it is plausible that the hanging wall of the fault returned to its original, pre-thrusting geometry (as shown in Fig. 7.6). Such a scenario is depicted in our structural reconstruction (Fig. 7.6) because it is the geometrically simplest scenario and is consistent with unit map thicknesses. Tectonic extension has been observed in other accretionary prisms (e.g., *Hosseini-Barzi and Talbot*, 2003) and is explored further in the Discussion section.

Subsurface duplication of the Vandam Zone tectonostratigraphic package is implied by shortening estimates from portions of the range closer to the foreland that indicate $\sim$20 km of shortening occurred over a 4-5 km deep basal detachment (Fig. 7.2, Agsu transect; Fig.

7.3; *Forte et al.*, 2013). A detachment depth of 4-5 km is consistent with a detachment located beneath the Vandam Zone tectonostratigraphic package based on map thicknesses (Fig. 7.6) and stratigraphic thickness estimates (*Bochud*, 2011). The estimate of ∼20 km shortening toward the foreland (Fig. 7.2, Agsu transect; Fig. 7.3; *Forte et al.*, 2013) indicates that the basal detachment must have at least 20 km of cumulative slip, requiring the Vandam Zone package to have been structurally duplexed and to have slipped at least 20 km over itself. The surface geology suggests that a basal detachment hanging wall ramp is located beneath and slightly to the north of the location of the Basgal nappe thrust sheet (Fig. 7.6). The equivalent footwall ramp must be located to the north, 20 km plus any hanging wall shortening in the Lahij transect. The footwall ramp is, therefore, to the north of the Lahij transect and is not depicted on the transect structural reconstruction (Fig. 7.6).

The location of ramps and flats on the Zangi thrust is related to the displacement of the Basgal nappe (Fig. 7.6). Based on the lithologically similar Upper Cretaceous strata exposed immediately above the Zangi thrust and within the Basgal nappe thrust sheet, we infer that the Basgal nappe thrust sheet was transported along the Zangi thrust (Fig. 7.6). Given the distance between the northern exposure of the Zangi thrust and the Basgal nappe, as well as the geometries of folds in the intervening Vandam Zone package that the thrust would have overlain, we infer that at least 24 km of slip on the Zangi thrust is implied. At the southern edge of the Basgal nappe thrust sheet, the distinctive chaotically folded red and blue mudstone sequence (UKrbfb) does not extend as far to the south as the overlying gray sandstone-shale sequence (UKblss), and we interpret this geometry as representing a hanging wall ramp. Given the minimum slip estimate of 24 km, the associated footwall ramp would be located in the northern portion of the Lahij transect (Fig. 7.6). However, based on the constraints provided by the Lahij transect outlined here, the footwall could be located further to the north, which would increase the amount of cumulative slip that must have occurred along the Zangi thrust. Because of the pervasive short-wavelength folding and faulting within the Lower to Upper Cretaceous strata of the Zangi thrust hanging wall (Fig. 7.2, Lahij transect; Fig. 7.6), it is difficult to use the geometry of surface exposures to determine the location of the footwall ramp associated with the Basgal nappe thrust sheet. The location of the ramp is constrained by other observations within the core of the range that are discussed and synthesized later.

7.4.2.4 Shortening estimate

Deformation within the Lahij transect yields constraints on the shortening accommodated by both the basal decollement of the range and the Zangi thrust (Fig. 7.6). The Vandam Zone tectonostratigraphic package is deformed by faults and folds in the southern to central

portion of the Lahij transect (Fig. 7.2, Lahij transect; Fig. 7.6). Line balancing of contacts within the Vandam Zone tectonostratigraphic package indicates ∼4 km of shortening is accommodated by faulting and folding within the Lahij transect. Given shortening estimates of 20 km to the south (Fig. 7.2, Agsu transect; Fig. 7.3; *Forte et al.*, 2013), our results indicate that a total of ∼24 km shortening is accommodated structurally below the Zangi thrust and above the basal detachment between the Lahij transect and the southern range front. This shortening is accommodated by slip along the basal detachment. Above the Zangi thrust, the structural reconstruction inferred here indicates that at least 24 km of shortening was accommodated by south-directed thrusting of the Basgal nappe thrust sheet. Folding of the middle Cretaceous strata at the northern end of the transect accounts for another 2.5 km of shortening, indicating that at least 26.5 km of shortening has been accommodated by slip on the Zangi thrust.

7.4.3 Salavat Transect

The Salavat transect is located about 40 km northwest along strike from the Lahij transect and extends across the entire range (Fig. 7.1; Fig. 7.2, Salavat panel). The transect extends from exposures of the Vandam Zone tectonostratigraphic package in the south, across the Jurassic core of the range, and to Jurassic and Cretaceous carbonates exposed on the northern slope of the Eastern Greater Caucasus (Fig. 7.1; Fig. 7.2, Salavat panel; *Nalivkin*, 1976; *Bairamov et al.*, 2008). In order to facilitate reporting of results from this transect, the transect is broken down into southern, central, and northern segments that are distinguished in the sections covering geologic descriptions, thermochronometry, structural interpretations, and shortening estimates. We report on these three segments in order from south to north.

7.4.3.1 Geological description

7.4.3.1.1 Southern segment

The southern segment of the Salavat transect extends from the vicinity of Gabala in the south to immediately south of Salavat Pass in the north (Fig. 7.1; Fig. 7.2, Salavat panel). Here, we report the observed lithologies in order from south to north.

The southernmost observed exposures are of the Lower Cretaceous calcareous sandstones (LKvcss) and middle Cretaceous volcaniclastic sandstones (MKvvc) of the Vandam Zone (Fig. 7.2, Salavat panel; *Nalivkin*, 1976). These exposures are lithologically similar to the equivalent units in the Lahij transect (Fig. 7.2, Lahij panel). The Vandam Zone tectonostratigraphic package observed here is folded. An anticline is inferred from exposures of the Lower Cretaceous calcareous sandstone sequence (LKvcss) observed near

the southern margin of the transect, which reveal a southern limb that is overturned and south-younging and a northern limb that dips moderately (30 - 60°) to the north (Fig. 7.2, Salavat panel). The stratigraphically overlying middle Cretaceous volcaniclastic sequence (MKvvc) is observed to the north, upsection within the northern limb of the anticline. To the north of these north dipping exposures of the middle Cretaceous volcaniclastic sequene (MKvvc), observations are limited. Previous mapping indicates that a syncline is centered in the middle Cretaceous (*Nalivkin*, 1976), which is broadly consistent with our observations and is a good match to the structure exposed along strike in the Lahij transect (Fig. 7.2, Lahij panel; Fig. 7.6).

To the north of the exposures of the Vandam Zone tectonostratigraphic sequence, a sequence of thin bedded (∼10 cm), locally calcareous, brown to gray turbidites mapped as Lower Cretaceous (LKtb) is exposed (Fig. 7.2, Salavat panel; *Nalivkin*, 1976; *Bairamov et al.*, 2008). This sequence is deformed in tight to isoclinal, asymmetric folds of wavelength 0.5 to 1 km in which south-younging limbs are often vertical or overturned (Fig. 7.2, Salavat panel). This sequence is similar lithologically and structurally to exposures along strike to the east in the northern portion of the Lahij transect above the Zangi thrust (Fig. 7.2, Lahij panel). A particularly well-exposed section is visible on the flank of Mt. Babadag (Fig. 7.4c; location of Babadag shown in Fig. 7.1). It is also likely that the Lower Cretaceous turbidite sequence (LKtb) is deformed by many small-offset thrust faults, as is observed in the Lahij transect (Fig. 7.2, Lahij panel). Though the contact between the Vandam Zone stratigraphic package (LKvcss, MKvvc) and the northern stratigraphic package (LKtb) is not well-exposed along the southern segment of the Salavat transect, exposures along strike in the Lahij transect of equivalent lithology and gross structural geometry (Fig. 7.2, Lahij panel; Fig. 7.6) suggest that the two stratigraphic packages are likely to be separated by a north dipping normal fault (Fig. 7.2, Salavat panel). The Lower Cretaceous brown to gray turbidite sequence (LKtb) is exposed over a length of ∼5 km across strike on the southern margin of the range.

To the north of the Lower Cretaceous turbidite sequence (LKtb) is a sequence of calcareous turbidites mapped as Upper Jurassic (Jctb; Fig. 7.2, Salavat panel; *Nalivkin*, 1976). These turbidites are distinguished by their light gray color and the resistance and conchoidal fracture of the fine grained beds, suggesting incorporation of carbonate mud. The Upper Jurassic calcareous turbidite sequence (Jctb) deforms in a similar fashion to the Lower Cretaceous turbidite sequence (LKtb), with asymmetric folds that have steeper to overturned south-younging limbs and wavelengths of 0.5 – 1 km (Fig. 7.2, Salavat panel).

7.4.3.1.2 Central segment

The central segment of the Salavat transect extends from just south of Salavat Pass to north of the town of Xinaliq on the northern slope of the Eastern Greater Caucasus (Fig. 7.1; Fig. 7.2, Salavat panel). Again, we report geologic observations from south to north.

At the southern end of the central segment is the contact between the Upper Jurassic calcareous turbidite sequence to the south (Jctb) and a black to dark brown, organic-rich turbidite sequence to the north mapped as Middle Jurassic (Jotb; Fig. 7.2, Salavat panel). Middle Jurassic, organic-rich turbidites are exposed over the entire central segment of the Salavat transect except at its extreme northern margin (Fig. 7.2, Salavat panel). The sequence is pervasively deformed, with bedding planes indicating moderate to isoclinal folds (interlimb angles $<90°$) that may be symmetric or asymmetric, with typical wavelengths of 0.5 – 1 km. The sequence is cut by many small-offset, intraformational thrust faults that can only be definitively observed in areas of extremely good exposure (Fig. 7.2, Salavat panel). The thicknesses of sandstone beds in the sequence is variable from 2-10 cm, which is typical, to $\sim$5 m, which is very rare. However, bedding thicknesses appear to be laterally variable such that particularly thick sand beds cannot be used to correlate sections across strike. A particularly large wavelength fold ($\sim$10 km) that can be traced between multiple river valleys in the northern part of the transect is cored by a $>$5 m thick sandstone bed, suggesting that fold wavelength is largely controlled by the thickness of overlying and underlying sandstone layers.

At the northern extent of the central segment of the Salavat transect, the Middle Jurassic, organic-rich turbidite lithology is in contact with a massive wackestone to grainstone carbonate sequence mapped as Upper Jurassic (Jmc; Fig. 7.2, Salavat panel). This contact has been mapped as an unconformity and as a fault (*Khain and Shardanov*, 1960; *Nalivkin*, 1976; *Bairamov et al.*, 2008; *Bochud*, 2011). Locally concentrated chaotic folding and oxidation of the Middle Jurassic organic-rich turbidite sequence (Jotb) suggests the contact is a fault (Fig. 7.2, Salavat panel). The Jurassic massive carbonate (Jmc) dips steeply to the north (Fig. 7.2, Salavat panel).

7.4.3.1.3 Northern segment

The northern segment of the Salavat transect extends from the vicinity of the village of Jek, which is located northeast of Xinaliq, northward to the town of Kusnatqazma (Fig. 7.1; Fig. 7.2, Salavat panel). Exposures within the segment range from the Jurassic organic-rich turbidite sequence (Jotb) at the southern end of the segment to Pliocene sandstones and gravels exposed at its northern margin. As we report below, the tectonic transport direction in this segment of the transect at the surface is to the north, and so we proceed from north

to south in discussing the geologic observations.

Exposure is poor at the northern end of this segment of the Salavat transect, but prior mapping indicates that the northernmost topography of the Eastern Greater Caucasus corresponds with a steeply north dipping fold limb composed of Lower Cretaceous to Quaternary strata that is structurally intact (*Khain and Shardanov*, 1960; *Nalivkin*, 1976). Observed bedding geometries at the northern end of the transect are consistent with this interpretation (Fig. 7.2, Salavat panel). There is no structural or topographic evidence to suggest any north directed thrusting to the north of the exposed Cretaceous strata.

The exposed Lower Cretaceous sequence in the northern portion of this segment is characterized by oolitic carbonates with well-defined bedding planes and interbedded gray shales (LKbc; Fig. 7.2, Salavat panel). This sequence is exposed throughout much of the northern segment of the Salavat transect, and exhibits significant lateral variability, transitioning from >2 m thick carbonates with minor shale in the north to a dominantly shale lithology in the south with discontinuous oolitic carbonate beds at irregular intervals. Exposures of the sequence in the northern part of the segment define a series of asymmetric folds of 0.5 to 1 km wavelength with north-younging limbs that dip steeply to the north or are overturned and south-younging limbs that dip gently to the south (Fig. 7.2, Salavat panel).

To the south, Jurassic to Cretaceous strata are involved in a structurally complex area whose interpretation is made more difficult by steep angular unconformities. The Lower Cretaceous bedded carbonate sequence (LKbc) is thrust over from the south by the Jurassic massive carbonate (Jmc) sequence (Fig. 7.2, Salavat panel). South of this north directed thrust, the Jurassic massive carbonate (Jmc) is disrupted by a south-dipping normal fault, which juxtaposes the massive carbonate in the footwall against the Lower Cretaceous bedded carbonate (LKbc) in the hanging wall (Fig. 7.2, Salavat panel; fault plane shown in Fig. 7.4e). The hanging-wall sequence dips slightly to the north, and so to the south the underlying Jurassic massive carbonate (Jmc) is again exposed (Fig. 7.2, Salavat panel). The Jurassic massive carbonate (Jmc) and Lower Cretaceous bedded carbonate (LKbc) are both unconformably overlain to the south and east by a sequence of red to white sandstone and gray shale mapped as Upper Cretaceous (UKwss; Fig. 7.2, Salavat panel; *Khain and Shardanov*, 1960; *Nalivkin*, 1976, Fig. 7.4d shows an image of the unconformity). The core of a syncline is located within this overlying Upper Cretaceous sequence, and moving south beyond the core of the syncline the Lower Cretaceous bedded carbonate (LKbc) is again exposed (Fig. 7.2, Salavat panel). The Lower Cretaceous sequence is defines a north-younging and subvertically bedded fold limb (Fig. 7.2, Salavat panel). This Lower Cretaceous sequence is in contact to the south with the Middle Jurassic organic-rich tur-

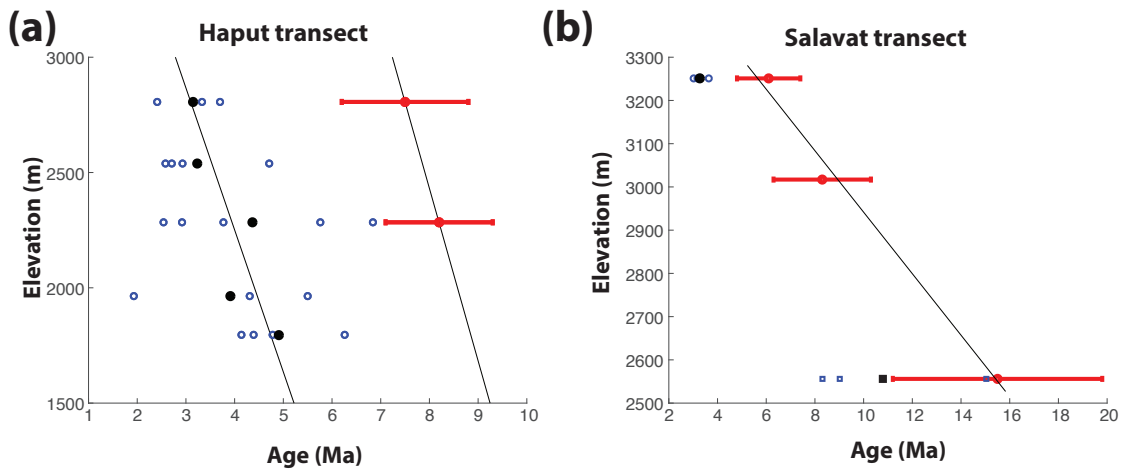

Figure 7.7: Age-elevation plots for thermochronometry samples of the Haput (a) and Salavat (b) thermochronometry transects.

bidite sequence (Jotb), which is also north-younging and subvertically-bedded. To the west along this contact, Upper Jurassic massive carbonate (Jmc) is exposed between the Middle Jurassic organic-rich turbidites (Jotb) to the south and the Lower Cretaceous bedded carbonates (LKbc) to the north, and localized folding and oxidation of the turbidites (Jotb) along this contact suggest that it is a detachment.

7.4.3.2 Thermochronometric data

7.4.3.2.1 Central segment

Thermochronometry data collected from the central segment of the Salavat transect comprise two near-vertical transects, located near Salavat Pass and the village of Haput, respectively (Figs. 7.1, 7.7; Fig. 7.2, Salavat panel; Tables 7.1, 7.2, 7.3, 7.4). Both vertical transects were collected from the Middle Jurassic, organic-rich turbidite sequence (Jotb; Fig. 7.2, Salavat panel). These data constrain the exhumation histories of the central portion of the Eastern Greater Caucasus. Analyses were limited by the sample yield of apatite sufficiently large enough for dating, resulting in a mix of different thermochronometric systems analyzed for each sample.

The Salavat thermochronometry transect (Figs. 7.1, 7.7; Fig. 7.2, Salavat panel; Tables 7.1, 7.2, 7.3, 7.4) includes three thermochronometry samples that span ~800 m of elevation. The lowest sample, S1, was analyzed for AFT and ZHe ages; the median sample, S2, was analyzed for an AFT age; and the upper sample, S3 was analyzed for AFT and AHe ages (Figs. 7.1, 7.7; Fig. 7.2, Salavat panel; Tables 7.1, 7.2, 7.3, 7.4). Central AFT ages for the three samples range from 6.1 Ma to 15.5 Ma, the mean AHe age from sample S3

is 3.3 Ma, and the mean ZHe age from sample S1 is 10.8 Ma (Figs. 7.1, 7.7; Fig. 7.2, Salavat panel; Tables 7.1, 7.2, 7.3, 7.4). Two major aspects of the data warrant attention. First, sample S1 has a sample mean ZHe age (10.8 Ma) that is younger than its AFT age (15.5 Ma) despite the fact that the ZHe system has a nominal closure temperature of ∼180° C (e.g., *Reiners et al.*, 2004; *Reiners*, 2005), whereas the AFT system has a nominal closure temperature of ∼110° C (e.g., *Donelick et al.*, 2005). Thermal modeling of these ages indicates ∼225° C cooling since ∼12 Ma (Fig. 7.4b), implying 7.5 – 11.25 km exhumation for geothermal gradients of 30° C/km and 20° C/km, respectively. Second, the AFT ages, the only system for which there exists ages for more than one sample, decrease with increasing elevation. Such an age-elevation relationship is the opposite of what would be expected for an exhuming rigid block (e.g., *Brandon et al.*, 1998; *Farley et al.*, 2001). One possible explanation for this inverted age-elevation relationship that will be explored further in the Discussion section is rotation of the sampled strata after cooling by folding. The constraint that 7.5 – 11.25 km of exhumation occurred since ∼12 Ma is not dependent on the age-elevation relationship displayed by the samples.

The Haput thermochronometry transect (Figs. 7.1, 7.7; Fig. 7.2, Salavat panel; Tables 7.1, 7.2, 7.3, 7.4) includes five thermochronometry samples that span ∼1 km of vertical elevation. The AHe system was analyzed for all five samples, resulting in sample mean ages that range between 3 and 5 Ma (Figs. 7.1, 7.7; Fig. 7.2, Salavat panel; Tables 7.1, 7.2). The AFT system was analyzed for samples H3 and H5, resulting in central ages of 7.5 Ma and 8.2 Ma, respectively (Figs. 7.1, 7.7; Fig. 7.2, Salavat panel; Tables 7.1, 7.4). The ZHe system was analyzed for sample H1, yielding a sample mean age of 91.8 Ma (Figs. 7.1, 7.7; Fig. 7.2, Salavat panel; Tables 7.1, 7.3). Like the AFT ages of the Salavat thermochronometry transect, the AHe ages of the Haput transect decrease with increasing elevation, which is the opposite of the age-elevation relationship that would characterize an exhuming rigid block (Figs. 7.1, 7.7; Fig. 7.2, Salavat panel; Tables 7.1, 7.2; *Farley et al.*, 2001, others). Of additional note about the Haput transect is the Cretaceous cooling age of the ZHe system in sample H1 (Figs. 7.1, 7.7; Fig. 7.2, Salavat panel; Tables 7.1, 7.3), which indicates that the sample was not warm enough to reset the system during the Cenozoic. Given a ZHe closure temperature of ∼180° C (e.g., *Reiners*, 2005) and a geothermal gradient of 20-30° C/km, the Cretaceous ZHe ages indicate that sample H1 resided at a depth of <6 – 9 km from the surface throughout the Cenozoic.

7.4.3.2.2 Northern segment

We report a single AHe age from the northern segment of the Salavat transect, sample N3 (Figs. 7.1, 7.7; Fig. 7.2, Salavat panel; Tables 7.1, 7.2; Avdeev, unpublished). The

sample was collected from a sandstone interbed within the Lower Cretaceous sequence of predominantly oolitic carbonate and gray shale (LKbc; Fig. 7.2, Salavat panel). The sample mean age of N3 is 92.3 Ma (Figs. 7.1, 7.7; Fig. 7.2, Salavat panel; Tables 7.1, 7.2; Avdeev, unpublished). Given typical closure temperatures of the AHe system of ∼60° C (e.g., *Farley*, 2002; *Ehlers and Farley*, 2003) and a geothermal gradient of 20-30° C/km, the Cretaceous AHe age indicates residence of the sample within the top 2-3 km of the crust since the Cretaceous.

7.4.3.3 Structural interpretation

7.4.3.3.1 Southern segment

Our structural interpretation of the southern segment of the Salavat transect (Fig. 7.8) is based on field observations (Fig. 7.2, Salavat panel) and analogy with the structure of the Lahij transect, located ∼40 km ESE along strike (Fig. 7.2, Lahij panel; Fig. 7.6). Here we discuss our structural interpretations from south to north.

The structural geometry of folded Vandam Zone strata at the southern end of the transect is constrained by the surface geology (Fig. 7.2, Salavat panel), age determinations from published mapping (e.g., *Nalivkin*, 1976), and shortening estimates from the transects to the south (Fig. 7.3). Observed bedding orientations of Lower Cretaceous Vandam calcareous sandstones (LKvcss) and middle Cretaceous Vandam volcaniclastic sandstones (MKvvc) indicate folding of the Vandam stratigraphic package asymmetrically, consistent with a fault-propagation fold over a south-vergent thrust (Fig. 7.2, Salavat panel; Fig. 7.8), similar to what is observed in the Lahij transect (Fig. 7.6). Previous mapping (*Nalivkin*, 1976) suggests an adjacent syncline to the north of this fault propagation anticline (Fig. 7.8), also similar to along-strike observations of the Lahij transect (Fig. 7.6). To the north of this syncline, the range is dominated by thinly bedded marine sandstone-shale sequences of the northern tectonostratigraphic package, suggesting that these sequences are separated from the Vandam Zone by lateral equivalents of the Zangi thrust and the normal fault observed in the Lahij transect (Figs. 7.6, 7.8). As with the Lahij transect, the net slip on the duplex within the Vandam Zone tectonostratigraphic package is constrained by shortening estimates of ∼20 km toward the range front on this fault (Fig. 7.2, Agsu panel; Fig. 7.3; forte2013structural). The subsurface geometry of the Vandam Zone tectonostratigraphic package is constrained by the detachment depths inferred from deformation towards the foreland (Fig. 7.2, Agsu panel; Fig. 7.3; *Forte et al.*, 2013) and map thicknesses of the Vandam Zone sequences.

The turbiditic strata observed in the northern portion of the segment are lithologically

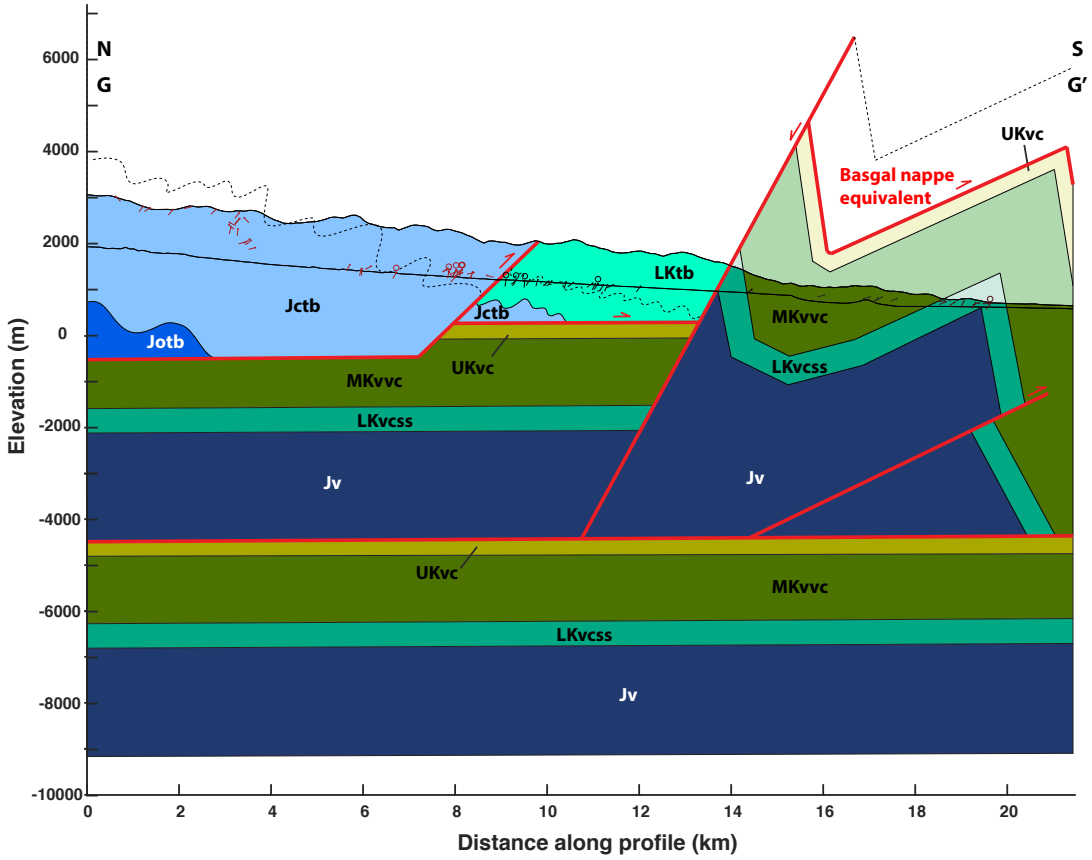

Figure 7.8: Interpretive structural cross section of the southern segment of the Salavat transect (Fig. 7.2, Salavat panel). Geologic units are as depicted in Figure 7.2 and Figure 7.6. Dipticks are projected from within 3 km of the line of section and are displayed as in previous cross section figures. Dashed lines are drawn approximately parallel with bedding plane orientations of mapped exposures and approximate the trace of a bedding plane. The two topographic profiles show the highest and lowest topography within 3 km perpendicular to the line of section.

similar to and deform similarly to the sequences of the northern Lahij transect (Figs. 7.6, 7.8). These sequences are deformed into asymmetric fold trains of 0.5 to 1 km wavelength that are consistent with formation above localized, south-vergent thrust faults (Fig. 7.8). It is likely that these sequences are affected by small displacement thrust faulting similarly to the northern tectonostratigraphic package observed in the Lahij transect (Fig. 7.6), although increased vegetation in the southern segment of the Salavat transect makes it difficult to confirm this. The localized, short wavelength deformation within these sequences makes it difficult to infer subsurface structure. The depicted contacts in the subsurface of the northern tectonostratigraphic package represent best guesses based on published stratigraphic thicknesses (e.g., *Khain and Shardanov*, 1960; *Bochud*, 2011, Fig. 7.8), and the location of the footwall ramp of the lateral equivalent of the Zangi thrust is inferred from the Lahij section (Figs. 7.6, 7.8). Because the Upper Jurassic calcareous turbidite sequence (Jctb) is exposed over a wide area, we infer that the sequence overlies a hanging wall flat, whereas the depicted portions of the Lower Cretaceous turbidite sequence (LKtb) and the Middle Jurassic organic-rich turbidite sequence (Jotb) are both inferred to overlie hanging wall ramps.

7.4.3.3.2 Central segment

Our structural interpretation of the central segment of the Salavat transect (Fig. 7.9) is based on field observations (Fig. 7.2, Salavat panel), with interpretations of subsurface structure also based on interpretations of detachment depth and net displacement from the transects to the south (Figs. 7.3, 7.6, 7.8). Exposed lithologies within the central segment of the Salavat transect consist entirely of the Middle Jurassic organic-rich turbidite sequence (Jotb), with the exception of the northernmost portion of the transect (Fig. 7.9). Again, we discuss our structural interpretations from south to north.

Bedding planes of the Middle Jurassic turbidite sequence indicate pervasive open to tight folding that is asymmetric in some areas and symmetric in other areas (Fig. 7.9). Regions of asymmetric folding include the extreme southernmost portion of this segment, where south-younging fold limbs are subvertical to overturned and north-younging limbs are less steeply dipping, as well as large portions of the segment where north-younging limbs are more steeply dipping than south-younging limbs (Fig. 7.9). In order to estimate the geometry of a single stratum within the sequence, we trace a line approximately parallel with observed bedding planes of surface exposures (Fig. 7.9). This tracing indicates a south-central region of the segment where the sequence is broadly north dipping beyond the wavelength of a single fold, a north-central region where the sequence is broadly horizontal, and a northern region where the sequence is broadly north dipping (Fig. 7.9). The largest

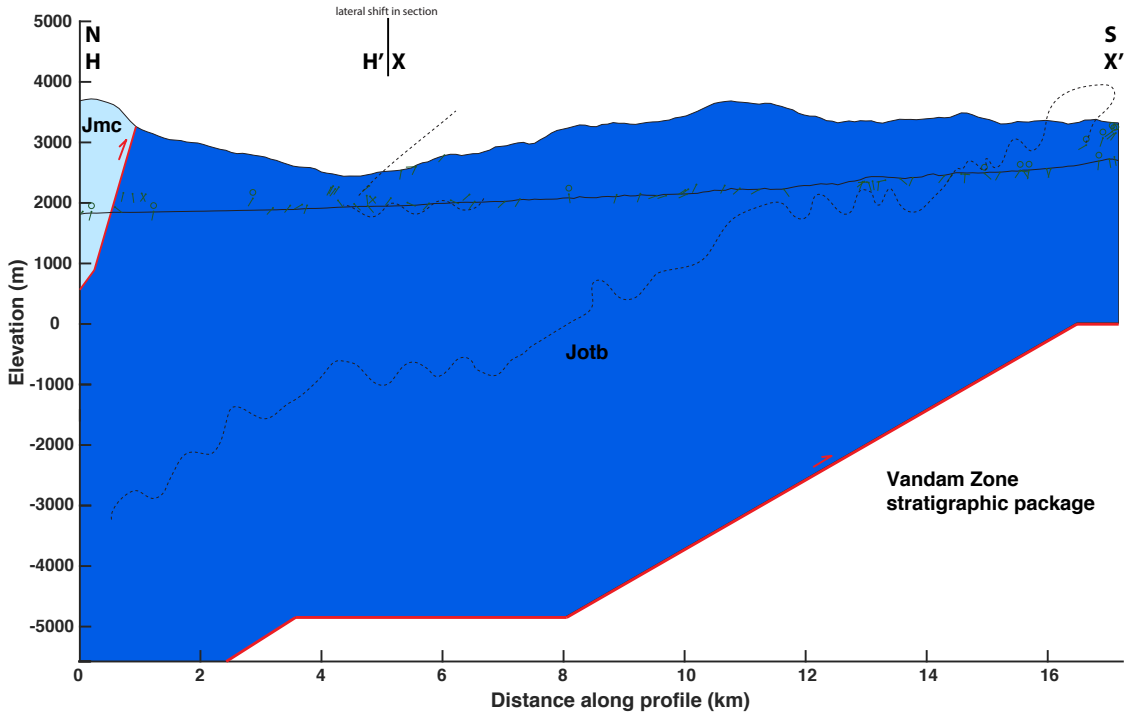

Figure 7.9: Interpretive structural cross section of the central segment of the Salavat transect (Fig. 7.2, Salavat panel). Geologic units are as depicted in Figure 7.2. Dipticks are projected from within 5 km of the line of section and are displayed as in previous cross section figures. Dashed lines are drawn approximately parallel with bedding plane orientations of mapped exposures and approximate the trace of a bedding plane. The two topographic profiles show the highest and lowest topography within 5 km perpendicular to the line of section.

of these broadly dipping regions, the south-central region of northward dip, corresponds spatially with a north-dipping panel of the Vandam Zone tectonostratigraphic sequence at depth inferred from constraints on the Vandam Zone duplex from shortening estimates to the south (Fig. 7.9; Fig. 7.2, Agsu panel; Fig. 7.3; *Forte et al.*, 2013). Thus, beyond the scale of the pervasive folding in the central segment of the Salavat transect, broad trends in bedding orientation may reflect structure at depth.

Exposures at the northernmost portion of the central segment of the Salavat transect are composed of the Upper Jurassic massive carbonate sequence (Jmc; Fig. 7.9). The contact between the organic-rich turbidite sequence (Jotb) and the massive carbonate sequence (Jmc) is inferred to be a fault for two reasons. First, as mentioned above, chaotic, short-wavelength deformation of the organic-rich turbidite sequence (Jotb) is observed to be locally concentrated along this contact, along with oxidation. Second, the deformation styles of the two sequences contrast markedly, with the organic-rich turbidite sequence (Jotb) deforming by folding on 0.5 – 1 km wavelengths and the massive carbonate sequence (Jmc) deforming largely by duplication along thrust faults, as will be discussed in the structural interpretation of the northern segment of the transect. If deformation occurred after the deposition of the upper sequence (Jmc), the fact that the lower sequence (Jotb) is pervasively folded and the upper sequence (Jmc) is not requires a detachment between the two sequences (Fig. 7.9). If the pin line for these sequences is located to the north of the Eastern Greater Caucasus, as is indicated by the northward dip of major orogen-scale structures, then folding of the lower sequence (Jotb) beneath the upper sequence requires top-to-the-south motion on the detachment separating the two sequences (Fig. 7.9). Locally, depending on the location and cumulative slip of faulting within the upper sequence (Jmc), it is possible that the net sense of motion on the detachment that separates the upper (Jmc) and lower (Jotb) sequences may be top-to-the-north.

7.4.3.3.3 Northern segment

Our structural interpretation of the northern segment of the Salavat transect (Fig. 7.10) is based largely on field observations (Fig. 7.2, Salavat panel). We describe our interpretations of major structures from north to south within the northern segment of the Salavat transect. We then discuss broad trends in the structure of this segment of the transect and potential implications for subsurface structural geometry.

The northern part of the segment consists of exposures of Lower Cretaceous bedded carbonate (LKbc) and Upper Jurassic massive carbonate (Jmc). As discussed above, there is no evidence that the deformed Mesozoic strata observed in the transect are thrust over the Cenozoic deposits to the north, meaning that the fault(s) that control deformation within

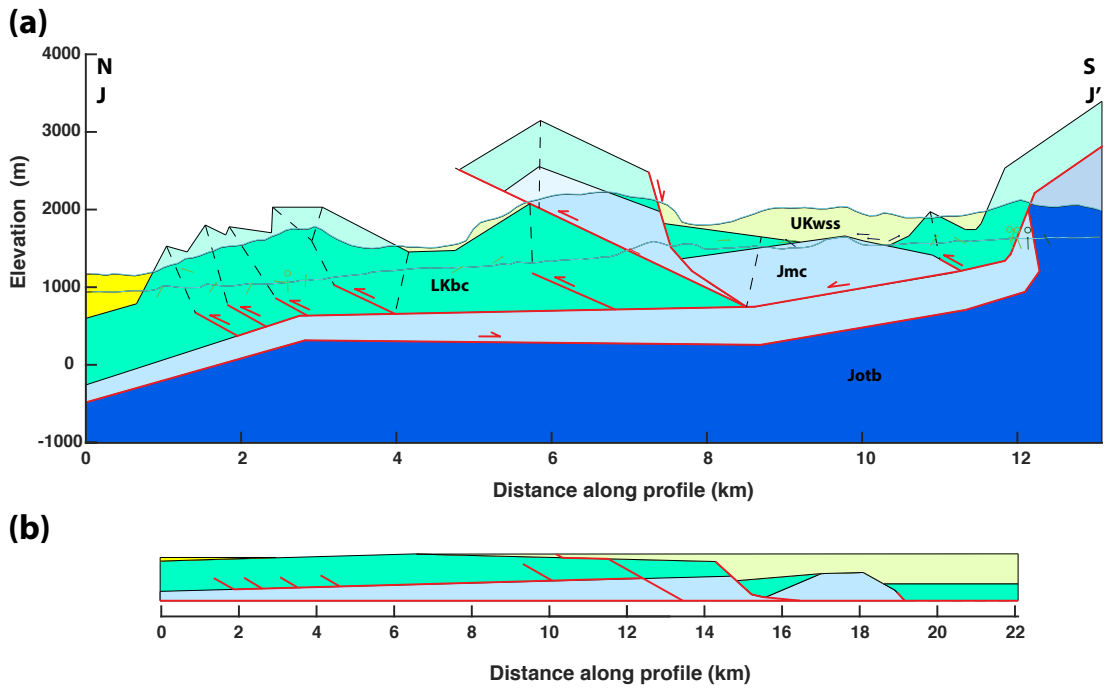

Figure 7.10: (a) Interpretive structural cross section of the northern segment of the Salavat transect (Fig. 7.2, Salavat panel). Geologic units are as depicted in Figure 7.2, except yellow is Cenozoic, undifferentiated. Dipticks are as previous cross section figures, projected from within 1 km. The two topographic profiles show the highest and lowest topography within 1 km perpendicular to the line of section. (b) Retrodeformed geometry of the cross section shown in (a), at half size.

the Upper Jurassic to Cretaceous strata likely terminate in the subsurface (Fig. 7.10). The asymmetric folds on ∼1 km wavelengths exhibited by the Lower Cretaceous bedded carbonate sequence (LKbc) in the northern part of the segment (Fig. 7.2, Salavat panel) are consistent with their formation as fault-propagation folds above north-vergent thrust faults (Fig. 7.10). To the south of these folds, the bedding geometries of the Upper Jurassic massive carbonate sequence (Jmc) and Lower Cretaceous bedded carbonate sequence (LKbc) indicates emplacement of the massive carbonate by north vergent thrusting over the bedded carbonate (Fig. 7.2, Salavat transect; Fig. 7.10). The geometries of the fault-propagation folds suggest that the faults controlling these folds root into the same detachment as the thrust at the base of the exposed Upper Jurassic massive carbonate (Jmc; Fig. 7.10). The shortening within the fault-propagation folds and the displacement inferred on the exposed thrust constrain the net slip on the inferred detachment (Fig. 7.10).

To the south of the surface-breaking, north-directed thrust that emplaced Upper Jurassic massive carbonates (Jmc) over Lower Cretaceous bedded carbonates (LKbc) is an exposed, south dipping normal fault that juxtaposes the Upper Jurassic sequence in the footwall against the overlying Lower Cretaceous sequence in the hanging wall (Fig. 7.4e; Fig. 7.2, Salavat panel; Fig. 7.10). Slip on this fault post-dated the Lower Cretaceous. Based on field observations and aerial photography, we tentatively conclude that the fault does not disrupt overlying Upper Cretaceous sandstones (UKwss), restricting the age of faulting to Early to Late Cretaceous, consistent with inferred rifting within the Caucasus region at the time (e.g., *Nikishin et al.*, 1998). The observed fault geometry is consistent with a listric geometry that soles into a detachment beneath the Upper Jurassic massive carbonate sequence (Jmc; Fig. 7.10).

The region to the south of the exposed normal fault includes exposures of the Upper Jurassic massive carbonate sequence (Jmc), the Lower Cretaceous bedded carbonate sequence (LKbc) and the Upper Cretaceous white sandstone sequence (UKwss), which overlies an angular unconformity (Fig. 7.2, Salavat transect; Fig. 7.10). The shortening observed in the fault-propagation folds to the north requires that the Upper Jurassic massive carbonate sequence (Jmc) was duplicated by thrusting in this region of the transect (Fig. 7.10). Such duplication is also implied by the outcrop pattern of the Upper Jurassic massive carbonate sequence, which includes exposures with subvertical bedding near the southern extent of this segment and subhorizontal exposures in a structurally overlying position to the north (Fig. 7.10). The southern margin of the palinspastically-restored Upper Jurassic massive carbonate sequence (Jmc) terminates in a steep angular unconformity over which Lower Cretaceous strata are deposited (Fig. 7.10). Olistoliths of the massive carbonate sequence (Jmc) up to kilometer-scale are present within younger strata, consistent with a

steep angular unconformity between the Upper Jurassic and Lower Cretaceous sequences (Fig. 7.2, Salavat transect; *Bochud*, 2011). To the south of the palinspastically-restored Upper Jurassic massive carbonate sequence (Jmc), a small fault-propagation fold is inferred above the detachment from an asymmetric fold in the Lower Cretaceous bedded carbonate sequence (LKbc; Fig. 7.10). As discussed above in the structural interpretation of the central segment of the Salavat transect (Fig. 7.2, Salavat panel; Fig. 7.9), the differing fold wavelengths observed in the Middle Jurassic organic-rich turbidite sequence (Jotb) and the overlying Upper Jurassic massive carbonate sequence (Jmc) require a detachment between the Middle Jurassic sequence and overlying sequences (Fig. 7.10).

Observed and inferred bedding plane orientations of the deformed Upper Jurassic and younger strata exposed in the northern segment of the Salavat transect may have implications for the deeper structure. The Upper Jurassic and younger strata define multiple areas of distinct dip. At the northern end of the segment, a moderate northward dip is required by the north-younging stratigraphic package that extends from the deformed Lower Cretaceous bedded carbonate sequence (LKbc) to Quaternary foreland basin deposits to the north of the mapped transect (Fig. 7.10; e.g., *Golubjatnikov and Dubogryzova*, 1959; *Khain and Shardanov*, 1960; *Nalivkin*, 1976). Our inferred structure for the deformed Upper Jurassic to Cretaceous sequences suggest a subhorizontal contact of these sequences with the underlying Middle Jurassic turbidite sequence (Jotb) over the area that Upper Jurassic to Cretaceous sequences outcrop at the surface (Fig. 7.10). Finally, near the southern terminus of this segment, a moderate to steep northward dip is dominant near the exposed contact between the Middle and Upper Jurassic strata (Fig. 7.10). The broad patterns of bedding orientation observed in the northern segment of the Salavat transect are controlled by the structure of the Middle Jurassic and older strata at depth, and the regions of moderate northward dip and subhorizontal bedding may correspond with footwall ramps and flats of a major structure at depth (Fig. 7.10).

7.4.3.4 Shortening estimates

7.4.3.4.1 Southern segment

In the southern segment of the Salavat transect, shortening is accommodated by folds and fault offsets within the Vandam Zone stratigraphic package and in the northern, dominantly turbiditic stratigraphic package (Fig. 7.8). We first discuss shortening inferred within the Vandam Zone stratigraphic package and then within the northern, turbiditic stratigraphic package.

Within the Vandam Zone package, the inferred geometry of fault-propagation folds

near the southern end of the transect accommodates 6 km of shortening (Fig. 7.8). This amount is approximately consistent with the ∼4 km of shortening from the along strike equivalent structures in the Lahij transect (Fig. 7.6). Along with the ∼20 km of shortening inferred in Cenozoic strata toward the range front (Fig. 7.2, Agsu transect; Fig. 7.3; forte2013structural), this 4-6 km shortening must be balanced by slip along the Vandam duplex thrust fault.

Within the northern, predominantly turbiditic tectonostratigraphic package, shortening is accommodated by faulting and pervasive folding of the thinly bedded turbiditic strata (Fig. 7.8). Balancing of a line approximately parallel with bedding plane orientations in the Lower Cretaceous turbidite (LKtb) sequence indicates that the sequence accommodates ∼30% horizontal shortening by folding, or ∼1.75 km in this segment of the Salavat transect (Fig. 7.8). Balancing a similar line within the Upper Jurassic calcareous turbidite (Jctb) sequence indicates a horizontal shortening of ∼35%, equating to 4.5 km in this segment of the transect (Fig. 7.8). Finally, the thrust fault separating these two sequences requires at least ∼1.75 km of slip, resulting in a total of at least 8 km of horizontal shortening accommodated within the northern, turbiditic tectonostratigraphic package in this segment of the Salavat transect (Fig. 7.8). This shortening estimate should be regarded as a minimum because our method of tracing a line parallel to observed bedding orientations may underestimate the amplitude of mapped folds, which was difficult to observe given the poor to moderate exposure of the transect. In addition, our line tracing method does not account for the many small-offset thrust faults that are observed in similar lithologies along strike where exposure is better (e.g., Fig. 7.2, Lahij panel; Fig. 7.2, Salavat panel).

7.4.3.4.2 Central segment

In the central segment of the Salavat transect, shortening is accommodated by folds and small-offset, intraformational thrust faults within the organic-rich Middle Jurassic turbidite sequence (Jotb; Fig. 7.9). Tracing a line parallel to exposed bedding plane orientations results in a minimum estimate of horizontal shortening from folding of ∼35%, equal to ∼8.5 km of shortening (Fig. 7.9). Because this tracing method may underestimate the amplitude of folds and does not account for slip on several small-offset thrust faults observed within the range (Fig. 7.2, Salavat panel), this should be regarded as a minimum estimate.

7.4.3.4.3 Northern segment

In the northern segment of the Salavat transect, shortening is accommodated within Upper Jurassic and younger strata by a north vergent thrust system that includes a surface breaking thrust and several fault propagation structures kinematically linked via a detachment

(Fig. 7.10). Retrodeforming this thrust system indicates that within the Upper Jurassic and younger strata, ∼9 km of shortening (40%) is accommodated (Fig. 7.10). Because these Upper Jurassic and younger strata are inferred to be separated from the Middle Jurassic organic-rich turbidite sequence (Jotb) by a detachment (Fig. 7.10), the shortening inferred for the Upper Jurassic and younger strata may be different from the shortening that occurred within the Middle Jurassic and older strata below.

7.4.4 Tahirjal transect

The Tahirjal transect is located about 30 km northwest of the northern end of the Salavat transect (Fig. 7.1, Fig. 7.2). The Tahirjal transect is on the eastern margin of a distinct portion of the Greater Caucasus where the range is significantly wider than the easternmost portion that is the subject of this study (Fig. 7.1). Mapped lithologies in the Tahirjal transect range in age from Middle Jurassic to Neogene (*Golubjatnikov and Dubogryzova*, 1959; *Nalivkin*, 1976). The transect represents an opportunity to observe the structure of these sequences to the north of the Salavat transect. Because the Tahirjal transect is within a distinct, wider portion of the Greater Caucasus than our primary area of interest for this study (Fig. 7.1), we do not undertake a shortening estimate within the Tahirjal transect because we could not apply such an estimate to a meaningful, range-wide calculation of shortening within our area of interest.

7.4.4.1 Geological description

The Tahirjal transect (Fig. 7.2, Tahirjal panel) consists of similar lithologies to those observed in the northern segment of the Salavat transect (Fig. 7.2, Salavat panel). The oldest exposed lithology is the Middle Jurassic organic-rich turbidite sequence (Jotb; Fig. 7.2, Tahirjal panel; *Golubjatnikov and Dubogryzova*, 1959; *Nalivkin*, 1976). Similarly to within the Salavat transect, this lithology is deformed by folding (interlimb angles $< 90°$, wavelengths 0.5 to 1 km) and small-offset thrust faulting (Fig. 7.2, Tahirjal panel). This sequence is overlain by the Upper Jurassic massive carbonate sequence (Jmc) in the southern portion of the transect, and is unconformably overlain by Pliocene (*Golubjatnikov and Dubogryzova*, 1959) or Quaternary (*Nalivkin*, 1976) sandstones in the northern portion of the transect (Fig. 7.2, Tahirjal panel). The Upper Jurassic massive carbonate sequence (Jmc) in the southern portion of the transect is overlain by the Lower Cretaceous bedded carbonate sequence (LKbc). In contrast to the Middle Jurassic turbidite sequence (Jotb), the Upper Jurassic and younger sequences have a subhorizontal bedding plane orientation that is uniform across the mapped area, similar to the deformation style observed in the

northern segment of the Salavat transect (Fig. 7.2, Tahirjal panel).

7.4.4.2 Thermochronometric data

The Tahirjal transect contains a single, previously published AFT age of 12.5 ± 2.4 Ma from an outcrop of Middle Jurassic turbidites (Jotb; Fig. 7.1; Fig. 7.2, Tahirjal panel; Tables 7.1, 7.4; *Bochud*, 2011). This age suggests that the Middle Jurassic turbidite sequence (Jotb) was exhumed sometime during the Miocene to Quaternary (*Bochud*, 2011).

7.4.4.3 Structural interpretation

Mapping in the Tahirjal transect reveals that the deformation styles observed in the Middle Jurassic organic-rich turbidite sequence (Jotb) and the overlying Upper Jurassic massive carbonate sequence (Jmc) differ (Fig. 7.2, Tahirjal panel). Whereas the underlying turbidite sequence (Jotb) is pervasively folded and faulted, the overlying massive carbonate sequence (Jmc) is barely deformed. If folding of the underlying strata occurred after deposition of the overlying strata, then a detachment between the two is required (Fig. 7.2, Tahirjal panel). In the next section, we will use thermochronometry data from the range to constrain the timing of folding.

7.5 Discussion

The geological observations, thermochronometry data, and structural interpretations presented above yield insight into the timing and style of deformation in an active accretionary prism. Here, we first use our structural interpretations from the transects reported above to develop a model of the geologic structure of the Eastern Greater Caucasus and estimate the total strike-perpendicular horizontal shortening accommodated within the range. We then explore the implications of our set of new and existing (*Bochud*, 2011, Avdeev, unpublished) thermochronometry data for the timing of deformation in the range. Finally, we synthesize the implications of deformation in the Eastern Greater Caucasus for the deformational processes in accretionary prisms generally.

7.5.1 Range-wide structure and total shortening

Our data and structural interpretations have several implications for the structure of the Eastern Greater Caucasus, including the locations and geometries of major faults; the relationship between the Vandam Zone tectonostratigraphic package and the northern, predom-

inantly turbiditic stratigraphic package; internal shortening within the pervasively folded and faulted sequences of the range; and net shortening accommodated by the range. Here, we address the implications for each of these points.

7.5.1.1 Geometry of major faults

Our geologic observations constrain the number of major faults that accommodate shortening within the range, the cumulative displacement on these faults, and their geometry (Fig. 7.11). The location of ramps and flats on these major faults is constrained by the cumulative displacements inferred from shortening estimates of the structural transects reported above, as well as the bedding-plane geometries of hanging walls overlying these major structures.

7.5.1.1.1 Modern basal detachment

The geometry of the current basal detachment of the Eastern Greater Caucasus accretionary prism is inferred from shortening estimates based on folding and thrusting near the southern extent of deformation and topography associated with the Eastern Greater Caucasus (Fig. 7.11). The basal detachment terminates in fault-propagation structures that generate the southernmost topography associated with the range (Fig. 7.2, Agsu transect; Fig. 7.3; Fig. 7.11; *Forte et al.*, 2013). Duplication of Cenozoic strata structurally above the basal detachment near the toe of the prism requires 20 km of cumulative slip on the basal detachment, which we infer is located at about 5 km below sea level (Fig. 7.3). Another 4-6 km of slip is required by shortening inferred in fault-propagation folds of the Vandam Zone tectonostratigraphic package directly above the basal detachment (Figs. 7.6, 7.8, 7.11), implying a total of $\sim$25 km of slip on the basal detachment. Within the Lahij and Gabala transects, we infer a hanging-wall ramp in the Jurassic to Cretaceous strata of the Vandam Zone package (Figs. 7.6, 7.8, 7.11), which must be located 25 km south of the associated footwall ramp (Figs. 7.9, 7.11). The inferred location of this footwall ramp corresponds spatially with the broadly north-dipping portion of the Middle Jurassic organic-rich turbidite sequence observed in the central segment of the Salavat transect (Figs. 7.9, 7.11). The shortening estimates from above the basal detachment and the broad region of north dip in the central part of the range provide two independent lines of evidence supporting the inferred location of the basal detachment footwall ramp (Fig. 7.11).

7.5.1.1.2 Zangi thrust

Besides the current basal detachment of the Eastern Greater Caucasus prism, the other fault on which significant displacement is inferred to have occurred is the Zangi thrust, which

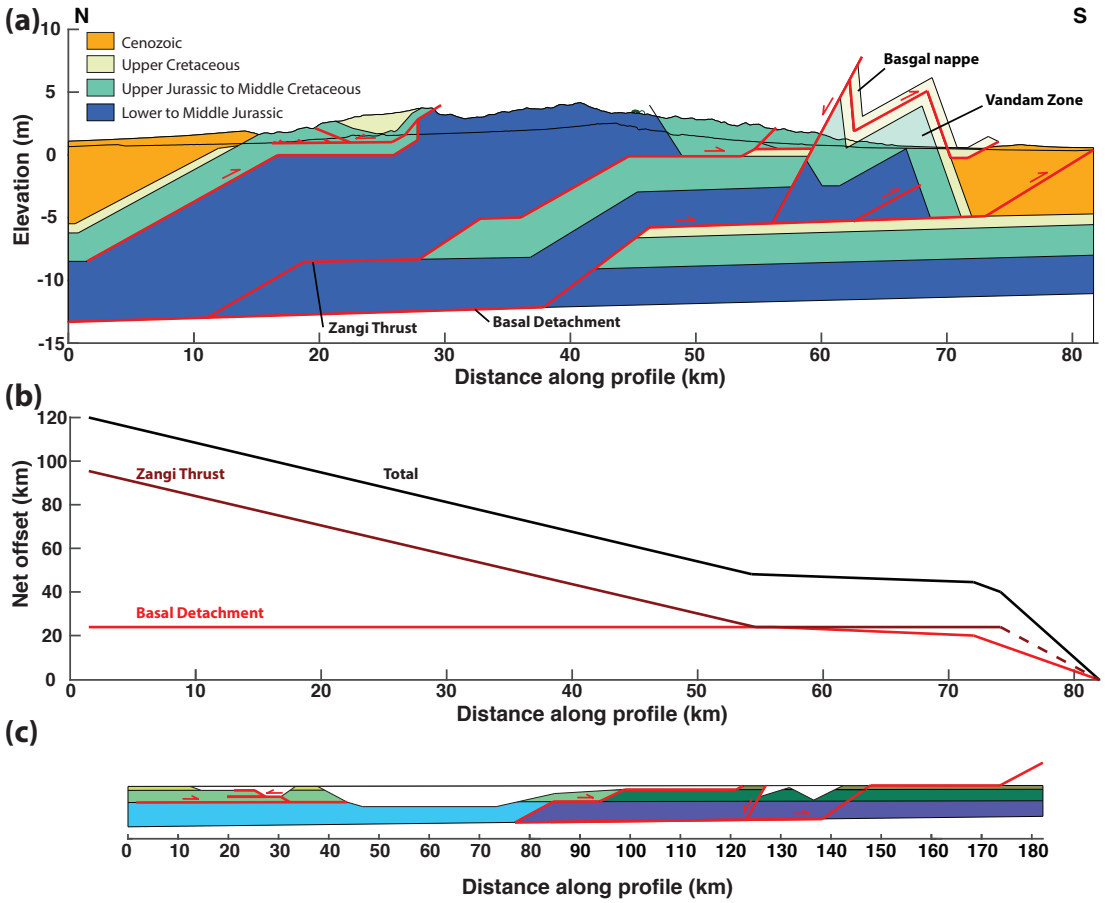

Figure 7.11: (a) Interpretive cross section of the structure of the entire range, based on compilation of observations and interpretations shown in Figures 7.3, 7.6, 7.8, 7.9, and 7.10. Geology is colored by age according to the key, rather than according to the units used elsewhere in the paper. The cross section is line-balanced. Note that we have no subsurface data and given the variability in stratigraphic thickness across the range (e.g., *Bochud*, 2011; *Alizadeh et al.*, 2016), the depicted thicknesses and depths should be viewed as best guesses that are consistent with the surface geology. (b) The spatial distribution of cumulative displacement on current basal detachment and the previous detachment, the Zangi thrust, is inferred from structural geometry of the range. (c) Retrodeformed geometry of the cross section shown in (a) at 40% size.

separates the Vandam Zone package in the footwall from the northern, largely turbiditic tectonostratigraphic package in the hanging wall in the Lahij transect (Figs. 7.6, 7.8, 7.9, 7.11). This fault is inferred to have three ramps and two flats (Fig. 7.11). We first discuss our inference of the locations of these ramps and flats in the hanging wall, then in the footwall.

Our inferred structural geometry for the Zangi thrust hanging wall has implications for the locations of the ramps and flats of the thrust. The stratigraphically highest ramp is inferred to cut through Upper Cretaceous strata including the Upper Cretaceous red and blue shale sequence (UKrbsh) and the Upper Cretaceous white-blue sandstone sequence (UKblss). This ramp is inferred to exist in the hanging wall at the southern edge of the Basgal nappe thrust sheet (Figs. 7.6, 7.11). To the north of this ramp is a flat that underlies the Upper Cretaceous red and blue shale sequence (UKrbsh), which is at least 24 km across strike, as demonstrated by the offset of the Basgal nappe thrust sheet (Figs. 7.6, 7.11). To the north of this flat is a ramp that is inferred to cut through the Upper Jurassic calcareous turbidite sequence (Jctb) and the Lower Cretaceous turbidite sequence (LKtb). This ramp is inferred to occur in the hanging wall directly to the north of where the Vandam Zone package outcrops in the Lahij transect and the southern segment of the Gabala transect (Figs. 7.6, 7.8, 7.11). To the north of this ramp is a flat beneath the Upper Jurassic calcareous turbidite sequence (Jctb), which is inferred to occur in the hanging wall in the northern portion of the Gabala transect (Figs. 7.8, 7.11). In that portion of the transect, the Upper Jurassic sequence (Jctb) is exposed for several kilometers across strike above a footwall flat (Figs. 7.8, 7.11). The volume of the Upper Jurassic sequence (Jctb) at this location requires that it overlies a hanging wall flat (Figs. 7.8, 7.11). The final hanging-wall ramp inferred to cut through Lower to Middle Jurassic strata including the organic-rich turbidite sequence (Jotb). This ramp is inferred to occur in the hanging wall immediately to the north of the flat beneath the Upper Jurassic sequence (Jctb; Figs. 7.8, 7.9, 7.11). We infer that the Zangi thrust roots into a detachment between the Lower Jurassic sequence and underlying basement (Fig. 7.11; e.g., *Green et al.*, 2009).

We infer the locations of footwall ramps and flats on the Zangi thrust from two independent lines of evidence, the retrodeformed across-strike lengths of hanging wall flats and broad trends in bedding orientation and exhumation depth observed in the hanging wall. The location of the hanging-wall ramp that cuts through Upper Cretaceous sequences (UKrbsh, UKblss) depends on the cumulative offset of the Basgal nappe thrust sheet (Figs. 7.6, 7.11). The southernmost permissible location for this ramp is directly north of where the Zangi thrust crops out in the Lahij transect (Fig. 7.6), which results in the minimum permissible offset of the Basgal nappe thrust sheet, 24 km. The location of this footwall

ramp is not directly evident in bedding-plane orientations of the deformed, predominantly turbiditic strata of the hanging wall, likely because it is the smallest of the three inferred ramps on the Zangi thrust. Nevertheless, we demonstrate below that the southernmost permissible location is the most likely given the overall geometry of the fault (i.e., the location shown on Fig. 7.6). The flat immediately to the north of this ramp is the same distance across-strike as the net offset of the Basgal nappe thrust sheet, 24 km (Figs. 7.6, 7.11). To the north of this flat is the ramp that cuts through Upper Jurassic to middle Cretaceous strata (Fig. 7.11). Remarkably, this inferred ramp location corresponds almost perfectly with the region of north dip and exhumation-depth change at the boundary between the central and northern segments of the Salavat transect (Figs. 7.9, 7.10, 7.11). In this region, at the surface, the Middle Jurassic organic-rich turbidite sequence (Jotb), Upper Jurassic massive carbonate sequence (Jmc), and Lower Cretaceous bedded carbonate sequence (LKbc) define a north-dipping and north-younging panel (Figs. 7.9, 7.10, 7.11), south of which middle Jurassic strata are exposed (Jotb), and north of which Upper Cretaceous strata (UKwss) are exposed. To the north of this ramp is a flat that was located beneath the Upper Jurassic calcareous turbidite sequence (Jctb). The across-strike length of this flat is estimated to be ∼9 km by line balancing of the corresponding hanging wall flat, which outcrops in the southern segment of the Salavat transect (Fig. 7.8). The ramp immediately north of this flat coincides exactly with the region of north dip and change in exhumation depth at the northern margin of the Salavat transect, where there is a transition from exposed Lower Cretaceous strata (LKbc) to the south to Neogene strata to the north (*Khain and Shardanov*, 1960; *Nalivkin*, 1976, Figs. 7.10, 7.11). Thus, the locations of footwall ramps on the Zangi thrust are constrained both by shortening and displacement estimates above up-dip regions of the fault and by broad trends in bedding-plane orientation and exhumation depth in the hanging wall. These two lines of evidence agree remarkably well (Fig. 7.11).

7.5.1.2 Stratigraphic relationship between the Vandam Zone and northern, turbiditic stratigraphic packages

Understanding the stratigraphic and structural relationship between the lithologically distinct tectonostratigraphic packages of the southern slope of the Greater Caucasus is important for characterizing the magnitude of shortening accommodated within the range (e.g., *Zonenshain and Le Pichon*, 1986; *Cowgill et al.*, 2016). Sedimentary rocks exposed on the southern slope of the range consist of two distinct tectonostratigraphic packages: a southern package that includes thick deposits of volcaniclastic sandstones and tuffs, which is known as the Vandam Zone in the eastern Greater Caucasus (e.g., *Kopp*, 1985); and a northern package that is composed predominantly of thinly bedded turbidites (e.g., *Nalivkin*, 1976;

Cowgill et al., 2016; *Khain*, 1975; *Adamia et al.*, 2011a). If these two packages were deposited entirely separate from one another on the opposite sides of a basin with minimal or no sediment deposited between them, then shortening estimates based on mapping of deformation of these two packages in the Greater Caucasus would provide a lower bound on the net convergence accommodated within the range (e.g., *Cowgill et al.*, 2016). If, however, the two packages interfingered or were stratigraphically continuous with one another, then shortening within these two packages should account for the entire budget of convergence accommodated by the Greater Caucasus.

Our structural interpretation of the range has implications for the stratigraphic continuity between the Vandam Zone and northern, predominantly turbiditic stratigraphic packages. Specifically, the fact that the Zangi thrust, which divides the surface exposures of these two packages from one another, is a thrust fault composed of multiple, well-defined ramps and flats (Fig. 7.11) suggests stratigraphic continuity between the Vandam Zone and northern, turbiditic stratigraphic packages. Thus, shortening calculated from the inferred structural geometries of these two packages should account for the entire budget of convergence that is accommodated by the eastern Greater Caucasus.

7.5.1.3 Total shortening and internal deformation within the pervasively folded sequences of the range

Because we infer stratigraphic continuity between the Vandam Zone and northern, turbiditic stratigraphic packages, the upper crustal shortening recorded in deformed sedimentary strata of the range should account for the complete budget of tectonic convergence that the range has accommodated. An independent estimate of the tectonic convergence accommodated within the range comes from vertical-axis rotations of paleomagnetic poles in the region, which suggest tectonic convergence of ∼120 km in the Eastern Greater Caucasus (*van der Boon et al.*, 2018). Of this total convergence budget, ∼25 km is accounted for by slip on the current basal detachment (Fig. 7.2, Agsu transect, Lahij transect, Gabala transect; Figs. 7.3, 7.6, 7.8; *Forte et al.*, 2013). Another ∼25 km is accounted for by slip on the Zangi thrust (Figs. 7.6, 7.8, 7.11). This leaves 70 km of shortening to be accounted for by internal deformation within the pervasively folded turbiditic strata of the range.

Based on the gross structure of the range (Fig. 7.11), folded and faulted turbiditic sequences (Jotb, Jctb, LKtb) are inferred to occupy an area of ∼60 km across-strike width in the Zangi thrust hanging wall (Fig. 7.11), which would have initially occupied an area 130 km wide across strike assuming that these deformed sequences account for all remaining shortening. Minimum estimates of shortening within these folded strata discussed above, which are based on conservative estimates of fold amplitude and ignore fault offsets, are

$\sim$35%, meaning that folding alone accounts for $>$32 km of shortening within a 60-km wide belt. These mud-rich lithologies could reasonably be expected to undergo 10-20% volume loss during tectonic compression and the development of their well-expressed cleavage (e.g., *Sorby*, 1908; *Ramsay and Wood*, 1973), accounting for another 13-26 km of shortening, assuming an initial across-strike width of 130 km. This leaves 22 – 35 km of shortening that must be attributed to a combination of fold amplitudes greater than estimated from our conservative line-tracing method and slip on intraformational thrust faults, which are common within the deformed turbitidic sequences of the range (Fig. 7.2, Lahij transect, Salavat transect). The accommodation of this shortening within the 60 km across-strike belt of mud rich turbidites means that folding and faulting in the belt accommodate 54 – 67 km of shortening (90 – 112% shortening), which we view as reasonable.

7.5.1.4 Finite strain partitioning in the range

Taken together, the available evidence of slip on major faults and shortening through hanging-wall folding and intraformational thrusting are consistent with all tectonic convergence accommodated within the eastern Greater Caucasus ($\sim$120 km; *van der Boon et al.*, 2018) being accommodated by upper-crustal deformation (Fig. 7.11). The multi-ramp structure inferred for the Zangi thrust is evidence that prior to deformation in the Greater Caucasus, the sedimentary rocks now exposed in the range were a stratigraphic sequence that was continuous from north to south (Fig. 7.11). Both of the major thrusts of the range, the Zangi and the modern basal detachment, terminate in fault propagation structures near the toe of the accretionary prism, and folding and minor thrusting in the hanging walls of these faults result in the cumulative displacement on the combination of these two major thrusts increasing from zero at the prism toe to 120 km in the rear of the accretionary prism (Fig. 7.11). The accommodation of 120 km shortening occurs within a prism that is $\sim$95 km wide from the northern extent of inferred deformation to the southern extent (Fig. 7.1), yielding an overall shortening of 55%, or 50-53% if we ignore the 13-26 km inferred to result from volume loss.

7.5.2 Temporal constraints on deformation

Our thermochronometry data have implications for the timing of deformation in the range and the spatial distribution of strain over time. Here we combine our thermochronometry data with geodetic and paleomagnetic data and geologic cross-cutting relationships in order to constrain the timing of deformation in the range. Specific questions we address include the timing of initiation of deformation in the Eastern Greater Caucasus, of initial slip on the

present basal detachment, and of potential changes in strain partitioning within the range.

7.5.2.1 Initiation of deformation within the Eastern Greater Caucasus

7.5.2.1.1 Constraints from geodesy and paleomagnetic data

Geodesy and paleomagnetic data provide estimates of present convergence rates and total tectonic convergence accommodated within the Eastern Greater Caucasus, which can be extrapolated to calculate the amount of time required to achieve the total tectonic convergence at present rates. Vertical-axis rotations of paleomagnetic poles suggest 120 km of tectonic convergence accommodated within the Eastern Greater Caucasus (*van der Boon et al.*, 2018), which is consistent with our structural interpretation, as discussed above (Fig. 7.11). Geodetic datasets indicate that 10-12 mm/yr of convergence is currently being accommodated within the Eastern Greater Caucasus (*Reilinger et al.*, 2006; *Kadirov et al.*, 2012, 2015). Thus, 10-12 Myr of convergence would be required at current rates in order to account for the total tectonic convergence inferred to have been accommodated within the range. Since the present tectonic configuration of north-directed subduction is unlikely to have changed during the lifespan of the Eastern Greater Caucasus orogen, such extrapolation of present rates is justified.

7.5.2.1.2 Constraints from thermochronometry

Thermochronometric ages reflect the time-temperature path of an analyzed mineral grain (e.g., *Wolf et al.*, 1998). For certain time-temperature paths, thermochronometry ages reflect the time at which a sample cooled to a temperature beneath the nominal closure temperature of a system (e.g., *Dodson*, 1973). However, any given age could also be produced by isothermal holding such that the age reflects the balance of production of radiogenic daughter products and fission tracks with their diffusive loss or annealing (e.g., *Gleadow et al.*, 1986). The range of temperatures at which such a scenario can occur is known as the partial annealing zone or partial retention zone of a given thermochronometric system (e.g., *Gleadow et al.*, 1986).

Thermochronometry ages within the Eastern Greater Caucasus cluster within several broad categories (Fig. 7.1). Several ages cluster around 90 Ma, likely reflecting Cretaceous tectonism and magmatism (samples N3, H1, L2, AZ089; *Nikishin et al.*, 1998). AFT ages from the northern part of the range are broadly clustered into age ranges of 30 – 50 Ma (5 samples; Fig. 7.1) and 0 – 20 Ma (7 samples, of which 3 have ages >10 Ma; Fig. 7.1). These ages could reflect either cooling by tectonic exhumation at the measured age or isothermal holding at a given temperature within the AFT partial annealing zone (e.g.,

Gleadow et al., 1986). If ages greater than 10-12 Ma do reflect cooling, such ages would imply that deformation within the Eastern Greater Caucasus began prior to the 10-12 Ma initiation inferred by extrapolating current geodetic convergence rates (*Reilinger et al.*, 2006; *Kadirov et al.*, 2012, 2015; *van der Boon et al.*, 2018).

The spatial distribution of AFT ages >10-12 Ma within the Eastern Greater Caucasus suggests that these ages result from isothermal holdling and partial annealing, rather than cooling at the nominal age (Fig. 7.1). Most of these ages occur within a single along-strike band near the northern margin of exposed Middle Jurassic organic-rich turbidites (Jotb) on the north side of the range (Fig. 7.1), where regional dips are broadly to the north and exhumation depth increases to the south. Samples AZ089 (*Bochud*, 2011), AZ083* (*Bochud*, 2011), and N1 (Avdeev, unpublished) define a dramatic age trend where AFT ages decrease sharply from 89.8 $\pm$ 9.8 Ma in the north, upsection, to 14 $\pm$ 1.6 Ma in the south, downsection. These samples are distributed over $\lesssim$1 km of stratigraphic thickness, so it is likely that the samples reflect a fossil partial annealing zone (*Gleadow et al.*, 1986). Thus, these >12 Ma AFT ages and others located along strike (samples AZ091, AZ092, AZ093; *Bochud*, 2011, and N2) are likely to reflect isothermal holding within the partial annealing zone rather than cooling.

Besides those >12 Ma AFT ages on the northern portion of the Eastern Greater Caucasus whose ages are attributed to isothermal holding in the partial annealing zone, the only other sample with a Cenozoic AFT age >12 Ma is sample S1 (Fig. 7.1; Fig. 7.2, Salavat transect). This sample is notable because its AFT age (15.5 $\pm$ 4.3 Ma) is greater than its mean ZHe age (10.3 $\pm$ 3.7 Ma; Fig. 7.1) despite the fact that the nominal closure temperature of the ZHe system is greater than the nominal closure temperature of the AFT system (e.g., *Reiners*, 2005; *Donelick et al.*, 2005). Thermal modeling of this sample suggests that cooling began around 12 Ma (Fig. 7.5b). Given the thermal modeling results and the peculiar ages of this sample, S1 does not provide compelling evidence for deformation within the Eastern Greater Caucasus beginning before 10-12 Ma. We thus regard the 10-12 Ma estimate from extrapolating current convergence rates as a good working hypothesis for the age of initiation of shortening in the Eastern Greater Caucasus.

7.5.2.2 Initiation of slip on the present basal detachment

7.5.2.2.1 Constraints from foreland basin deformation and stratigraphy

The present basal detachment controls deformation within the Miocene to Quaternary strata observed along the southern margin of the Eastern Greater Caucasus, so any deformation of these strata must post-date the initiation of slip on the present basal detach-

ment. Several stratigraphic lines of evidence can be used to bracket the onset of deformation on the modern basal detachment. In the Agsu transect (Fig. 7.1; Fig. 7.2, Agsu panel), deformed Eocene to Miocene turbidites (EMtb) are unconformably overlain by less-deformed, younger strata, the oldest of which is Upper Miocene (MPss), of the Pontian regional stage (*Voronin et al.*, 1959; *Nalivkin*, 1976) that was deposited 7.0 – 5.5 Ma (*Jones and Simmons*, 1998). The age of this unconformable deposition indicates that at least some deformation of the Eocene to Miocene turbidite strata occurred before the latest Miocene.

An indirect means of constraining the age of the present basal detachment is by determining when the previous basal detachment was active. The Zangi thrust represents the basal detachment of the Eastern Greater Caucasus accretionary prism that was active before the present detachment. Previous geologic mapping reveals that the Basgal nappe thrust sheet, the southernmost preserved remnant of the Zangi thrust (Fig. 7.2, Lahij transect; Fig. 7.6), structurally overlies strata of Upper Miocene age of the Sarmatian regional stage (*Khain and Shardanov*, 1960), which was deposited between 10.5 and 8.2 Ma (*Jones and Simmons*, 1998). It is unlikely that the tip of the previous basal detachment would continue to advance after establishment of a new basal detachment. Thus, 10.5 Ma is an upper age bound on the establishment of the present basal detachment.

7.5.2.2.2 Constraints from thermochronometry

Vandam Zone thermochronometry samples L1 – L6 are in the thrust sheet directly overlying the modern basal detachment, so their cooling histories may disclose the timing of accretion of this thrust sheet to the Eastern Greater Caucasus accretionary prism. All six samples have mean AHe ages $<$4 Ma, and sample L2 also has an AFT age of 88.4 $\pm$ 5.7 Ma (Avdeev, unpublished). Thermal modeling of sample L2 indicates that the sample underwent $\sim$90° C cooling, or 3.0 – 4.5 km of exhumation at a geothermal gradient of 20-30° C, since $\sim$6 Ma (Fig. 7.5a). This exhumation likely resulted from slip on the normal fault that bounds the north end of the Vandam Zone tectonostratigraphic package or from a combination of slip on that fault and on the modern basal detachment (Fig. 7.6). Slip on the normal fault that bounds the Vandam Zone package is likely to post-date initiation of slip on the present basal detachment for two reasons. First, the orientation of the normal-fault footwall suggests that folding as a result of propagation of south-directed thrust faults preceded normal fault slip. Second, if the modern basal detachment was already established, then slip on the observed normal fault would result in the toe of the accretionary prism being propagated forward, which is a common occurrence in prisms (*Hosseini-Barzi and Talbot*, 2003). The breaking of a new basal detachment may have provided the change in stress state that caused the

formation of the observed normal fault. Because we infer that slip on the normal fault that bounds the northern extent of the Vandam Zone tectonostratigraphic package is likely to have followed initiation of slip on the modern basal detachment, the 6 Ma initiation of exhumation in sample L2 is a lower bound on the age of the modern basal detachment.

Thermochronometry and cross-cutting relationships yield compatible estimates of the initiation of slip on the present basal detachment of the Eastern Greater Caucasus. Upper Miocene deposits of age 10.5 to 8.2 Ma that were thrust over by the previous basal detachment provide an upper bound of the age of the presently active detachment. Uppermost Miocene deposits of age 7.0 to 5.5 Ma that unconformably overlie a sequence deformed above the present basal detachment provide a lower bound on the age of the active detachment. Thus, cross-cutting relationships indicate that slip on the modern basal detachment must have initiated between 10.5 and 5.5 Ma. Thermochronometry results from the thrust sheet that overlies the present basal detachment imply that slip on the modern detachment began prior to 6 Ma. Thus, the initiation of slip on the modern basal detachment is bracketed to between 10.5 and 6 Ma.

7.5.2.3 Strain partitioning between the basal detachment and the prism interior through time

Our mapping and structural interpretation of the Eastern Greater Caucasus indicate that folding and small-offset thrust faults play an important role in accommodating shortening within the range. This observation raises questions about the temporal relationship between deformation in the prism interior, slip on the basal detachment, and accretion of material to the toe of the prism. Specifically, does accommodation of shortening proceed temporally from the core of the prism toward the toe or does the shortening rate remain uniform throughout the prism even as new material is accreted to the toe? Here, we discuss the constraints from thermochronometry and cross-cutting relationships on the temporal relationship between shortening and accretion in the Eastern Greater Caucasus prism.

7.5.2.3.1 Constraints from thermochronometry

Given the timing of accretion of the Vandam Zone tectonostratigraphic package inferred above (>5.5 Ma), we can use our thermochronometry results (Fig. 7.1, Tables 7.1, 7.2, 7.3, 7.4) to test whether deformation occurred in the range interior after accretion to the toe. Most of the sample mean AHe ages observed in the turbiditic core of the Eastern Greater Caucasus are <5.5 Ma (Fig. 7.1), requiring at least $\sim$60° C cooling or 2-3 km of exhumation assuming a geothermal gradient of 20-30° C, after Vandam Zone accretion and initial slip on the current basal detachment of the range. However, such cooling and

exhumation could occur passively as the result of slip on the current basal detachment at depth. Here, we use the geometric relationships of measured thermochronometric ages as a test for deformation following cooling.

A notable feature of the measured thermochronometric ages is the inverted age-elevation relationships observed in subvertical transects in the deformed, turbiditic (Jotb) core of the range (Fig. 7.7). Given the lack of Cenozoic volcanism in the Eastern Greater Caucasus (e.g., *Nalivkin*, 1976), these ages most likely result from exhumation. However, exhumation of a rigid block results in increasing thermochronometric ages with increasing elevation (e.g., *Farley et al.*, 2001), which is the opposite of the negative age-elevation relationship observed in our transects (Fig. 7.7). Thus, one alternative explanation is that the transects were rotated during folding after their thermochronometric ages were set. If so, such folding would post-date accretion of the Vandam Zone tectonostratigraphic package and initiation of slip on the modern basal detachment.

We undertook a simple test to determine whether post-cooling folding of the thermochronometry transects in the core of the range is a reasonable explanation for their inverted age-elevation relationships (Fig. 7.12). For each vertical transect, we tested a range of paleo-orientations rotated about a horizontal axis parallel to the strike of the orogen, which is the approximate orientation of most fold axes observed and inferred in the range (Fig. 7.12). The samples of a given vertical axis are treated as being attached to a rigid, rotating block. For each candidate paleo-orientation, the age-elevation relationship among the samples implies an exhumation rate for the transect (e.g., *Brandon et al.*, 1998; *Farley et al.*, 2001). We then test the implied exhumation rate against independent estimates of exhumation rates in order to determine which candidate paleo-rotations are plausible (Fig. 7.12a-c). Below, we show that the samples from the Haput (Fig. 7.12a) and Salavat (Fig. 7.12b) vertical transects are both fit by reasonable paleo-orientations, as are the samples from a closely spaced horizontal sampling transect near Lahij (Fig. 7.12c).

Haput Transect

For the Haput transect (Fig. 7.1; Fig. 7.2, Salavat panel; Fig. 7.12a), independent estimates of cooling/exhumation rate are provided by two samples with both AHe and AFT ages (samples H3 and H5; Fig. 7.1), which the exhumation rates implied by candidate paleo-orientations can be tested against. Assuming that the measured AHe and AFT ages result from cooling beneath the nominal closure temperatures of 110° C and 60° C, then the difference between the ages of each system reflects the time required for 50° C of cooling. Sample H3 has a sample mean AHe age of 4.4 $\pm$ 0.8 Ma and an AFT age of 8.2 $\pm$ 1.1 Ma, so the difference between the two systems is 3.8 $\pm$ 1.4 Myr, equating to a cooling rate of 10-21° C/Myr or 0.33-1.05 mm/yr for a geothermal gradient of 20-30°

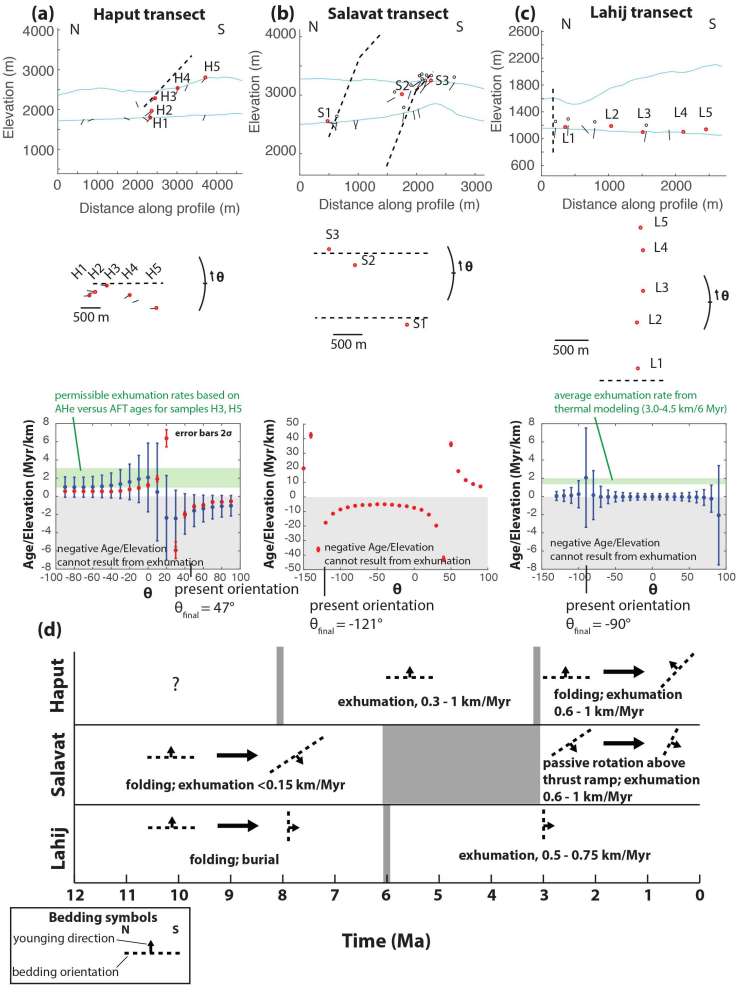

Figure 7.12: Results of thermochronometric folding tests for vertical and horizontal thermochronometry transects in the Eastern Greater Caucasus. (a) Results for the Haput transect. From top to bottom, panels indicate cross sectional view of the current orientation of the samples (samples shown in red, bedding measurements in black; dashed line shows overall bedding orientation); cross sectional view of the orientation of the samples on deposition inferred from mapped bedding planes; plot of age/elevation relationship for the sample thermochronometric ages (blue – AHe; red – AFT) as a function of rotation from their depositional orientation about a horizontal, WNW-trending rotation axis perpendicular to the displayed cross sections. On the plot of age/elevation relationship, age/elevation slopes of less than zero, which could not be formed except by post-cooling rotation, are grayed out. Green boxes indicate permissible age/elevation slopes based on independent constraints, where applicable. (b) Results for the Salavat transect, all plots equivalent to (a). (c) Results for the horizontal Lahij transect, all plots equivalent to (a). (d) Timeline of folding and exhumation inferred from the three transects. Gray bars mark transitions between distinct periods of folding and exhumation recorded in the transects. The width of the bar indicates the range of time in which the transition may have occurred. Bedding symbols are described in a key below the plot.

C. Sample H5 has a sample mean AHe age of 3.1 ± 0.4 Ma and an AFT age of 7.5 ± 1.3 Ma, with a difference of 4.4 ± 1.4 Ma, and resulting cooling and exhumation rates of 9-17° C/Myr and 0.3-0.85 mm/yr. The exhumation rates suggested by paired AHe and AFT ages from these two samples are in close agreement with one another and indicate ∼0.3-1.0 mm/yr exhumation of the samples in this transect at the time they cooled (Fig. 7.12a). For the range of candidate paleo-orientations considered for the Haput transect, orientations from θ = 10° to θ = -20° (10° NNE dip to 20° SSW dip) have AHe and AFT age-elevation relationships that are consistent with the inferred permissible range of ∼0.3-1.0 mm/yr (Fig. 7.12a). Thus, the observed ages of the Haput transect are consistent with cooling when the sampled strata were approximately flat lying until 3.1 ± 0.4 Ma followed by post-cooling folding into their present orientation, dipping ∼47° toward the NNE (Fig. 7.12a, 11d). Such folding could accommodate as much as 32% horizontal shortening (1 – cos 47°) over the area it occurred.

Salavat transect

Rotating the Salavat sample AFT ages, which range from 6.1 to 15.5 Ma, results in several candidate paleoorientations that have positive age-elevation relationships, as are expected from exhumation (Fig. 7.12b; e.g., *Farley et al.*, 2001). The exhumation rates implied by age-elevation relationships of paleo-rotated samples for the Salavat transect are all significantly lower than the exhumation rates inferred for Haput, however. In the Salavat transect, the positive age-elevation slopes that follow from rotating the samples are all <0.15 mm/yr (Fig. 7.12b). Such exhumation rates are significantly lower than present exhumation rates of the Salavat transect, which are constrained by the mean AHe age of sample S3, 3.3 ± 0.13 Ma, to be ∼0.6 to 1.0 mm/yr (Fig. 7.1; Tables 7.1, 7.2, 7.3, 7.4). We thus infer that the Salavat samples underwent a two-stage cooling/exhumation history that began with slow rates and then accelerated. The sample AFT ages could have attained a positive age-elevation relationship at a paleo-orientation angle of θ = -140 to -150° (dip angle of 40° to 30° NNE overturned; Fig. 7.12b). Such a paleo-orientation differs only 20 - 30° from the present day orientation of θ = -121° (dip of 59° NNE overturned; Fig. 7.12b; Fig. 7.2, Salavat transect) and is comparable to the orientation of many overturned, south-younging fold limbs observed in the Jurassic to Cretaceous thinly bedded sandstone-shale sequences of the Eastern Greater Caucasus (Figs. 7.6, 7.9; Fig. 7.2, Lahij transect, Salavat transect). The post-cooling, 20 - 30° top-to-the-north rotation then required for the Salavat thermochronometry transect to reach its current orientation (Fig. 7.12b, d) could be explained by transport up the basal detachment ramp that underlies the transect. Riding up such a ramp can also explain the increase in exhumation rate inferred for the samples between when the AFT ages were set and the present (Fig. 7.12d).

Lahij transect

In order to check that the paleo-rotation test we apply here produces sensible results, we also applied the technique to a set of closely-spaced, horizontally arrayed samples in the Lahij mapping transect (L1-L5; Fig. 7.12c). These samples have mean AHe ages ranging from 1-3 Ma (Fig. 7.1; Tables 7.1, 7.2), and are located in the footwall of the normal fault that bounds the northern extent of the exposed Vandam Zone tectonostratigraphic package (Fig. 7.12c, Fig. 7.2, Lahij transect). The samples are inferred to have cooled during slip on this normal fault and/or during accretion of the Vandam Zone package to the Eastern Greater Caucasus prism, as discussed above. The present vertical and south-younging orientation of the fold limb from which the samples were collected likely resulted from fault-propagation folding and is inferred to have been attained prior to cooling. Thus, the paleo-rotation technique should reveal that cooling in the present orientation is consistent with inferred exhumation rates. An independent constraint on exhumation rate for the Lahij samples is provided by thermal modeling of sample L2, which has an AFT age of 88.4 $\pm$ 5.7 Ma and an AHe age of 2.85 $\pm$ 0.2 Ma (Avdeev, unpublished). Modeled time-temperature pathways for this sample indicate 90° C of cooling since 6 Ma (Fig. 7.5a), equivalent to an exhumation rate of 0.5 to 0.75 mm/yr at geothermal gradients of 20-30° C. Comparing the age/elevation slopes attained by paleo-rotation of the Lahij AHe ages to this independent estimate of exhumation rate indicates that cooling in the present orientation is consistent with the independently estimated exhumation rates (Fig. 7.12c). This result validates the paleo-rotation method (Fig. 7.12).

Summary of thermochronometric evidence

Paleo-rotation modeling of the three thermochronometry sample transects (Haput, Salavat, Lahij; Fig. 7.1) yields new insights into the exhumation and deformation history of each region. The thermochronometric ages of the Haput transect reflect cooling in a flat-lying orientation, after which the transect was rotated into its present, moderately north-dipping orientation by post-cooling folding (Fig. 7.12a, d). The cooling ages of the transect, which are 3.1 $\pm$ 0.4 Ma and greater (Fig. 7.1; Tables 7.1, 7.2), place an upper bound on the age of the post-cooling folding, indicating that the folding occurred after 3 Ma (Fig. 7.12d). The AFT ages of the Salavat transect are consistent with exhumation at rates of 0.02 – 0.05 mm/yr in a gently NNE-dipping, overturned orientation until after 6.1 Ma (Fig. 7.12b, d). Following this slow cooling, the rocks of the Salavat transect were rotated 20-30° northward into their present, moderately NNE dipping and overturned orientation (Fig. 7.12b, d). In addition, an AHe age of 3.3 $\pm$ 0.13 Ma from sample S3 shows that exhumation rates increased to an average of 0.6 – 1 mm/yr from 3 Ma until the present (Fig. 7.12d). The northward rotation of 20-30° and increase in exhumation rates are both consistent with

tectonic motion up the ramp in the present basal detachment that the transect overlies (Figs. 7.9, 7.11, 7.12d). The AHe ages of the samples in the Lahij transect are consistent with cooling in their present orientation, which matches our interpretation based on the structural geometry of the Lahij mapping transect (Figs. 7.6, 7.11, 7.12c, d). The fact that folding of the Haput transect occurred after 3 Ma indicates that internal deformation in the core of the range above the Zangi thrust was still active after accretion of the Vandam Zone and initiation of slip on the present basal detachment, which is inferred to have occurred >6 Ma, as discussed above (Fig. 7.12d).

7.5.2.3.2 Constraints from stratigraphy

Cross-cutting relationships between faults and sedimentary strata can provide constraints on the timing of deformation in different parts of the Eastern Greater Caucasus accretionary prism. One such constraint comes from deformation of Quaternary foreland-basin strata along the southern margin of the Eastern Greater Caucasus from the longitude of Ismaili to the west (*Forte et al.*, 2013). Based on the inferred shortening of a 0.88 – 1.8 Ma regional unconformity during slip on the basal detachment, *Forte et al.* (2013) concluded that deformation of Quaternary sediments at the toe of the Eastern Greater Caucasus prism has accounted for 83-100% of shortening accommodated within the prism since 0.88-1.8 Ma. Our new structural model permits assessment of whether such a shortening pattern has persisted over the entire history of the orogen (Fig. 7.11). Within the Eastern Greater Caucasus, uppermost Cretaceous strata are offset by ∼25 km on the modern basal detachment and ∼25 km on the Zangi thrust, the inferred previous basal detachment (Fig. 7.11). Because both the Zangi thrust and the modern basal detachment are inferred to terminate in fault-propagation structures at the surface (Figs. 7.3, 7.6, 7.11), these offsets imply that a total of 50 km of shortening has been accommodated by folding and small-offset faulting of Cenozoic strata near the toe of the prism. Given that total tectonic convergence in the range is ∼120 km (*van der Boon et al.*, 2018, Fig. 7.11), deformation of Cenozoic strata near the toe of the prism accounts for ∼42% of shortening, whereas folding and faulting within the Mesozoic core of the range is estimated to account for 58% of shortening (Fig. 7.11). Of the 50 km of shortening accommodated within Cenozoic hanging walls of the Zangi thrust and modern basal detachment, the 25 km associated with the Zangi hanging wall is likely to have occurred while the Zangi thrust was the active basal detachment, before 6 Ma, whereas the 25 km associated with the hanging wall of the modern basal detachment is likely to have occurred since 6 Ma. Thus, the rate of shortening within Cenozoic strata near the toe of the prism is roughly constant on timescales of $\geq$ 6 Myr. Therefore, the situation inferred by *Forte et al.* (2013), in which shortening of Quaternary strata accounts

for 83-100% of Eastern Greater Caucasus shortening since 0.88-1.8 Ma is likely a transient pulse of deformation in the toe of the prism.

7.5.3 Implications for tectonics of the Greater Caucasus and the Arabia-Eurasia collision zone

7.5.3.1 Along-strike variation in the magnitude of shortening accommodated within the Greater Caucasus

The Greater Caucasus represents an important region of strain accommodation within the Arabia-Eurasia collision zone (e.g., *Cowgill et al.*, 2016) and is also valuable as a natural laboratory for the initiation of continental collision (*Mumladze et al.*, 2015, Tye et al., submitted). In order to refine our understanding of the tectonic history of the Greater Caucasus, we compare our structural interpretations and shortening estimates for the Eastern Greater Caucasus with structural (*Cowgill et al.*, 2016; *Trexler*, 2018) and paleomagnetic (*van der Boon et al.*, 2018) shortening estimates for other parts of the Greater Caucasus. The Greater Caucasus shows marked along-strike variations in width, structural style, and exhumation depth (*Forte et al.*, 2014). Structural models of the western Greater Caucasus indicate the accommodation of ∼230 km of shortening (*Trexler*, 2018), while paleomagnetic vertical-axis rotations indicate 200-280 km shortening (*van der Boon et al.*, 2018). Our structural model for the Eastern Greater Caucasus is consistent with 120 km of shortening inferred from paleomagnetic vertical-axis rotations (*van der Boon et al.*, 2018). Thus, structural and paleomagnetic datasets are in agreement that there is a marked difference in the amount of shortening accommodated in the western and eastern Greater Caucasus.

The along-strike difference in shortening accommodated within the Greater Caucasus implies the existence of a strike-slip fault somewhere in the lower plate of the system that enabled convergence to occur more quickly or for a longer time in the western Greater Caucasus than in the Eastern Greater Caucasus (e.g., *van der Boon et al.*, 2018). Because existing shortening estimates for the entire orogen are restricted to western Georgia and eastern Azerbaijan, there is a vast swath of the central to central-eastern portion of the Greater Caucasus for which whole-orogen shortening magnitudes are not constrained by geologic investigation, so it is difficult to pinpoint the location of the lower plate strike-slip structure (Fig. 7.1a). Because much of the central to central-eastern portion of the range is similar to our study area in lithology and exhumation depth (e.g., *Nalivkin*, 1976), we investigate first-order along-strike variations in shortening by assuming that the central to central-eastern Greater Caucasus accommodates 50-55% shortening, as in our study area (Fig. 7.11). Under this assumption, the shortening accommodated is proportional to the

width of the range. Immediately to the west of our study area, the range widens considerably to a width of >200 km from the southernmost foreland basin fold-thrust structures to the northern extent of the orogen (Fig. 7.1a). At such a width, assuming the same finite strain as in our study area, total shortening accommodated by the range >200 km, equivalent to the shortening accommodated in the western Greater Caucasus (*Trexler*, 2018; *van der Boon et al.*, 2018). Thus, given our assumptions, a discontinuity in cumulative shortening exists between the western to central-eastern segments of the Greater Caucasus, which accommodate >200 km of shortening, and the Eastern Greater Caucasus, which accommodates 120 km of shortening. This discontinuity is the most likely location for the proposed lower plate strike-slip fault to intersect the Greater Caucasus (Fig. 7.1a). Such a strike-slip fault has proven difficult to identify, potentially because it may no longer be active, though two proposed structures that could generate the along-strike differences in shortening inferred in the Greater Caucasus are the West Caspian fault (*Khain et al.*, 1966) and the Arax fault (e.g., *van der Boon et al.*, 2018).

7.5.3.2 Evolution of the Arabia-Eurasia collision zone

The Eastern Greater Caucasus is part of the Arabia-Eurasia collision zone, and the timing and magnitude of shortening that we infer for the Eastern Greater Caucasus have implications for the evolution of strain accumulation in the region. We infer that deformation in the Eastern Greater Caucasus began 10-12 Ma. Such timing is consistent with the inferred initiation of northward subduction in the South Caspian Basin, which sits immediately to the east of the Eastern Greater Caucasus, at ∼10 Ma (*Hollingsworth et al.*, 2008), as well as the onset of rapid exhumation in the Alborz mountains to the south-southeast of the Eastern Greater Caucasus at 12 Ma (*Guest et al.*, 2006). The timing of initiation of deformation in the Eastern Greater Caucasus, South Caspian Basin, and Alborz at 10-12 Ma is distinct from the timing of deformation in the western Greater Caucasus, which is inferred to have begun at ∼35 Ma (e.g., *Vincent et al.*, 2007; *Adamia et al.*, 2011a). These differences in initiation of convergence can be explained by slip on the same strike-slip structure inferred to be responsible for the difference in shortening magnitude between the Eastern Greater Caucasus and the western to central-eastern segments of the Greater Caucasus, discussed above. Such a structure would have been active from 35 Ma or earlier until 10-12 Ma or later. The initiation of deformation in the Eastern Greater Caucasus, South Caspian Basin, and Alborz at 10-12 Ma is likely to reflect the earliest strain accommodation to the north of the Zagros belt in southern Iran, which sits along the Arabia-Eurasia plate boundary (e.g., *Pirouz et al.*, 2017).

7.5.4 Implications for accretionary prism deformation

The constraints on cumulative shortening and the timing of deformation in the Eastern Greater Caucasus that our data provide have implications for the internal deformation and evolution of accretionary prisms. This study provides insight into the modes of internal thickening of prisms, the spatial distribution of strain in prisms, the temporal relationship between in-sequence and out-of-sequence deformation, and prism growth.

7.5.4.1 Modes of internal thickening of prisms

Our mapping and structural interpretation of the Eastern Greater Caucasus indicate that folding and small-offset thrust faults play an important role in thickening the accretionary prism (Figs. 7.6, 7.8, 7.9, 7.11). The marked structural contrast we observe between the Vandam Zone and northern, turbiditic tectonostratigraphic packages indicates that lithology plays an important role in the mechanisms of strain accommodation (Figs. 7.6, 7.11). Because the Eastern Greater Caucasus is dominantly composed of marine sandstone-shale sequences similar to those accreted to typical prisms (e.g., *Moore*, 1989), the mechanisms of deformation observed in the Eastern Greater Caucasus are likely to be characteristic of typical accretionary prisms.

In the northern, turbiditic tectonostratigraphic package that dominates the Eastern Greater Caucasus, the deformation style depends in part on the depth to the basal detachment. On the southern slope of the range, where the Zangi thrust is inferred to be 2-3 km beneath the surface, close asymmetric folds imply formation as fault-propagation structures above closely-spaced, south-vergent thrusts that root into the basal detachment (e.g., *Suppe*, 1990; *Ghisetti et al.*, 2016). In contrast, in the core of the range and on its northern slope, where the Zangi thrust dips northward and is located 5-10 km beneath the surface, folds are largely symmetric and wider, with 90° interlimb angles common (Fig. 7.2, Salavat panel; Fig. 7.9). The symmetry of these folds, as well as the fact that the thickness of over- and underlying sandstone layers is observed in some cases to determine fold wavelength (Fig. 7.2, Salavat transect), indicates they are more likely to have formed from buckling than from fault propagation (e.g., *Butler et al.*, 2019). Concomitantly, the thrust faults observed in the core of the range and inferred to have limited net offsets (Fig. 7.2, Salavat transect) may be explained as accommodation faults that do not root into basal detachment (e.g., *Butler et al.*, 2019). Overall, our structural observations suggest that within 2-3 km of the basal detachment, deformation is dominated by closely spaced thrusts that root into the detachment and fault-propagation folding, whereas 5-10 km above the basal detachment, deformation occurs primarily by buckling and formation of accommodation faults that do

not root into the detachment.

7.5.4.2 Strain partitioning in accretionary prisms

Our mapping and structural interpretation of the Eastern Greater Caucasus reveal how strain is partitioned in the orogen between slip on the basal detachment and internal deformation by folding and small-offset thrusting above the detachment (Fig. 7.11). The previous basal detachment (Zangi thrust) and the current basal detachment are both inferred to have had negligible cumulative slip at their terminations at the toe of the accretionary prism. The negligible offset inferred at the tip of the two basal detachments means that the hanging walls of the faults are pinned to the footwalls at the toe of the accretionary prism (Fig. 7.11a, b). Thus, the pervasive internal deformation by folding and small-scale faulting that we observe within the hanging walls of the basal detachments requires a gradual increase in cumulative offset on the basal detachments moving northward (Fig. 7.11b). At the northward boundary of the region of internal deformation, cumulative offset on the basal detachment equals the total shortening accommodated by the accretionary prism (Fig. 7.11b). Because the lithologies that constitute the bulk of the Eastern Greater Caucasus orogen are likely typical for accretionary prisms (e.g., *Moore*, 1989), the pattern of pervasive internal deformation and gradually increasing cumulative basal slip from prism toe to prism rear is likely characteristic of accretionary prisms generally.

7.5.4.3 Temporal relationship between in-sequence and out-of-sequence prism deformation

Though deformation in orogenic wedges and accretionary prisms is commonly conceived of as proceeding forward in the direction of tectonic transport, deformation within the interiors of orogens is required in order to maintain critical taper and drive forward motion (e.g., *Davis et al.*, 1983; *Morley*, 1988). The mode of accommodation of such out-of-sequence, internal deformation in accretionary prisms is largely unconstrained, though slip on orogen-scale faults has been proposed (e.g., *Moore and Silver*, 1987). Our dataset from the Eastern Greater Caucasus provides new insight into how and when accretionary prisms deform internally (Fig. 7.12). The most significant accretionary event recorded by our data is the accretion of the Vandam Zone tectonostratigraphic package at or before 6 Ma (Fig. 7.12d), in which a new basal detachment broke along a surface inferred to be the contact between the Vandam Zone package and its underlying basement (e.g., *Green et al.*, 2009). Following this event, active folding within the core of the range intensified and/or began to affect previously undeformed strata (Fig. 7.12a, d; e.g., *Espina et al.*, 1996). There is

no evidence for the formation of any new range-scale faults in order to thicken the wedge, though slip on the Zangi thrust would be required to accommodate folding in the range core (Fig. 7.11). Thus, buckle folding within the turbiditic core of the range appears to be a primary mechanism of internal prism thickening in the Eastern Greater Caucasus. It may be that this is due in part to the youth of the Eastern Greater Caucasus prism, with more mature prisms possibly developing orogen-scale, out-of-sequence thrusts after folding has become tight to isoclinal throughout the prism (e.g., *Butler et al.*, 2019).

Though critical taper theory implies uniform thickening throughout an accretionary prism (*Davis et al.*, 1983), pulses of deformation within accretionary prisms, including compressional and extensional deformation, have been recognized at a variety of timescales (e.g., *Hosseini-Barzi and Talbot*, 2003; *Davis et al.*, 2006). The timescales over which accretionary-prism deformation is unsteady and the causes of this unsteadiness are poorly constrained, but may have implications for accretion processes or hazards (e.g., *Davis et al.*, 2006). Combining our results with previous interpretations of deformation within the Eastern Greater Caucasus (*Forte et al.*, 2013) yields insight into the timing and nature of such pulses in the Eastern Greater Caucasus. As discussed above, *Forte et al.* (2013) infer that 83-100% of total range shortening over the past 0.88-1.8 Myr has been accommodated by deformation of Cenozoic strata near the prism toe. We infer that since the most recent episode of major accretion in the Eastern Greater Caucasus, $\geq$6 Ma, $\sim$25 km shortening has been accommodated within Cenozoic strata near the prism toe. Extrapolating modern convergence rates of 10-12 mm/yr over the past 6 Myr, a pulse of deformation near the toe of the prism that accommodates 83-100% of total orogen shortening could only last for a maximum of 2-3 Myr. Thus, 2-3 Myr is the maximum permissible length for pulses of shortening in the Eastern Greater Caucasus, which is consistent with the timing inferred for ongoing deformation in the interior of the range (Fig. 7.12d).

7.5.4.4 Prism growth

Our structural and thermochronometric data record the growth of the Eastern Greater Caucasus accretionary prism in the pro-wedge direction and potentially also in the retro-wedge direction. Growth in the pro-wedge direction is evidenced by the accretion of the Vandam Zone tectonostratigraphic package and initial slip on the modern basal detachment at $\geq$6 Ma, which is recorded by cross-cutting relationships and thermochronometry (Fig. 7.12d). We tentatively infer growth in the retro-wedge direction from the fact that the Haput thermochronometry transect suggests that initial folding of the northern portion of the turbiditic core of the range occurred after 3 Ma (Fig. 7.12a, d). An interesting feature of the current structural geometry of the range is that, through folding of the turbidites that constitute the

bulk of the orogen, deformation in the upper plate can propagate to the north without any major north-vergent faults (Fig. 7.11). Retro-wedge growth of accretionary prisms in this way may be an important mechanism by which prisms thicken enough to expand in the pro-wedge direction by accretion.

7.6 Conclusions

The structural and thermochronometric data presented here provide insight into the internal architecture and deformation history of an active accretionary prism, the Eastern Greater Caucasus. Balanced cross sections of the orogen reveal that ∼120 km of shortening is accommodated within the prism, much of which is accommodated by buckle folding in the core of the range. Slip on the basal detachment of the prism (megathrust) works primarily to accommodate this internal deformation of the prism, and cumulative displacement on the basal detachment decreases to zero at the toe of the prism. Thermochronometric data from the range indicate that out-of-sequence deformation by folding in the core of the prism proceeds simultaneously with growth of the prism by accretion. Together, these observations provide a natural example of accretionary prism deformation over geologic timescales that implicates out-of-sequence folding as a significant mechanism of prism thickening.

Our data also provide new insight into strain accommodation in the Arabia-Eurasia collision zone. We infer from the geometry of the Greater Caucasus that an abrupt along-strike transition in finite strain accommodated within the range occurs immediately to the west of our study area, with >200 km of range-perpendicular shortening accommodated to the west of this transition and only ∼120 km accommodated to the east. Whereas deformation in the western Greater Caucasus is likely to have begun ∼35 Ma (*Vincent et al.*, 2007; *Adamia et al.*, 2011a), deformation in the Eastern Greater Caucasus, South Caspian Basin (*Hollingsworth et al.*, 2008), and Alborz orogen (*Guest et al.*, 2006) began 12-10 Ma. The later initiation of deformation in the Eastern Greater Caucasus, South Caspian Basin, and Alborz is consistent with accommodation of all collision-related shortening within the Zagros orogen to the south prior to 12-10 Ma. The west to east difference in the age of shortening initiation in the Caucasus, South Caspian Basin, and Alborz also suggests activity from 35 Ma to 12-10 Ma on a roughly orogen perpendicular, right lateral strike slip fault that cut across most or all of the Arabia-Eurasia collision zone.

Acknowledgments

The authors benefitted from conversations with Adam Forte, Eric Cowgill, Nikolas Middtun, and Chad Trexler that contributed to our understanding of the Eastern Greater Caucasus. Megan Hendrick, Amanda Maslyn, and Stuart Thomson provided help with sample collection, preparation, and analysis. This study was supported by the University of Michigan via a Rackham International Research Award and a Rackham Predoctoral Fellowship (A. Tye) and NSF EAR-1524304 (NAN). Thermochronometry data credited to Avdeev (unpublished) was collected by Boris Avdeev, now deceased, in the course of his dissertation research. Apatite fission track grain data and track length data are available at https://doi.org/10.7302/gkqx-rc70. Geologic swath mapping data across the Eastern Greater Caucasus (Fig. 7.2) are available at https://doi.org/10.7302/gc06-q290.

CHAPTER 8

Conclusions

8.1 Introduction

This short chapter draws together some of the strands emerging from the content chapters of the dissertation and then discusses some of the significant contributions of the dissertation. The dissertation includes three broad foci. Chapters 2 and 3 introduce and develop a new statistical method that can be used to better interpret the sediment provenance record of topographic growth, changing sediment routing, and exhumation in orogens. Chapters 4 and 5 develop a new method for interpreting the record of paleoseismic slip events on bedrock normal fault scarps, which is likely to be of use in constraining the spatial and temporal distribution of strain in continental orogens on 1,000 - 10,000 year timescales. Chapters 6 and 7 use a combination of structural geologic mapping, geo- and thermochronometry, and foreland basin stratigraphy to investigate the evolution of an orogen transitioning from subduction to collision, the Greater Caucasus. Together, the chapters present an account of the evolution of an orogen undergoing a key transition in the plate tectonic cycle and present several new techniques that are likely to be of interest in characterizing the evolution of other orogens.

8.2 Contributions

8.2.1 Interpretation of detrital geochronology data

The new statistical technique presented in Chapters 2 and 3, Bayesian Population Correlation (BPC), makes significant progress toward resolving a longstanding issue with interpreting detrital geochronology data. Specifically, because most detrital geochronology datasets are complex and multi-peaked, geological interpretations of the data are limited by how representative a detrital geochronology age sample is of its population (*Andersen*,

2005; *Pullen et al.*, 2014; *Ibañez-Mejia et al.*, 2018; *Tye et al.*, 2019). The representativeness of a sample increases with sample size, but at typical detrital zircon sample sizes significant uncertainty persists in inferring population characteristics from samples. BPC addresses this issue by using a Bayesian method to estimate the uncertainty of a population age distribution inferred from a sample (*Tye et al.*, 2019). Although the distribution of ages in a smaller sample may not be accurately representative of the sampled population, the inferred uncertainties will be greater, and the true population distribution is typically included in the envelope of permissible age distributions inferred for a given sample (*Tye et al.*, 2019). The ability of BPC to account for sampling-related uncertainties in detrital geochronology age distributions means that samples of differing size can be quantitatively compared to one another in an unbiased fashion for the first time. BPC also permits new quantitative estimates of detrital zircon mixing and dilution in sedimentary systems.

8.2.2 Interpreting the paleoseismic slip history of bedrock fault scarps

Chapters 4 and 5 present a new method for inferring the number of earthquake ruptures over which a bedrock normal fault scarp was exposed and the extents of the rupture patches. Such a method may be used to quickly and inexpensively assess first order aspects of the slip history of a bedrock normal fault scarp and potentially target portions of the scarp for subsequent analysis (*Tye and Stahl*, 2018). In regions of distributed continental deformation where bedrock normal fault scarps are associated with a significant portion of active faults, such as the Apennines, this technique may provide insight into the spatial and temporal distribution of continental strain on 1,000 - 10,000 year timescales.

8.2.3 Sedimentary record of continental collision

Chapter 6 uses the Greater Caucasus as a natural laboratory in which to determine the sedimentary response of an orogen to continental collision. Determining the timing of initial collision in mature collisional orogens is key to testing hypotheses about the effects of collision on climate, ocean circulation, species migration, topography, and the consumption of lithosphere. In the case of Earth's largest collisional orogen, the India-Asia collision zone, a consensus regarding the timing of collision has not been reached because of uncertainties about how the stratigraphic record is correlated with the transition to collision. The Caucasus is a young orogen currently transitioning from subduction to collision and has excellent preservation of foreland basin stratigraphy, making it an ideal location in which to constrain the stratigraphic record of collision. Chapter 6 outlines a set of sedimentary responses to collision in the Caucasus, including the temporal offsets between these responses, and cor-

relates changes in sedimentation with other records of the timing of collision, including geodetic records and paleomagnetic records. Our results show that the initial entrance of thinned lower plate continental lithosphere into the subduction zone, which marks the beginning of the transition to collision, preceded plate kinematic and exhumational effects of collision in the Caucasus by between 3 and 10 Myrs. Changes in plate convergence rates and accelerated exhumation inferred to be caused by collision coincide with the initiation of erosion in the foreland basin between the two colliding continents and the development of an axial drainage network in the basin.

8.2.4 Internal deformation within an active accretionary prism

Chapter 7 uses a combination of structural geology and thermochronometry to investigate internal deformation within an active accretionary prism, the Eastern Greater Caucasus. Despite the fact that accretionary prisms are ubiquitous tectonic features that record convergent tectonic deformation and pose significant geologic hazards, the submarine setting of most accretionary prisms has hampered observation of the processes by which they deform internally over geologic timescales. Chapter 7 reveals that in the Eastern Greater Caucasus, deformation of the active prism is accomplished largely by folding and minor thrusting within thinly bedded turbidites that make up most of the orogen. Thermochronometry data and shortening estimates from the range indicate that such folding continues to occur as the prism expands by accretion.

8.3 Synthesis and future directions

Together, the chapters of the dissertation enhance our understanding of continental deformation and how that deformation is reflected in the stratigraphic record. The work foregrounds the relationship between tectonic deformation of the lithosphere and Earth surface processes, which together determine what is preserved in the sedimentary rock record. Because of the complex combination of tectonic and surface processes that determine sedimentary records and influence the development of orogenic belts, significant uncertainties persist in inferences of tectonic deformation from such records. This dissertation illustrates the promise that Bayesian methods show for interpreting the signals of tectonic processes in these records.

The work presented here grants insight into the Greater Caucasus as a case example for subduction zones and the initiation of continental collision. By showing a temporally coupled record of orogenic deformation and foreland basin sedimentation in the Cauca-

sus, this dissertation presents a detailed picture of orogenic evolution at an important stage of development, the transition from subduction to collision. This work advances our understanding of deformation along convergent margins and of the geologic record of early collision, which may help to resolve outstanding questions in other collisional orogens.

APPENDIX A

Supporting information for Chapter 2. Bayesian Population Correlation: A Probabilistic Approach to Inferring and Comparing Population Distributions for Detrital Zircon Ages

A.1 Introduction

This supporting text includes additional discussions of some aspects of our PME and BPC methods, comparison of BPC to previous methods, and detailed derivations of formulas for expected values of BPC under several conditions. The MATLAB® scripts mentioned above are also available at https://github.com/alextye/BPC and are packaged with an introductory PDF that describes their use in detail. Any updates to the scripts will be available (and may only be available) at https://github.com/alextye/BPC.

A.2 Effects of logarithmic age and probability scales

In constructing PMEs, we model detrital zircon PDFs with natural, or base-e, logarithmic scales for probability and for part of the age scale. For ages $<$1 Ga, we construct basis functions such that they have equal width in log-age space, meaning resolution is finer at younger ages and coarser at older ages. For zircons within this age range, a logarithmic age scale mirrors the proportional relationship between age and analytical uncertainty (*Gehrels*, 2000). Logarithmic age scales have been used for other radiometric dating systems, as well (*Brandon*, 1996). The age scale we implement is discussed in detail in Section 2.2.1.

Using a logarithmic scale to describe probability simplifies the functional forms of probability distributions. For example, a PDF curve that is Gaussian on a linear probability scale is quadratic when using a logarithmic probability scale. Thus, cubic spline basis

functions are more apt for representing detrital zircon PDFs if a logarithmic probability scale is used than if a linear probability scale is used. A logarithmic probability scale also allows preservation of small probability values that might be subject to machine precision issues and prevents complications to model parameter selection involving unphysical negative likelihoods. Using a logarithmic probability scale also better preserves the shapes of minor age peaks.

The PMEs that result from our procedure can be transformed onto linear age and probability scales. While the transformation from logarithmic to linear probability is straightforward, the transformation of logarithmic to linear age requires rescaling PDF age peaks. On a logarithmic x axis, a fixed interval of age is represented by a decreasing amount of horizontal space as the age increases. For example, on a logarithmic scale, the interval from 1-10 occupies more space than the interval 91-100. Thus, when a PDF is transformed from a linear age scale to a logarithmic age scale, older age peaks will become horizontally narrowed relative to younger age peaks. In order to ensure that all age peaks retain their respective probability masses through this transformation, the heights of older peaks must be increased proportional to the narrowing they undergo during the logarithmic age transformation. The opposite occurs when a PDF is transformed from logarithmic to linear age space: young age peaks that occupied a large portion of the x axis in logarithmic space become drastically narrowed and therefore must be much higher (Fig. A.1).

A.3 MCMC Convergence

MCMC convergence in our inference method is facilitated by our problem setup and can be verified by examination of typical Markov chains. Our problem setup facilitates MCMC convergence because it assures the existence of a single posterior maximum, simplifying the optimization used to find the Markov chain starting point. A single posterior maximum is guaranteed by the distributions of the prior and likelihood in our model space. Each parameter controls the likelihood of observing a specific and fixed set of sample ages (Fig. A.2a). The likelihood distribution for each parameter has (at most) one peak because increasing the coefficient increases the likelihood of the observations within the domain of its basis function, but increasing the coefficient value too much robs probability mass from other age peaks, driving total likelihood down (Fig. A.2b). If a basis function includes no observations in its domain, then the likelihood distribution of its associated parameter will be monotonically decreasing, because adding probability mass to this basis function reduces the likelihood of all observations. The prior distribution for each parameter is defined to have a single peak centered on the coefficient value needed for a uniform model

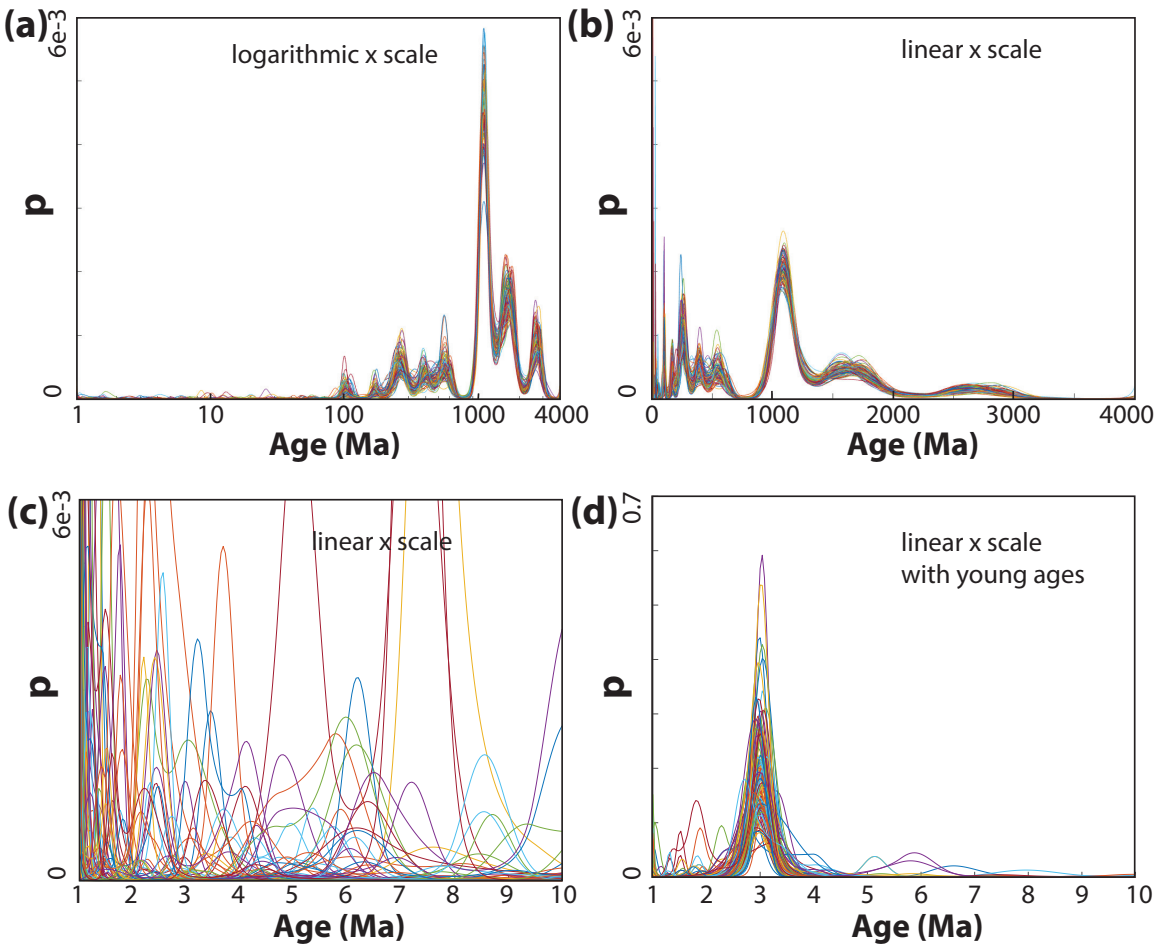

Figure A.1: Peak heights are scaled differently depending on whether a PDF has a linear or logarithmic age scale (see discussion in Section A.2). (a, b, c) show the same set of PDFs (a PME inferred for a n = 300 subsample of data from *Pullen et al.*, 2014), plotted on logarithmic (a) and linear (b) age scales, with a focused view of the 1-10 Ma age range of the linear age scale (c). The PDFs are inferred using a logarithmic age scale. As discussed in the text, the random noise visible in the 1-100 Ma range of (a) is increased in amplitude on a linear age scale (b, c), though these peaks are so narrow that their probability mass (the quantity of interest in probability distributions) is very small. For comparison, we add a set of synthetic young ages (2.7, 2.8, 2.9, 3.0, 3.1, 3.2, and 3.3 Ma, analytical uncertainties equal 1% of value) to a random subsample (n = 60; *Pullen et al.*, 2014) and plot the 1-10 Ma age range (linear scale) of the inferred PME (d). It can be seen that when there are young observed ages, the young age peaks become higher in amplitude than when there are no young data (c), and are observed consistently in multiple models.

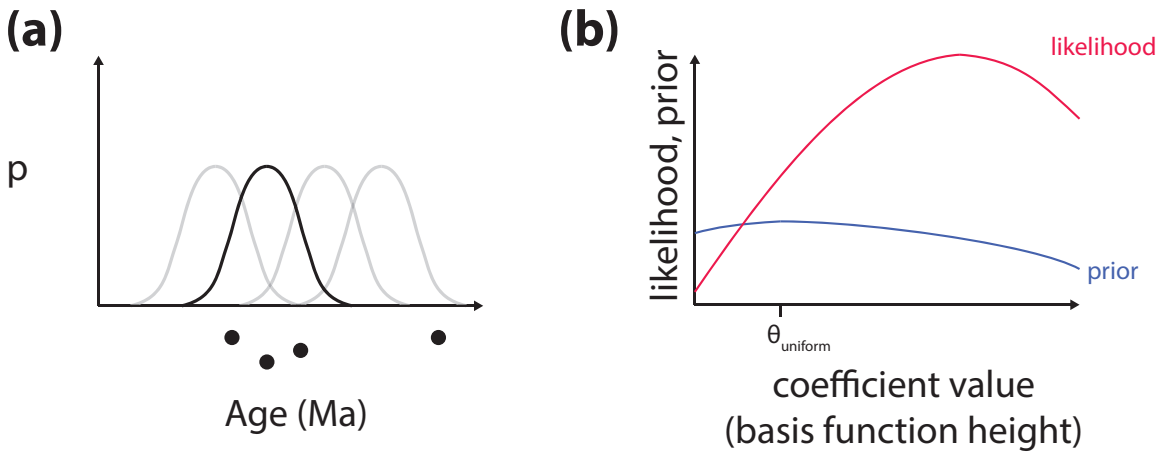

Figure A.2: Our problem setup greatly simplifies the distributions of likelihood, posterior, and prior ensuring MCMC convergence is adequately achieved. (a) Because each basis function is fixed on the x (Age) axis, the value of each coefficient controls the likelihood of a specific and fixed set of age observations (black dots). (b) The likelihood and prior distributions the parameter bolded in (a) will each have one peak, leading to a posterior distribution with a single peak. See text for discussion.

PDF (Eqn. 2.5, Fig. A.2b). Because the prior will have a single peak and the likelihood has at most a single peak, the posterior distribution for each parameter will have a single peak. This is true for all model parameters, so the multivariate posterior distribution will have a single peak.

Examination of typical Markov chains indicates straightforward behavior and efficient convergence (Fig. A.3). The walker begins at the point of maximum posterior value, but quickly moves to explore the surrounding region of more moderate posterior (Fig. A.3a). Over the length of the Markov chain, both log posterior and log likelihood vary randomly about a central value (Fig. A.3a, b). Model parameters are distributed in a nearly symmetric fashion about a central point (Fig. A.3c). Our routine saves the likelihood, posterior, and model parameter data for each PME so that users are free to examine the Markov chains in more detail.

A.4 Priors for accurate scaling of probability masses

As discussed in Section 2.2.3, the typical variation in each model parameter θ_i is tuned such that modeled PDFs have an appropriate level of fit for their sample size n. Here, we use a longer and more rigorous analogy to substantiate the reasoning presented in the text for why the probability mass outside of recognized age peaks should be $\sim \frac{1}{2n}$, where n is sample size. Consider an urn with blue balls and green balls, where x_b is the proportion of

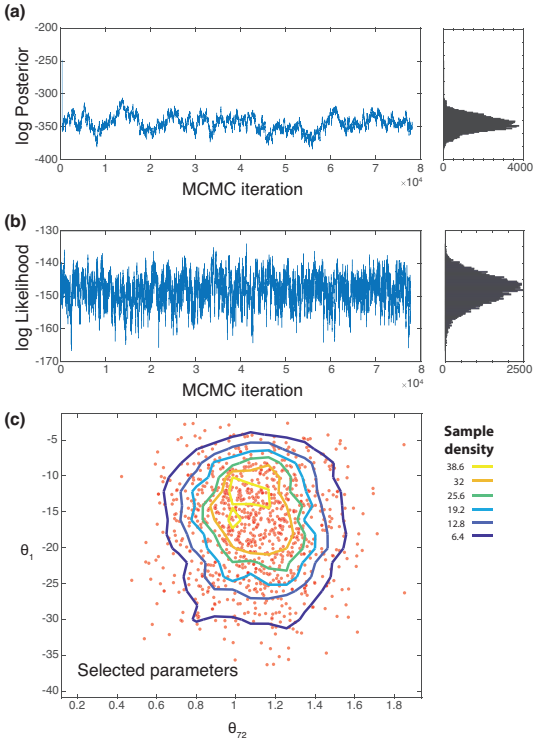

Figure A.3: Markov chain for typical PME inference. The sample is a n=300 random subsample of the dataset of *Pullen et al.* (2014) and the Markov chain has 77,687 steps. (a) Log posterior plotted against Markov chain step number (offset slightly to the right so that the initial high posterior values are visible). (b) Log likelihood plotted against Markov chain step number. Righthand panels of (a, b) show histograms of log posterior and log likelihood values. (c) Distribution of two representative model parameters (out of 100 total). The parameters chosen for the plot are the most variable parameter (θ_1) and the least variable parameter (θ_{72}). Contours show the density of MCMC steps in each region, and 1,000 (θ_{72}, θ_1) pairs were randomly chosen for plotting.

balls that are blue and x_g is the proportion of balls that are green. All the balls are blue or green, so $x_b + x_g = 1$, and balls are selected at random so the probability of selecting a blue ball, P(b), equals x_b, and the probability of selecting a green ball, P(g), equals x_g. If a single ball is drawn at random and it is blue, then it is reasonable to expect that there are more blue than green balls in the urn, i.e., the observed outcome is more likely if $x_b > \frac{1}{2}$ than if $x_b < \frac{1}{2}$, or equivalently P(b) is likely to be greater than $\frac{1}{2}$. However, most would agree that there are limits on what we might reasonably conclude from a single draw. For instance, it would be unreasonable to conclude that $x_b \gtrsim \frac{9}{10}$ on the basis of this single observation. Thus, the inequality P(b) $> \frac{1}{2}$ represents the limit of our constraint on the likely value of P(b). Concomitantly, P(g) $< \frac{1}{2}$ represents the limit of our constraint on the likely value of P(g). This constraint can be generalized to other sample sizes. Consider a situation where n balls are drawn and all are blue. Based on the above logic, we can assert that given this observation, it is reasonable to expect that the probability of drawing one or more green balls over n samples, P(g over n samples), is less than $\frac{1}{2}$:

$$\mathrm{P}(g \text{ over } n \text{ samples}) < \frac{1}{2} \tag{A.1}$$

P(g over n samples) can be independently expressed in terms of P(b) and P(g), the probabilities of observing a blue or green ball on a single draw. If n balls are drawn independently, then the probability of observing only blue balls is P(b)^n. Then, the probability of observing one or more green balls over n independent draws, P(g over n samples), is $1 - \mathrm{P}(b)^n$. Thus we can rewrite the above:

$$1 - \mathrm{P}(b)^n < \frac{1}{2} \tag{A.2}$$

which is equivalent to

$$\mathrm{P}(b) > \sqrt[n]{\frac{1}{2}} \tag{A.3}$$

To reiterate, this is the limit of reasonable constraint on the likely value of P(b) if n independent random draws all produce blue balls. Applying this logic to detrital zircon age distributions, we can treat blue and green balls as equivalent to two age peaks, which we term age peak A and age peak B. If a sample of n grains contains only grains of peak A, we conclude that the integrated area underneath peak A in the resulting age distribution should not exceed $\sqrt[n]{\frac{1}{2}}$ by very much, because this is the limit of the constraint on P(A), or the proportion of age A present in the sampled parent population. Plotting 1-$\sqrt[n]{\frac{1}{2}}$ and $\sim \frac{1}{2n}$ indicates that the two values, which we conclude are two estimates of the probability mass

that should be left unassigned to any recognized age peak in a probability distribution, are similar.

A.5 Effect of sample size and KDE method on established zircon correspondence metrics

The sample size bias of existing metrics is well established (*Satkoski et al.*, 2013; *Saylor and Sundell*, 2016). Sample size biasing is undesirable in a metric of detrital zircon population correspondence because the relative effects of population characteristics (the desired signal) and sample size on a single metric value are unclear.

Here, we use the same set of resampling experiments that show the lack of sample size biasing in BPC (Fig. 2.7) to further test the effects of sample size on published detrital zircon correspondence metrics. Random synthetic samples are drawn from real detrital zircon datasets (*Pullen et al.*, 2014; *Thomson et al.*, 2017) and compared using existing metrics. Cases of both identical and distinct parent populations were used: in the first case, both random subsamples in each experiment were drawn from the zircon age dataset of *Pullen et al.* (2014), and in the second case, one random subsample was drawn from the dataset of *Pullen et al.* (2014) and the other was drawn from *Thomson et al.* (2017). In order to generate random synthetic samples, we modeled PDF curves for the two complete datasets using the KDE method of *Botev et al.* (2010) and sampled zircon ages directly from these PDFs. These synthetic ages were assigned analytical uncertainty values of 1% of their age for ages $<$1 Ga, or 10 Ma for ages $>$1 Ga, roughly consistent with the analytical uncertainties that arise from laser ablation ICP-MS analyses of detrital zircons (*Gehrels et al.*, 2008). For both of these tests, the parent populations remain constant across all sample sizes, meaning any observed metric variation is solely a function of sampling effects and has no implications for earth processes. We test sample sizes from n = 60 to n = 400, a representative range of typical detrital zircon sample sizes, with twenty experiments conducted for each tested sample size in order to estimate the standard deviation of each metric. Tested metrics include the test statistics and p-values of the Kologorov-Smirnov (K-S) and Kuiper tests, which are functions of empirical cumulative distribution functions (CDFs; e.g., *DeGraaff-Surpless et al.*, 2003; *Lawrence et al.*, 2011; *Vermeesch*, 2013; *Saylor and Sundell*, 2016), as well as Similarity (*Gehrels*, 2000), Likeness (*Satkoski et al.*, 2013) and Cross Correlation (*Saylor et al.*, 2012, 2013), which are functions of PDFs inferred for detrital zircon age samples using KDE methods (e.g., *Botev et al.*, 2010; *Shimazaki and Shinomoto*, 2010; *Vermeesch*, 2012). PDF-based metrics calculated using the popular KDE method of *Botev*

et al. (2010) are shown in the main text (Fig. 2.7). Here, we test the effect of KDE method choice on metric value by calculating Similarity, Likeness, and Cross Correlation using two other KDE methods (*Hurford et al.*, 1984; *Shimazaki and Shinomoto*, 2010).

For the K-S and Kuiper tests, the test statistics appear to be biased with respect to sample size in some cases, depending on whether samples are drawn from identical or different parent populations (Fig. A.4). Such biasing is undesirable for the reasons discussed above. Test p-values vary uniformly between 0 and 1 for samples drawn from identical parents and for samples drawn from different parents, p-values decrease with increasing sample size. The high scatter of p-values suggests that p-values do not scale in a way that makes the degree of parent population correspondence interpretable. Other authors have found that p-values are correlated with sample size (*Vermeesch*, 2017).

PDF-based metrics used to compare detrital zircon data have an added complication, which is that these metrics, though they are functions of KDE curves, do not specify which KDE method should be used in their calculation. Therefore, we investigate the effect of sample size and KDE method on these metrics.

When samples are drawn from identical parent populations (Fig. 2.7b, A.5a), values of existing PDF-based metrics increase with increasing sample size. Because these samples are drawn from identical parent populations, metric values closer to 1 are more desirable from the perspective of estimating the correspondence between detrital zircon parent populations. Of the three existing metrics compared, Cross Correlation shows the greatest change in mean metric value with increasing sample size, regardless of KDE method. Likeness consistently shows a somewhat greater sample size dependence than Similarity, and the values of Similarity are significantly closer to 1 than are the values of other methods, regardless of sample size and KDE method. For all three metrics, sample size dependence is most pronounced when calculated using the probability density plot (PDP) method. The locally adaptive (LA-KDE) method (Fig. A.5a; *Shimazaki and Shinomoto*, 2010) produces results that are slightly less dependent on sample size (less change in metric value from n = 60 to n = 400) than the diffusion based (D-KDE) method (Fig. 2.7b; *Botev et al.*, 2010). However, the values of the metrics calculated using the D-KDE method are typically greater and less scattered than the values calculated using the LA-KDE method. To summarize the case of identical parent populations, the D-KDE method yields less scattered metric values that are closer to 1, but the LA-KDE method results in metric values less dependent on sample size. Similarity is the metric whose values are closest to the ideal value of 1 and are the least biased according to sample size of the three metrics (though some bias is visually apparent).

When samples are drawn from two different populations (Fig. 2.7c, A.5b), the behav-

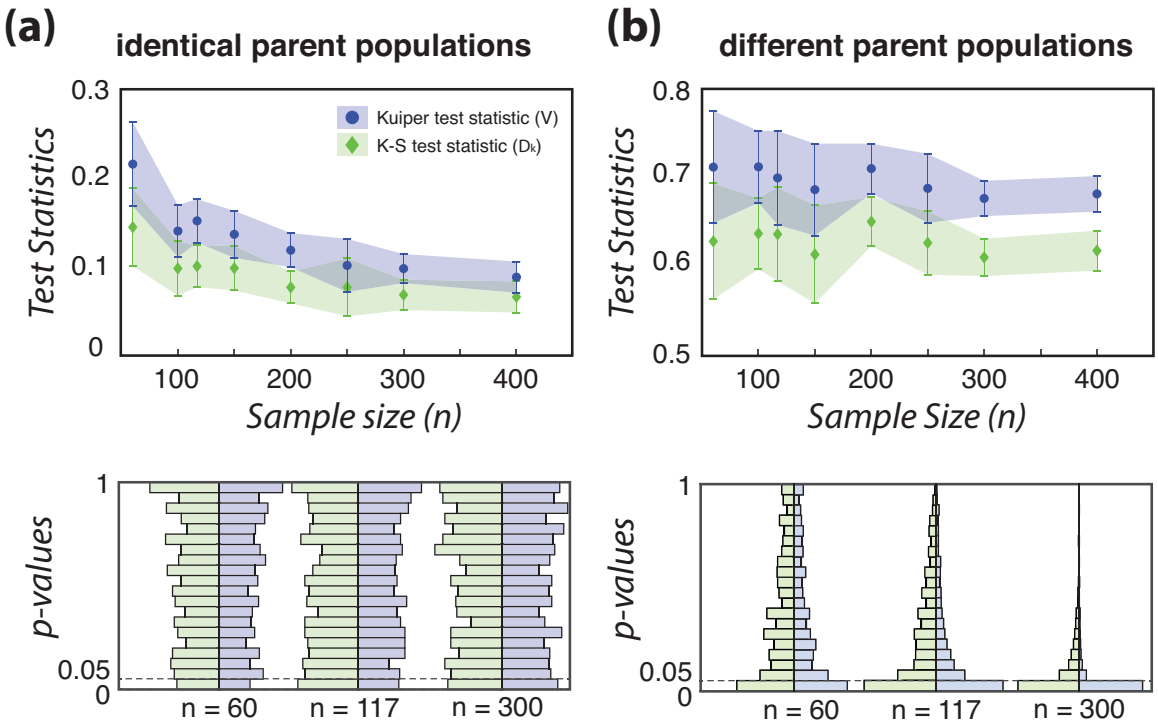

Figure A.4: K-S test statistic D_k and Kuiper test statistic V are biased according to sample size in some cases. (a) For samples drawn from identical parent populations, the K-S and Kuiper test statistics are biased according to sample size. Resulting p-values (shown in lower panel for selected sample sizes) are uniformly distributed between 0 and 1, as expected because in this case the null hypothesis is true for both tests. (b) For samples drawn from different parent populations, K-S and Kuiper tests appear to be less biased or unbiased with respect to sample size, and p-values are increasingly less than 0.05, the cutoff for a significance test at 95% confidence, with increasing sample size. p-values were calculated using 1,000 experiments per sample size to adequately characterize the uniform distribution. Subsample sizes used for p-value calculations differ from one another by 4 to avoid a quantization we observed in D_k and V values from samples with similar size that lead to spurious p-values distributions.

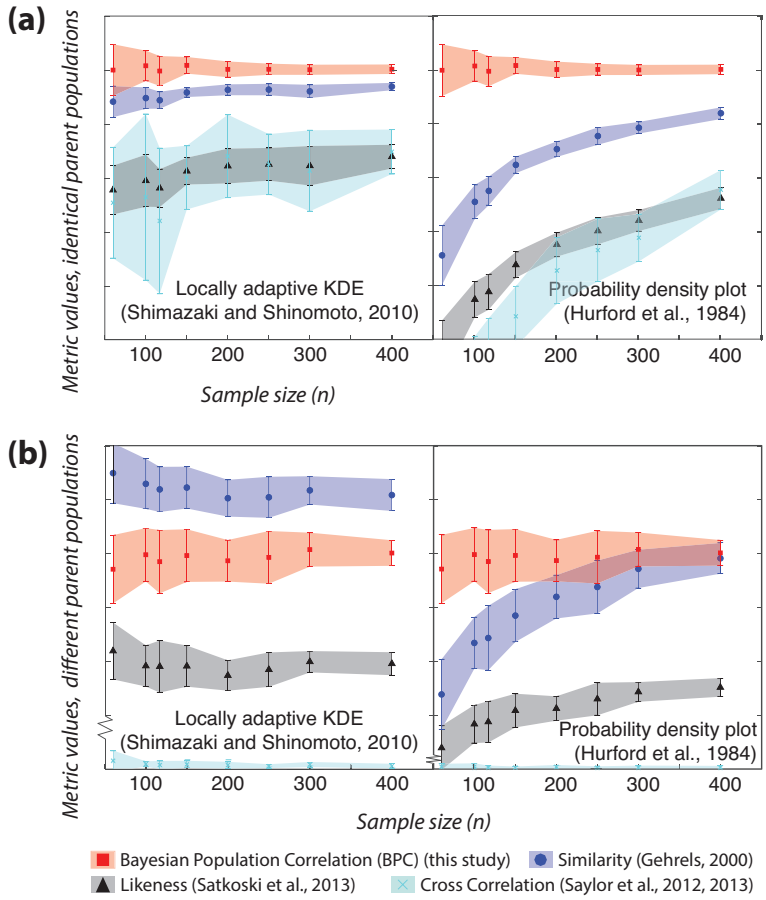

Figure A.5: Resampling experiments with PDF-based metrics show that behavior of existing metrics Similarity, Likeness, and Cross Correlation is influenced by sample size and choice of KDE method. BPC results (from Fig. 2.7) are shown for reference. (a) Metric results are shown for when two subsamples of a single population (the dataset of *Pullen et al.*, 2014) are compared. (b) Results are shown for when subsamples are drawn from two different populations (the datasets of *Pullen et al.*, 2014; *Thomson et al.*, 2017). Figure 2.7a shows the parent population datasets. The key shows the plotted metrics, and each panel has written which method of kernel density estimation is used. Figure 2.7 shows results for the KDE method of *Botev et al.* (2010). Where KDE method is indicated, it only applies to the previously published metrics; BPC does not use a KDE method and is shown for reference. In (b), note the broken vertical axis, where Cross Correlation plots near zero but other metrics are shown on a scale of 0.1 to 0.7.

ior of existing PDF-based metrics is markedly different from the case of identical parent populations. In the case of different parent populations, values of Cross Correlation are near zero across the board. Likeness and Similarity both have non-zero value, but Likeness shows a lesser dependence on sample size than Similarity for all KDE methods. Of the three tested KDE methods, the PDP method produces the greatest sample size dependence in Similarity and Likeness, and the D-KDE method minimizes the sample size dependence of these two metrics. To summarize this case of two different populations, Cross Correlation values are the least sample size dependent because they are uniformly near zero. Of metrics with non-zero value, Likeness is the least sample size dependent, and the D-KDE method minimizes the sample size dependence of Similarity and Likeness.

Comparing the results of resampling experiments on identical and different populations (Fig. 2.7, A.5) yields several insights into the effects of sample size and KDE method choice on metric values. The fact that Cross Correlation values are near zero for the case of different parent populations is problematic for the use of Cross Correlation as a metric of degree of correspondence. There is significant overlap between the different parent populations (Fig. 2.7a), yet this comparison yields the lowest possible values of the Cross Correlation metric. Therefore, Cross Correlation could not be used to distinguish between the case of different, but overlapping, parent populations explored here and a case of two parent populations with no overlap at all. Where parent populations are identical, Similarity is the least dependent on sample size of existing metrics and shows the desirable characteristic of being close to an ideal value of 1. However, in the case of different parent populations, Likeness is the least sample size dependent of the tested existing metrics. Therefore, there is no single metric that shows the least sample size dependence in the cases of both identical and different parent populations. The results of our numerical experiments show that there is no single existing correspondence metric and no KDE method that minimize sample size dependence across all tested scenarios. For a more thorough and generalized review of these metrics, the reader is directed to *Saylor and Sundell* (2016).

A.6 Calculation of expected BPC values

Expected BPC values can be calculated, similarly to Λ_{min} (Section 2.3), as a function of sample size (n_1, n_2) and the shared proportions of parent populations (f_1, f_2; defined as in Fig. 2.8). We consider simplified categorical models in developing the formula for expected BPC, but the predictions of this formula agree closely with BPC values observed from resampling experiments (Fig. 2.8). In the following calculations, for clarity we define

$$x_1 = \left(\frac{n_1}{n_1 + n_2}\right), \quad x_2 = \left(\frac{n_2}{n_1 + n_2}\right), \quad n = n_1 + n_2 \tag{A.4}$$

Consider detrital zircon samples to be random draws from 3 categories (A, B, C; similar to the young, middle, and old categories of Fig. 2.8): sample 1 is from a population containing zircons of categories A and B; sample 2 is from a population that contains zircons of categories B and C. Category B is the only category of zircons that may be part of both populations. The respective proportions of populations 1 and 2 drawn from category B are labeled f_1 and f_2, and the proportions of both populations that fall into all categories are as follows:

Category	A	B	C
population 1	$1 - f_1$	f_1	0
population 2	0	f_2	$1 - f_2$

Table A.1: Set-up for simplified categorical model for calculating expected BPC. Rows correspond to two compared populations and columns represent 3 distinct age categories (similar to Fig. 2.8). Table values show the proportion of each population that falls into each category.

Assuming that samples are large and parent populations well characterized, simple probability functions can be constructed for each sample. Because this example is categorical rather than continuous, probability mass functions are used rather than density functions. Each category is assigned a probability mass for a particular sample, and for a single sample the masses must sum to 1. Because the likelihood of observing multiple independent events is the product of their individual likelihoods, the likelihood of observing sample 1 is:

$$L_1 = \mathrm{P}_1(\mathrm{A})^{n_{A1}} \mathrm{P}_1(\mathrm{B})^{n_{B1}} \mathrm{P}_1(\mathrm{C})^{n_{C1}} \tag{A.5}$$

where $\mathrm{P}_1(\mathrm{A})$ is the probability mass of category A in population 1, n_{A1} is the number of data in sample 1 that are from category A, etc. Because we assume that each sample is large and therefore reflects the underlying statistics of its parent population, the probability mass of each category $(\mathrm{P}(\mathrm{A}), \mathrm{P}(\mathrm{B}), \mathrm{P}(\mathrm{C}))$ is the proportion of data that falls into that category, such that P_1(B) is equal to f_1, etc (see Table A.1). Recognizing that $\mathrm{P}_1(\mathrm{A}) = 1 - f_1$, $n_{A1} = nx_1(1 - f_1)$, $\mathrm{P}_1(\mathrm{B}) = f_1$, and $n_{B1} = nx_1 f_1$, L_1 can be restated:

$$L_1 = (1 - f_1)^{nx_1(1-f_1)} f_1^{nx_1 f_1} \tag{A.6}$$

The likelihood of observing sample 2 can be found by replacing $\mathrm{P}_1(\mathrm{B})^{n_{B1}}$ with $\mathrm{P}_2(\mathrm{B})^{n_{B2}}$, etc., and their respective values (see Table A.1).

BPC is based on a comparison of the likelihood that two samples are taken from a joint distribution with the likelihood that they are taken from two individual distributions (see Eqn. 2.8). In this categorical model, if we assume that each sample reflects the underlying statistics of its parent population, then the hypothetical joint population distribution is the sum of the two sample distributions each weighted by the relative size of the sample, similar to Eqn. (2.9), and the likelihood of observing both of the two samples given the joint distribution is:

$$\begin{aligned} L_J &= x_1[\mathrm{P}_1(\mathrm{A})^{n_{A1}}\mathrm{P}_1(\mathrm{B})^{n_{B1}}\mathrm{P}_1(\mathrm{C})^{n_{C1}}] + x_2[\mathrm{P}_2(\mathrm{A})^{n_{A2}}\mathrm{P}_2(\mathrm{B})^{n_{B2}}\mathrm{P}_2(\mathrm{C})^{n_{C2}}] \\ &= [x_1(1-f_1)]^{nx_1(1-f1)}(x_1f_1+x_2f_2)^{n(x_1f_1+x_2f_2)}[x_2(1-f_2)]^{nx_2(1-f2)} \end{aligned} \tag{A.7}$$

where L_J is the likelihood of all data of samples 1 and 2 under the joint distribution. Restating Eqn. (2.8) for this simplified categorical model, we define

$$\Lambda_{ideal} = \ln\left[\frac{L_J}{L_1 \cdot L_2}\right] \tag{A.8}$$

This expression, combined with Eqns. (A.6) and (A.7), can be expanded and some terms canceled to yield

$$\Lambda_{ideal} = \ln\left[\frac{x_1^{nx_1(1-f1)}(x_1f_1+x_2f_2)^{n(x_1f_1+x_2f_2)}x_2^{nx_2(1-f2)}}{f_1^{nx_1f_1}f_2^{nx_2f_2}}\right] \tag{A.9}$$

It can be seen that in the case where there are no zircons in the overlapping age category ($f_1 = f_2 = 0$), $\Lambda_{ideal} = \ln[x_1^{nx_1}x_2^{nx_2}]$, defined as Λ_{min}, equivalently to Eqn. (2.12).

BPC_{ideal} is calculated from Λ_{ideal} and Λ_{min} following Eqn. (2.13):

$$\begin{aligned} \mathrm{BPC}_{ideal} &= 1 - \left(\frac{\Lambda_{ideal}}{\Lambda_{min}}\right) \\ &= 1 - \left(\frac{\ln[x_1^{x_1(1-f_1)}(x_1f_1+x_2f_2)^{x_1f_1+x_2f_2}x_2^{x_2(1-f_2)}] - \ln[f_1^{x_1f_1}f_2^{x_2f_2}]}{\ln[x_1^{x_1}x_2^{x_2}]}\right) \end{aligned} \tag{A.10}$$

where all instances of n cancel when evaluating $\Lambda_{ideal}/\Lambda_{min}$, indicating that BPC_{ideal} does not depend on sample size. The lack of sample size bias shown by BPC in resampling experiments (Fig. 2.7) corroborates this theoretical finding. It should be noted that Eqn.

(A.10) will become less accurate as either n_1 or n_2 becomes small because of the assumption in Eqn. (A.10) that each sample accurately represents its underlying parent population. In such cases BPC uncertainties will be large, as well. Additionally, we note that Eqn. (A.10) makes no prediction about BPC uncertainties, only the expected BPC value, BPC_{ideal}.

As noted above, resampling experiment results are consistent with expected values from Eqn. (A.10) in virtually all cases. Due to this correspondence between expected and observed values, we suggest that observed BPC values can be used to find ranges of possible f_1 and f_2 values by numerical solution of Eqn. (A.10). If the value of f_1 or f_2 can be assumed, the value of the other can be solved for uniquely. Given a single fluvial system with two samples collected such that the contributing catchment of the upstream sample is completely contained within the catchment of the downstream sample, the portion of zircons in the downstream sample that originated in the upstream catchment can be expressed by $\mathrm{zr_d}$. In this situation, f_1 is 1 because any zircons in the upstream sample could theoretically be passed to the downstream sample, and f_2 is mathematically equivalent to $\mathrm{zr_d}$, allowing BPC_{ideal} (Eqn. A.10) to be related directly to $\mathrm{zr_d}$:

$$\mathrm{BPC}_{ideal} = 1 - \left(\frac{\ln[(x_1 + x_2\mathrm{zr_d})^{x_1+x_2\mathrm{zr_d}} x_2^{x_2(1-\mathrm{zr_d})}] - \ln[\mathrm{zr_d}^{x_2\mathrm{zr_d}}]}{\ln[x_1^{x_1} x_2^{x_2}]} \right) \tag{A.11}$$

Estimates of $\mathrm{zr_d}$ can be obtained from this equation by substituting a calculated BPC value for BPC_{ideal} and solving numerically for $\mathrm{zr_d}$, though such an estimate is subject to many assumptions. This estimate of $\mathrm{zr_d}$ assumes that the upper and lower catchments contain zircon sources of entirely distinct age. In practice, this is not true in many cases, so BPC-derived $\mathrm{zr_d}$ estimates should usually be taken as upper bounds on the proportion of zircons in the downstream sample that originated in the upper catchment. It is also important to note that these $\mathrm{zr_d}$ values are agnostic as to the physical process responsible for the transmission or lack thereof of zircons through a sedimentary system. For instance, a low $\mathrm{zr_d}$ value may indicate that zircons from the upstream catchment became trapped in a swamp or other low energy environment on their way to the downstream catchment sample locality. In this case, the $\mathrm{zr_d}$ value would not have any implication for factors such as zircon fertility, catchment erosion rates, or distance from the upstream to the downstream sample.

APPENDIX B

Supporting information for Chapter 4. Field Estimate of Paleoseismic Slip on a Normal Fault Using the Schmidt Hammer and Terrestrial LiDAR: Methods and Application to the Hebgen Fault (Montana, USA)

B.1 Use of BIC vs. AICc in Schmidt hammer data

In addition to the Bayesian Information Criterion, we considered using AIC/AICc (*Akaike*, 1998, with correction by *Sugiura* (1978)). However, we prefer the BIC for model selection in this situation due to the slightly different uses of the criteria and our aims. *Burnham and Anderson* (2004) note that models selected by AIC tend to reflect the activity of a multitude of processes of decreasing, but still finite, importance. In contrast, BIC is preferred when data are determined by a small number of processes, all of which have substantial influence. In some situations AIC may be seen as over-fitting, while in other situations BIC may under-fit data. We choose to use BIC because we want to distinguish between first-order processes shaping Schmidt hammer R-values, rather than develop a comprehensive model that can predict R-values.

B.2 Exponential curve-fitting

All possible combinations of break points were examined. The attenuation length λ for all exponential functions was taken to be constant and was calculated to be $\sim$1.1 m. This calculation reflects the assumptions that cosmic rays influencing the samples of *Zreda and Noller* (1998) were traveling through a colluvial wedge with density 1.5 g cm^{-3} adjacent

to a fault scarp dipping at 65°. The apparent attenuation length in terms of g/cm^2 was taken from (*Schlagenhauf et al.*, 2010, their Figure A2d), using a flat colluvial wedge for simplicity. Our analysis assumes that the height of the colluvial apron on the fault scarp has not changed over time. Topography is ignored on the side of the valley opposite the fault scarp, which is estimated to have blocked cosmic rays of incidence angle far less than 30° from the sample site, and would have had a negligible effect on attenuation length at the sample site. Our analysis also ignores the effects of cosmic rays penetrating from the top of the fault scarp.

For a given exponential 'step', there are two parameters to estimate: the age offset y_0 and the coefficient of the exponential function A. For a given age offset and set of observed ages, the maximum likelihood value of A can be calculated by an analytical expression that weights each observed age according to the inverse of its analytical uncertainty, as reported in *Zreda and Noller* (1998) (Fig. 4.8A). The best-fit coefficient A is subsequently modified in order to ensure that the overall function is both continuous and monotonically increasing. The modified best fit coefficient A is then used to calculate L2 misfits for the given observed ages, incorporating weighting by the inverse of each analytical uncertainty. L2 misfit is therefore a function of age offset y_0 for a given set of apparent ages. Candidate values for the age offset y_0 of each exponential step are perturbed simultaneously, minimizing the possibility of an erroneous result arising from the modification of A. The set of y_0 values that minimizes the L2 misfit is found by a pattern search algorithm, regardless of whether or not weighting by analytical uncertainty is incorporated into the model (Fig. 4.8B).

We used both Bayesian and Corrected Akaike Information Criteria (BIC and AICc; *Akaike*, 1998; *Sugiura*, 1978; *Schwarz et al.*, 1978) to assess the best-fitting stepwise exponential functions. In our models, some slip patches initially contained only a single observed age, which is geologically unlikely and not statistically robust. When our analysis mandates that each slip patch must contain at least 2 observed ages, BIC and AICc both suggest that a model with 2-3 slip patches is preferred (Fig. 4.8B).

Figure B.1: Full-size photograph of the Hebgen fault exposure showing string line and orange flagging to locate Schmidt hammer sample locations every 0.25 m.

BIBLIOGRAPHY

Aa, A. R., J. Sjåstad, E. Sønstegaard, and L. H. Blikra (2007), Chronology of Holocene rock-avalanche deposits based on Schmidt-hammer relative dating and dust stratigraphy in nearby bog deposits, Vora, inner Nordfjord, Norway, *The Holocene*, *17*(7), 955–964.

Abdullayev, N. R., J. Weber, C. G. van Baak, E. Aliyeva, C. Leslie, G. W. Riley, P. O'Sullivan, and R. Kislitsiyn (2018), Detrital zircon and apatite constraints on depositional ages, sedimentation rates and provenance: Pliocene Productive Series, South Caspian Basin, Azerbaijan, *Basin Research*, *30*(5), 835–862.

Adamia, S., G. Zakariadze, T. Chkhotua, N. Sadradze, N. Tsereteli, A. Chabukiani, and A. Gventsadze (2011a), Geology of the Caucasus: A review, *Turkish Journal of Earth Sciences*, *20*(5), 489–544.

Adamia, S., V. Alania, A. Chabukiani, Z. Kutelia, and N. Sadradze (2011b), Great Caucasus (Cavcasioni): A long-lived north-Tethyan back-arc basin, *Turkish Journal of Earth Sciences*, *20*(5), 611–628.

Adamia, S. A., T. Chkhotua, M. Kekelia, M. Lordkipanidze, I. Shavishvili, and G. Zakariadze (1981), Tectonics of the Caucasus and adjoining regions: Implications for the evolution of the Tethys ocean, *Journal of Structural Geology*, *3*(4), 437–447.

Agabekov, M., and A. Moshashvili (1978), Kyurdamir-Saatly buried uplift of the Kura basin, an integral part of the Lesser Caucasus geosyncline in Cretaceous time, *Dokl. National Acad. Sci. USSR*, *232*, 120–122.

Ahnert, F. (1984), Local relief and the height limits of mountain ranges, *American Journal of Science*, *284*(9), 1035–1055.

Akaike, H. (1981), Likelihood of a model and information criteria, *Journal of econometrics*, *16*(1), 3–14.

Akaike, H. (1998), Information theory and an extension of the maximum likelihood principle, in *Selected papers of hirotugu akaike*, pp. 199–213, Springer.

Alizadeh, A. A., I. S. ogly Guliyev, F. A. Kadirov, and L. V. Eppelbaum (2016), *Geosciences of Azerbaijan*, Springer.

Allen, M., J. Jackson, and R. Walker (2004), Late Cenozoic reorganization of the Arabia-Eurasia collision and the comparison of short-term and long-term deformation rates, *Tectonics*, *23*(2).

Allen, M. B., and H. A. Armstrong (2008), Arabia–Eurasia collision and the forcing of mid-Cenozoic global cooling, *Palaeogeography, Palaeoclimatology, Palaeoecology*, *265*(1), 52–58.

Allen, M. B., A. C. Morton, C. M. Fanning, A. J. Ismail-Zadeh, and S. B. Kroonenberg (2006), Zircon age constraints on sediment provenance in the Caspian region, *Journal of the Geological Society*, *163*(4), 647–655.

Amidon, W. H., D. W. Burbank, and G. E. Gehrels (2005), U–Pb zircon ages as a sediment mixing tracer in the Nepal Himalaya, *Earth and Planetary Science Letters*, *235*(1), 244–260.

Andersen, T. (2005), Detrital zircons as tracers of sedimentary provenance: Limiting conditions from statistics and numerical simulation, *Chemical Geology*, *216*(3), 249–270.

Anderson, R., and M. Machette (2000), *Fault number 1136c, Pleasant Valley fault zone, Pearce section. Quaternary fault and fold database of the United States*, U.S. Geological Survey website, https://earthquakes.usgs.gov/hazards/qfaults, accessed 11/02/2018 06:15 PM.

Andrews, D., and R. C. Bucknam (1987), Fitting degradation of shoreline scarps by a non-linear diffusion model, *Journal of Geophysical Research: Solid Earth*, *92*(B12), 12,857–12,867.

Andrews, D., and T. Hanks (1985), Scarp degraded by linear diffusion: Inverse solution for age, *Journal of Geophysical Research: Solid Earth*, *90*(B12), 10,193–10,208.

Asch, K., C. for the Geological Map of the World, and S. Bellenberg (2005), *The 1:5 million international geological map of Europe and adjacent areas (IGME 5000)*, Bundesanstalt für Geowissenschaften und Rohstoffe.

Austermann, J., and G. Iaffaldano (2013), The role of the Zagros orogeny in slowing down Arabia-Eurasia convergence since 5 Ma, *Tectonics*, *32*(3), 351–363.

Avdeev, B., and N. A. Niemi (2011), Rapid Pliocene exhumation of the Central Greater Caucasus constrained by low-temperature thermochronometry, *Tectonics*, *30*(2).

Avdeev, B., N. A. Niemi, and M. K. Clark (2011), Doing more with less: Bayesian estimation of erosion models with detrital thermochronometric data, *Earth and Planetary Science Letters*, *305*(3), 385–395.

Axen, G. J., P. S. Lam, M. Grove, D. F. Stockli, and J. Hassanzadeh (2001), Exhumation of the west-central Alborz Mountains, Iran, Caspian subsidence, and collision-related tectonics, *Geology*, *29*(6), 559–562.

Aydin, A. (2008), ISRM suggested method for determination of the Schmidt hammer rebound hardness: revised version, in *The ISRM Suggested Methods for Rock Characterization, Testing and Monitoring: 2007-2014*, pp. 25–33, Springer.

Aydin, A., and A. Basu (2005), The Schmidt hammer in rock material characterization, *Engineering Geology*, *81*(1), 1–14.

Bairamov, A., G. Aliyev, G. Hasanov, H. Hasanov, T. Hasanov, A. Ismail-Zadeh, T. Kangarli, V. Korobanov, A. Mamedov, A. Mamedov, et al. (2008), Geological Map of Azerbaijan Republic, *National Academy of Sciences of Azerbaijan Republic, Ministry of Ecology and Natural Resources of Azerbaijan Republic and Ministry of Fuel and Energetics of Azerbaijan Republic, Baku*.

Baldwin, J. A., K. X. Whipple, and G. E. Tucker (2003), Implications of the shear stress river incision model for the timescale of postorogenic decay of topography, *Journal of Geophysical Research: Solid Earth*, *108*(B3).

Belov, A. (1981), Tectonic Development of the Alpine Fold Area in the Paleozoic.

Belov, A., M. Somin, and S. A. Adamiya (1978), Precambrian and Paleozoic of the Caucasus (brief synthesis), *Jahrbuch für Geologie und Mineralogie*, *121*, 155–175.

Benedetti, L., R. Finkel, D. Papanastassiou, G. King, R. Armijo, F. Ryerson, D. Farber, and F. Flerit (2002), Post-glacial slip history of the Sparta fault (Greece) determined by ^{36}Cl cosmogenic dating: Evidence for non-periodic earthquakes, *Geophysical Research Letters*, *29*(8), 87–1.

Benedetti, L. C., and J. van Der Woerd (2014), Cosmogenic nuclide dating of earthquakes, faults, and toppled blocks, *Elements*, *10*(5), 357–361.

Benedict, J. B. (1985), *Arapaho Pass: glacial geology and archeology at the crest of the Colorado Front Range*, 3, Center for Mountain Archeology.

Berberian, M. (1997), Seismic sources of the Transcaucasian historical earthquakes, *Historical and prehistorical earthquakes in the Caucasus*, *28*, 233–311.

Birkeland, P. W. (1982), Subdivision of Holocene glacial deposits, Ben Ohau Range, New Zealand, using relative-dating methods, *Geological Society of America Bulletin*, *93*(5), 433–449.

Birkeland, P. W., and J. S. Noller (2000), Rock and mineral weathering, *Quaternary Geochronology: Methods and Applications*, *4*, 293–312.

Bochud, M. (2011), *Tectonics of the Eastern Greater Caucasus in Azerbaijan*, Département de géosciences, sciences de la terre, Université de Fribourg.

Bogdanova, S., B. Bingen, R. Gorbatschev, T. Kheraskova, V. Kozlov, V. Puchkov, and Y. A. Volozh (2008), The East European Craton (Baltica) before and during the assembly of Rodinia, *Precambrian Research*, *160*(1-2), 23–45.

Boncio, P., P. Galli, G. Naso, and A. Pizzi (2012), Zoning Surface Rupture Hazard along Normal Faults: Insight from the 2009 Mw 6.3 L'Aquila, Central Italy, Earthquake and Other Global Earthquakes, *Bulletin of the Seismological Society of America*, *102*(3), 918–935.

Bonilla, M. G., H. A. Villalobos, and R. E. Wallace (1980), Exploratory trench across the Pleasant Valley fault, Nevada, *Tech. rep.*, US Geological Survey.

Bosi, C., F. Galadini, and P. Messina (1993), Neotectonic significance of bedrock fault scarps: case studies from the Lazio-Abruzzi Apennines (central Italy), *Z. Geomorph. Suppl.-Bd*, *94*, 187–206.

Botev, Z. I., J. F. Grotowski, D. P. Kroese, et al. (2010), Kernel density estimation via diffusion, *The annals of Statistics*, *38*(5), 2916–2957.

Brandon, M. T. (1996), Probability density plot for fission-track grain-age samples, *Radiation Measurements*, *26*(5), 663–676.

Brandon, M. T., M. K. Roden-Tice, and J. I. Garver (1998), Late Cenozoic exhumation of the Cascadia accretionary wedge in the Olympic Mountains, northwest Washington State, *Geological Society of America Bulletin*, *110*(8), 985–1009.

Brodsky, E. E., J. D. Kirkpatrick, and T. Candela (2016), Constraints from fault roughness on the scale-dependent strength of rocks, *Geology*, *44*(1), 19–22.

Bronk Ramsey, C. (2009), Bayesian analysis of radiocarbon dates, *Radiocarbon*, *51*(1), 337–360.

Bull, W. B. (1996), Prehistorical earthquakes on the Alpine fault, New Zealand, *Journal of Geophysical Research: Solid Earth*, *101*(B3), 6037–6050.

Burnham, K. P., and D. R. Anderson (2004), Multimodel inference: Understanding AIC and BIC in model selection, *Sociological methods & research*, *33*(2), 261–304.

Butler, R. W. (1982), The terminology of structures in thrust belts, *Journal of Structural Geology*, *4*(3), 239–245.

Butler, R. W., C. E. Bond, M. A. Cooper, and H. Watkins (2019), Fold–thrust structures–where have all the buckles gone?, *Geological Society, London, Special Publications*, *487*, SP487–7.

Candela, T., F. Renard, M. Bouchon, A. Brouste, D. Marsan, J. Schmittbuhl, and C. Voisin (2009), Characterization of fault roughness at various scales: Implications of three-dimensional high resolution topography measurements, in *Mechanics, structure and evolution of fault zones*, pp. 1817–1851, Springer.

Carcaillet, J., I. Manighetti, C. Chauvel, A. Schlagenhauf, and J.-M. Nicole (2008), Identifying past earthquakes on an active normal fault (Magnola, Italy) from the chemical analysis of its exhumed carbonate fault plane, *Earth and Planetary Science Letters*, *271*(1-4), 145–158.

Cherniak, D., and E. Watson (2001), Pb diffusion in zircon, *Chemical Geology*, *172*(1-2), 5–24.

Chung, S.-L., M.-F. Chu, Y. Zhang, Y. Xie, C.-H. Lo, T.-Y. Lee, C.-Y. Lan, X. Li, Q. Zhang, and Y. Wang (2005), Tibetan tectonic evolution inferred from spatial and temporal variations in post-collisional magmatism, *Earth-Science Reviews*, *68*(3-4), 173–196.

Cloos, M. (1993), Lithospheric buoyancy and collisional orogenesis: Subduction of oceanic plateaus, continental margins, island arcs, spreading ridges, and seamounts, *Geological Society of America Bulletin*, *105*(6), 715–737.

Colman, S., and D. Dethier (1986), *Rates of Chemical Weathering of Rocks and Minerals*, Academic Press: Orlando, Florida.

Copley, A., and J. Jackson (2006), Active tectonics of the Turkish-Iranian plateau, *Tectonics*, *25*(6).

Cowgill, E., A. M. Forte, N. Niemi, B. Avdeev, A. Tye, C. Trexler, Z. Javakhishvili, M. Elashvili, and T. Godoladze (2016), Relict basin closure and crustal shortening budgets during continental collision: An example from Caucasus sediment provenance, *Tectonics*, *35*(12), 2918–2947.

Cowie, P., R. Phillips, G. P. Roberts, K. McCaffrey, L. Zijerveld, L. Gregory, J. F. Walker, L. Wedmore, T. Dunai, S. Binnie, et al. (2017), Orogen-scale uplift in the central Italian Apennines drives episodic behaviour of earthquake faults, *Scientific reports*, *7*, 44,858.

Crook, R., and A. R. Gillespie (1986), Weathering rates in granitic boulders measured by P-wave speeds, in *Rates of Chemical Weathering of Rocks and Minerals*, edited by S. Colman and D. Dethier, pp. 395–417, Academic Press, Orlando, Florida.

Şengör, A. C. (1976), Collision of irregular continental margins: Implications for foreland deformation of Alpine-type orogens, *Geology*, *4*(12), 779–782.

Dahlstrom, C. (1969), Balanced cross sections, *Canadian Journal of Earth Sciences*, *6*(4), 743–757.

Dahlstrom, C. D. (1970), Structural geology in the eastern margin of the Canadian Rocky Mountains, *Bulletin of Canadian Petroleum Geology*, *18*(3), 332–406.

Darvill, C. M., M. J. Bentley, and C. R. Stokes (2015), Geomorphology and weathering characteristics of erratic boulder trains on Tierra del Fuego, southernmost South America: implications for dating of glacial deposits, *Geomorphology*, *228*, 382–397.

Davis, D., J. Suppe, and F. Dahlen (1983), Mechanics of fold-and-thrust belts and accretionary wedges, *Journal of Geophysical Research: Solid Earth*, *88*(B2), 1153–1172.

Davis, E. E., K. Becker, K. Wang, K. Obara, Y. Ito, and M. Kinoshita (2006), A discrete episode of seismic and aseismic deformation of the Nankai trough subduction zone accretionary prism and incoming Philippine Sea plate, *Earth and Planetary Science Letters*, *242*(1-2), 73–84.

Day, M., and A. Goudie (1977), Field assessment of rock hardness using the Schmidt test hammer, *British Geomorphological Research Group Technical Bulletin*, *18*, 19–29.

Day, M. J. (1980), Rock hardness: field assessment and geomorphic importance, *The Professional Geographer*, *32*(1), 72–81.

De Boor, C. (1978), *A practical guide to splines*, vol. 27, springer-verlag New York.

DeCelles, P. G., G. E. Gehrels, Y. Najman, A. Martin, A. Carter, and E. Garzanti (2004), Detrital geochronology and geochemistry of Cretaceous–Early Miocene strata of Nepal: implications for timing and diachroneity of initial Himalayan orogenesis, *Earth and Planetary Science Letters*, *227*(3-4), 313–330.

DeCelles, P. G., P. Kapp, G. E. Gehrels, and L. Ding (2014), Paleocene-Eocene foreland basin evolution in the Himalaya of southern Tibet and Nepal: Implications for the age of initial India-Asia collision, *Tectonics*, *33*(5), 824–849.

DeGraaff-Surpless, K., J. B. Mahoney, J. L. Wooden, and M. O. McWilliams (2003), Lithofacies control in detrital zircon provenance studies: Insights from the Cretaceous Methow basin, southern Canadian Cordillera, *Geological Society of America Bulletin*, *115*(8), 899–915.

Demirdag, S., H. Yavuz, and R. Altindag (2009), The effect of sample size on Schmidt rebound hardness value of rocks, *International Journal of Rock Mechanics and Mining Sciences*, *46*(4), 725–730.

dePolo, C. M. (2013), Magnitude values used for M$\geq$ 6 earthquakes in earthquakes in Nevada: 1840s to 2010, NBMG map 179, *Nevada Bureau of Mines and Geology Open-File Rept. 13*, *7*(6).

Dewey, J., and M. Mange (1999), Petrography of Ordovician and Silurian sediments in the western Irish Caledonides: tracers of a short-lived Ordovician continent-arc collision orogeny and the evolution of the Laurentian Appalachian-Caledonian margin, *Geological Society, London, Special Publications*, *164*(1), 55–107.

Dewey, J., M. Helman, S. Knott, E. Turco, and D. Hutton (1989), Kinematics of the western Mediterranean, *Geological Society, London, Special Publications*, *45*(1), 265–283.

Dickin, A. P. (2018), *Radiogenic isotope geology*, Cambridge university press.

Dickinson, W. R. (2008), Impact of differential zircon fertility of granitoid basement rocks in North America on age populations of detrital zircons and implications for granite petrogenesis, *Earth and Planetary Science Letters*, *275*(1), 80–92.

Dietrich, W. E. (1982), Settling velocity of natural particles, *Water resources research*, *18*(6), 1615–1626.

Dilek, Y., N. Imamverdiyev, and Ş. Altunkaynak (2010), Geochemistry and tectonics of Cenozoic volcanism in the Lesser Caucasus (Azerbaijan) and the peri-Arabian region: collision-induced mantle dynamics and its magmatic fingerprint, *International Geology Review*, *52*(4-6), 536–578.

Ding, L., P. Kapp, and X. Wan (2005), Paleocene–Eocene record of ophiolite obduction and initial India-Asia collision, south central Tibet, *Tectonics*, *24*(3).

Dodson, M., W. Compston, I. Williams, and J. Wilson (1988), A search for ancient detrital zircons in Zimbabwean sediments, *Journal of the Geological Society*, *145*(6), 977–983.

Dodson, M. H. (1973), Closure temperature in cooling geochronological and petrological systems, *Contributions to Mineralogy and Petrology*, *40*(3), 259–274.

Donelick, R. A., P. B. O'Sullivan, and R. A. Ketcham (2005), Apatite fission-track analysis, *Reviews in Mineralogy and Geochemistry*, *58*(1), 49–94.

Doser, D. I. (1988), Source parameters of earthquakes in the Nevada seismic zone, 1915–1943, *Journal of Geophysical Research: Solid Earth*, *93*(B12), 15,001–15,015.

Dupont-Nivet, G., C. Hoorn, and M. Konert (2008), Tibetan uplift prior to the Eocene-Oligocene climate transition: Evidence from pollen analysis of the Xining Basin, *Geology*, *36*(12), 987–990.

Duretz, T., T. V. Gerya, and D. A. May (2011), Numerical modelling of spontaneous slab breakoff and subsequent topographic response, *Tectonophysics*, *502*(1-2), 244–256.

Duretz, T., S. Schmalholz, and T. Gerya (2012), Dynamics of slab detachment, *Geochemistry, Geophysics, Geosystems*, *13*(3).

Duvall, A. R., M. K. Clark, B. Avdeev, K. A. Farley, and Z. Chen (2012), Widespread late Cenozoic increase in erosion rates across the interior of eastern Tibet constrained by detrital low-temperature thermochronometry, *Tectonics*, *31*(3), TC3014.

Dzhanelidze, A., and N. Kandelaki (1957), Geological map of the USSR, Caucasus series sheet K-38-XIII, scale 1:200,000, *Ministry of Geology and Mineral Protection USSR, Moscow*.

Edilashvili, V. (1957), Geological map of the USSR, Caucasus series sheet K-38-XXII, scale 1:200,000, *Ministry of Geology and Mineral Protection USSR, Moscow*.

Edmond, J. (1992), Himalayan tectonics, weathering processes, and the strontium isotope record in marine limestones, *Science*, *258*(5088), 1594–1597.

Ehlers, T. A., and K. A. Farley (2003), Apatite (U–Th)/He thermochronometry: methods and applications to problems in tectonic and surface processes, *Earth and Planetary Science Letters*, *206*(1-2), 1–14.

Eilers, P. H., and B. D. Marx (1996), Flexible smoothing with B-splines and penalties, *Statistical science*, pp. 89–102.

England, P., and G. Houseman (1986), Finite strain calculations of continental deformation: 2. Comparison with the India-Asia collision zone, *Journal of Geophysical Research: Solid Earth*, *91*(B3), 3664–3676.

Erslev, E. A. (1991), Trishear fault-propagation folding, *Geology*, *19*(6), 617–620.

Espina, R. G., J. L. Alonso, and J. A. Pulgar (1996), Growth and propagation of buckle folds determined from syntectonic sediments (the Ubierna Fold Belt, Cantabrian Mountains, N Spain), *Journal of Structural Geology*, *18*(4), 431–441.

Farley, K., M. Rusmore, and S. Bogue (2001), Post–10 Ma uplift and exhumation of the northern Coast Mountains, British Columbia, *Geology*, *29*(2), 99–102.

Farley, K. A. (2002), (U-Th)/He dating: Techniques, calibrations, and applications, *Reviews in Mineralogy and Geochemistry*, *47*(1), 819–844.

Faure, G. (1977), *Principles of isotope geology*, John Wiley and Sons, Inc., New York, NY.

Fedo, C. M., K. N. Sircombe, and R. H. Rainbird (2003), Detrital zircon analysis of the sedimentary record, *Reviews in Mineralogy and Geochemistry*, *53*(1), 277–303.

Ferguson, T. S. (1962), A representation of the symmetric bivariate Cauchy distribution, *The Annals of Mathematical Statistics*, *33*(4), 1256–1266.

Fitzgerald, P. G., S. M. Roeske, J. A. Benowitz, S. J. Riccio, S. E. Perry, and P. A. Armstrong (2014), Alternating asymmetric topography of the Alaska range along the strike-slip Denali fault: Strain partitioning and lithospheric control across a terrane suture zone, *Tectonics*, *33*(8), 1519–1533.

Forte, A. M., and E. Cowgill (2013), Late Cenozoic base-level variations of the Caspian Sea: a review of its history and proposed driving mechanisms, *Palaeogeography, Palaeoclimatology, Palaeoecology*, *386*, 392–407.

Forte, A. M., E. Cowgill, I. Murtuzayev, T. Kangarli, and M. Stoica (2013), Structural geometries and magnitude of shortening in the eastern Kura fold-thrust belt, Azerbaijan: Implications for the development of the Greater Caucasus Mountains, *Tectonics*, *32*(3), 688–717.

Forte, A. M., E. Cowgill, and K. X. Whipple (2014), Transition from a singly vergent to doubly vergent wedge in a young orogen: The Greater Caucasus, *Tectonics*, *33*(11), 2077–2101.

Gallagher, K. (2012), Transdimensional inverse thermal history modeling for quantitative thermochronology, *Journal of Geophysical Research: Solid Earth*, *117*(B2).

Galoyan, G., Y. Rolland, M. Sosson, M. Corsini, S. Billo, C. Verati, and R. Melkonyan (2009), Geology, geochemistry and ^{40}Ar/^{39}Ar dating of Sevan ophiolites (Lesser Caucasus, Armenia): evidence for Jurassic back-arc opening and hot spot event between the South Armenian Block and Eurasia, *Journal of Asian Earth Sciences*, *34*(2), 135–153.

Gamkrelidze, I. P., and D. M. Shengelia (2007), Pre-Alpine geodynamics of the Caucasus, suprasubduction regional metamorphism and granitoid magmatism, *Bull. Georg. Natl. Acad. Sci*, *175*, 57–65.

Gamkrelidze, P., and I. Kakhazdze (1959), Geological map of the USSR, Caucasus series sheet K-38-VII, scale 1:200,000, *Ministry of Geology and Mineral Protection USSR, Moscow*.

Garcia-Castellanos, D., F. Estrada, I. Jiménez-Munt, C. Gorini, M. Fernández, J. Vergés, and R. De Vicente (2009), Catastrophic flood of the Mediterranean after the Messinian salinity crisis, *Nature*, *462*(7274), 778.

Garçon, M., and C. Chauvel (2014), Where is basalt in river sediments, and why does it matter?, *Earth and Planetary Science Letters*, *407*, 61–69.

Garzanti, E., A. Baud, and G. Mascle (1987), Sedimentary record of the northward flight of India and its collision with Eurasia (Ladakh Himalaya, India), *Geodinamica Acta*, *1*(4-5), 297–312.

Garzanti, E., S. Andò, and G. Vezzoli (2008), Settling equivalence of detrital minerals and grain-size dependence of sediment composition, *Earth and Planetary Science Letters*, *273*(1), 138–151.

Gehrels, G. (2012), Detrital zircon U-Pb geochronology: Current methods and new opportunities, in *Tectonics of Sedimentary Basins: Recent Advances*, edited by C. Busby and A. Azor, pp. 45–62, Blackwell Publishing Ltd.

Gehrels, G. E. (2000), Introduction to detrital zircon studies of Paleozoic and Triassic strata in western Nevada and northern California, *Special Paper of the Geological Society of America*, *347*, 1–17.

Gehrels, G. E., V. A. Valencia, and J. Ruiz (2008), Enhanced precision, accuracy, efficiency, and spatial resolution of U-Pb ages by laser ablation–multicollector–inductively coupled plasma–mass spectrometry, *Geochemistry, Geophysics, Geosystems*, *9*(3), Q03,017.

Gelman, A., H. S. Stern, J. B. Carlin, D. B. Dunson, A. Vehtari, and D. B. Rubin (2013), *Bayesian data analysis*, Chapman and Hall/CRC.

Geyer, C. J. (1992), Practical Markov chain Monte Carlo, *Statistical science*, pp. 473–483.

Ghisetti, F. C., P. M. Barnes, S. Ellis, A. A. Plaza-Faverola, and D. H. Barker (2016), The last 2 Myr of accretionary wedge construction in the central Hikurangi margin (North Island, New Zealand): Insights from structural modeling, *Geochemistry, Geophysics, Geosystems*, *17*(7), 2661–2686.

Giaccio, B., F. Galadini, A. Sposato, P. Messina, M. Moro, M. Zreda, A. Cittadini, S. Salvi, and A. Todero (2003), Image processing and roughness analysis of exposed bedrock fault planes as a tool for paleoseismological analysis: results from the Campo Felice fault (central Apennines, Italy), *Geomorphology*, *49*(3-4), 281–301.

Gleadow, A. J., I. R. Duddy, P. F. Green, and K. A. Hegarty (1986), Fission track lengths in the apatite annealing zone and the interpretation of mixed ages, *Earth and planetary science letters*, *78*(2-3), 245–254.

Golubjatnikov, V., and A. Dubogryzova (1959), Geological map of the USSR, Caucasus series sheet K-39-XIX, scale 1:200,000, *Ministry of Geology and Mineral Protection USSR, Moscow*.

Gosse, J. C., and F. M. Phillips (2001), Terrestrial in situ cosmogenic nuclides: theory and application, *Quaternary Science Reviews*, *20*(14), 1475–1560.

Goudie, A. S. (2006), The Schmidt Hammer in geomorphological research, *Progress in Physical Geography*, *30*(6), 703–718.

Green, T., N. Abdullayev, J. Hossack, G. Riley, and A. M. Roberts (2009), Sedimentation and subsidence in the south Caspian Basin, Azerbaijan, *Geological Society, London, Special Publications*, *312*(1), 241–260.

Guest, B., D. F. Stockli, M. Grove, G. J. Axen, P. S. Lam, and J. Hassanzadeh (2006), Thermal histories from the central Alborz Mountains, northern Iran: Implications for the spatial and temporal distribution of deformation in northern Iran, *Geological Society of America Bulletin*, *118*(11-12), 1507–1521.

Gupta, V., R. Sharma, and M. P. Sah (2009), An evaluation of surface hardness of natural and modified rocks using Schmidt hammer: study from northwestern Himalaya, India, *Geografiska Annaler: Series A, Physical Geography*, *91*(3), 179–188.

Hack, J. T. (1957), *Studies of longitudinal stream profiles in Virginia and Maryland: U.S. Geological Survey Professional Paper 294-B*, US Government Printing Office.

Hanchar, J., and C. Miller (1993), Zircon zonation patterns as revealed by cathodoluminescence and backscattered electron images: implications for interpretation of complex crustal histories, *Chemical geology*, *110*(1-3), 1–13.

Hanks, T. C., R. C. Bucknam, K. R. Lajoie, and R. E. Wallace (1984), Modification of wave-cut and faulting-controlled landforms, *Journal of Geophysical Research: Solid Earth*, *89*(B7), 5771–5790.

He, H., Z. Wei, and A. Densmore (2016), Quantitative morphology of bedrock fault surfaces and identification of paleo-earthquakes, *Tectonophysics*, *693*, 22–31.

Hecker, S., H. D. Stenner, D. P. Schwartz, and J. C. Hamilton (2000), Paleoseismic results from the central part of the 1959 Hebgen fault rupture, Montana, in *EOS Transactions, American Geophysical Union*, vol. 81.

Hecker, S., H. D. Stenner, C. H. Costa, D. P. Schwartz, and J. C. Hamilton (2002), New paleoseismic results from the central part of the 1959 Hebgen fault rupture, Montana, in *Geological Society of America Abstracts with Programs*, vol. 34.

Hess, J., J. Aretz, A. Gurbanov, R. Emmermann, and H. Lippolt (1995), Subduction-related Jurassic andesites in the northern Great Caucasus, *Geologische Rundschau*, *84*(2), 319–333.

Hietpas, J., S. Samson, D. Moecher, and S. Chakraborty (2011), Enhancing tectonic and provenance information from detrital zircon studies: Assessing terrane-scale sampling and grain-scale characterization, *Journal of the Geological Society, London*, *168*(2), 309–318.

Hinds, D., E. Aliyeva, M. Allen, C. Davies, S. Kroonenberg, M. Simmons, and S. Vincent (2004), Sedimentation in a discharge dominated fluvial-lacustrine system: The Neogene Productive Series of the South Caspian Basin, Azerbaijan, *Marine and Petroleum Geology*, *21*(5), 613–638.

Hines, T., and E. Hetland (2017), Revealing transient strain in geodetic data with Gaussian process regression, *Geophysical Journal International*, *212*(3), 2116–2130.

Hollingsworth, J., J. Jackson, R. Walker, and H. Nazari (2008), Extrusion tectonics and subduction in the eastern South Caspian region since 10 Ma, *Geology*, *36*(10), 763–766.

Hooke, R., and T. A. Jeeves (1961), "Direct Search" Solution of Numerical and Statistical Problems, *Journal of the ACM (JACM)*, *8*(2), 212–229.

Horton, B., J. Hassanzadeh, D. Stockli, G. Axen, R. Gillis, B. Guest, A. Amini, M. Fakhari, S. Zamanzadeh, and M. Grove (2008), Detrital zircon provenance of Neoproterozoic to Cenozoic deposits in Iran: Implications for chronostratigraphy and collisional tectonics, *Tectonophysics*, *451*(1-4), 97–122.

Hosseini-Barzi, M., and C. J. Talbot (2003), A tectonic pulse in the Makran accretionary prism recorded in Iranian coastal sediments, *Journal of the Geological Society*, *160*(6), 903–910.

Hu, X., H. D. Sinclair, J. Wang, H. Jiang, and F. Wu (2012), Late Cretaceous-Palaeogene stratigraphic and basin evolution in the Zhepure Mountain of southern Tibet: implications for the timing of India-Asia initial collision, *Basin Research*, *24*(5), 520–543.

Hu, X., E. Garzanti, T. Moore, and I. Raffi (2015), Direct stratigraphic dating of India-Asia collision onset at the Selandian (middle Paleocene, 59$\pm$1 Ma), *Geology*, *43*(10), 859–862.

Hurford, A., F. Fitch, and A. Clarke (1984), Resolution of the age structure of the detrital zircon populations of two Lower Cretaceous sandstones from the Weald of England by fission track dating, *Geological Magazine*, *121*(04), 269–277.

Ibañez-Mejia, M., A. Pullen, M. Pepper, F. Urbani, G. Ghoshal, and J. C. Ibañez-Mejia (2018), Use and abuse of detrital zircon U-Pb geochronology—A case from the Río Orinoco delta, eastern Venezuela, *Geology*.

Ingalls, M., D. B. Rowley, B. Currie, and A. S. Colman (2016), Large-scale subduction of continental crust implied by India–Asia mass-balance calculation, *Nature Geoscience*, *9*(11), 848.

Ito, Y., and K. Obara (2006), Dynamic deformation of the accretionary prism excites very low frequency earthquakes, *Geophysical Research Letters*, *33*(2).

Ivanov, A. V., E. I. Demonterova, L. Z. Reznitskii, I. G. Barash, S. G. Arzhannikov, A. V. Arzhannikova, C.-H. Hung, S.-L. Chung, and Y. Iizuka (2016), Catastrophic outburst and tsunami flooding of Lake Baikal: U–Pb detrital zircon provenance study of the Palaeo-Manzurka megaflood sediments, *International Geology Review*, *58*(14), 1818–1830.

Jaeger, J.-J., V. Courtillot, and P. Tapponnier (1989), Paleontological view of the ages of the Deccan Traps, the Cretaceous/Tertiary boundary, and the India-Asia collision, *Geology*, *17*(4), 316–319.

Jagoutz, O., F. A. Macdonald, and L. Royden (2016), Low-latitude arc–continent collision as a driver for global cooling, *Proceedings of the National Academy of Sciences*, *113*(18), 4935–4940.

Jaques, A., and G. Robinson (1977), The continent-arc collision in northern Papua New Guinea, *BMR Journal of Australian Geology and Geophysics*, *2*, 289–303.

Jeffreys, H. (1998), *The theory of probability (3rd ed.)*, Oxford University Press.

Jerolmack, D. J., and C. Paola (2010), Shredding of environmental signals by sediment transport, *Geophysical Research Letters*, *37*(19).

Johnson, K. (2017), *Applications of High Resolution Topography in Tectonic Geomorphology, PhD Thesis*, Colorado School of Mines, Golden, CO.

Johnson, P. R., and B. Woldehaimanot (2003), Development of the Arabian-Nubian Shield: perspectives on accretion and deformation in the northern East African Orogen and the assembly of Gondwana, *Geological Society, London, Special Publications*, *206*(1), 289–325.

Jones, R., and M. Simmons (1998), A review of the stratigraphy of Eastern Paratethys (Oligocene-Holocene), with particular emphasis on the Black Sea, *Memoirs-American Association of Petroleum Geologists*, pp. 39–52.

Jones, R. R., and P. G. Tanner (1995), Strain partitioning in transpression zones, *Journal of Structural Geology*, *17*(6), 793–802.

Judge, P. A., and R. W. Allmendinger (2011), Assessing uncertainties in balanced cross sections, *Journal of Structural Geology*, *33*(4), 458–467.

Kadirov, F., M. Floyd, A. Alizadeh, I. Guliev, R. Reilinger, S. Kuleli, R. King, and M. N. Toksoz (2012), Kinematics of the eastern Caucasus near Baku, Azerbaijan, *Natural Hazards*, *63*(2), 997–1006.

Kadirov, F., M. Floyd, R. Reilinger, A. A. Alizadeh, I. Guliyev, S. Mammadov, and R. Safarov (2015), Active geodynamics of the Caucasus region: implications for earthquake hazards in Azerbaijan, *Proceedings of Azerbaijan National Academy of Sciences, The Sciences of Earth*, *3*, 3–17.

Karig, D. E., and G. F. Sharman III (1975), Subduction and accretion in trenches, *Geological Society of America Bulletin*, *86*(3), 377–389.

Kass, R. E., and A. E. Raftery (1995), Bayes factors, *Journal of the american statistical association*, *90*(430), 773–795.

Kastelic, V., P. Burrato, M. M. Carafa, and R. Basili (2017), Repeated surveys reveal non-tectonic exposure of supposedly active normal faults in the central Apennines, Italy, *Journal of Geophysical Research: Earth Surface*, *122*(1), 114–129.

Khain, V. (1975), Structure and main stages in the tectono-magmatic development of the Caucasus: an attempt at geodynamic interpretation, *American Journal of Science*, *275*, 131–156.

Khain, V. (2007), Mesozoic-Cenozoic accretionary complexes of the Greater Caucasus, in *Doklady Earth Sciences*, vol. 413, pp. 376–379, Springer.

Khain, V., and A. Shardanov (1960), Geological map of the USSR, Caucasus series sheet K-39-XXV, scale 1:200,000, *Ministry of Geology and Mineral Protection USSR, Moscow*.

Khain, V. Y., B. Grigoryants, and B. Isayev (1966), The West Caspian Fault and factors governing the formation of transverse faults in geosynclinal fold belts, *MOIP Bull*, *41*, 5–23.

Kimbrough, D. L., M. Grove, G. E. Gehrels, R. J. Dorsey, K. A. Howard, O. Lovera, A. Aslan, P. K. House, and P. A. Pearthree (2015), Detrital zircon U-Pb provenance of the Colorado River: A 5 My record of incision into cover strata overlying the Colorado Plateau and adjacent regions, *Geosphere*, *11*(6), 1719–1748.

Klootwijk, C., P. Conaghan, and C. M. Powell (1985), The Himalayan Arc: large-scale continental subduction, oroclinal bending and back-arc spreading, *Earth and Planetary Science Letters*, *75*(2-3), 167–183.

Kolmogorov, A. N. (1933), Sulla determinazione empirica di una legge di distribuzione, *Giornale dell'Istituto Italiano degli Attuari*, *4*, 83–91.

Kong, P., J. Jia, and Y. Zheng (2014), Time constraints for the Yellow River traversing the Sanmen Gorge, *Geochemistry, Geophysics, Geosystems*, *15*(2), 395–407.

Kopp, M. (1985), Age and nature of deformations of sediments comprising the Lagich syncline (southeastern Caucasus), *Geologiya*, *40*(1), 25–34.

Kopp, M., and I. Shcherba (1985), Late Alpine development of the east Caucasus, *Geotectonics*, *19*(6), 497–507.

Krijgsman, W., F. Hilgen, I. Raffi, F. J. Sierro, and D. Wilson (1999), Chronology, causes and progression of the Messinian salinity crisis, *Nature*, *400*(6745), 652.

Krijgsman, W., M. Stoica, I. Vasiliev, and V. Popov (2010), Rise and fall of the Paratethys Sea during the Messinian Salinity Crisis, *Earth and Planetary Science Letters*, *290*(1-2), 183–191.

Kroonenberg, S., N. Alekseevski, E. Aliyeva, M. Allen, D. Aybulatov, A. Baba-Zadeh, E. Badyukova, C. Davies, D. Hinds, R. Hoogendoorn, et al. (2005), Two deltas, two basins, one river, one sea: the modern Volga Delta an as analogue of the Neogene productive series, South Caspian Basin, *Special Publications of SEPM No. 83*.

Kruschke, J. K. (2013), Bayesian estimation supersedes the t Test, *Journal of Experimental Psychology: General*, *142*(2), 573.

Lallemand, S. E., J. Malavieille, and S. Calassou (1992), Effects of oceanic ridge subduction on accretionary wedges: experimental modeling and marine observations, *Tectonics*, *11*(6), 1301–1313.

Lange, K. L., R. J. Little, and J. M. Taylor (1989), Robust statistical modeling using the t distribution, *Journal of the American Statistical Association*, *84*(408), 881–896.

Laustela, M., M. Egli, R. Frauenfelder, A. Kääb, M. Maisch, and W. Haeberli (2003), Weathering rind measurements and relative age dating of rockglacier surfaces in crystalline regions of the Eastern Swiss Alps, in *Permafrost: Proceedings of the Eighth International Conference on Permafrost*, pp. 627–632.

Lawrence, R. L., R. Cox, R. W. Mapes, and D. S. Coleman (2011), Hydrodynamic fractionation of zircon age populations, *Geological Society of America Bulletin*, *123*(1-2), 295–305.

Le Roux, J. (2005), Grains in motion: A review, *Sedimentary Geology*, *178*(3), 285–313.

Lee, T.-Y., and L. A. Lawver (1995), Cenozoic plate reconstruction of Southeast Asia, *Tectonophysics*, *251*(1-4), 85–138.

Leggett, J., W. t. McKerrow, and M. Eales (1979), The Southern Uplands of Scotland: a lower Palaeozoic accretionary prism, *Journal of the Geological Society*, *136*(6), 755–770.

Licciardi, J. M., and K. L. Pierce (2008), Cosmogenic exposure-age chronologies of Pinedale and Bull Lake glaciations in greater Yellowstone and the Teton Range, USA, *Quaternary Science Reviews*, *27*(7-8), 814–831.

Link, P. K., C. M. Fanning, and L. P. Beranek (2005), Reliability and longitudinal change of detrital-zircon age spectra in the Snake River system, Idaho and Wyoming: An example of reproducing the bumpy barcode, *Sedimentary Geology*, *182*(1), 101–142.

Lipman, P. W., O. Bogatikov, A. Tsvetkov, C. Gazis, A. G. Gurbanov, K. Hon, N. V. Koronovsky, V. Kovalenko, and P. Marchev (1993), 2.8-Ma ash-flow caldera at Chegem River in the northern Caucasus Mountains (Russia), contemporaneous granites, and associated ore deposits, *Journal of Volcanology and Geothermal Research*, *57*(1-2), 85–124.

Litty, C., P. Lanari, M. Burn, and F. Schlunegger (2017), Climate-controlled shifts in sediment provenance inferred from detrital zircon ages, western Peruvian Andes, *Geology*, *45*(1), 59–62.

Maizels, J. K. (1989), Differentiation of late Pleistocene terrace outwash deposits using geomorphic criteria: Tekapo valley, South Island, New Zealand, *New Zealand Journal of Geology and Geophysics*, *32*(2), 225–241.

Malusa, M. G., A. Resentini, and E. Garzanti (2016), Hydraulic sorting and mineral fertility bias in detrital geochronology, *Gondwana Research*, *31*, 1–19.

Manighetti, I., E. Boucher, C. Chauvel, A. Schlagenhauf, and L. Benedetti (2010), Rare earth elements record past earthquakes on exhumed limestone fault planes, *Terra Nova*, *22*(6), 477–482.

Marinos, V., P. Marinos, and E. Hoek (2005), The geological strength index: applications and limitations, *Bulletin of Engineering Geology and the Environment*, *64*(1), 55–65.

Matthews, J. A., and G. Owen (2008), Endolithic lichens, rapid biological weathering and Schmidt hammer R-values on recently exposed rock surfaces: Storbreen glacier foreland, Jotunheimen, Norway, *Geografiska Annaler: Series A, Physical Geography*, *90*(4), 287–297.

Matthews, J. A., and G. Owen (2010), Schmidt hammer exposure-age dating: developing linear age-calibration curves using Holocene bedrock surfaces from the Jotunheimen–Jostedalsbreen regions of southern Norway, *Boreas*, *39*(1), 105–115.

Matthews, J. A., and R. A. Shakesby (1984), The status of the 'Little Ice Age' in southern Norway: relative-age dating of Neoglacial moraines with Schmidt hammer and lichenometry, *Boreas*, *13*(3), 333–346.

Matthews, J. A., L. J. McEwen, and G. Owen (2015), Schmidt-hammer exposure-age dating (SHD) of snow-avalanche impact ramparts in southern Norway: approaches, results and implications for landform age, dynamics and development, *Earth Surface Processes and Landforms*, *40*(13), 1705–1718.

Matthews, J. A., G. Owen, S. Winkler, A. E. Vater, P. Wilson, R. W. Mourne, and J. L. Hill (2016), A rock-surface microweathering index from Schmidt hammer R-values and its preliminary application to some common rock types in southern Norway, *Catena*, *143*, 35–44.

Mayringer, F., P. J. Treloar, A. Gerdes, F. Finger, and D. Shengelia (2011), New age data from the Dzirula massif, Georgia: Implications for the evolution of the Caucasian Variscides, *American Journal of Science*, *311*(5), 404–441.

McCarroll, D. (1987), The Schmidt hammer in geomorphology: five sources of instrument error, *British Geomorphological Research Group Technical Bulletin*, *36*, 16–27.

McCarroll, D. (1991), The Schmidt hammer, weathering and rock surface roughness, *Earth Surface Processes and Landforms*, *16*(5), 477–480.

McQuarrie, N., and B. P. Wernicke (2005), An animated tectonic reconstruction of southwestern North America since 36 Ma, *Geosphere*, *1*(3), 147–172.

Mechernich, S., S. Schneiderwind, J. Mason, I. D. Papanikolaou, G. Deligiannakis, A. Pallikarakis, S. A. Binnie, T. J. Dunai, and K. Reicherter (2018), The seismic history of the Pisia fault (eastern Corinth rift, Greece) from fault plane weathering features and cosmogenic ^{36}Cl dating, *Journal of Geophysical Research: Solid Earth*, *123*(5), 4266–4284.

Mekhtiev, S., V. Gorin, M. Agabekov, and M. Voronin (1962), Geological map of the USSR, Caucasus series sheet K-39-XXXII, scale 1:200,000, *Ministry of Geology and Mineral Protection USSR, Moscow*.

Mellors, R., J. Jackson, S. Myers, R. Gok, K. Priestley, G. Yetirmishli, N. Turkelli, and T. Godoladze (2012), Deep earthquakes beneath the Northern Caucasus: evidence of active or recent subduction in western Asia, *Bulletin of the Seismological Society of America*, *102*(2), 862–866.

Mengel, K., A. Borsuk, A. Gurbanov, K. Wedepohl, A. Baumann, and J. Hoefs (1987), Origin of spilitic rocks from the southern slope of the Greater Caucasus, *Lithos*, *20*(2), 115–133.

Mitchell, S. G., A. Matmon, P. R. Bierman, Y. Enzel, M. Caffee, and D. Rizzo (2001), Displacement history of a limestone normal fault scarp, northern Israel, from cosmogenic ^{36}Cl, *Journal of Geophysical Research: Solid Earth*, *106*(B3), 4247–4264.

Molnar, P., R. S. Anderson, and S. P. Anderson (2007), Tectonics, fracturing of rock, and erosion, *Journal of Geophysical Research: Earth Surface*, *112*(F3).

Molnar, P., W. R. Boos, and D. S. Battisti (2010), Orographic controls on climate and paleoclimate of Asia: thermal and mechanical roles for the Tibetan Plateau, *Annual Review of Earth and Planetary Sciences*, *38*, 77–102.

Montgomery, D. R., and W. E. Dietrich (1992), Channel initiation and the problem of landscape scale, *Science*, *255*(5046), 826–830.

Montgomery, D. R., G. Balco, and S. D. Willett (2001), Climate, tectonics, and the morphology of the Andes, *Geology*, *29*(7), 579–582.

Moore, J. C. (1989), Tectonics and hydrogeology of accretionary prisms: role of the décollement zone, *Journal of Structural Geology*, *11*(1-2), 95–106.

Moore, J. C., and D. Saffer (2001), Updip limit of the seismogenic zone beneath the accretionary prism of southwest Japan: An effect of diagenetic to low-grade metamorphic processes and increasing effective stress, *Geology*, *29*(2), 183–186.

Moore, J. C., and E. A. Silver (1987), Continental margin tectonics: submarine accretionary prisms, *Reviews of Geophysics*, *25*(6), 1305–1312.

Morley, C. (1988), Out-of-sequence thrusts, *Tectonics*, *7*(3), 539–561.

Mouslopoulou, V., D. Moraetis, and C. Fassoulas (2011), Identifying past earthquakes on carbonate faults: Advances and limitations of the 'Rare Earth Element' method based on analysis of the Spili Fault, Crete, Greece, *Earth and Planetary Science Letters*, *309*(1-2), 45–55.

Mouslopoulou, V., D. Moraetis, L. Benedetti, V. Guillou, O. Bellier, and D. Hristopulos (2014), Normal faulting in the forearc of the hellenic subduction margin: Paleoearthquake history and kinematics of the Spili Fault, Crete, Greece, *Journal of Structural Geology*, *66*, 298–308.

Mulugeta, G., and H. Koyi (1992), Episodic accretion and strain partitioning in a model sand wedge, *Tectonophysics*, *202*(2-4), 319–333.

Mumladze, T., A. M. Forte, E. S. Cowgill, C. C. Trexler, N. A. Niemi, M. B. Yıkılmaz, and L. H. Kellogg (2015), Subducted, detached, and torn slabs beneath the Greater Caucasus, *GeoResJ*, *5*, 36–46.

Nalivkin, D. (1976), Geologic Map of the Caucasus (in Russian). scale 1: 500,000, *Ministry of Geology, USSR, Moscow*.

Nance, R. D., J. B. Murphy, and M. Santosh (2014), The supercontinent cycle: a retrospective essay, *Gondwana Research*, *25*(1), 4–29.

Natal'in, B. A., and A. C. Şengör (2005), Late Palaeozoic to Triassic evolution of the Turan and Scythian platforms: the pre-history of the Palaeo-Tethyan closure, *Tectonophysics*, *404*(3-4), 175–202.

Nazarevich, B., I. Nazarevich, and N. Shvydko (1986), The Upper Triassic Nogai volcanosedimentary formation of Eastern Fore-Caucasus: composition, constitution, and relations to earlierand later-formed volcanics, *The Formations of Sedimentary Basins. Nauka, Moscow (In Russian)*, pp. 67–86.

Nicholson, D. T. (2009), Holocene microweathering rates and processes on ice-eroded bedrock, Røldal area, Hardangervidda, southern Norway, *Geological Society, London, Special Publications*, *320*(1), 29–49.

Nicol, A., J. Walsh, K. Berryman, and P. Villamor (2006), Interdependence of fault displacement rates and paleoearthquakes in an active rift, *Geology*, *34*(10), 865–868.

Nie, J., T. Stevens, M. Rittner, D. Stockli, E. Garzanti, M. Limonta, A. Bird, S. Andò, P. Vermeesch, J. Saylor, H. Lu, D. Breecker, X. Hu, S. Liu, A. Resentini, G. Vezzoli, W. Peng, A. Carter, S. Ji, and B. Pan (2015), Loess plateau storage of northeastern Tibetan plateau-derived Yellow River sediment, *Nature communications*, *6*, 8511.

Niedzielski, T., P. Migoń, and A. Placek (2009), A minimum sample size required from Schmidt hammer measurements, *Earth Surface Processes and Landforms: The Journal of the British Geomorphological Research Group*, *34*(13), 1713–1725.

Niemi, N. A. (2013), Detrital zircon age distributions as a discriminator of tectonic versus fluvial transport: An example from the Death Valley, USA, extended terrane, *Geosphere*, *9*(1), 126–137.

Niemi, N. A., B. P. Wernicke, R. J. Brady, J. B. Saleeby, and G. C. Dunne (2001), Distribution and provenance of the middle Miocene Eagle Mountain Formation, and implications for regional kinematic analysis of the Basin and Range province, *Geological Society of America Bulletin*, *113*(4), 419–442.

Nikishin, A. M., S. Cloetingh, M.-F. Brunet, R. A. Stephenson, S. N. Bolotov, and A. V. Ershov (1998), Scythian platform, Caucasus and Black Sea region: Mesozoic–Cenozoic tectonic history and dynamics, *Peri-Tethys Memoir*, *3*, 163–176.

Nikonov, A. (1982), A very powerful earthquake in the Greater Caucasus Mountains, January 14, 1668, *Izv Phys Solid Earth*, *18*, 713–24.

Nishiizumi, K., C. Kohl, J. Arnold, R. Dorn, I. Klein, D. Fink, R. Middleton, and D. Lal (1993), Role of in situ cosmogenic nuclides ^{10}Be and ^{26}Al in the study of diverse geomorphic processes, *Earth surface processes and landforms*, *18*(5), 407–425.

Oldow, J. S., A. W. Bally, and H. G. Avé Lallemant (1990), Transpression, orogenic float, and lithospheric balance, *Geology*, *18*(10), 991–994.

O'Neill, J. M., and R. L. Christiansen (2004), *Geologic map of the Hebgen Lake Quadrangle, Beaverhead, Madison, and Gallatin Counties, Montana, Park and Teton Counties, Wyoming, and Clark and Fremont Counties, Idaho*, 2816, US Geological Survey.

Page, B. M. (1935), Basin-range faulting of 1915 in Pleasant Valley, Nevada, *The Journal of Geology*, *43*(7), 690–707.

Patriat, P., and J. Achache (1984), India–Eurasia collision chronology has implications for crustal shortening and driving mechanism of plates, *Nature*, *311*(5987), 615.

Perchuk, A., and P. Philippot (1997), Rapid cooling and exhumation of eclogitic rocks from the Great Caucasus, Russia, *Journal of Metamorphic Geology*, *15*(3), 299–310.

Philip, H., A. Cisternas, A. Gvishiani, and A. Gorshkov (1989), The Caucasus: an actual example of the initial stages of continental collision, *Tectonophysics*, *161*(1-2), 1–21.

Philippot, P., J. Blichert-Toft, A. Perchuk, S. Costa, and V. Gerasimov (2001), Lu–Hf and Ar–Ar chronometry supports extreme rate of subduction zone metamorphism deduced from geospeedometry, *Tectonophysics*, *342*(1-2), 23–38.

Pierce, K., D. Lageson, C. Ruleman, and R. Hintz (2000), Holocene paleoseismology of Hebgen Lake normal fault, MT: The Cabin Creek site of the Hebgen Lake Paleoseismology Working Group, *EOS Transactions, American Geophysical Union*, *81*, F1170.

Pierce, K. L. (2003), Pleistocene glaciations of the Rocky Mountains, *Developments in Quaternary Sciences*, *1*, 63–76.

Pirouz, M., J.-P. Avouac, J. Hassanzadeh, J. L. Kirschvink, and A. Bahroudi (2017), Early Neogene foreland of the Zagros, implications for the initial closure of the Neo-Tethys and kinematics of crustal shortening, *Earth and Planetary Science Letters*, *477*, 168–182.

Platt, J., J. Leggett, J. Young, H. Raza, and S. Alam (1985), Large-scale sediment underplating in the Makran accretionary prism, southwest Pakistan, *Geology*, *13*(7), 507–511.

Pound, K., R. Norris, and C. Landis (2014), Eyre Creek mélange: An accretionary prism shear-zone mélange in Caples terrane rocks, Eyre Creek, northern Southland, New Zealand, *New Zealand Journal of Geology and Geophysics*, *57*(1), 1–20.

Pullen, A., M. Ibáñez-Mejía, G. E. Gehrels, J. C. Ibáñez-Mejía, and M. Pecha (2014), What happens when n= 1000? Creating large-n geochronological datasets with LA-ICP-MS for geologic investigations, *Journal of Analytical Atomic Spectrometry*, *29*(6), 971–980.

Pusok, A., and B. J. Kaus (2015), Development of topography in 3-D continental-collision models, *Geochemistry, Geophysics, Geosystems*, *16*(5), 1378–1400.

Raftery, A. E. (1995), Bayesian model selection in social research, *Sociological methodology*, pp. 111–163.

Ramsay, J. G., and D. S. Wood (1973), The geometric effects of volume change during deformation processes, *Tectonophysics*, *16*(3-4), 263–277.

Raymo, M. E., and W. F. Ruddiman (1992), Tectonic forcing of late Cenozoic climate, *nature*, *359*(6391), 117.

Reilinger, R., S. McClusky, P. Vernant, S. Lawrence, S. Ergintav, R. Cakmak, H. Ozener, F. Kadirov, I. Guliev, R. Stepanyan, et al. (2006), GPS constraints on continental deformation in the Africa-Arabia-Eurasia continental collision zone and implications for the dynamics of plate interactions, *Journal of Geophysical Research: Solid Earth*, *111*(B5).

Reiners, P. W. (2005), Zircon (U-Th)/He thermochronometry, *Reviews in Mineralogy and Geochemistry*, *58*(1), 151–179.

Reiners, P. W., and M. T. Brandon (2006), Using thermochronology to understand orogenic erosion, *Annu. Rev. Earth Planet. Sci.*, *34*, 419–466.

Reiners, P. W., T. L. Spell, S. Nicolescu, and K. A. Zanetti (2004), Zircon (U-Th)/He thermochronometry: He diffusion and comparisons with ^{40}Ar/^{39}Ar dating, *Geochimica et cosmochimica acta*, *68*(8), 1857–1887.

Renik, B., N. Christie-Blick, B. W. Troxel, L. A. Wright, and N. A. Niemi (2008), Re-evaluation of the middle Miocene Eagle Mountain Formation and its significance as a piercing point for the interpretation of extreme extension across the Death Valley region, California, USA, *Journal of Sedimentary Research*, *78*(3), 199–219.

Rolland, Y., M. Sosson, S. Adamia, and N. Sadradze (2011), Prolonged Variscan to Alpine history of an active Eurasian margin (Georgia, Armenia) revealed by ^{40}Ar/^{39}Ar dating, *Gondwana Research*, *20*(4), 798–815.

Rolland, Y., M. Hässig, D. Bosch, M. Meijers, M. Sosson, O. Bruguier, S. Adamia, and N. Sadradze (2016), A review of the plate convergence history of the East Anatolia-Transcaucasus region during the Variscan: Insights from the Georgian basement and its connection to the Eastern Pontides, *Journal of Geodynamics*, *96*, 131–145.

Rusmore, M. E., G. Gehrels, and G. Woodsworth (2001), Southern continuation of the Coast shear zone and Paleocene strain partitioning in British Columbia–southeast Alaska, *Geological Society of America Bulletin*, *113*(8), 961–975.

Sagy, A., E. E. Brodsky, and G. J. Axen (2007), Evolution of fault-surface roughness with slip, *Geology*, *35*(3), 283–286.

Sahakyan, L., D. Bosch, M. Sosson, A. Avagyan, G. Galoyan, Y. Rolland, O. Bruguier, Z. Stepanyan, B. Galland, and S. Vardanyan (2017), Geochemistry of the Eocene magmatic rocks from the Lesser Caucasus area (Armenia): evidence of a subduction geodynamic environment, *Geological Society, London, Special Publications*, *428*(1), 73–98.

Saintot, A., R. A. Stephenson, S. Stovba, M.-F. Brunet, T. Yegorova, and V. Starostenko (2006a), The evolution of the southern margin of Eastern Europe (Eastern European and Scythian platforms) from the latest Precambrian-Early Palaeozoic to the Early Cretaceous, *Geological Society, London, Memoirs*, *32*(1), 481–505.

Saintot, A., M.-F. Brunet, F. Yakovlev, M. Sébrier, R. Stephenson, A. Ershov, F. Chalot-Prat, and T. McCann (2006b), The Mesozoic-Cenozoic tectonic evolution of the Greater Caucasus, *Geological Society, London, Memoirs*, *32*(1), 277–289.

Sak, P. B., D. M. Fisher, T. W. Gardner, K. Murphy, and S. L. Brantley (2004), Rates of weathering rind formation on Costa Rican basalt, *Geochimica et Cosmochimica Acta*, *68*(7), 1453–1472.

Sample, J. C., and D. M. Fisher (1986), Duplex accretion and underplating in an ancient accretionary complex, Kodiak Islands, Alaska, *Geology*, *14*(2), 160–163.

Satkoski, A. M., B. H. Wilkinson, J. Hietpas, and S. D. Samson (2013), Likeness among detrital zircon populations–An approach to the comparison of age frequency data in time and space, *Geological Society of America Bulletin*, *125*(11-12), 1783–1799.

Saylor, J. E., and K. E. Sundell (2016), Quantifying comparison of large detrital geochronology data sets, *Geosphere*, *12*(1), GES01,237–1.

Saylor, J. E., D. F. Stockli, B. K. Horton, J. Nie, and A. Mora (2012), Discriminating rapid exhumation from syndepositional volcanism using detrital zircon double dating: Implications for the tectonic history of the Eastern Cordillera, Colombia, *Geological Society of America Bulletin*, *124*(5-6), 762–779.

Saylor, J. E., J. N. Knowles, B. K. Horton, J. Nie, and A. Mora (2013), Mixing of source populations recorded in detrital zircon U-Pb age spectra of modern river sands, *The Journal of Geology*, *121*(1), 17–33.

Schlagenhauf, A., Y. Gaudemer, L. Benedetti, I. Manighetti, L. Palumbo, I. Schimmelpfennig, R. Finkel, and K. Pou (2010), Using in situ chlorine-36 cosmonuclide to recover past earthquake histories on limestone normal fault scarps: a reappraisal of methodology and interpretations, *Geophysical Journal International*, *182*(1), 36–72.

Schwartz, D., S. Hecker, H. Stenner, K. M. Haller, K. L. Pierce, D. R. Lageson, and M. Machette (2009), The 1959 Hebgen Lake, Montana, surface rupture and record of Late-Pleistocene-Holocene earthquakes, in *2009 Portland GSA Annual Meeting*.

Schwarz, G., et al. (1978), Estimating the dimension of a model, *The annals of statistics*, *6*(2), 461–464.

Şengör, A., and W. Kidd (1979), Post-collisional tectonics of the Turkish-Iranian plateau and a comparison with Tibet, *Tectonophysics*, *55*(3-4), 361–376.

Sengör, A., and Y. Yilmaz (1981), Tethyan evolution of Turkey: a plate tectonic approach, *Tectonophysics*, *75*(3-4), 181–241.

Şengör, A., Y. Yılmaz, and O. Sungurlu (1984), Tectonics of the Mediterranean Cimmerides: Nature and evolution of the western termination of Palaeo-Tethys, *Geological Society, London, Special Publications*, *17*(1), 77–112.

Şengör, A. C. (1984), The Cimmeride orogenic system and the tectonics of Eurasia, *Geological Society of America Special Papers*, *195*, 1–74.

Shakesby, R. A., J. A. Matthews, and G. Owen (2006), The Schmidt hammer as a relative-age dating tool and its potential for calibrated-age dating in Holocene glaciated environments, *Quaternary Science Reviews*, *25*(21-22), 2846–2867.

Shakesby, R. A., J. A. Matthews, W. Karlén, and S. O. Los (2011), The Schmidt hammer as a Holocene calibrated-age dating technique: testing the form of the R-value-age relationship and defining the predicted-age errors, *The Holocene*, *21*(4), 615–628.

Shanno, D. F. (1970), Conditioning of quasi-Newton methods for function minimization, *Mathematics of computation*, *24*(111), 647–656.

Sharman, G. R., and S. A. Johnstone (2017), Sediment unmixing using detrital geochronology, *Earth and Planetary Science Letters*, *477*, 183–194.

Sharman, G. R., J. P. Sharman, and Z. Sylvester (2018), detritalPy: A Python-based toolset for visualizing and analysing detrital geo-thermochronologic data, *The Depositional Record*, *4*(2), 202–215.

Shimazaki, H., and S. Shinomoto (2010), Kernel bandwidth optimization in spike rate estimation, *Journal of computational neuroscience*, *29*(1-2), 171–182.

Shiraiwa, T., and T. Watanabe (1991), Late Quaternary glacial fluctuations in the Langtang valley, Nepal Himalaya, reconstructed by relative dating methods, *Arctic and Alpine Research*, *23*(4), 404–416.

Sholpo, V. (1978), Alpine Geodynamics of the Greater Caucasus (in Russian), 176 pp, *Nedra, Moscow*.

Sickmann, Z. T., C. K. Paull, and S. A. Graham (2016), Detrital-zircon mixing and partitioning in fluvial to deep marine systems, central California, USA, *Journal of Sedimentary Research*, *86*(11), 1298–1307.

Silverman, B. W. (1986), *Density estimation for statistics and data analysis*, vol. 26, CRC press.

Sircombe, K. N. (2000), Quantitative comparison of large sets of geochronological data using multivariate analysis: A provenance study example from Australia, *Geochimica et Cosmochimica Acta*, *64*(9), 1593–1616.

Smirnov, N. (1948), Table for estimating the goodness of fit of empirical distributions, *The annals of mathematical statistics*, *19*(2), 279–281.

Sokhadze, G., M. Floyd, T. Godoladze, R. King, E. Cowgill, Z. Javakhishvili, G. Hahubia, and R. Reilinger (2018), Active convergence between the Lesser and Greater Caucasus in Georgia: Constraints on the tectonic evolution of the Lesser–Greater Caucasus continental collision, *Earth and Planetary Science Letters*, *481*, 154–161.

Somin, M. L. (2011), Pre-Jurassic basement of the Greater Caucasus: brief overview, *Turkish Journal of Earth Sciences*, *20*(5), 545–610.

Sorby, H. C. (1908), On the application of quantitative methods to the study of the structure and history of rocks, *Quarterly Journal of the Geological Society*, *64*(1-4), 171–233.

Soreghan, M. J., G. Soreghan, and M. A. Hamilton (2002), Paleowinds inferred from detrital-zircon geochronology of upper Paleozoic loessite, western equatorial Pangea, *Geology*, *30*(8), 695–698.

Soria, J., J. Fernández, and C. Viseras (1999), Late Miocene stratigraphy and palaeogeographic evolution of the intramontane Guadix Basin (Central Betic Cordillera, Spain): implications for an Atlantic–Mediterranean connection, *Palaeogeography, Palaeoclimatology, Palaeoecology*, *151*(4), 255–266.

Sosson, M., Y. Rolland, C. Müller, T. Danelian, R. Melkonyan, S. Kekelia, S. Adamia, V. Babazadeh, T. Kangarli, A. Avagyan, et al. (2010), Subductions, obduction and collision in the Lesser Caucasus (Armenia, Azerbaijan, Georgia), new insights, *Geological Society, London, Special Publications*, *340*(1), 329–352.

Spencer, C. J., and C. L. Kirkland (2016), Visualizing the sedimentary response through the orogenic cycle: A multidimensional scaling approach, *Lithosphere*, *8*(1), 29–37.

Stahl, T., S. Winkler, M. Quigley, M. Bebbington, B. Duffy, and D. Duke (2013), Schmidt hammer exposure-age dating (SHD) of late Quaternary fluvial terraces in New Zealand, *Earth Surface Processes and Landforms*, *38*(15), 1838–1850.

Stahl, T., M. Quigley, and M. Bebbington (2016), Tectonic geomorphology of the Fox Peak and Forest Creek Faults, South Canterbury, New Zealand: slip rates, segmentation and earthquake magnitudes, *New Zealand Journal of Geology and Geophysics*, *59*(4), 568–591.

Stampfli, G., C. Hochard, C. Vérard, C. Wilhem, et al. (2013), The formation of Pangea, *Tectonophysics*, *593*, 1–19.

Stampfli, G. M. (2013), Response to the comments on "the formation of Pangea" by DA Ruban, *Tectonophysics*, *608*, 1445–1447.

Stevens, T., A. Carter, T. Watson, P. Vermeesch, S. Andò, A. Bird, H. Lu, E. Garzanti, M. Cottam, and I. Sevastjanova (2013), Genetic linkage between the Yellow River, the Mu Us desert and the Chinese Loess Plateau, *Quaternary Science Reviews*, *78*, 355–368.

Stewart, I. (1996), A rough guide to limestone fault scarps, *Journal of structural geology*, *18*(10), 1259–1264.

Stewart, J. H., and J. E. Carlson (1976), *Geologic map of north-central Nevada*, University of Nevada.

Stock, G. M., T. A. Ehlers, and K. A. Farley (2006), Where does sediment come from? Quantifying catchment erosion with detrital apatite (U-Th)/He thermochronometry, *Geology*, *34*(9), 725–728.

Sugiura, N. (1978), Further analysts of the data by Akaike's information criterion and the finite corrections, *Communications in Statistics-Theory and Methods*, *7*(1), 13–26.

Sumner, P., and W. Nel (2002), The effect of rock moisture on Schmidt hammer rebound: tests on rock samples from Marion Island and South Africa, *Earth Surface Processes and Landforms: The Journal of the British Geomorphological Research Group*, *27*(10), 1137–1142.

Sundell, K. E., and J. E. Saylor (2017), Unmixing detrital geochronology age distributions, *Geochemistry, Geophysics, Geosystems*, *18*(8), 2872–2886, doi:10.1002/2016GC006774.

Suppe, J. (1983), Geometry and kinematics of fault-bend folding, *American Journal of science*, *283*(7), 684–721.

Suppe, J. (1990), Geometry and kinematics of fault-propagation folding., *Ecologae Geologias Helvetiae*, *83*, 409–454.

Teng, L. S. (1990), Geotectonic evolution of late Cenozoic arc-continent collision in Taiwan, *Tectonophysics*, *183*(1-4), 57–76.

Tesson, J., B. Pace, L. Benedetti, F. Visini, M. Delli Rocioli, M. Arnold, G. Aumaître, D. Bourlès, and K. Keddadouche (2016), Seismic slip history of the Pizzalto fault (central Apennines, Italy) using in situ-produced ^{36}Cl cosmic ray exposure dating and rare earth element concentrations, *Journal of Geophysical Research: Solid Earth*, *121*(3), 1983–2003.

Thomson, K. D., D. F. Stockli, J. D. Clark, C. Puigdefàbregas, and A. Fildani (2017), Detrital zircon (U-Th)/(He-Pb) double-dating constraints on provenance and foreland basin evolution of the Ainsa Basin, south-central Pyrenees, Spain, *Tectonics*, *36*(7), 1352–1375, doi:10.1002/2017TC004504, 2017TC004504.

Török, Á., L. Forgó, T. Vogt, S. Löbens, S. Siegesmund, and T. Weiss (2007), The influence of lithology and pore-size distribution on the durability of acid volcanic tuffs, Hungary, *Geological Society, London, Special Publications*, *271*(1), 251–260.

Tranel, L. M., J. A. Spotila, M. J. Kowalewski, and C. M. Waller (2011), Spatial variation of erosion in a small, glaciated basin in the Teton Range, Wyoming, based on detrital apatite (U-Th)/He thermochronology, *Basin Research*, *23*(5), 571–590.

Trexler, C. C. (2018), *Structural Investigations of the Tectonic History of the Western Greater Caucasus Mountains, Republic of Georgia*, University of California, Davis.

Tricart, P. (1984), From passive margin to continental collision; a tectonic scenario for the Western Alps, *American Journal of Science*, *284*(2), 97–120.

Tucker, G. E., S. W. McCoy, A. C. Whittaker, G. P. Roberts, S. T. Lancaster, and R. Phillips (2011), Geomorphic significance of postglacial bedrock scarps on normal-fault footwalls, *Journal of Geophysical Research: Earth Surface*, *116*(F1).

Tye, A., and T. Stahl (2018), Field estimate of paleoseismic slip on a normal fault using the Schmidt hammer and terrestrial LiDAR: Methods and application to the Hebgen fault (Montana, USA), *Earth Surface Processes and Landforms*, *43*(11), 2397–2408.

Tye, A., A. Wolf, and N. Niemi (2019), Bayesian population correlation: A probabilistic approach to inferring and comparing population distributions for detrital zircon ages, *Chemical Geology*, *518*, 67–78.

van Baak, C. G., E. P. Radionova, L. A. Golovina, I. Raffi, K. F. Kuiper, I. Vasiliev, and W. Krijgsman (2015), Messinian events in the Black Sea, *Terra Nova*, *27*(6), 433–441.

van Baak, C. G., A. Grothe, K. Richards, M. Stoica, E. Aliyeva, G. R. Davies, K. F. Kuiper, and W. Krijgsman (2019), Flooding of the Caspian Sea at the intensification of Northern Hemisphere Glaciations, *Global and Planetary Change*, *174*, 153–163.

van Der Boon, A., K. Kuiper, G. Villa, W. Renema, M. Meijers, C. Langereis, E. Aliyeva, and W. Krijgsman (2017), Onset of Maikop sedimentation and cessation of Eocene arc volcanism in the Talysh Mountains, Azerbaijan, *Geological Society, London, Special Publications*, *428*(1), 145–169.

van der Boon, A., D. van Hinsbergen, M. Rezaeian, D. Gürer, M. Honarmand, D. Pastor-Galán, W. Krijgsman, and C. Langereis (2018), Quantifying Arabia–Eurasia convergence accommodated in the Greater Caucasus by paleomagnetic reconstruction, *Earth and Planetary Science Letters*, *482*, 454–469.

van der Woerd, J., L. Benedetti, M. Caffee, and R. Finkel (2000), Slip-rate and earthquake recurrence time on the Hebgen Lake fault (Montana): Constraints from surface exposure dating of alluvial terraces and bedrock fault scarp, *Eos (Transactions, American Geophysical Union)*, *81*(48), F1160.

van Hinsbergen, D. J., P. C. Lippert, G. Dupont-Nivet, N. McQuarrie, P. V. Doubrovine, W. Spakman, and T. H. Torsvik (2012), Greater India Basin hypothesis and a two-stage Cenozoic collision between India and Asia, *Proceedings of the National Academy of Sciences*, *109*(20), 7659–7664.

Vasiliev, I., G.-J. Reichart, and W. Krijgsman (2013), Impact of the Messinian Salinity Crisis on Black Sea hydrology: Insights from hydrogen isotopes analysis on biomarkers, *Earth and Planetary Science Letters*, *362*, 272–282.

Verdel, C., B. P. Wernicke, J. Hassanzadeh, and B. Guest (2011), A Paleogene extensional arc flare-up in Iran, *Tectonics*, *30*(3).

Vermeesch, P. (2004), How many grains are needed for a provenance study?, *Earth and Planetary Science Letters*, *224*(3), 441–451.

Vermeesch, P. (2012), On the visualisation of detrital age distributions, *Chemical Geology*, *312*, 190–194.

Vermeesch, P. (2013), Multi-sample comparison of detrital age distributions, *Chemical Geology*, *341*, 140–146.

Vermeesch, P. (2017), Dissimilarity measures in detrital geochronology, *Earth-Science Reviews*.

Villamor, P., N. Litchfield, D. Barrell, R. van Dissen, S. Hornblow, M. Quigley, S. Levick, W. Ries, B. Duffy, J. Begg, et al. (2012), Map of the 2010 Greendale Fault surface rupture, Canterbury, New Zealand: application to land use planning, *New Zealand Journal of Geology and Geophysics*, *55*(3), 223–230.

Vincent, S. J., A. C. Morton, A. Carter, S. Gibbs, and T. G. Barabadze (2007), Oligocene uplift of the Western Greater Caucasus: an effect of initial Arabia–Eurasia collision, *Terra Nova*, *19*(2), 160–166.

Vincent, S. J., A. C. Morton, F. Hyden, and M. Fanning (2013), Insights from petrography, mineralogy and U–Pb zircon geochronology into the provenance and reservoir potential of Cenozoic siliciclastic depositional systems supplying the northern margin of the Eastern Black Sea, *Marine and Petroleum Geology*, *45*, 331–348.

Vincent, S. J., F. Hyden, and W. Braham (2014), Along-strike variations in the composition of sandstones derived from the uplifting western Greater Caucasus: causes and implications for reservoir quality prediction in the Eastern Black Sea, *Geological Society, London, Special Publications*, *386*(1), 111–127.

Vincent, S. J., W. Braham, V. A. Lavrishchev, J. R. Maynard, and M. Harland (2016), The formation and inversion of the western Greater Caucasus Basin and the uplift of the western Greater Caucasus: Implications for the wider Black Sea region, *Tectonics*, *35*(12), 2948–2962.

Voronin, M., M. Gavrilov, and V. Khain (1959), Geological map of the USSR, Caucasus series sheet K-39-XXXI, scale 1:200,000, *Ministry of Geology and Mineral Protection USSR, Moscow*.

Wallace, R. E., M. G. Bonilla, and H. A. Villalobos (1984), Faulting related to the 1915 earthquakes in Pleasant Valley, Nevada, *Tech. rep.*, USGPO.

Wang, C. Y., I. H. Campbell, A. S. Stepanov, C. M. Allen, and I. N. Burtsev (2011), Growth rate of the preserved continental crust: II. Constraints from Hf and O isotopes in detrital zircons from Greater Russian Rivers, *Geochimica et Cosmochimica Acta*, *75*(5), 1308–1345.

Wei, Z., H. He, et al. (2013), Weathering history of an exposed bedrock fault surface interpreted from its topography, *Journal of Structural Geology*, *56*, 34–44.

Weislogel, A. L., S. A. Graham, E. Z. Chang, J. L. Wooden, G. E. Gehrels, and H. Yang (2006), Detrital zircon provenance of the Late Triassic Songpan-Ganzi complex: Sedimentary record of collision of the North and South China blocks, *Geology*, *34*(2), 97–100.

Wells, D. L., and K. J. Coppersmith (1994), New empirical relationships among magnitude, rupture length, rupture width, rupture area, and surface displacement, *Bulletin of the seismological Society of America*, *84*(4), 974–1002.

Wernicke, B., J. L. Davis, N. A. Niemi, P. Luffi, and S. Bisnath (2008), Active megadetachment beneath the western United States, *Journal of Geophysical Research: Solid Earth*, *113*(B11).

Wesnousky, S. G. (2008), Displacement and geometrical characteristics of earthquake surface ruptures: Issues and implications for seismic-hazard analysis and the process of earthquake rupture, *Bulletin of the Seismological Society of America*, *98*(4), 1609–1632.

Wiatr, T., I. Papanikolaou, T. Fernández-Steeger, and K. Reicherter (2015), Bedrock fault scarp history: Insight from t-LiDAR backscatter behaviour and analysis of structure changes, *Geomorphology*, *237*, 119–129.

Wicks, C. W., W. Thatcher, D. Dzurisin, and J. Svarc (2006), Uplift, thermal unrest and magma intrusion at Yellowstone caldera, *Nature*, *440*(7080), 72.

Winkler, S. (2005), The Schmidt hammer as a relative-age dating technique: potential and limitations of its application on Holocene moraines in Mt Cook National Park, Southern Alps, New Zealand, *New Zealand Journal of Geology and Geophysics*, *48*(1), 105–116.

Winkler, S., J. A. Matthews, R. W. Mourne, and P. Wilson (2016), Schmidt-hammer exposure ages from periglacial patterned ground (sorted circles) in Jotunheimen, Norway, and their interpretative problems, *Geografiska Annaler: Series A, Physical Geography*, *98*(3), 265–285.

Witkind, I. J., W. B. Myers, J. B. Hadley, W. Hamilton, and G. D. Fraser (1962), Geologic features of the earthquake at Hebgen Lake, Montana, August 17, 1959, *Bulletin of the Seismological Society of America*, *52*(2), 163–180.

Wobus, C., K. X. Whipple, E. Kirby, N. Snyder, J. Johnson, K. Spyropolou, B. Crosby, D. Sheehan, and S. Willett (2006), Tectonics from topography: Procedures, promise, and pitfalls, *Special papers-Geological Society of America*, *398*, 55.

Wolf, R., K. Farley, and D. Kass (1998), Modeling of the temperature sensitivity of the apatite (U–Th)/He thermochronometer, *Chemical Geology*, *148*(1-2), 105–114.

Woodward, N. B., S. E. Boyer, and J. Suppe (1989), Balanced geological cross-sections, *Short Course in Geology*, *6*, 132.

Wu, F.-Y., W.-Q. Ji, J.-G. Wang, C.-Z. Liu, S.-L. Chung, and P. D. Clift (2014), Zircon U–Pb and Hf isotopic constraints on the onset time of India-Asia collision, *American Journal of Science*, *314*(2), 548–579.

Yang, J., S. Gao, C. Chen, Y. Tang, H. Yuan, H. Gong, S. Xie, and J. Wang (2009), Episodic crustal growth of North China as revealed by U-Pb age and Hf isotopes of detrital zircons from modern rivers, *Geochimica et Cosmochimica Acta*, *73*(9), 2660–2673.

Zagorevski, A., and C. van Staal (2011), The record of Ordovician arc–arc and arc–continent collisions in the Canadian Appalachians during the closure of Iapetus, in *Arc-continent collision*, pp. 341–371, Springer.

Zakariadze, G. S., Y. Dilek, S. A. Adamia, R. Oberhänsli, S. Karpenko, B. Bazylev, and N. Solov'eva (2007), Geochemistry and geochronology of the Neoproterozoic Pan-African Transcaucasian Massif (Republic of Georgia) and implications for island arc

evolution of the late Precambrian Arabian–Nubian Shield, *Gondwana Research*, *11*(1-2), 92–108.

Zhuang, G., Y. Najman, S. Guillot, M. Roddaz, P.-O. Antoine, G. Métais, A. Carter, L. Marivaux, and S. H. Solangi (2015), Constraints on the collision and the pre-collision tectonic configuration between India and Asia from detrital geochronology, thermochronology, and geochemistry studies in the lower Indus basin, Pakistan, *Earth and Planetary Science Letters*, *432*, 363–373.

Zonenshain, L. P., and X. Le Pichon (1986), Deep basins of the Black Sea and Caspian Sea as remnants of Mesozoic back-arc basins, *Tectonophysics*, *123*(1-4), 181–211.

Zreda, M., and J. S. Noller (1998), Ages of prehistoric earthquakes revealed by cosmogenic chlorine-36 in a bedrock fault scarp at Hebgen Lake, *Science*, *282*(5391), 1097–1099.

Zubakov, V. (2001), History and causes of variations in the Caspian Sea level: The Mio-pliocene, 7.1–1.95 million years ago, *Water Resources*, *28*(3), 249–256.